

Experimental and Numerical Studies on Low Emission Syngas Combustion

A Thesis

Submitted for the Degree of

Doctor of Philosophy

by

Santanu Pramanik



Department of Mechanical Engineering

Indian Institute of Science

Bengaluru, India

September, 2018

Dedicated to

My Parents

and

My Teachers

Table of Contents

Contents.....	i
Abstract	vii
Acknowledgments.....	ix
List of Tables	x
List of Figures.....	xi
Chapter 1 Introduction	1
1.1 Integrated gasification combined cycle	1
1.2 Challenges with syngas as a fuel.....	2
1.3 Low-emission combustion strategies	3
1.4 Objectives of the current study	5
1.5 Organization of the thesis	6
Chapter 2 Literature review	8
2.1 Air pre-heating and exhaust gas recirculation.....	8
2.2 Reverse flow combustion chamber	10
2.2.1 Circular turbulent jet in confined counterflow	12
2.2.2 Mixing in coaxial jets	14
2.3 MILD combustion	14

2.3.1 MILD combustion in the reverse flow configuration	18
2.3.2 MILD combustion of syngas	21
2.3.3 Jet in hot coflow (JHC)	23
2.3.4 Flame structure under MILD conditions.....	24
2.4 Numerical studies on combustion in the reverse flow configuration	28
2.4.1 Numerical studies on the jet in hot coflow (JHC) burner	29
2.5 Scaling of combustion chambers.....	31
2.5.1 Scaling of MILD combustion chambers	33
2.6 Summary	35
Chapter 3 Experimental facilities.....	36
3.1 Combustor test rig	36
3.2 Other components of the experimental setup.....	40
3.3 Optical diagnostic techniques and system	42
3.3.1 Single pulse Nd:YAG laser	44
3.3.2 Dye laser	45
3.3.3 Divergent laser sheet optics and collimator	46
3.3.4 Imaging system: Camera and intensifier.....	48
3.3.5 Programmable timing unit (PTU).....	48
3.4 Exhaust gas analyzer	49
3.5 Microphone	50
3.6 Summary	50

Chapter 4 Transient combustion characteristics	51
4.1 Experimental details	52
4.1.1 Operating conditions	52
4.1.2 Measurement techniques and data processing	55
4.2 Results and discussions.....	57
4.2.1 Flame visualization	57
4.2.2 Mean and standard deviation of the OH* chemiluminescence	59
4.2.3 Ignition kernel and stabilization	63
4.2.4 Sound pressure level (SPL) measurements	65
4.2.5 Power spectral density of the chemiluminescence and noise signal	65
4.2.6 Effect of oxidizer preheat temperature	69
4.3 Summary	75
Chapter 5 Laser diagnostics of combustion.....	76
5.1 Measurement techniques and data processing	76
5.1.1 Rayleigh thermometry	76
5.1.2 OH planar laser-induced fluorescence	81
5.2 Results and discussion	84
5.2.1 Mean centreline temperature.....	84
5.2.2 Temperature variation in the radial direction	87
5.2.3 Standard deviation of temperature along the centreline	91
5.2.4 Mean OH distribution	92

5.2.5 Average profiles of OH in the radial direction.....	95
5.2.6 Standard deviation of OH in the radial direction.....	98
5.2.7 Instantaneous OH distribution.....	99
5.2.8 Near-nozzle flame structure	103
5.2.9 OH quantification at the downstream locations	106
5.2.10 Modeling	107
5.3 Summary	110
Chapter 6 Combustor Emissions.....	112
6.1 Results and discussions.....	112
6.1.1 Emissions of CO and NO _x	112
6.1.2 Comparison of emissions with PSR	113
6.1.3 Effect of chamber temperature	116
6.1.4 Effect of H ₂ content in the fuel.....	122
6.2 Summary	124
Chapter 7 Numerical modelling studies	125
7.1 Experimental conditions modelled.....	126
7.2 Numerical formulation.....	127
7.2.1 Computational domain and boundary conditions.....	127
7.2.2 Numerical details	130
7.2.3 Governing equations	131
7.2.4 Chemical kinetics	136

7.3 Results and discussions.....	136
7.3.1 Comparison with temperature measurements	136
7.3.2 Comparison with OH-PLIF	142
7.3.3 Comparison with measured CO emissions	150
7.3.4 Mean velocity	151
7.3.5 Mixing between the oxidizer and the exhaust in the outer shear layer	154
7.3.6 Mixing between the fuel and oxidizer in the inner shear layer	155
7.3.7 Early ignition in FGM models.....	157
7.4 Summary	161
Chapter 8 Scaling of the combustor	163
8.1 Scaling criteria	163
8.1.1 Constant velocity	164
8.1.2 Constant residence time	164
8.1.3 Constant volume to jet momentum ratio (CM)	166
8.1.4 Constant volume to jet kinetic energy ratio (CK)	166
8.2 Problem formulation.....	167
8.3 Results and discussions.....	169
8.3.1 Pressure drop	169
8.3.2 Axial velocity along the centreline	170
8.3.3 Mean axial velocity along the radius	174
8.3.4 Standard deviation of the velocity along the radius	176

8.3.5 Recirculation ratio	178
8.3.6 Residence time.....	181
8.3.7 Instantaneous and mean temperature distribution	183
8.3.8 Instantaneous and mean OH mass fraction	187
8.3.9 CO emissions.....	191
8.4 Summary.....	193
Chapter 9 Conclusions	195
9.1 Summary of present work.....	195
9.2 Contributions of the present work.....	198
9.3 Recommendations for future work.....	199
Bibliography	200

Abstract

The present study concerns experimental and numerical investigation of the combustion of low-calorific value syngas in an optically accessible reverse flow combustion chamber. Several modes of operation are investigated to identify the best strategy for stable operation with low emissions of NO_x and CO. The first part of the study investigates the combustion dynamics in the chamber and establishes the range of parameters for stable operation using OH^* chemiluminescence (5 kHz), noise (50 kHz), and exhaust emissions measurements (NO_x and CO). The combustion dynamics have been investigated as a function of the global equivalence ratio (0.32 - 0.89), $\text{O}_2\%$ in the co-flow (7.6 - 21%), and the oxidizer preheat temperature ($\sim 400 - 800$ K). The variation of these parameters resulted in different operating conditions designated as: conventional ($\Phi_{\text{global}} = 0.8$), ultra-lean ($\Phi_{\text{global}} = 0.32$), transition ($\Phi_{\text{global}} = 0.47$, $\text{O}_2 = 14.3\%$ in oxidizer), and MILD ($\Phi_{\text{global}} = 0.89$, $\text{O}_2 = 7.6\%$ in oxidizer) combustion modes. For all cases, autoignition was observed to be the mode of flame stabilization that indicated the role of H_2 in reducing the ignition delay. The conventional mode displayed the highest sound pressure level (SPL) and fluctuations in the reaction zone (OH^*). The most stable operation was obtained for the MILD case where the SPL decreased by 6 dB caused by a suppression of the high-frequency (> 800 Hz) longitudinal modes. In the second part of the study, OH concentration and temperature are measured using Planar Laser-induced Fluorescence (PLIF) and Rayleigh thermometry to provide a detailed understanding of the reaction zone structure. The OH radical, which is a marker of the reaction zone, shows maximum intensity for the conventional case and lowest intensity for the MILD case. The instantaneous images show a complex reaction zone with thin structures near the inlet and progressive distribution of OH at the bottom. The

temperature measurements reveal a uniform thermal field throughout except very close to the centreline. Such a distribution can provide superior heat transfer characteristics in furnaces. The maximum temperature is measured for the conventional case (~ 1700 K), while the temperature is similar for the ultra-lean, transition, and MILD cases (~ 1300 K) supporting the observations of low NO_x emissions.

In the third part of the study, we evaluate the performance of the combustor by measuring NO_x and CO emissions. The NO_x emission is less than 1-ppm for all the cases, while the CO emission is highest for the MILD case (461-ppm) and lowest for the conventional case (32-ppm). In the last two parts of the study, the experimentally generated data is used to validate models that are subsequently used to numerically simulate scaled-up designs of the combustor with power ranging from 3.3 kW to 25 kW. The influence of four different scaling criteria on the performance of the combustor is evaluated. These are constant velocity (CV), constant residence time (CRT), constant volume-to-jet momentum ratio (CM), and constant volume-to-jet kinetic energy ratio (CK). The CV criterion performs the best in terms of pressure drop and CO emissions. Overall, the current investigation establishes that the combustion of low calorific value syngas can be performed in a reverse flow configuration with low emissions and potential for scaling to industrial sizes.

Acknowledgments

I express my sincere gratitude to my advisor, Prof. R. V. Ravikrishna, for his constant support and guidance through several hurdles of academic and personal life. Above all, he has provided us with a wonderful lab environment and relaxed intellectual atmosphere where each individual can nurture and express their true potential. In him, I have found a Guru whose path and life I would like to emulate. I would also like to thank Prasad Sir and Amrit for their help in conducting the experiments and providing valuable guidance on a regular basis. I thank Kuppuraj for helping with some experiments. Life in the lab would have been very different without the presence of Madan Sir, Krishna, Surya, Saurav, Atanu, Pabitra, Anupam, Pallav and Nishanth. Special thanks to Sindhu, professor's secretary, for handling all the paperwork that allowed us to focus on the research. Academic life would have been much difficult without the help from the ME Department and office staff in handling the official paperwork.

Life at IISc would have been incomplete without the presence of dear friends - Harsha, Dilip, Dipanjan, Arka, Vighnesh, Ankush, Ramya, and Priya. I have been fortunate to come in contact with Vivekananda Study Circle and Gokul Sir. I owe a lot of my personal and spiritual growth to them. Although far away, my parents and four sisters have been the greatest source of inspiration and support in my life. I am what I am today because of them. I thank Sri for her love and gentle presence that makes my life complete. Finally, I bow down to The Lord Almighty for this blessed life.

List of Tables

Table 1.1: Comparison of the properties of methane with a particular composition of syngas.	3
Table 2.1: Lowest emissions of NO _x and CO reported from selected publications available in the literature	18
Table 4.1: Experimental conditions.	52
Table 4.2: Estimated Damköhler number for the conventional, ultra-lean, and the MILD cases	54
Table 5.1: OH radical mole fraction at various axial locations in the chamber.	106
Table 6.1: Emissions of CO and NO _x from the combustion chamber normalized to 15% O ₂	113
Table 7.1: Turbulence and combustion models	125
Table 7.2: Boundary conditions for the MILD and the ultra-lean cases.	126
Table 8.1: Summary of the scaling approaches	167
Table 8.2: Summary of the dimensions and inlet conditions for the baseline and the scaled-up models.	168

List of Figures

Figure 1.1: Schematic diagram of an IGCC plant with pre-combustion carbon capture [3]. ..	2
Figure 1.2: Image of the computed mean axial velocity in the reverse flow configuration with superimposed streamlines.	5
Figure 2.1: (a) Schematic of the stagnation point reverse flow (SPRF) combustion chamber (adapted from [19]) and (b) flame luminosity image in the SPRF chamber (adapted from [20]).	11
Figure 2.2: (a) Schematic diagram of a circular turbulent jet in confined counterflow [25]. The jet to counterflow velocity ratio is u_j/u_o while the diameter ratio is d_j/D_o . (b) Variation of the non-dimensional jet penetration length to the jet-to-counterflow momentum flux ratio parameter [25].	13
Figure 2.3: Flame luminosity images under MILD (adapted from [33]) and colourless distributed combustion (CDC) (adapted from [34]) conditions.	15
Figure 2.4: The combustion regimes diagram proposed by Rao and Levy [36] (adapted from [35]) showing the relationship between the inlet temperature, O_2 concentration, and percentage of diluents (or recirculation ratio) in establishing flameless combustion.	17
Figure 2.5: Reverse flow MILD combustion furnaces investigated by (a) Plessing et al. (adapted from [38]) and (b) Li et al. (adapted from [33]).	20
Figure 2.6: Reverse flow MILD combustion furnaces investigated by (a) Arghode et al. (adapted from [45]) and (b) Ye et al. (adapted from [42]).	21

Figure 2.7: MILD combustion of syngas in three different configurations namely coflow (left), cross jets (middle) and cyclonic cross jets (right) [50].	22
Figure 2.8: Schematic diagram of the jet in hot coflow burner (left); images of ethylene JHC flames at different O ₂ concentrations in the coflow (right) [54].	24
Figure 2.9: Instantaneous OH-PLIF images at $\Phi = 0.65$ and loadings of 2, 4.5, 7.2, 9.4, 10.7 g/s (from left to right) in the SPRF combustor [58].	25
Figure 2.10: Flame luminosity and instantaneous OH-PLIF images for the flame, transition, and flameless cases [49].	27
Figure 2.11: Isosurface of normalized heat release rates under MILD conditions [61].	28
Figure 2.12: Details of a 150-kW MILD combustion burner scaled from 3 kW using constant velocity (CV), constant residence time (CRT) and Cole's approach [90].	34
Figure 3.1: Schematic diagram of the combustion chamber (left) and the combustion chamber in operation (right). All dimensions are in millimeter.	37
Figure 3.2: A cross-sectional view of the combustion chamber showing the optical access.	38
Figure 3.3: Schematic diagram of the experimental setup	41
Figure 3.4: Species, temperature, and heat release rate profiles in a laminar counterflow diffusion flame. The fuel is syngas with 20% H ₂ , 20% CO and 60% N ₂ . The oxidizer is air (top) and air/N ₂ with 6% O ₂ (bottom) at 1000 K. The strain rate is maintained at 230s ⁻¹ . The heat release rate profiles closely follow that of OH and OH* profiles.	43
Figure 3.5: Optical pathway of the pump beam through the dye laser showing various components [95].	46
Figure 3.6: Schematic diagram of the divergent sheet optics coupled with the collimator showing the laser beam path [96].	47
Figure 4.1: Schematic diagram of the experimental setup. (Acronyms: TC – thermocouple, DAQ – data acquisition system, MP - microphone).	56

Figure 4.2: Natural flame luminosity images for the cases (a) conventional, (b) ultra-lean, (c) transition, and (d) MILD have been shown. The camera exposure time was 0.5 seconds. 58

Figure 4.3: Mean and standard deviation images of OH* chemiluminescence signal. From left, the images are for the cases (a) conventional (A50), (b) ultra-lean (A125), (c) transition (A85N40), and (d) MILD (A45N80), respectively. Z refers to the distance from the exit plane of the reactants while R is the radial distance. (Acronym: SD - standard deviation). 60

Figure 4.4: Histogram of the global OH* counts for the conventional, ultra-lean, transition, and the MILD cases. 62

Figure 4.5: Instantaneous OH* chemiluminescence images showing the formation and merging of autoignition kernels for the conventional (top), ultra-lean (middle) and the MILD (bottom) cases. Z refers to the distance from the exit plane of the reactants while R is the radial distance. 64

Figure 4.6: Power spectral density of the OH* chemiluminescence signal for the conventional (A50), ultra-lean (A125), transition (A85N40), and MILD (A45N80) cases. .. 66

Figure 4.7: Power spectral density of the acoustic signal for the conventional (A50), ultra-lean (A125), transition (A85N40), and MILD (A45N80) cases..... 67

Figure 4.8: Variation of temperature and CO emissions with a decrease in the oxidizer preheat temperature..... 70

Figure 4.9: Flame visualization at different preheat temperatures of the oxidizer. 71

Figure 4.10: Variation of oxidizer temperature and sound pressure level (dB) with time. The dotted lines represent linear fits to the SPL data. 72

Figure 4.11: Power spectral density (*PSD*) of the noise signal at various inlet temperatures of the oxidizer stream. 74

Figure 5.1: Schematic diagram of the laser diagnostics setup for Rayleigh thermometry measurements. (Acronyms: IRO – intensified relay optics, EM - energy monitor, BD - beam dump, PR - polarization rotator, FOV - field of view). All dimensions are in-mm.	77
Figure 5.2: Sample sheet profile (blue line) obtained from Rayleigh scattering images in air (295 K) at an axial location of 100-mm from the injection plane. The region marked in red represents the area over which the signal was averaged to obtain the Rayleigh scattering signal.	78
Figure 5.3: Variation of Rayleigh scattering cross section simulated in a counterflow diffusion flame of syngas with air and N ₂ diluted air at two different strain rates. The oxidizer is at 1000 K.	81
Figure 5.4: Schematic diagram of the laser diagnostics setup for OH-PLIF. (Acronyms: IRO – intensified relay optics, BD - beam dump, FOV - field of view). All dimensions are in-mm.	82
Figure 5.5: Image of the McKenna flat flame burner (left) and a sample OH PLIF image (right).....	83
Figure 5.6: Axial variation of the centreline temperature for the 4 cases. The dashed red lines indicate the adiabatic flame temperatures calculated for the inlet conditions mentioned in Table 4.1	86
Figure 5.7: Radial distribution of temperature at various axial locations for the conventional (A50) case.	88
Figure 5.8: Radial distribution of temperature at various axial locations for the MILD (A45N80) case.	89
Figure 5.9: Radial distribution of temperature at various axial locations for the transition (A85N40) case.	90

Figure 5.10: Radial distribution of temperature at various axial locations for the ultra-lean (A125) case.....	90
Figure 5.11: Standard deviation of temperature along the centreline at various axial locations for the conventional (A50), MILD (A45N80), transition (A85N40) and the ultra-lean (A125) cases	91
Figure 5.12: Mean OH contours for the conventional, ultra-lean, transition, and MILD cases. The color bar represents OH counts in arbitrary units.	93
Figure 5.13: Mean OH distribution along the chamber centerline for the conventional, ultra-lean, transition, and MILD cases.	94
Figure 5.14: Mean OH distribution along the chamber radius for the conventional (C), ultra-lean (UL), transition (T), and MILD (M) cases at axial locations of 25-mm, 50-mm, 75-mm, 100-mm, 150-mm, and 200-mm. The axis for the OH counts for the conventional case is on the right side of the plots.	96
Figure 5.15: Distribution of OH standard deviation along the chamber radius for the conventional (C), ultra-lean (UL), transition (T), and MILD (M) cases at axial locations of 25-mm, 50-mm, 75-mm, 100-mm, 150-mm, and 200-mm. The axis for the OH counts for the conventional case is on the right side of the plots.	99
Figure 5.16: Instantaneous OH-PLIF images for the conventional, ultra-lean, transition, and MILD cases. Selected images captured at 5 axial locations (consecutively) in the chamber were stitched to generate these images. The colour bar represents OH counts in arbitrary units.	102
Figure 5.17: Instantaneous OH (top), the norm of the 2D OH gradient (middle), and the mean OH (bottom) for the (from left) conventional, ultra-lean, transition, and MILD cases. Z refers to the distance from the exit plane of the reactants while R is the radial distance.	104

Figure 5.18: PDF of the maximum values of the norm of the 2D OH gradient obtained from 250 instantaneous images for each of the conventional, ultra-lean, transition, and MILD cases. 105

Figure 5.19: Schematic diagram of the plug flow reactor model. 108

Figure 5.20: (a) OH mass fraction, (b) heat release rate, and (c) rate of production of OH with axial distance for the isothermal plug flow reactor with 3% and 21% O₂. 109

Figure 6.1: Reactor network diagram for comparison of emissions. Here, R is the recirculation ratio. The value of R varies from 0 - 2. 114

Figure 6.2: Comparison of CO emissions from the chamber and that from the perfectly stirred reactor model. Acronyms: τ_{res} = residence time, R = recirculation ratio. The R varies from 0 - 2 while τ_{res} varies from 0.05 - 0.15s. 115

Figure 6.3: Variation of CO emissions (normalized to 15% O₂) with exhaust temperature using the PSR model. The fuel is 20% CO, 20% H₂, and 60% N₂. The temperature has been varied by changing the temperature of the exhaust that is recirculated. The recirculation ratio $R = 2$ and $\tau_{res} = 0.15$ s. The emission corresponding to the experimental conditions is shown with larger markers. 118

Figure 6.4: Variation of NO emissions (normalized to 15% O₂) with exhaust temperature using the PSR model. The fuel is 20% CO, 20% H₂, and 60% N₂. The temperature has been varied by changing the temperature of the exhaust that is recirculated. The recirculation ratio $R = 2$ and $\tau_{res} = 0.15$ s. The emission corresponding to the experimental conditions is shown with larger markers. 119

Figure 6.5: Quantitative reaction path diagram (QRPD) with the absolute rate of production (ROP) from various reactions showing the pathways for NO formation for the cases conventional (A50), ultra-lean (A125), and MILD (A45N80) cases at 1650 K and 1850 K. 121

Figure 6.6: Comparison of CO emissions (normalized to 15% O₂) for 10%, 20% (base case), and 30% H₂ (by vol.) in the fuel (30%, 20%, and 10% CO, respectively) with 60% N₂ in all the cases using the PSR model. The recirculation ratio $R = 2$ and $\tau_{res} = 0.15$ s. Acronyms: τ_{res} = residence time, UL - ultra-lean, Conv. - conventional, Tr. - transition, M - MILD, C1 - conventional case with $\Phi = 0.89$, R = recirculation ratio..... 123

Figure 7.1: (a) Image of the experimental test rig in operation where the flame is visible through the optical access, (b) flame luminosity images for the ultra-lean (UL) and the MILD (M) cases, (c) wall temperature profile for the ultra-lean and the MILD cases. 127

Figure 7.2: (a) Schematic of the combustion chamber with boundary conditions, (b) Power spectrum of the axial turbulent kinetic energy at two different locations in the outer shear layer, $(r, z) = (7, 64)$ -mm and $(7, 144)$ -mm from the injection plane, (c) image of the grid used for simulations. 129

Figure 7.3: Comparison of the experimentally measured mean centerline temperature with the predictions of the numerical simulations for the MILD (top) and ultra-lean (bottom) cases. 138

Figure 7.4: Comparison of the experimentally measured mean radial temperature with the predictions of the numerical simulations for the MILD case. 140

Figure 7.5: Comparison of the experimentally measured mean radial temperature with the predictions of the numerical simulations for the ultra-lean case. 141

Figure 7.6: Qualitative comparison of the experimentally obtained instantaneous OH-PLIF images with the predictions of the numerical simulations for the MILD and the ultra-lean cases. 143

Figure 7.7: Comparison of the experimentally measured mean OH distribution with the predictions of the numerical simulations for the MILD (top) and ultra-lean (bottom) cases. 144

Figure 7.8: Comparison of the experimentally measured mean OH distribution with the predictions of the numerical simulations for the MILD case.	146
Figure 7.9: Comparison of the experimentally measured mean OH distribution with the predictions of the numerical simulations for the ultra-lean case.	147
Figure 7.10: Comparison of the experimentally measured mean OH volume fraction (ppm) with the predictions of the numerical simulations for the MILD (top) and ultra-lean (bottom) cases.	149
Figure 7.11: Comparison of the experimentally measured CO emissions with the numerically predicted values for the MILD (top) and the ultra-lean (bottom) cases.	151
Figure 7.12: (a) Streamlines superimposed over the mean axial velocity for the MILD case obtained from DES-EDC simulation. Variation of axial velocity along the centerline with axial distance for the (b) MILD and the (c) ultra-lean cases.	153
Figure 7.13: Variation of the recirculation ratio (R) with axial distance for the MILD and the ultra-lean cases.	155
Figure 7.14: Variation of the mean mixture fraction with radial distance for the MILD (top) and the ultra-lean (bottom) cases. The green dashed line shows the stoichiometric mixture fraction for the two cases.	157
Figure 7.15: Contours of predicted OH mole fraction (X_{OH}) and temperatures (T) for the MILD and ultra-lean cases. The green line represents instantaneous isoline for the stoichiometric mixture fraction (f_{st}). The f_{st} for the MILD and the ultra-lean cases are 0.23 and 0.45, respectively.	158
Figure 7.16: Contours of predicted time-averaged progress variable for the FGM and the EDC cases under MILD conditions.	161
Figure 8.1: Comparison of the sizes of the baseline and the scaled-up combustion chambers.	168

Figure 8.2: (a) Variation of the non-dimensional axial velocity ($U^* = U/U_{o,f}$) along the centreline with non-dimensional axial distance (x/D_f) for the baseline, constant velocity (CV), constant residence time (CRT), constant volume to jet momentum (CM), and constant volume to jet kinetic energy (CK) cases. (b) Plot showing a quadratic fit to the non-dimensional velocity profiles, overlapped with velocity correlations for unconfined circular turbulent jet [128], confined circular turbulent jet [129], and circular turbulent jets with strong coflow [27]..... 172

Figure 8.3: Variation of the non-dimensional axial velocity ($U^* = U/U_{o,f}$) with non-dimensional radial distance ($r^* = r/D_f$) at various axial distances (x/D_f) for the baseline, constant velocity (CV), constant residence time (CRT), constant volume to jet momentum (CM), and constant volume to jet kinetic energy (CK) cases..... 175

Figure 8.4: Radial variation of the standard deviation of the velocity normalized by mean inlet velocity along the centreline at various axial distances for the baseline, constant velocity (CV), constant residence time (CRT), constant volume to jet momentum (CM), and constant volume to jet kinetic energy (CK) cases. 178

Figure 8.5: (a) Variation of the recirculation ratio (R) with non-dimensional axial distance for the baseline, constant velocity (CV), constant residence time (CRT), constant volume to jet momentum (CM), and constant volume to jet kinetic energy (CK) cases. (b) Instantaneous velocity vectors with streamlines for the CK case showing the entrainment of returning exhaust gases. 180

Figure 8.6: Estimated forward (τ_f), reverse flow (τ_r), and global (τ_G) residence times for the baseline, constant velocity (CV), constant residence time (CRT), constant volume to jet momentum (CM), and constant volume to jet kinetic energy (CK) cases. 182

Figure 8.7: Instantaneous temperature contours for the baseline, constant velocity (CV), constant residence time (CRT), constant volume to jet momentum (CM), and constant volume to jet kinetic energy (CK) cases 185

Figure 8.8: Variation of the mean temperature with non-dimensional axial and radial distances for the baseline, constant velocity (CV), constant residence time (CRT), constant volume to jet momentum (CM), and constant volume to jet kinetic energy (CK) cases. 186

Figure 8.9: Instantaneous OH mass fraction contours and contourlines at OH mass fractions of 1×10^{-4} , 2×10^{-4} , and 3×10^{-4} for the baseline, constant velocity (CV), constant residence time (CRT), constant volume to jet momentum (CM), and constant volume to jet kinetic energy (CK) cases..... 189

Figure 8.10: Variation of the mean OH mass fraction with non-dimensional axial and radial distances for the baseline, constant velocity (CV), constant residence time (CRT), constant volume to jet momentum (CM), and constant volume to jet kinetic energy (CK) cases. 191

Figure 8.11: Mean CO emissions for the baseline, constant velocity (CV), constant residence time (CRT), constant volume to jet momentum (CM), and constant volume to jet kinetic energy (CK) cases. 193

Chapter 1

Introduction

Energy security, global warming, and climate change concerns have renewed our interest in alternative fuels such as syngas. Syngas is a mixture of $\text{CO}/\text{H}_2/\text{CO}_2/\text{CH}_4/\text{N}_2$ that can be obtained from the gasification of solid fuels such as coal and biomass. Although there is growing consensus among developed and developing countries in replacing fossil fuels with renewables such as solar and wind, coal will remain a significant contributor to our future energy mix due to its large deposits in the US, China, and India. However, coal combustion, while being a major producer of CO_2 , has also been associated with the destruction of the water resources, air quality, and the environment. This has intensified the search for novel technologies that can address some of these global challenges while providing energy security to both the developed and developing nations. The use of syngas obtained from gasified coal or biomass in Integrated Gasification Combined Cycle (IGCC) technology is a promising near-term solution that can potentially address these concerns.

1.1 Integrated gasification combined cycle

Integrated gasification combined cycle (IGCC) combines coal gasification with combined cycle (Brayton and Rankine) for power generation. The schematic of a typical IGCC power plant with pre-combustion carbon capture is shown in **Figure 1.1**. As compared to its nearest competitor - the super-critical pulverized coal boiler plant - the IGCC technology can reduce emission of carbon monoxide by 82%, oxides of nitrogen by 24%, sulphur dioxide by 71%, mercury by 66%, fluorides by 97%, sulphuric acid mist by 90%, and

Introduction

particulate matter by 58% [1]. Further, gasification of coal provides the lowest-cost method of CO₂ mitigation by the capture of carbon and storage in geologic beds [2]. The gasification of bio-resources such as wood residues, paper, pulp, and agricultural waste to produce syngas is also promising as it results in near-zero net CO₂ emissions.

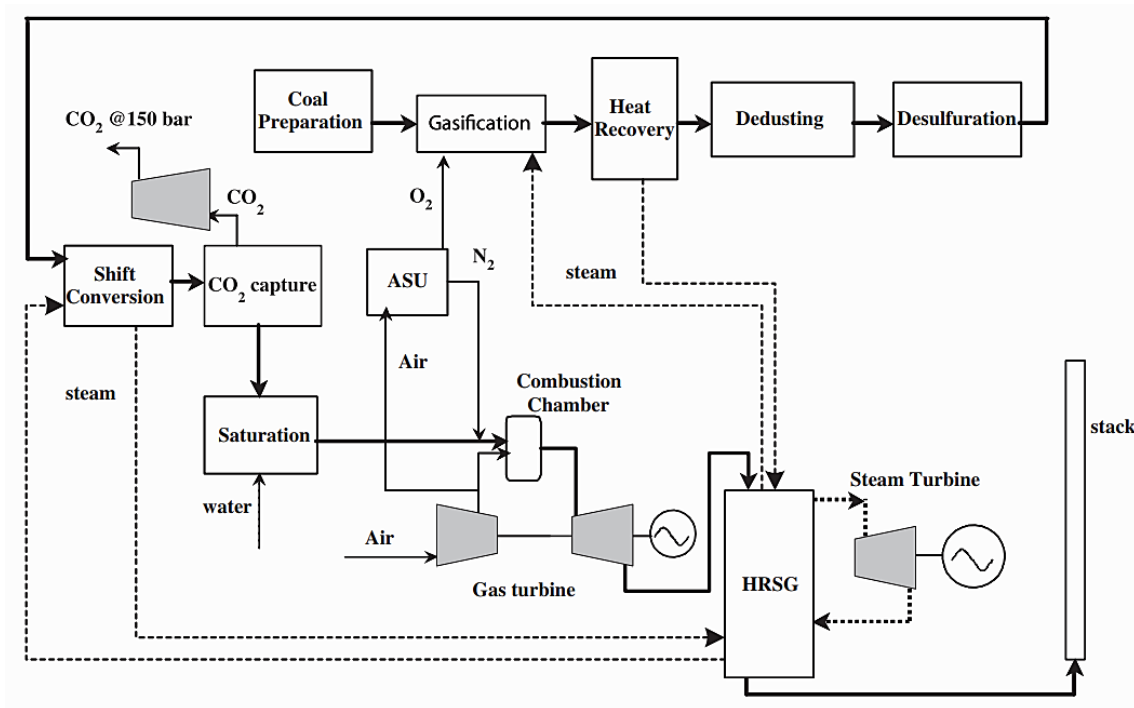


Figure 1.1: Schematic diagram of an IGCC plant with pre-combustion carbon capture [3].

1.2 Challenges with syngas as a fuel

However, properties of syngas such as calorific value, ignition delay, and flammability limits (**Table 1.1**) that control the combustion process differ significantly from those of other conventional fuels such as methane. Methane as a fuel has been widely used and investigated over several decades resulting in optimized combustion devices. This also implies that devices optimized for methane combustion may not be suitable for syngas. Even within syngas, the composition and properties can vary significantly based on the type of gasification technology and biomass resource. As a result, there is significant interest in the

Introduction

research and development of newer and more efficient combustion technologies for coal and biomass-derived syngas that offer stable combustion with low emissions of pollutants.

Table 1.1: Comparison of the properties of methane with a particular composition of syngas.

Properties	Methane	Syngas
Composition	CH ₄	20% CO, 20% H ₂ , 60% N ₂
Mol. wt. (kg/kmol)	16	22.8
ρ (kg/m ³) at NTP	0.67	0.95
C_p (kJ/kg.K) at NTP	2.2203	1.2754
LHV (kJ/kg)	50032	4600
Stoichiometric A/F ratio	17.16	1.20
τ_{ig} (s) [$\Phi = 1$ with air, 1000 K, 1 atm]*	~ 1	~ 0.0004
T_{ad} (K) [$\Phi = 1$ with air]	2226	1930
Rich flammability limit (Φ) GRI 3.0, 298 K*	1.67	3.4
Lean flammability limit (Φ) GRI 3.0, 298 K*	0.5	0.55

* All simulations have been conducted in Chemkin using GRI 3.0. The ignition delay time (τ_{ig}) has been determined using homogeneous constant volume 0-D reactor. The flammability limit has been determined using premixed laminar flame speed calculations. Acronyms: LHV - lower heating value, T_{ad} - adiabatic flame temperature, Φ - equivalence ratio

1.3 Low-emission combustion strategies

Several strategies for combustion of methane can be adapted for syngas with the ultimate objectives of achieving combustion stability and low emissions of pollutants such as NO_x and CO. One such combustion strategy is lean premixed combustion that has been known to reduce thermal NO_x emissions by lowering the peak flame temperatures below 1800 K. However, these systems can suffer from critical issues such as flashback and autoignition that can damage an engine [4]. The presence of H₂ in syngas can only aggravate such situations due to its low autoignition delay (**Table 1.1**) and high flame speed. Lean premixed systems can also experience various combustion instabilities [5] and significant attention has been directed towards the control of these instabilities using active and passive methods. The composition of syngas can also influence multi-mode combustion instabilities in model gas turbine combustors [6]. Air staging is another combustion strategy that has been

Introduction

known to reduce NO_x emissions by enabling combustion at fuel-lean or rich conditions. Such techniques have been used in the trapped vortex combustor (TVC) that employs this RQL (rich-burn quick-quench lean-burn) strategy to reduce the overall NO_x emissions, while achieving combustion stability over a wide range of equivalence ratios [7]. The TVC has also been shown to operate stably on low-calorific value syngas obtained from biomass gasification [8][9][10] with $< 3\text{-ppm}$ NO_x emissions, but high emission of CO (0.03 - 0.2%). Such systems also require careful optimization, control, and sophisticated hardware for staging the air and fuel flows that can incur increased capital expenditure. The recirculation of cooled and inert exhaust gases (EGR) has also been known to reduce the NO_x emissions by increasing the ignition delay and reducing the peak flame temperatures [11], although these systems are prone to static instabilities due to the weakening of the combustion process.

Internal exhaust gas recirculation (IEGR) is another combustion strategy that has gained significant attention in recent times for increased combustion stability and reduced emissions. Here, the chamber geometry is modified to entrain the products of combustion into the incoming fresh reactants. The entrainment of the exhaust gases increases the combustion stability by increasing the temperature of the reactants, while the diluents when coupled with a heat loss mechanism reduce the peak temperatures, thereby decreasing the production and emission of thermal NO_x . Many such systems also use preheated air to enhance the stability limits of the system [12]. The residence time in such systems is also higher due to the longer traverse within the chamber. The reverse flow (RF) shown in **Figure 1.2** is one such promising configuration that can achieve high internal recirculation (IEGR) due to strong shear between the incoming and the outgoing streams. This allows an extended operation range similar to TVC, EGR due to internal recirculation and good mixing similar to premixed systems. Also, under some special circumstances, the reverse flow chamber can be operated in a mode with a nearly invisible flame known as MILD (moderate or intense low

Introduction

oxygen dilution) combustion with very low emissions of pollutants and noise. Such modes are also known as colourless distributed combustion (CDC) or flameless oxidation (FLOX) in the literature.

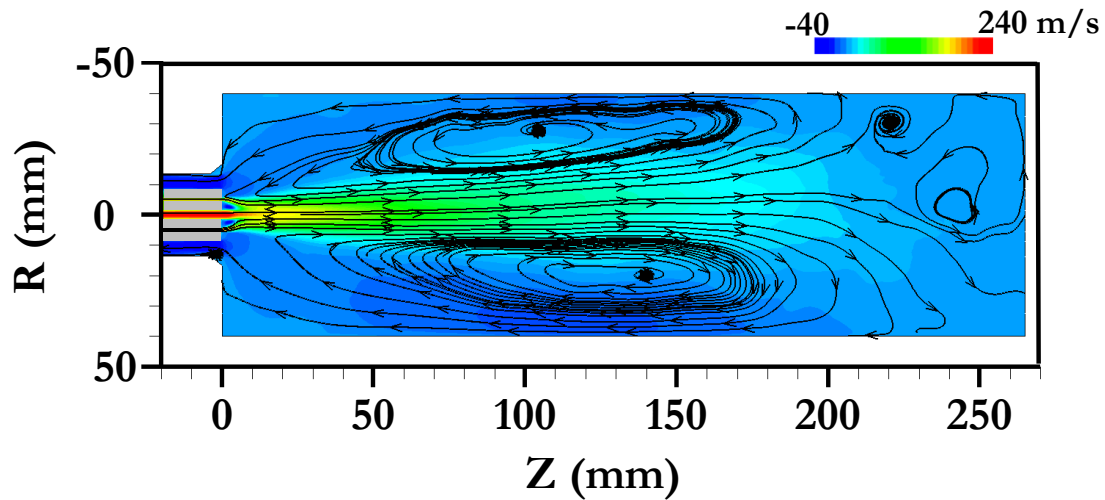


Figure 1.2: Image of the computed mean axial velocity in the reverse flow configuration with superimposed streamlines.

1.4 Objectives of the current study

The underlying objective of the current investigation is to explore various combustion strategies using low calorific value syngas in the reverse flow configuration for stability and low emissions. This has been conducted by employing experimental laser diagnostic techniques, emissions measurements, and simulations using various CFD models. The particular objectives of the thesis are as follows:

- Investigate the global and transient characteristics of various combustion modes as a function of flow parameters such as equivalence ratio, O_2 content in the oxidizer, and inlet temperature.

Introduction

- Study of reaction zone structure of these combustion modes using in-situ laser diagnostics. Also, generate quantitative experimental data for syngas combustion in the combustor that can be used for model validation.
- Performance evaluation of the combustion modes using emissions of NO_x and CO.
- Validation and identification of numerical models that can simulate the combustion phenomenon in the chamber.
- Develop and compare global scaling laws for larger power output using the validated numerical models.

1.5 Organization of the thesis

The thesis is divided into several chapters detailing the current state-of-the-art in the literature, results from the present work, and conclusions with directions for future research. Chapter 1 provides a background to the current work while explaining the specific objectives. Chapter 2 reviews the literature pertinent to the current work to identify the gaps and areas for further investigation. The relevant literature on various topics such as MILD combustion in the reverse flow configuration, MILD combustion of syngas, jet-in-hot-coflow, numerical studies on the reverse flow configuration, and scaling of combustion chambers have been summarized. In Chapter 3, details of the experimental test rig and measuring instruments have been presented. The results on global and transient operation characteristics of syngas combustion in the current combustor test rig have been presented in Chapter 4. Chapter 5 presents the results of laser diagnostic studies for a more detailed understanding of the reaction-zone structure. Quantitative data of temperature and OH concentration have also been presented in the combustor. Chapter 6 presents the results on the performance assessment of the combustor in terms of NO_x and CO emissions. Simple zero-dimensional reactor models have also been developed and validated to predict the influence of chamber

Introduction

temperature and syngas composition on the emissions. In Chapter 7, several numerical models are compared and validated using the experimental data presented in Chapter 5. The best model is identified and the discrepancies in the predictions of the other models with suggestions for improvements are presented. Chapter 8 presents the results on scaling of the combustion chamber to higher power outputs using the model validated in Chapter 7. Two new scaling criteria have been proposed based on phenomenological observations of the combustion occurring in the reverse flow configuration. Finally, Chapter 9 presents a summary of the major conclusions with recommendations for future work.

Chapter 2

Literature review

2.1 Air pre-heating and exhaust gas recirculation

Research on combustion with pre-heated premixed fuel-air mixtures was originally aimed at burning ultra-lean or using low-calorific value fuels which are discarded [13]. Pre-heating expands the flammability limits thereby enabling combustion with low NO_x emissions. Heat recirculation from the exhaust to the incoming reactants also improves fuel saving. However, non-premixed systems are frequently used in industrial applications because of their controllability and safety. Preheating the air to high temperatures increases the peak flame temperatures thereby significantly increasing the emissions of thermal NO_x . Here, high temperature refers to the autoignition temperature of the fuel with the air. This has led to numerous efforts to simultaneously reduce NO_x emissions while improving fuel saving [14][15].

Recirculation of low-temperature exhaust gases into the fresh reactants can reduce the peak flame temperatures, thereby reducing NO_x emissions. The temperature of the recycled exhaust gas is determined by heat abstraction and heat losses to the surroundings. At low rates of exhaust gas recirculation (EGR), defined as the ratio of the mass of the recirculating exhaust to that of the fresh reactants, the combustion becomes unstable [16]. However, the combustion can be stabilized at high rates of EGR if the temperature of the preheated air exceeds the autoignition temperature of the fuel. It is suggested that such preheating and

Literature review

dilution with exhaust results in extended flame lengths and distributed reaction zones that yields a uniform and moderate temperature rise.

Reverse flow is suitable for preheating and dilution with exhaust due to internal recirculation. The bottom wall of the combustion chamber acts as a forward stagnation plane that forces the flow to reverse 180° before exiting from the same plane as that of the injectors. The parameters influencing the recirculation in these systems can be understood by considering a non-reacting turbulent jet model as proposed by Han and Mungal [17]. The mass recirculation along the axial direction near the nozzle exit (momentum driven region of the jet) can be described as:

$$\frac{d\dot{m}_{rec}}{dx} = C_e \left[\frac{\dot{m}_o}{d^*} \right] \quad (2.1)$$

$$d^* = d_o \left(\frac{\rho_o}{\rho_\infty} \right)^{1/2} \quad (2.2)$$

$$C_e = 0.32(1 - e^{-0.036(r-1)}) \quad (2.3)$$

$$r = \left[\frac{\rho_o u_o^2}{\rho_\infty u_\infty^2} \right]^{1/2} \quad (2.4)$$

Here, ρ is the density, u is the velocity, d is the jet diameter, and subscripts ‘ o ’ and ‘ ∞ ’ refer to the jet and the surrounding conditions, respectively. The parameter C_e can be assumed to be constant as r is large in the reverse flow configuration. Hence, the recirculated mass increases with a decrease in the jet diameter (increase in velocity) or density (increase in temperature) of the jet in comparison to the surrounding medium. As a result, high injection velocities and preheating can be used in these systems to increase the recirculation. The intensity of recirculation is usually characterized by the recirculation ratio (R) that is defined as follows:

Literature review

$$R = \frac{\dot{m}_{total} - \dot{m}_{in}}{\dot{m}_{in}} \quad (2.5)$$

Here, \dot{m}_{in} represents the net mass of the incoming fresh reactants while \dot{m}_{total} is the total flow rate (reactants + entrained diluents) in the forward axial direction.

2.2 Reverse flow combustion chamber

The reverse flow (RF) is a generic combustor configuration that can incorporate air preheating and exhaust gas recirculation. In this design, the inlet to the chamber and the outlet are located on the same side of the combustor, while the opposite end is closed. This closed-end forms a stagnation plane for the high-velocity incoming reactants which are then reversed to exit from the incoming plane as observed in **Figure 2.1a**. The returning exhaust after combustion gets entrained into the incoming fresh reactants due to shear. This entrainment results in both dilution and preheating of the reactants before the onset of combustion. The RF configuration can cause intense mixing even with non-premixed injection such that the mixture is nearly premixed before the onset of combustion. This has been shown by Bobba et al. [18][19] in the combustion of methane in the stagnation point reverse flow (SPRF) combustion chamber leading to low NO_x (~ 1 -ppm) and CO (< 10 -ppm) emissions both with premixed and non-premixed injections. The SPRF chamber has also been shown to operate with liquid fuels [20] and low-grade solid fuels [21]. The reverse flow configuration has been investigated both for gas turbine and industrial applications. The technologies are mature for application in industrial furnaces. The N_2 that may be used for dilution of the oxidizer stream can be obtained from air separation units [22]. However, the application is challenging in aerospace industry due to space and weight constraints. More work need to be done, particularly at higher pressures, for application of this configuration in gas turbines.

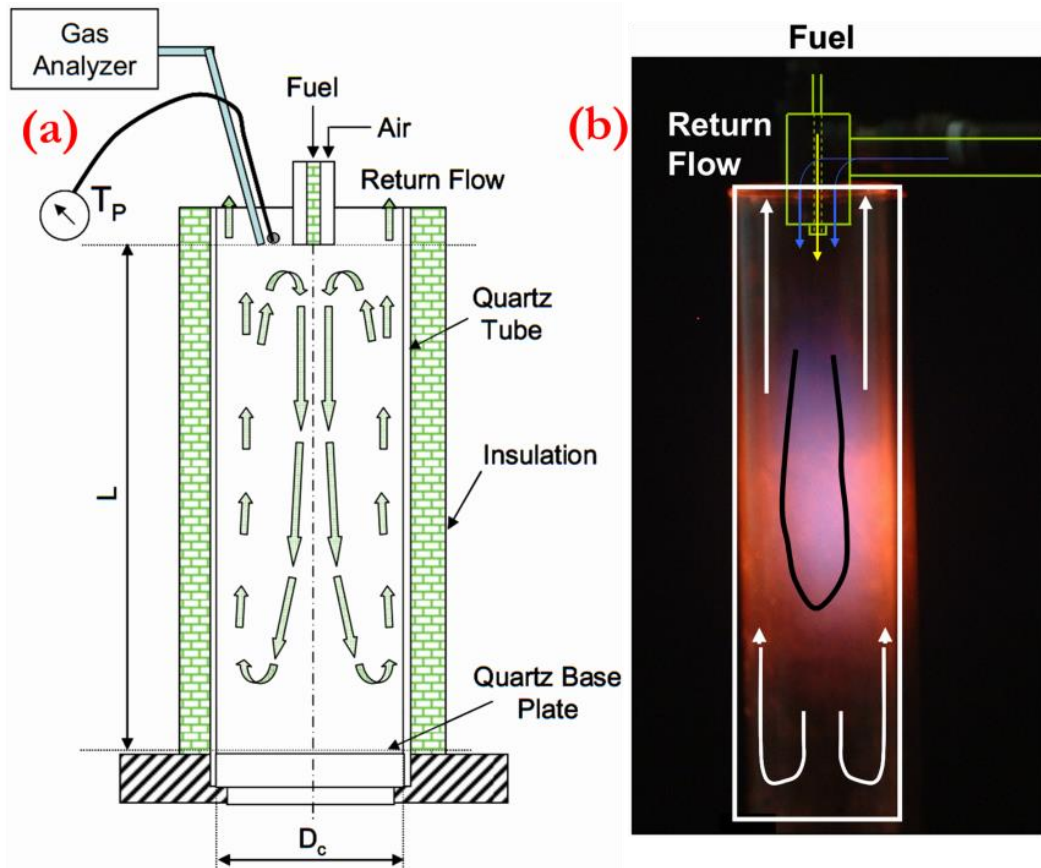


Figure 2.1: (a) Schematic of the stagnation point reverse flow (SPRF) combustion chamber (adapted from [19]) and (b) flame luminosity image in the SPRF chamber (adapted from [20]).

2.2.1 Circular turbulent jet in confined counterflow

The flow within the reverse flow chamber can be approximated by the classical configuration of circular jets in confined counterflow as observed in **Figure 2.2a**. Of the few studies on this configuration, most have focussed on an unconfined flow field [23][24]. The jet penetration in such a configuration is linearly proportional to the ratio of the jet to the counterflow velocity. The jet penetration (l_p) can be expressed by the following relation:

$$\frac{l_p}{d_j} = c \frac{u_j}{u_o} \quad (2.6)$$

where, d_j is the jet diameter, u_j is the jet exit velocity, u_o is the counterflow velocity, and the value of the constant c varies from 2.4 to 2.9. However, the presence of the confinement reduces the jet penetration length and causes deviation of the linear relationship of the penetration length. The jet is said to be unconfined for $D_o/l_p \geq 2$. The penetration length follows the following functional form for a confined jet:

$$\frac{l_p}{D_o} = f\left(\frac{u_j d_j}{u_o D_o}\right) = f(R) \quad (2.7)$$

where, D_o is the confinement diameter, and R is the momentum-flux-ratio parameter. The slope of the non-dimensional penetration length curve decreases with increase in R and reaches zero asymptotically as observed in **Figure 2.2b**. The asymptotic value for the maximum jet penetration is 3.57 times the confinement diameter.

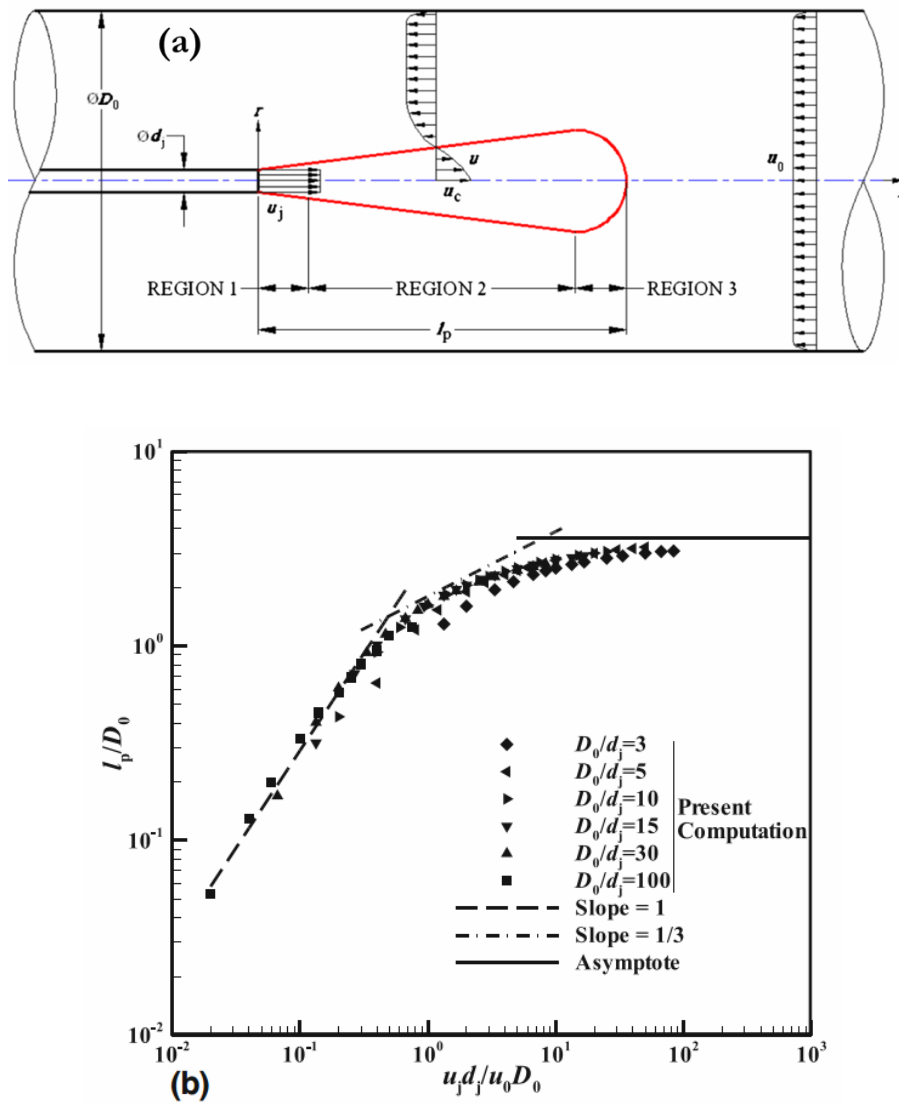


Figure 2.2: (a) Schematic diagram of a circular turbulent jet in confined counterflow [25]. The jet to counterflow velocity ratio is u_j/u_0 while the diameter ratio is d_j/D_0 . (b) Variation of the non-dimensional jet penetration length to the jet-to-counterflow momentum flux ratio parameter [25].

2.2.2 Mixing in coaxial jets

Circular coaxial jets are of interest to several applications pertaining to mixing and combustion chambers. The velocity ratio between the outer and the inner jets (U_o/U_i) is the most important parameter governing the flow and mixing in this configuration [26]. For jets issuing at different densities, the momentum ratio instead of the velocity ratio governs the flow characteristics. For the case where the coflow velocity is much lower than the central velocity ($U_o/U_i \ll 1$), the flow resembles a free turbulent jet and the velocity decay is hyperbolic with axial distance ($U \propto 1/x$). However, for the case where the coflow velocity is similar to the central jet velocity ($U_o/U_i \gg 1$), the velocity decay follows an $x^{-2/3}$ profile [27]. The mixing in such a jet is defined by the dilution length as follows [26]:

$$L_D \sim D_i \left(\frac{U_i}{U_o} \right) \left(\frac{C_i}{C_s} \right) \quad (2.8)$$

Here, C_i is the concentration of the fuel in the inner jet and C_s is the desired dilution level. However, very small dilution length implies early mixing between the fuel and the oxidizer jets. This won't allow sufficient time for mixing with the exhaust and the mixture may ignite close to the nozzle leading to a flame stabilized near the inlet. For the case where $U_o \sim U_c$ which more closely represents the present case due to the high specific flow rate of syngas, a simple relation of the above type may not be possible.

2.3 MILD combustion

Moderate or intense low oxygen dilution combustion, commonly referred to as MILD combustion is a recent technology characterized by high temperature of the reactants and low rise in the temperature during the combustion process. While working on a self-recuperative furnace, Wüning [28] surprisingly observed that at furnace temperatures of 1000° C and air preheat temperature of 650° C, no flame luminosity or UV signal could be detected. The fuel

Literature review

was completely burnt with CO emissions below 1-ppm and NO_x emissions nearly zero while the combustion was stable. Wüning named this combustion as “flameless oxidation” or FLOX [16]. A similar technology was also called MILD combustion by Dally et al. [29] as shown in **Figure 2.3** and Mild combustion by Cavaliere et al. [30]. Katsuki et al. [13] and Tsuji et al. [31] also found that high-temperature air combustion (HiTAC) was similar to MILD combustion. Colourless distributed combustion (CDC) [32] is also a similar technology that produces a uniform and non-luminous reaction zone with very low emissions. MILD combustion provides many distinct advantages over other combustion technologies including uniform temperature distribution in the combustion chamber, excellent combustion stability, high efficiency and near-zero emissions of NO_x.

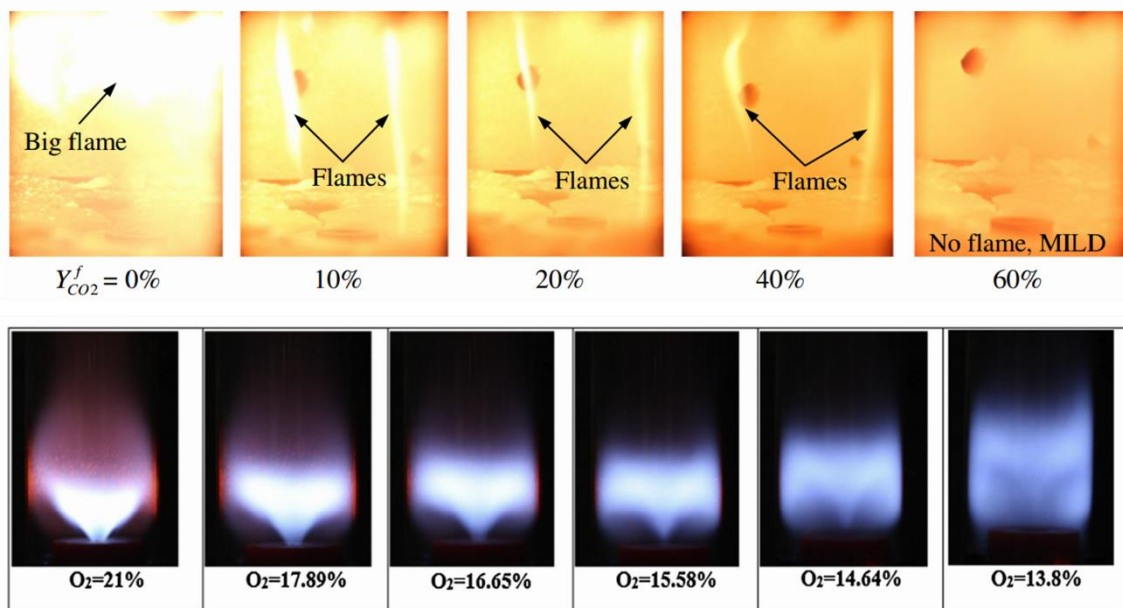


Figure 2.3: Flame luminosity images under MILD (adapted from [33]) and colourless distributed combustion (CDC) (adapted from [34]) conditions.

Literature review

According to Cavaliere and de Joannon [30], MILD combustion is defined as a combustion process in which the inlet temperature of the reactant mixture is higher than mixture autoignition temperature whereas the temperature rise as compared to the inlet temperature is lower than the mixture autoignition temperature (in Kelvin). The autoignition temperature is defined with respect to a perfectly stirred reactor (PSR) in which any differential increase in temperature shifts the system to the higher branch of the S-shaped ignition curve. Again, with dilution, the maximum temperature rise is reduced as compared to the undiluted case. In this respect, the final temperature should not be very high to qualify as MILD combustion, although this temperature rise is defined arbitrarily considering the same autoignition temperature as a threshold [35]. A more comprehensive definition of MILD combustion was proposed by Rao and Levy [36] that considers the roles of the inlet temperature, recirculation ratio, and the O₂ concentration (**Figure 2.4**). However, the specific values of the parameters vary significantly depending on the particular application [35]. The MILD combustion regime is established due to the ‘internal’ recirculation of heat and exhaust gases. The recirculation of exhaust gases decrease the oxygen concentration in the reactants and increase its temperature. The dilution decreases the reaction rates, such that a MILD combustor operates in the regime of Damköhler number (Da) ~ 1 . No distinct flame fronts can be observed in a combustor operating in the MILD regime. The distribution of heat release results in a nearly uniform temperature over a larger volume and lower peak temperatures. The high inlet temperature is a requirement in the establishment of MILD combustion as the dilution levels are very high and beyond the critical limits of conventional flame stabilization. In this respect, MILD combustion is different from combustion with exhaust gas recirculation. Based on the current literature, the consensus for MILD combustion appears to be in the following points:

- (a) High preheat temperature of combustion air and high injection velocity of the reactants.

Literature review

(b) High recirculation ratio, i.e., entrainment of exhaust gases to dilute the incoming reactants. Recirculation ratio has been defined by Wüning [16] as

$$K_v = \frac{M_E}{M_F + M_A} = \frac{M_J - M_F - M_A}{M_F + M_A} \quad (2.9)$$

where $M_E = M_J - (M_F + M_A)$ is the total mass of exhaust gas entrained by the fuel and oxidizer jets. M_J is the net mass flow rate of the jet, whereas M_F and M_A are the mass flow rates of the fuel and oxidizer jets.

- Reaction zone temperature must be greater than the autoignition temperature and oxygen concentration in the reaction zone must be less than 5 – 10%. This is not an independent criterion and depends on the criteria (a) and (b).
- When a regenerator is used for waste heat recycling, the thermal efficiency of MILD combustion can improve by more than 30% while the NO_x emissions can decrease by more than 70% [31].

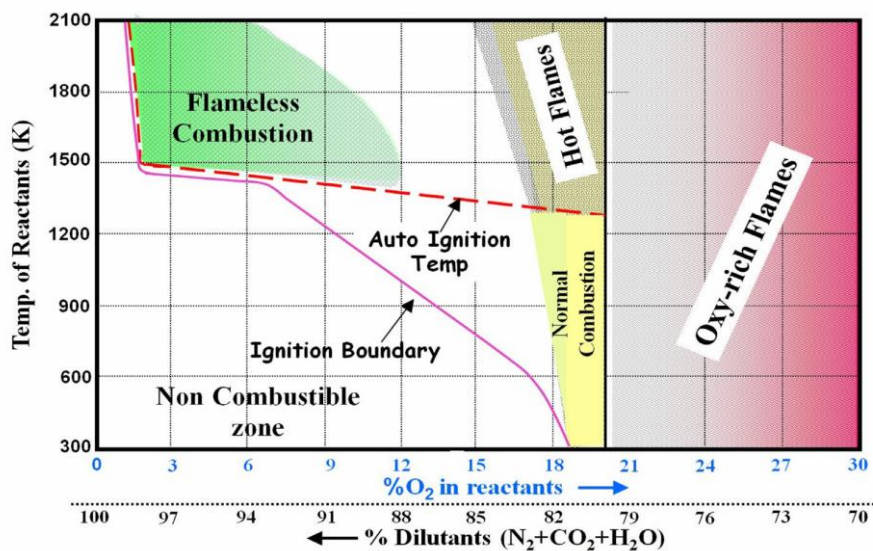


Figure 2.4: The combustion regimes diagram proposed by Rao and Levy [36] (adapted from [35]) showing the relationship between the inlet temperature, O_2 concentration, and percentage of diluents (or recirculation ratio) in establishing flameless combustion.

Literature review

Figure 2.4 shows the influence of K_v on the regime of methane non-premixed combustion. Cavigiolo et al. [37] studied the influence of K_v on the reaction zone temperature and emissions of NO_x and CO in natural gas combustion. They found that the emission of NO_x and CO was independent of the furnace temperature, fuel type or fuel calorific value due to the stable nature of MILD combustion. They also observed that different values of K_v and furnace temperature are required to establish MILD combustion in different fuels.

Table 2.1: Lowest emissions of NO_x and CO reported from selected publications available in the literature

Authors	Configuration	Fuel	CO (ppm @15% O_2)	NO_x (ppm @15% O_2)
Bobba et al. [19]	Reverse flow	Methane	< 10	~ 1
Plessing et al. [38]	Reverse flow (flameless)	Methane	-	< 10
Kruse et al. [39]	Reverse flow (MILD)	Methane	< 10	< 5
Szegö et al. [40]	Reverse flow (MILD)	LPG, NG	-	~ 2
Szegö et al. [41]	Reverse flow (MILD)	LPG, NG	~ 33	~ 5
Ye et al. [42]	Reverse flow (MILD)	Ethanol, acetone, n-heptane	< 10	< 10
Castela et al. [43]	Reverse flow	NG	1	1
Verissimo et al. [44]	Reverse flow	Methane	< 21	< 7
Arghode et al. [32]	Reverse flow (CDC)	Methane	~ 20	2
Arghode et al. [45]	Reverse flow (CDC)	Methane	~ 30	1 - 5
Khalil et al. [46]	Reverse flow (CDC)	Methane	~ 100	< 5
Huang et al. [47]	Forward flow (MILD)	Syngas	~ 15	~ 5
Zornek et al. [48]	Forward flow (FLOX)	Syngas	15	< 5

2.3.1 MILD combustion in the reverse flow configuration

Although the reverse flow (RF) is a generic configuration for achieving flame stabilization and low emissions (**Table 2.1**), it has most often been used in flameless oxidation (FLOX) or MILD (moderate or intense low-oxygen dilution) burners to achieve a nearly non-luminous and distributed reaction zone with very low NO_x emissions [38]. In these systems, the flame is stabilized downstream of the injection plane due to the high injection velocities and shear near the nozzle. This can be observed in the temperature and OH distribution reported by Plessing et al. [38] in an RF furnace shown in **Figure 2.5** where no OH signal could be detected close to the burner. They also report NO_x emissions < 10-

Literature review

ppm in the flameless combustion mode. Scaling analysis of NO_x emission in a 20 kW parallel-jet RF MILD combustion furnace has been performed by Szegö et al. [40]. They report NO_x emissions less than 5-ppmv dry at 3% O₂ that was attributed mostly to prompt and N₂O intermediate pathways. In another study of the same furnace, Szegö et al. [41] report less than 10-ppm NO_x and less than 100-ppm CO at 3% O₂ during the combustion of LPG and natural gas. Combustion at high thermal intensities relevant to gas turbine applications is also possible in the reverse flow configuration as shown by Arghode et al. [32]. The authors have investigated the combustion of methane at thermal intensities of 28 MW/m³ and 57 MW/m³ to achieve colorless distributed combustion. Both premixed and non-premixed modes of operation were investigated with low NO_x (~ 2-ppm) and CO (~ 57 - 96-ppm) emissions. The authors conclude that the reverse-cross-flow non-premixed configuration as shown in **Figure 2.6** is most promising in reducing the NO_x and CO emissions. Experiments in the reverse flow configuration at even higher thermal intensities of 53 - 85 MW/m³ [45] and 270 - 420 MW/m³ [46] have been reported with low emissions of NO_x and CO. The influence of parameters such as air inlet velocity and preheat temperature on the combustion of methane in the reverse flow configuration has been studied by Veríssimo et al. [43][44]. In another study, Zhou et al. [49] have investigated the reaction zone structures using OH*, OH-PLIF and CH₂O-PLIF from the flame to the flameless mode during the combustion of methane in the reverse flow configuration. The authors observed the uniform instantaneous distribution of OH with low standard deviation in the flameless mode. The effect of pressure in the reverse flow configuration has been studied by Kruse et al. [39] and Ye et al. [42]. The study by Kruse et al. [39] focusses specifically on MILD combustion of methane at elevated pressures of 2.5 bar and 5 bar. They report that the range of operation regime with low NO_x and CO emissions decreases at high pressure, thereby increasing the challenges of achieving MILD combustion at gas turbine relevant conditions. Ye et al. [42] have focussed on the

Literature review

MILD combustion of prevaporised liquid fuels such as ethanol, acetone, and n-heptane in the pressure range of 1 - 5 bar. The authors report that the NO_x emissions increased with pressure which can be attributed to higher temperatures, higher residence times, and the N_2O intermediate pathway.

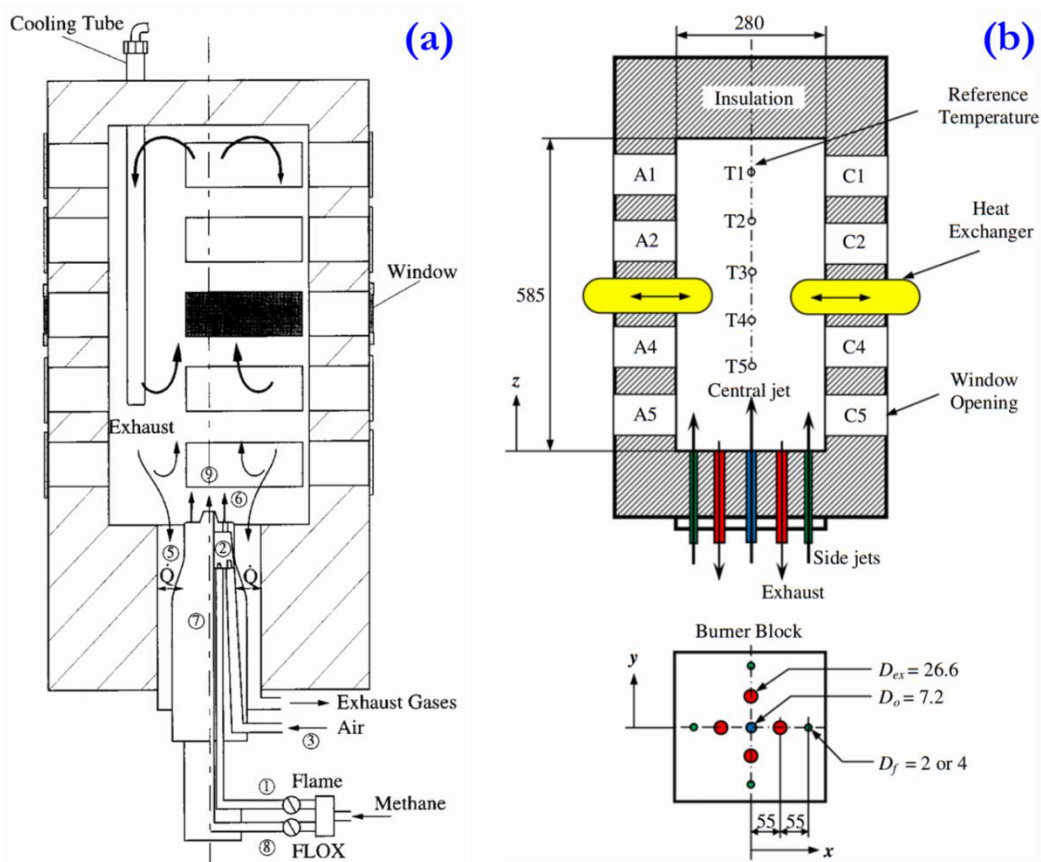


Figure 2.5: Reverse flow MILD combustion furnaces investigated by (a) Plessing et al. (adapted from [38]) and (b) Li et al. (adapted from [33]).

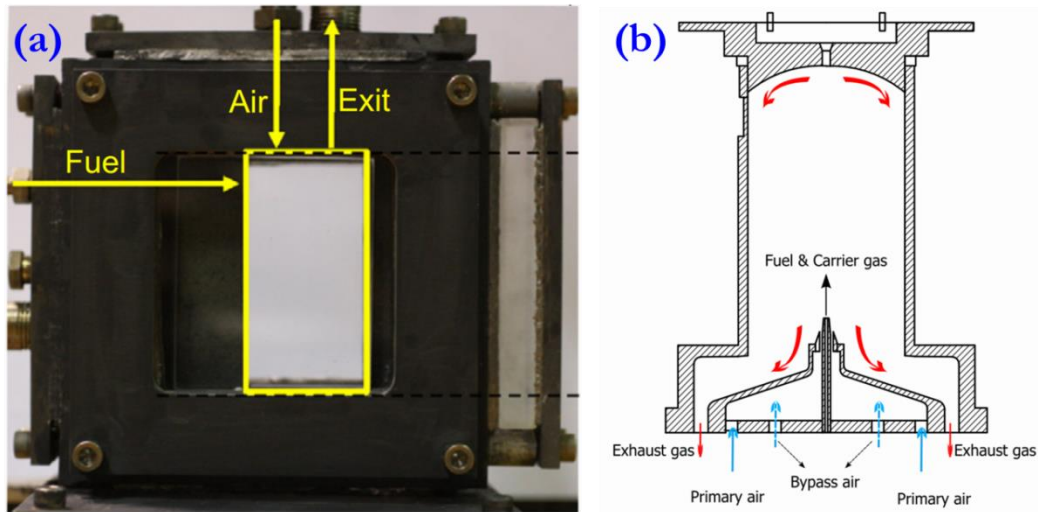


Figure 2.6: Reverse flow MILD combustion furnaces investigated by (a) Arghode et al. (adapted from [45]) and (b) Ye et al. (adapted from [42]).

2.3.2 MILD combustion of syngas

Combustion of syngas with internal recirculation in other configurations has been reported by a few authors (**Table 2.1**). Huang et al. [47] have investigated the effect of air preheat temperature on the MILD combustion of syngas (12 MJ/kg) in a parallel-jet forward-flow combustor at a heat load of 15.3 - 29.9 kW and equivalence ratio range of 0.27 - 0.54. The authors report that the NO_x emissions increase while the CO emissions decrease with increase in preheating and equivalence ratio. Flameless oxidation (FLOX) of low calorific value syngas (3.5 - 5 MJ/kg) for micro-turbine applications (50 - 100 kW_{el}) has been reported by Zornek et al. [48]. This forward-flow combustion chamber uses fuel staging between a pilot and the main stage to operate with improved stability, reliable startup, and low emissions (~ 15 -ppm CO, < 6 -ppm NO_x). Kwiatkowski et al. [50] have investigated several injection configurations such as coflow, cross jets, and cyclonic cross jets (**Figure 2.7**) to

Literature review

show that MILD combustion of syngas is less sensitive to the combustor configuration and more sensitive to dilution and preheating. They have also shown that the syngas composition can have a significant influence in achieving MILD combustion. So, while MILD combustion could be easily achieved with syngas obtained from gasification of feathers, it was difficult to achieve the same with gasified wood chips. A few recent studies report the OH distribution [51] and emissions [52] during the combustion of low-calorific value syngas obtained from biomass gasification both experimentally and numerically [53] in the reverse flow configuration.

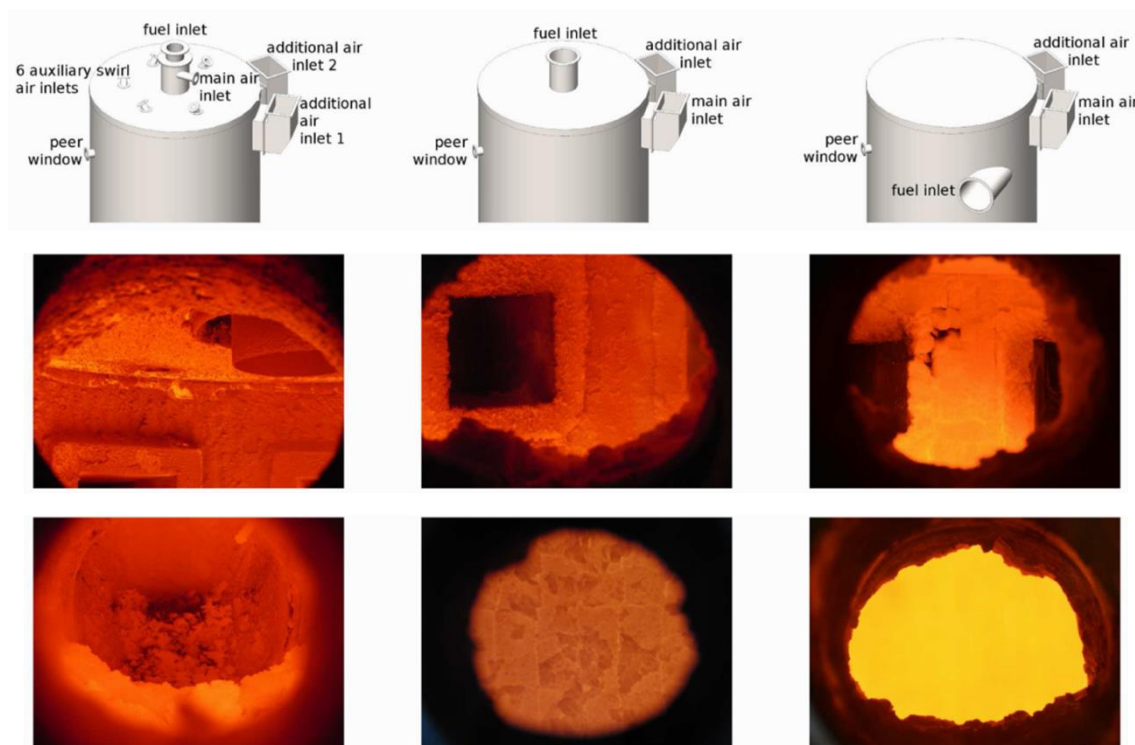


Figure 2.7: MILD combustion of syngas in three different configurations namely coflow (left), cross jets (middle) and cyclonic cross jets (right) [50].

2.3.3 Jet in hot coflow (JHC)

The jet-in-hot-coflow is a canonical burner configuration to simulate heat and exhaust gas recirculation under MILD conditions [29]. The burner consists of an insulated and cooled central fuel jet. An annular secondary burner is mounted upstream of the exit plane of the fuel exit plane. The exhaust from the secondary burner is mixed with additional O₂ and N₂ to control the temperature and the O₂ content in the coflow. This allows the burner to operate at different levels of coflow temperature and O₂ concentration, thus simulating various degrees of heat and exhaust gas recirculation. The burner provides easy optical access for detailed measurements of velocity, temperature, species, and other scalars at the boundaries and throughout the flame.

Several workers have performed detailed measurements in the jet in hot coflow configuration under various inlet conditions. Dally et al. [29] have performed measurements of reactive scalars on H₂/CH₄ non-premixed flames at three different oxygen levels in the coflow. The authors observe a significant difference in the flame structure and appearance with a change in O₂ levels. Measurements of OH, H₂CO radical, and temperature in a non-premixed ethylene jet flame in a hot diluted coflow has been performed by Medwell et al. [54] as shown in **Figure 2.8**. The authors observed the presence of H₂CO radical in the lifted region of the flame, suggesting the role of preignition reactions. Further, Oldenhof et al. [55] have observed the formation of ignition kernels in the lift-off region, showing that the flame base in a JHC burner is fundamentally different as compared to a lifted flame in cold air coflow. Increase in H₂ percentage in the H₂/CH₄ mixture increases the frequency of ignition kernel formation [56]. However, the kernels become non-detectable and continuous at sufficiently high H₂ percentages.

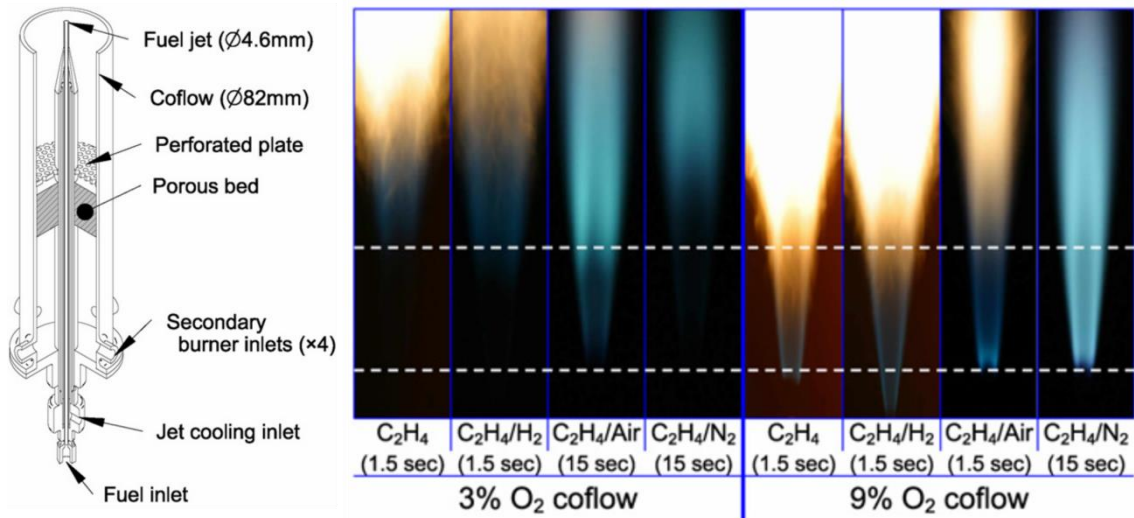


Figure 2.8: Schematic diagram of the jet in hot coflow burner (left); images of ethylene JHC flames at different O₂ concentrations in the coflow (right) [54].

2.3.4 Flame structure under MILD conditions

The flame structure under MILD conditions is not fully understood and is a matter of intense research. It is believed to deviate from conventional flames where the reaction and heat release is predominantly restricted to thin reaction zones. Simultaneous measurements of temperature and OH have been performed by Plessing et al. [38] in a reverse flow flameless oxidation furnace operating with methane. The authors have compared the results with a turbulent lean premixed flame of methane. The results show that the premixed flame is highly wrinkled with high OH in the vicinity of the thin reaction zones. The flameless burner shows that the OH is more uniform with a lower peak and less wrinkling of the reaction zone, although it is not completely devoid of thin structures. This was attributed to the dilution that increased the chemical timescales as compared to the turbulent timescales. The thickening of the reaction zone with a decrease in O₂ levels was also observed from Raman measurements

Literature review

in a JHC flame [29]. Simultaneous OH-PLIF and OH* chemiluminescence measurements of premixed and non-premixed combustion in the stagnation point reverse flow (SPRF) combustor under various loadings also suggests a distinct flame-like structure and not widely distributed reaction zones (**Figure 2.9**). Investigations on MILD combustion from jets in hot and diluted cross-flow configuration [57] also show the presence of wide OH regions with sharp gradients, similar to conventional combustion regimes. Thus, discrete flame fronts are also observed under MILD conditions and this combustion mode may not be truly distributed as previously thought.

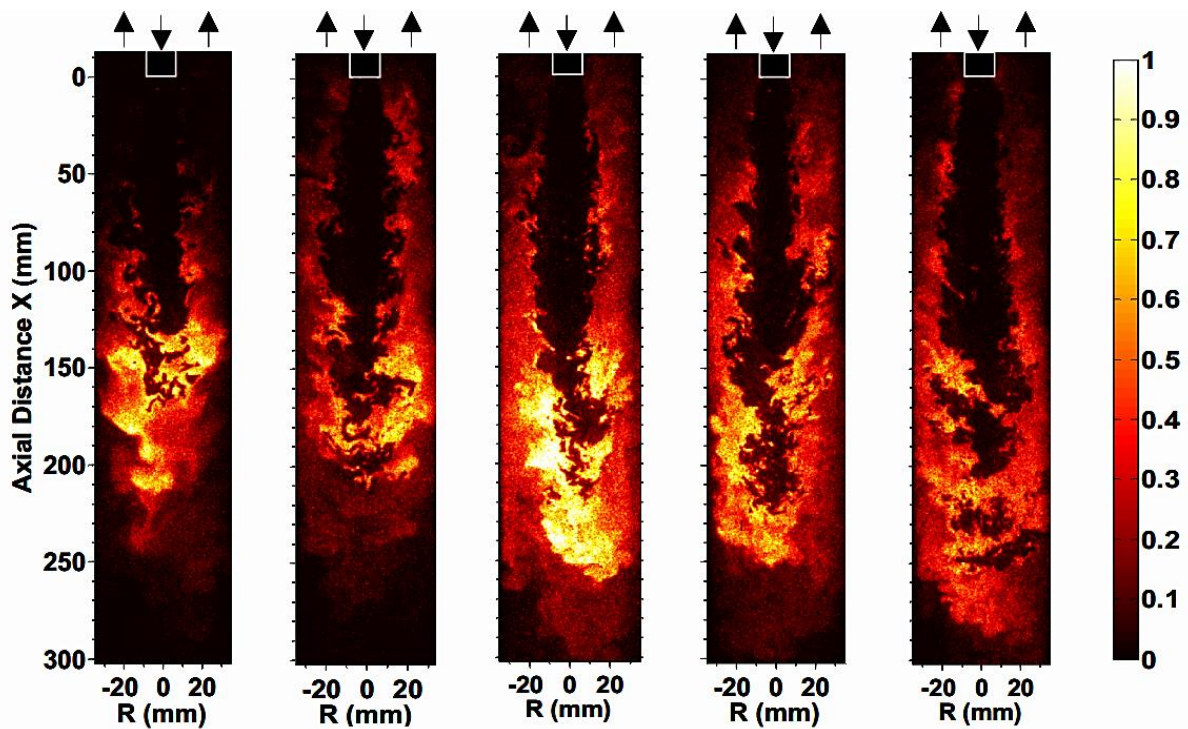


Figure 2.9: Instantaneous OH-PLIF images at $\Phi = 0.65$ and loadings of 2, 4.5, 7.2, 9.4, 10.7 g/s (from left to right) in the SPRF combustor [58].

Literature review

A recent study by Zhou et al. [49] in a reverse flow chamber operating under the conventional flame, transition, and flameless cases show that distinct flame luminosity could be observed in the conventional flame mode, while it became nearly invisible under the flameless mode (**Figure 2.10**). Spectroscopic measurements showed that this flame invisibility in the flameless mode could be attributed to the suppression of the CH* and C₂* emissions with a significant increase in the broadband CO₂ emissions from the background. However, the OH-PLIF images showed distinct flame-like structures for all the three cases in spite of the flame invisibility under flameless conditions. This implies that visual observations may not be true representatives of the heat release and reaction zones in the flame.

Finally, recent DNS studies (**Figure 2.11**) have also provided evidence that the MILD combustion regime is not an idealized homogeneous reaction zone but shares common characteristics with conventional combustion [59][60][61]. The reaction occurs over a wider region of the computational domain as compared to conventional premixed flames but is characterized by frequent interactions of convoluted reaction zones that give the flameless appearance. The assessment of flame index shows that the reaction zone consists of lean premixed, rich premixed and non-premixed reaction zones when the initial mixture is non-homogeneous [61].

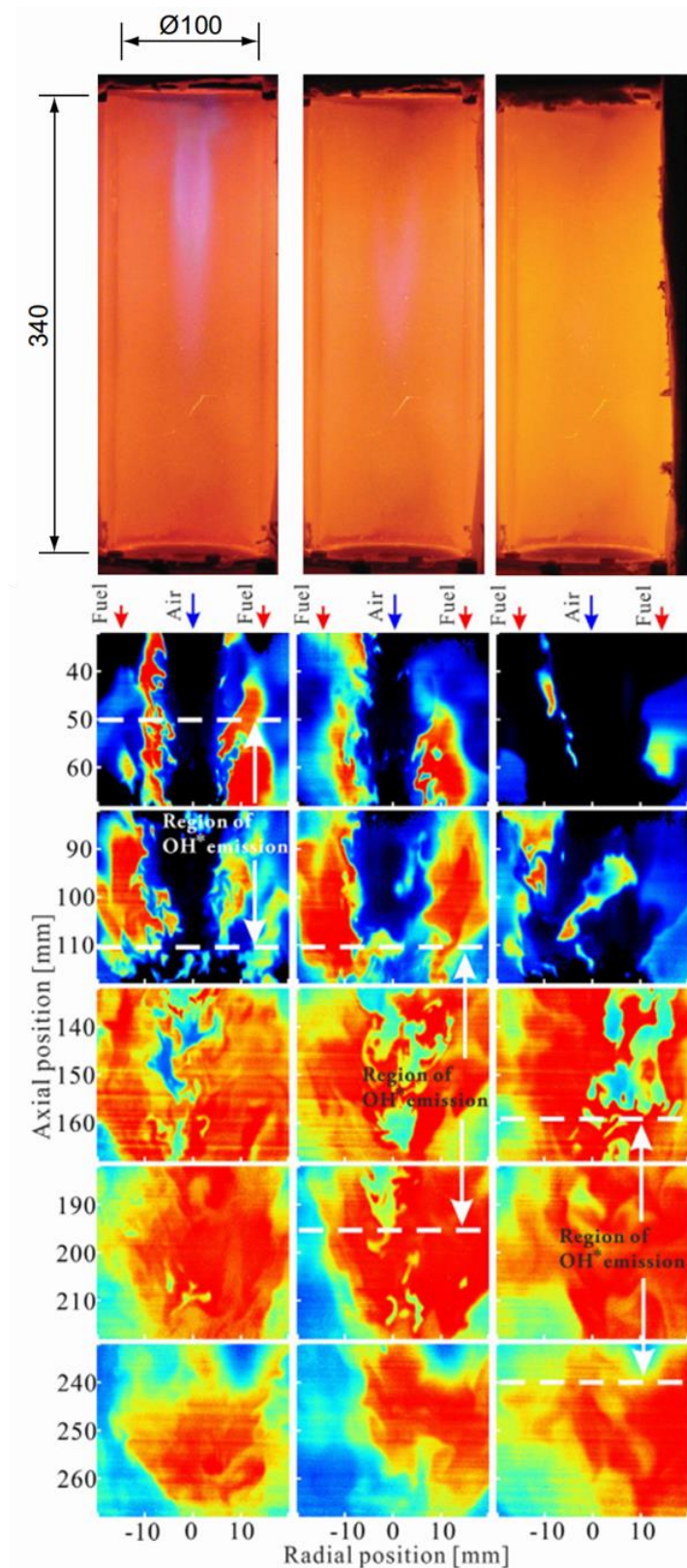


Figure 2.10: Flame luminosity and instantaneous OH-PLIF images for the flame, transition, and flameless cases

[49].

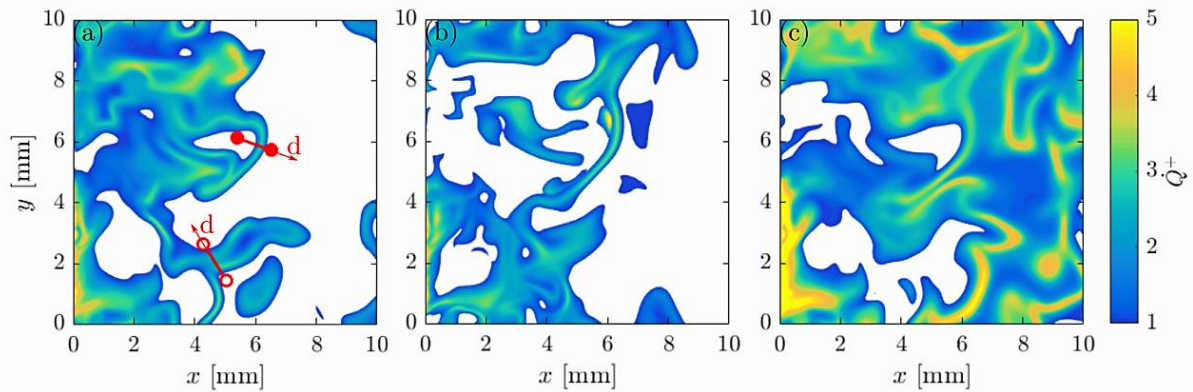


Figure 2.11: Isosurface of normalized heat release rates under MILD conditions [61].

2.4 Numerical studies on combustion in the reverse flow configuration

Numerical investigation of combustion in the reverse flow (RF) configuration has been performed by several authors. Coelho and Peters [62] used the Eulerian Particle Flamelet model with RANS to investigate a RF MILD combustion furnace operating on methane. The authors observed discrepancies in the predictions of the mean and fluctuating velocity quantities by the RANS model. The steady flamelet library was also unable to predict the NO emissions correctly. A comparison of the Eddy Dissipation Concept (EDC) and the composition joint PDF (CPDF) models in predicting the combustion of natural gas in a small scale RF chamber has been performed by Graça et al. [63]. The inability of both the models to predict the ignition location as compared to the experimental data led them to speculate the need for LES models to capture the mixing. Duwig et al. [64] investigated the influence of simulation parameters and detailed chemistry on the LES of the SPRF combustion chamber. They concluded that the intermediate species are more sensitive to the

Literature review

heat loss mechanism, while there was only a little difference between the detailed and the skeletal mechanisms. Linear Eddy Model (LEM) LES of premixed and non-premixed methane combustion in the SPRF combustion chamber has been performed by Undapalli et al. [65] using a 4-step 7-species reduced chemical mechanism. While the LEMLES model predicted the data with reasonable accuracy, it is five times more expensive than the Thickened Flame (TF) LES and Eddy Breakup (EBU) LES models. Ihme et al. [66][67] extended the flamelet/progress variable approach by including the effect of dilution and heat loss in the tabulated chemistry. Lamouroux et al. [68] validated this model in a reverse flow and a forward-flow combustor operating under highly diluted conditions and obtained reasonable agreement with experimental data. However, the authors noted the limitation of the inherent assumption of the turbulent flame front being close to a laminar flame which may not be valid under low-temperature conditions. While most studies in the RF configuration have focussed on methane, a few studies have numerically investigated the combustion of low calorific value (LCV) fuels. Experimental and numerical investigation of a forward-flow FLOX combustor firing LCV gases ($\sim 6 - 8.5 \text{ MJ/m}^3$) has been performed by Danon et al. [69] using Reynolds Stress Model for turbulence and EDC for turbulence-chemistry interaction. The discrepancies between the experimental results and numerical predictions were attributed to the uncertainties in the model constants.

2.4.1 Numerical studies on the jet in hot coflow (JHC) burner

The canonical investigation of MILD combustion conditions is often performed in the jet in hot coflow (JHC) burner [70][71] with its three-stream configuration representing fuel, hot diluted coflow, and air. Significant research effort has been directed towards generating experimental data and validating combustion models using this burner. Several authors

Literature review

[70][72][73] have used RANS and EDC model with skeletal and reduced mechanisms to numerically investigate the JHC burner. The effect of H₂ on H₂/CH₄ flame structure in the JHC burner has been investigated numerically by Afarin et al. [74] using LES and a modified EDC model. Others have also observed improvements in the predictions of the EDC model by changing the model constants [71][75]. Recently, Cifuentes et al. [76] have performed chemical explosive mode analysis (CEMA) for a JHC burner operating under MILD conditions using LES and direct Arrhenius closure. The authors note that CEM is a good marker to locate the flame fronts in the MILD regime. Kulkarni et al. [77] used the stochastic fields model to capture the decrease in the lift-off height with an increase in Reynolds number in the DJHC burner. The transported PDF combustion model [78] predicted early ignition in the JHC burner resulting in higher radial temperatures at the burner exit. DNS studies of turbulent mixing [79] and combustion [80] under MILD conditions have also been performed by some authors, although they cannot be currently applied to laboratory or industrial furnaces due to computational costs.

Thus, it is clear that several combustion and turbulence models have been applied in modelling MILD combustion in the reverse flow (RF) configuration and the jet in hot coflow (JHC) burner with varying degree of accuracy. However, there are several gaps in the current literature that needs to be addressed for a more comprehensive understanding. Few studies have investigated the combustion of low calorific value (LCV) fuels such as syngas in the RF configuration. These H₂ containing fuels have a low adiabatic flame temperature ($T_{ad} \sim 1930$ K), while their ignition delay is 3 orders of magnitude lower than that of methane. Also, LES with detailed chemistry is costly due to requirements of high resolution near the walls. This is particularly relevant for MILD combustion ($Da \sim 1$) where finite-rate kinetic effects also play a crucial role. In this context, hybrid RANS/LES models such as the Detached Eddy Simulation (DES) can significantly reduce the computational cost by resolving the mixing in

Literature review

regions away from the wall, while the near-wall region is handled by RANS models. Such models have seldom been used in the literature for investigating MILD combustion. The prediction of minor species such as OH by the various models also needs detailed investigation as MILD combustion is volumetric in nature. This is particularly relevant for syngas as OH distribution is closely associated with the heat release rate and has not been suitably addressed in the literature. Finally, the RF configuration can operate under MILD as well as ultra-lean [81] conditions and detailed numerical simulations can allow us to better understand the physics of these different modes of combustion.

2.5 Scaling of combustion chambers

Scaling of laboratory-scale combustion chambers to industrial requirements poses practical as well as fundamental challenges. Challenges with detailed in-situ measurements, full-scale experimentation, and enhanced construction costs are some of the practical difficulties at the industrial scales that can stymie the application of novel technologies developed in the laboratory. Fundamental challenges include understanding and development of scaling laws for the fluid dynamic, thermal, and kinetic interactions to maintain similarity in the processes and performance. Although Spalding [82] recognized a large number of non-dimensional parameters that govern a combustion process, only a few can be held constant while scaling due to conflicting requirements of the particular combustion system. The development and large-scale implementation of novel combustion systems to address the pressing needs of global warming and climate change may thus require newer sets of scaling parameters.

Several scaling criteria for combustion chambers have been proposed in the literature. Weber et al. [83] have reviewed the applicability of constant velocity (CV) and constant residence time (CRT) approaches to gaseous, spray-oil, and pulverized coal flames. The

Literature review

authors demonstrated the limitations of the CV and CRT criteria, particularly in capturing the interactions between the gaseous and the solid/liquid phase for two-phase combustion. In another study, Weber et al. [84] have used the CV and CRT approaches to scale swirling pulverized coal flames in the range of 176-kW to 50-MW with particular emphasis on NO_x emissions. The authors demonstrated that the thermal input of the prototype experiments has a significant influence on the performance of the scaling criteria used. Smart et al. [85][86] have also investigated CV and CRT scaling for 2.5-MW swirl stabilized pulverized coal burners that have been scaled-down from a 50-MW conceptual burner. The authors reported higher NO_x emissions in the CV approach as compared to the CRT approach which was explained based on differences in flame propagation. Hsieh et al. [87] have performed a comprehensive analysis of scaling of NO_x emissions from swirl-stabilized non-premixed industrial gas burners operating in the range of 30-kW to 12-MW. The authors pointed out the inadequacies of CV and CRT approaches while proposing a unified scaling model for NO_x emissions which is a function of volume, temperature, [O₂], and [N₂] concentrations in several NO producing regions of the chamber. The correlation performs well for the entire range of burner scales and operating conditions. Cole et al. [88] have proposed a different set of scaling criteria for acoustically stabilized dump combustor from the laboratory scale (4.75-kW) to industrial scale (700-kW). The burner provided excellent emissions performance at the smaller scales although the improvement in the performance due to acoustic forcing at the larger scales (510-kW and 700-kW) was not very significant. Al-Fawaz et al. [89] have investigated CV scaling experimentally and theoretically for a 67-kW and a 266-kW industrial natural-gas burners. The authors highlighted the importance of prompt NO_x in the near-burner region which contributed to 21% and 16% of the total NO_x formed, respectively.

2.5.1 Scaling of MILD combustion chambers

Scaling of MILD combustion chambers has not been investigated thoroughly and is a growing and active field of research. Earlier studies include that of Kumar et al. [90] in which the authors have proposed a new criterion to scale a MILD combustion burner from 3-kW to 150-kW at a high heat release rate of 5 MW/m^3 (**Figure 2.12**). The maximum velocity was limited to 100 m/s to contain the pressure drop while the major dimensions were scaled as $\sim D^{1/3}$. While MILD combustion was achieved in the 3-kW burner the injector had to be reconfigured and a recirculating cone had to be inserted into the 150-kW scaled chamber to attain MILD combustion. The authors made elaborate use of CFD to optimize the configurations for the injector and positioning of the recirculation cone. Scaling of NO_x emissions from a 20-kW MILD combustion burner has been reported by Szegö et al. [40]. The authors reported a global NO_x production rate as a function of the global residence time and a characteristic furnace temperature that provides the best NO_x scaling across all the operating conditions. Bobba et al. [19] have also investigated the scaling of a reverse flow combustion chamber operating in the non-premixed mode by varying the combustor diameter and length. The authors observed that the near-nozzle mixing is a function of the air to fuel momentum ratio and independent of the chamber diameter for the range of dimensions investigated. The authors also noted that enhanced mixing at larger scales can be obtained at lower velocities (and hence, pressure drop) by modifying the injectors to maintain a constant air to fuel momentum ratio. Such studies on the scaling of MILD combustion are few and hence require further investigation. Also, unlike standardized industrial burners for coal and natural gas, the area of MILD combustion is still evolving with various geometries and configurations such as the reverse flow [40], jet in hot cross flow [57], forward flow [90], and swirl [91]. This makes repeated experimentation for scaling both challenging and costly. On

Literature review

the contrary, CFD models once validated are not only cost effective but also provide more detailed insights into the combustion phenomenon encompassing all the variables.

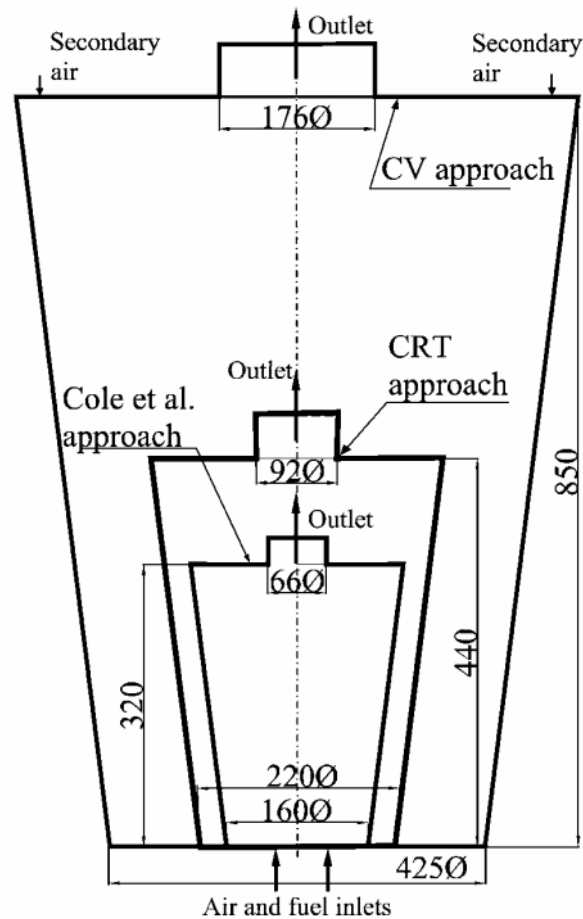


Figure 2.12: Details of a 150-kW MILD combustion burner scaled from 3 kW using constant velocity (CV), constant residence time (CRT) and Cole's approach [90].

2.6 Summary

In this chapter, a review of literature on air-preheating and exhaust gas recirculation (EGR) as a means to improve combustion stability and reduce emissions was presented. This was followed by a review of reverse flow combustor geometry as an efficient configuration for EGR. The parameters governing such mixing have been discussed using canonical configurations and theoretical models. A special combustion regime known as MILD combustion has been thoroughly discussed that can reduce emissions of NO_x while improving combustion stability. Literature pertaining to MILD combustion, its canonical configuration - the jet in hot coflow burner, MILD combustion of syngas, and flame structure under MILD conditions have been reviewed. An important gap concerning the comprehensive investigation of syngas combustion in the reverse flow configuration has been identified. Also, literature pertaining to numerical studies on combustion in the reverse flow configuration was presented. It was observed that several models have been used to predict combustion characteristics with varying degrees of accuracy. Finally, literature on scaling of combustion chambers in general and MILD combustion chambers in particular has been presented and a gap in global scaling criteria for scaling reverse flow chambers under MILD conditions has been identified. The current work aims to address these gaps in the literature.

Chapter 3

Experimental facilities

3.1 Combustor test rig

The experimental test rig consists of a cylindrical reverse flow combustion chamber made of forged SS304 with optical access as observed in **Figure 3.1** and **Figure 3.2**. While fused-silica cylinders can provide complete access, they suffer from optical distortions and are prone to cracking under high thermal loads. The stainless-steel chamber with flat fused-silica windows eliminates such challenges. Several mountings such as a thermocouple can be mounted on the chamber to obtain boundary conditions such as wall temperature profiles. The chamber has a length of $L = 265$ -mm and diameter of $D = 80$ -mm. The length is less than the asymptotic limit of the jet penetration described in **Section 2.2.1** such that the entire chamber is utilized. The dimensions were chosen based on residence time calculations, zero dimensional perfectly stirred reactor calculations and CFD simulations of the chamber. The inside of the chamber is viewed through a 30-mm wide fused-silica window. Two additional 10-mm fused-silica windows provide access to the laser sheet in the perpendicular plane. Fused-silica plates are used as they provide high transmission ($> 98\%$) to UV radiation used for laser diagnostic purposes. The contacts between the fused-silica plates and metal have been sealed using soft ceramic gaskets ($t = 1$ -mm). The gaskets also act as a cushion against the differential thermal expansion of metal and fused-silica at high temperatures. The rig is mounted on a jack-bolt for vertical traverse of the test section. This helps in visualization and imaging of the entire chamber while keeping the laser sheet and camera positions unchanged.

Experimental facilities

The bottom plate of the chamber creates a stagnation plane causing the flow to reverse direction. A spark plug and thermocouple are mounted on the bottom plate.

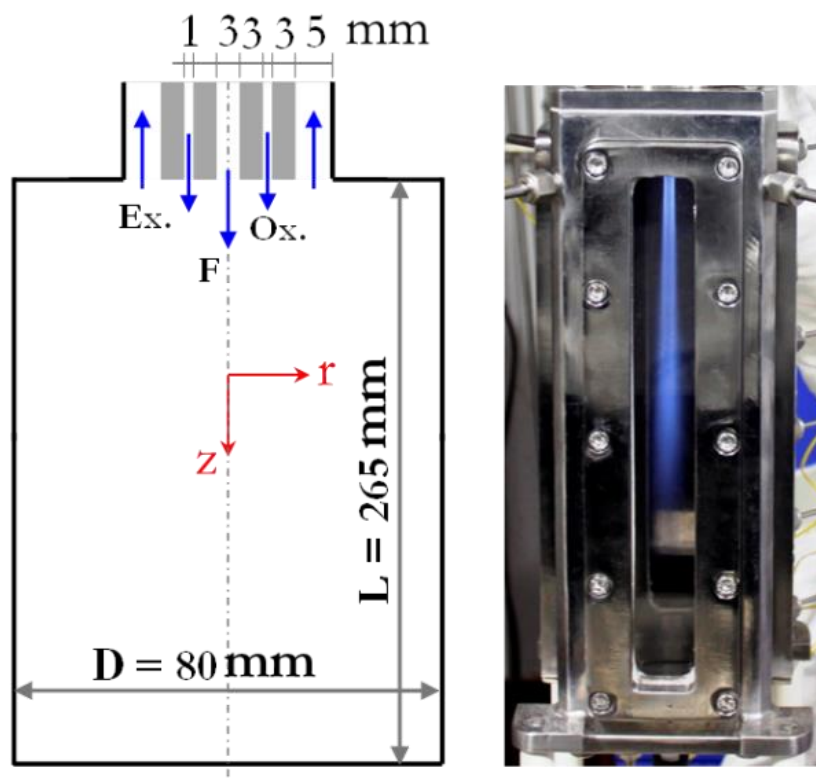


Figure 3.1: Schematic diagram of the combustion chamber (left) and the combustion chamber in operation (right). All dimensions are in millimeter.

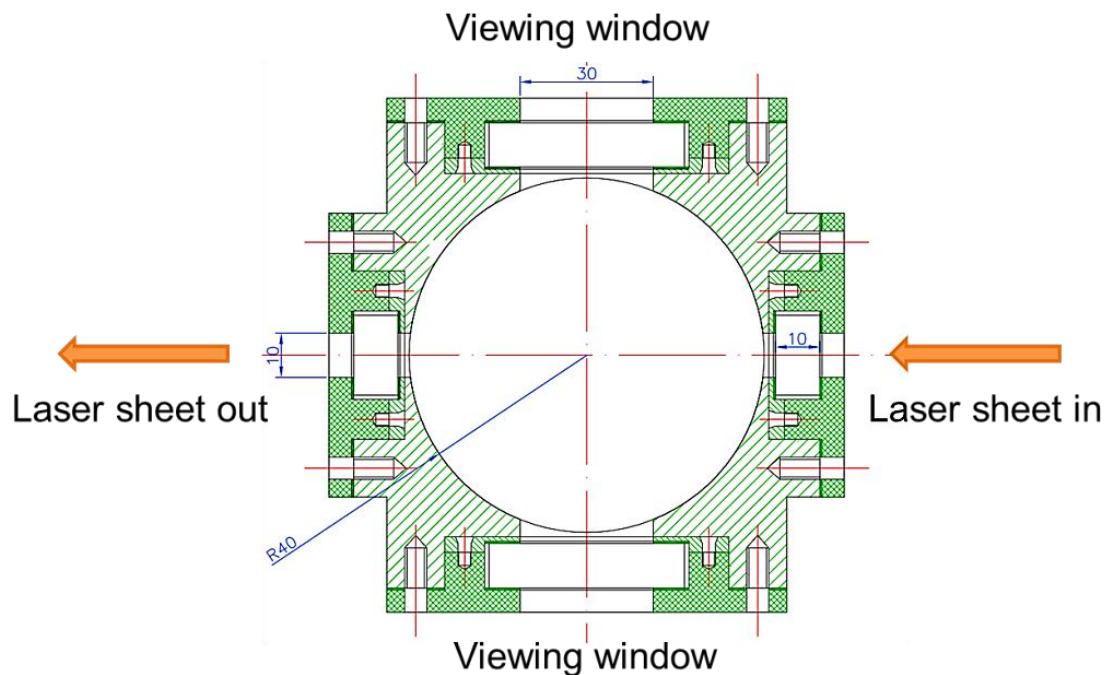


Figure 3.2: A cross-sectional view of the combustion chamber showing the optical access.

The injector assembly has a central fuel port ($D_f = 3\text{-mm}$) surrounded by a $t_{ox} = 1\text{-mm}$ wide annular port for oxidizer (air + N_2) injection. The small injector dimensions result in high inlet velocities that enhance internal recirculation (**Eqn. 2.1 - 2.4**). The oxidizer nozzle is again surrounded by an annular exhaust manifold of width $t_{ex} = 5\text{-mm}$. The fuel and oxidizer are injected separately into the chamber and the flow rates are controlled using digital mass flow controllers (Make: Alicat Scientific, Model: MCR-250SLPM-D/5M,5IN). The air is mixed with additional nitrogen (N_2) to vary the level of dilution within the chamber [92]. The air and N_2 are considered perfectly mixed as the mixing is initiated far upstream of the injector. The oxidizer is preheated upto temperatures ranging from 600 - 790 K in a 9-kW furnace-type air heater before entering the chamber.

Experimental facilities

To observe the wall and chamber temperatures, several ports were provided in the main chamber. Two through-ports were made for measuring the chamber temperature, one at the bottom while the other at the top. The thermocouples were secured in its position using ferrule fittings that also prevented leakage of exhaust gases. Six dummy holes were drilled radially into the chamber wall, spaced 50-mm apart, to measure the wall temperature along the length of the combustion chamber. The wall thickness between the thermocouples and the inside of the chamber was 2-mm. However, due to the high thermal conductivity of stainless steel (~ 16 W/mK), the temperature measured effectively represented the temperature at the inner wall of the chamber.

The chamber is insulated on all sides using 2-inch thick layers of ceramic wool placed in plates made of sheet aluminum. The combustion chamber is insulated using glass wool that is secured in position using aluminium sheet metal plates. The plates create a jacket around the chamber in which the glass wool is packed. The plates are secured using screws and can be unmounted easily. Rectangular slots have been provided on the plates near the windows to enable optical access. As fused-silica has low thermal conductivity (~ 1.5 W/mK), it acts as an insulator and prevents significant heat loss even though it is not insulated. This enables faster heating of the chamber walls and stabilization of the flame at high injection velocities and dilution.

A spark plug is mounted at the bottom plate of the combustion chamber that ignites a laminar nozzle-stabilized non-premixed flame at the beginning of the operation. The spark plug was switched-off after ignition. The spark plug is located along the central axis of the combustion chamber where the velocity is a minimum due to the creation of a stagnation point.

3.2 Other components of the experimental setup

Several auxiliary components form an integral part of the experimental setup as shown in **Figure 3.3**. Air is supplied to the setup from pressurized air receivers (upto 20 bar) filled with moisture and oil-free air by a reciprocating compressor. This can provide an operation time of 8 hours at the maximum flow rates in the current experiment. The air is made dust free using a 5-micron dust filter mounted on the supply line downstream of the receivers. The maximum error in the flow rate measurements is ± 1.5 SLPM. The air is occasionally diluted by mixing with N_2 supplied from pressurized cylinders. The air-line and the N_2 line are connected through a T-joint and the diluted oxidizer is subsequently passed through a 9-kW furnace type heater as observed in **Figure 3.3** where it is preheated to the desired temperature. The heated air is supplied to the test rig through a high-temperature flexible hose (upto 900°C) that is insulated using glass wool.

The fuel supply system delivers combustible and inert gases to the experimental test rig from pressurized cylinders as shown in **Figure 3.3**. Fuel ($\text{CO}/\text{H}_2/\text{N}_2$ mixture) and diluent (N_2) gases are stored in 46 liter cast iron cylinders filled to a pressure of approximately 140-bar. Non-return valves are attached to the hoses to prevent any back-flow of gases from the test rig. The line pressure in the test rig is regulated by spring loaded single stage pressure regulators. The fuel and diluent flow rates are controlled by digital mass flow controllers with maximum flow rates of 100 SLPM and 250 SLPM, respectively. All supply lines to the combustor are made of flexible hoses to allow vertical movement of the test section for alignment with the laser and optics.

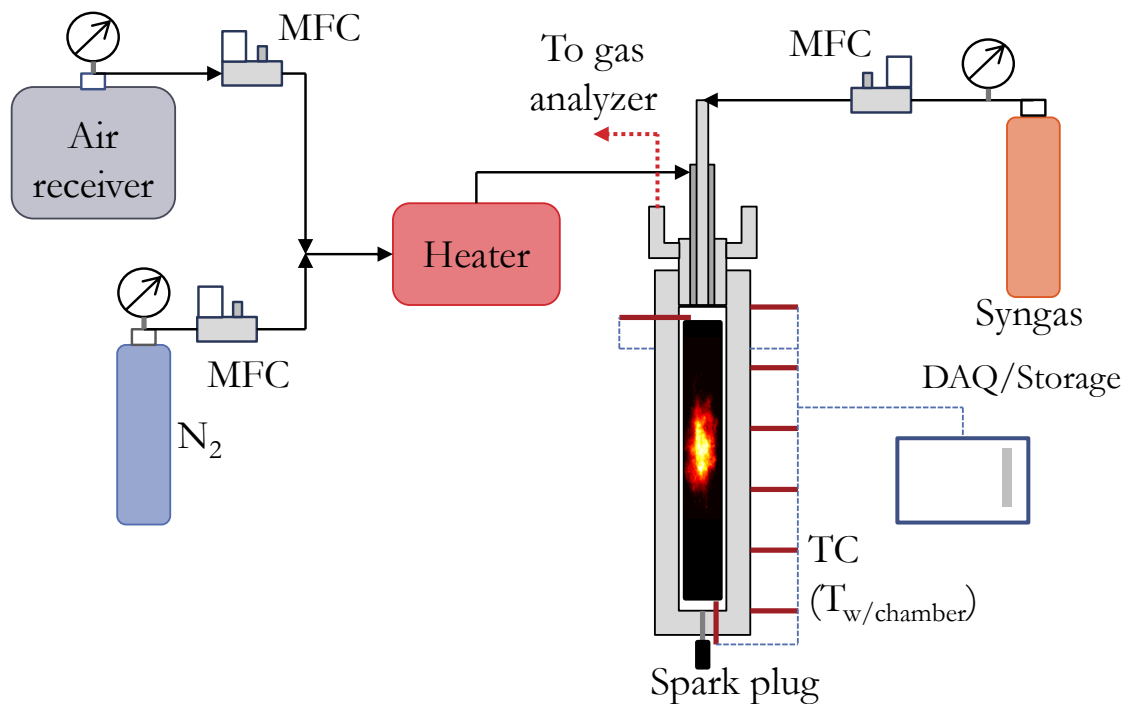


Figure 3.3: Schematic diagram of the experimental setup

Temperature measurements both within and outside the combustion chamber are performed using shielded K-type (chromel-alumel) thermocouples. Two thermocouples measure the temperature near the bottom and the top of the combustor. Six thermocouples are placed in radial slots drilled into the chamber walls to measure the wall temperature. Two additional thermocouples measure the temperature at the exit of the air-preheater and at the inlet to the setup. The data is acquired using a National Instruments Data Acquisition system (NI-DAQ, TB-4353) at 1-Hz. The DAQ device has an in-built system for cold junction compensation. The actual temperature value is different from the measured value, and the correction is given by [40]:

Experimental facilities

$$T_g = T_t + \frac{e_t \sigma D_t [T_t^4 - T_w^4]}{kNu} \quad (3.1)$$

where T_g is the actual gas temperature (K), T_t is the measured thermocouple temperature (K), emissivity e is a constant = 0.6, σ is the Stefan Boltzmann constant ($= 5.67 \times 10^{-8} \text{ W/m}^2\text{K}^4$), D is the thermocouple diameter (m), k is the gas thermal conductivity (W/m-K), Nu is the Nusselt number for a cylinder in cross-flow [93], T_w is the chamber inner wall temperature.

The oxidizer (air + N₂) passes through an Inconel tube placed within a furnace type air-preheater with a maximum capacity of 9-kW. The furnace can be heated to a maximum temperature of 1000° C using silicon carbide heating elements. The temperature of the furnace is controlled to a pre-set value using thyristor-based PID temperature controller. A thermocouple placed inside the furnace measures the temperature which is used by the controller.

3.3 Optical diagnostic techniques and system

Several optical diagnostic techniques are utilized to measure distributions of various scalar quantities under reacting conditions. The OH* chemiluminescence and OH planar laser-induced fluorescence (PLIF) techniques are used to measure the OH radical distribution and concentration, while Rayleigh thermometry is used to measure the temperature. The OH radical is chosen since the peak of the heat release rate (HRR) in counterflow diffusion flame simulations is closely correlated with the OH profiles as observed in **Figure 3.4**. This is because the primary reaction for the conversion of H₂ to H₂O is $\text{OH} + \text{H}_2 \rightarrow \text{H} + \text{H}_2\text{O}$, while that for the conversion of CO to CO₂ is $\text{CO} + \text{OH} \rightarrow \text{H} + \text{CO}_2$. Both these reactions are exothermic and major sources of heat release. The OH radical has earlier been used in several studies as markers of heat release in syngas flames [6][94]. The details of the experimental

Experimental facilities

systems for measuring OH radical distribution and temperature are described in the next few sections.

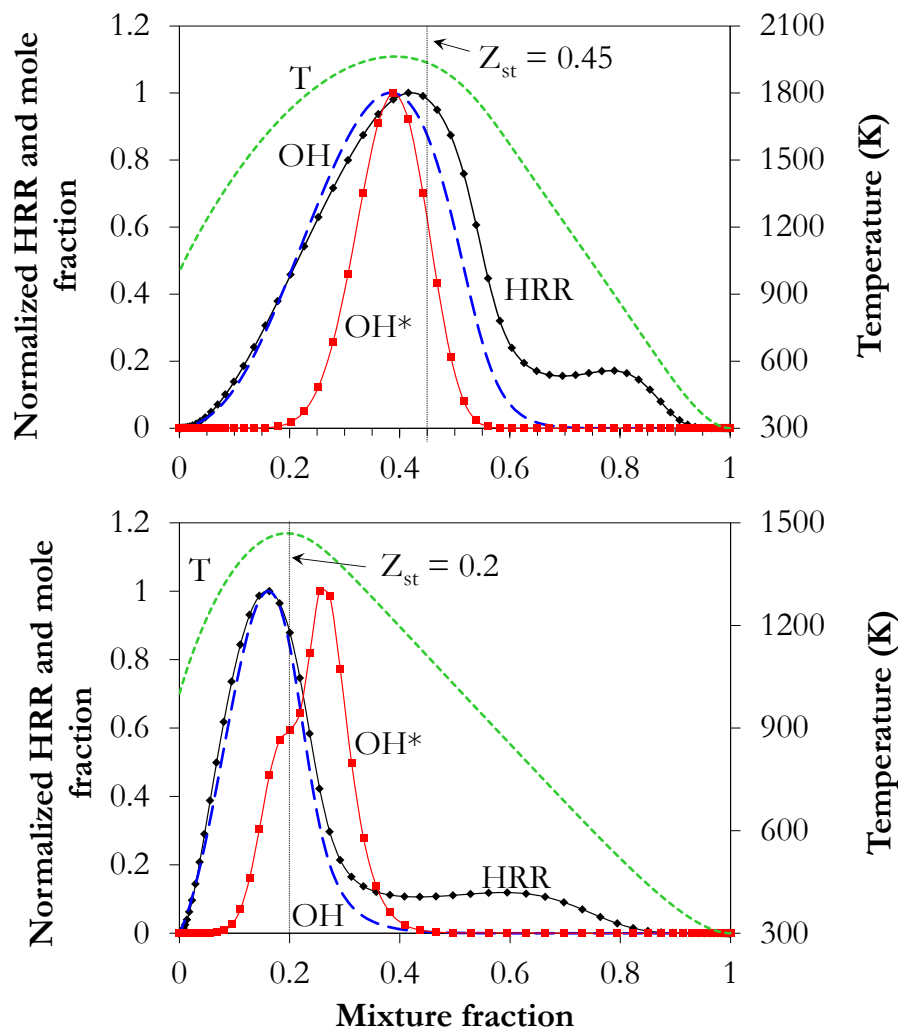


Figure 3.4: Species, temperature, and heat release rate profiles in a laminar counterflow diffusion flame. The fuel is syngas with 20% H₂, 20% CO and 60% N₂. The oxidizer is air (top) and air/N₂ with 6% O₂ (bottom) at 1000 K. The strain rate is maintained at 230s⁻¹. The heat release rate profiles closely follow that of OH and OH* profiles.

3.3.1 Single pulse Nd:YAG laser

The laser utilized for OH-PLIF diagnostics and Rayleigh Thermometry is an Nd:YAG single pulse laser (Make: Spectra Physics, Model: Quanta Ray Lab series L130). The laser consists of two high-power Xenon flash lamps that act as the light source at 1024-nm. This light is amplified in the laser cavity due to continuous reflections between the cavity mirrors. A crystal (Neodymium-doped Yttrium Aluminium Garnet) is then used to generate various harmonics of the amplified light of wavelength 1024-nm. There are two crystals placed in a housing through which the fundamental wavelength is passed. The orientation of the crystals and the light pathway inside determines the various harmonics generated. The current laser can generate second, third and fourth harmonics at 532, 355 and 266 nm, respectively. The second harmonic of 532-nm is used as the pump beam for dye-laser in OH-PLIF studies while the third harmonic of 355-nm is used for the Rayleigh thermometry experiments. The energy of the laser beam is also strongly dependent on the crystal orientation and is adjusted prior to the experiments. The power of the laser beam is measured using a power meter (Make: Gentec, Model: UP19K-30H-VR) and was observed to be 350 mJ/pulse at 532 nm and 250 mJ/pulse at 355 nm.

The beam has a circular cross-section with a diameter of around 10-mm. In the radial direction, the beam energy distribution is Gaussian. The laser beam exiting the housing is then passed through dichroic mirrors that reflect wavelengths selectively and ensure that a single wavelength laser beam is obtained at the exit. High-power laser mirrors are used to direct the laser beam from the Nd:YAG laser or the dye laser to the experimental test rig. These laser line mirrors (LaVision) reflect harmonics of 1024/ 532/ 355 nm. The mirrors have high reflectivity ($\sim 99\%$) and high damage threshold of $5\text{J}/\text{cm}^2$. The mirrors are 25-mm in diameter and are mounted on adjustable heads to vary the laser beam path. For UV

Experimental facilities

applications in the wavelength range of 245 – 390 nm, front coated mirrors with 99% reflectivity and damage threshold of 1 J/cm^2 were used.

The Nd:YAG laser has a fixed repetition rate of 10 Hz. The laser system is cooled by circulating deionized water. This is essential as the crystals are sensitive to temperature and can cause a drift in power output due to variations in temperature. The deionized water is, in turn, cooled by an external supply of cold water from a cooler through a water pump. The temperature is always maintained below 25°C .

3.3.2 Dye laser

The dye laser is used to produce light of various wavelengths using the pump laser beam as the energy input. The output of the dye laser is used for PLIF experiments of various species such as OH, NO, etc. The pump laser beam enters the dye laser where it is divided into two beams through a series of optical paths involving mirrors and lenses. One beam is directed to a preamplifier dye cell where a particular dye solution is circulated. The dye fluoresces when a pump beam is incident on it and produces a broadband radiation. This emitted radiation is then passed through a pair of diffraction gratings that determines the wavelength of the output beam depending on the angle between the gratings. The resultant beam is then passed through a coupler and a set of Brewster plates to change its polarisation. The other portion of the pump beam along with preamplified beam is then passed through the main amplifier similar to the preamplifier. The pump beam and preamplified beam needs to be properly aligned to obtain high power.

The fundamental wavelength beam is then passed through the frequency conversion unit (FCU) that contains a Barium Borate crystal (BBo). The FCU halves the wavelength (frequency doubling) of the fundamental beam such that the desired wavelength for various

Experimental facilities

PLIF experiments can be obtained. For OH PLIF experiments, the fundamental beam is around 566 nm and the excitation beam after frequency doubling is around 283 nm, which is one of the excitation wavelengths of the OH radical. The optical pathway through the dye laser with all the components is shown in **Figure 3.5**.

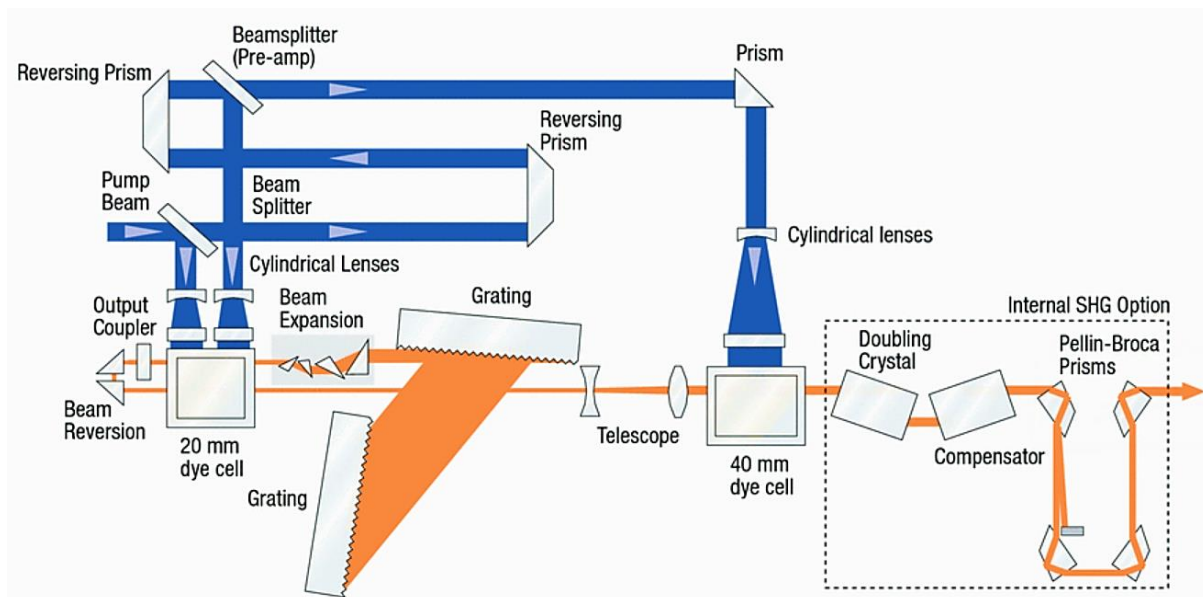


Figure 3.5: Optical pathway of the pump beam through the dye laser showing various components [95].

3.3.3 Divergent laser sheet optics and collimator

The laser diagnostic experiments carried out were planar measurements that use a laser sheet instead of a laser beam. The laser sheet is passed through a diametrical plane of the setup and provides information in that plane. The sheet is obtained using divergent laser sheet optics that consists of convex and concave lenses as shown in **Figure 3.6**. The convex lens focusses the beam at a point whereas the cylindrical concave lens expands it in the perpendicular direction to obtain a sheet. The sheet obtained is divergent and the laser

Experimental facilities

intensity is not uniform as the original beam had a Gaussian energy distribution along its diameter. This inhomogeneity is accounted for in the image processing stage by a procedure called sheet correction.

In situations where a parallel laser sheet is required, a device called a collimator is used. The collimator is mounted with the sheet making optics sans the cylindrical lens as it consists of a set of cylindrical lenses that can produce a parallel laser sheet with minimum thickness. The collimator employed by us can produce a laser sheet of height 50-mm with a thickness of around 0.5-mm. Specific details of the optics and configurations for OH-PLIF and Rayleigh measurements will be provided in the subsequent sections.

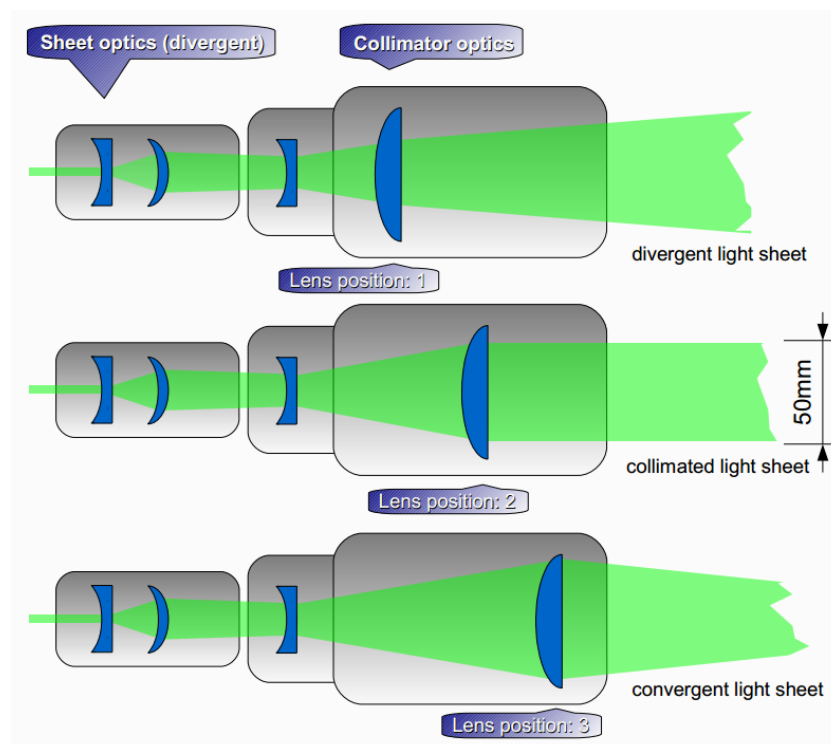


Figure 3.6: Schematic diagram of the divergent sheet optics coupled with the collimator showing the laser beam path [96].

3.3.4 Imaging system: Camera and intensifier

The imaging system for the OH-PLIF and Rayleigh thermometry experiments consists of a charged coupled device (CCD) based camera and collection optics. A CCD sensor works on the principle of photoelectric emission of electrons due to the incidence of photons. For OH-PLIF, 12-bit CCD camera (Make: Lavigation, Model: Imager SX) with 2360x1776 pixels is used. For Rayleigh thermometry, a 14-bit CCD camera (Make: LaVision, Model: Imager ProX) with a sensor resolution of 1600 pixels x 1200 pixels is used. The camera is mounted with a UV lens (Nikor, focal length = 105-mm, $f4.5$) for both the experiments. For the high-speed OH* chemiluminescence imaging, a CMOS camera (Make:Photron, Model: Fastcam SA-5, 1024 x 1024 pixels upto 7000 fps) is used. Another device called intensified relay optics (IRO, Make: LaVision) is set up to amplify the signal. This is particularly useful as the CCD or CMOS camera is not sensitive enough to capture the weak fluorescence and Rayleigh signal that lasts for a few nanoseconds (~ 10 ns). The IRO consists of a photocathode and a phosphor screen that provides the signal amplification based on the gain that has been set. Further details of the imaging systems pertaining to the specific experimental techniques will be discussed in the relevant sections.

3.3.5 Programmable timing unit (PTU)

The programmable timing unit (LaVision, PTU v9) is used to synchronize and provide trigger signals to the various components of the laser diagnostic system such as the laser, intensifier, camera, shutter, etc. The trigger is a transistor-transistor logic (TTL) pulse with a square wave profile and ± 5 V amplitude. The laser pulse triggers the flash lamps and the Q-switch. The PTU also provides the camera trigger that controls the gate opening for CCD exposure. The Image Intensifier is also synchronized with the camera gate opening using the PTU. The laser shutter trigger is provided prior to the camera trigger to account for

Experimental facilities

the delay in the generation of the fluorescence signal. The delays in the various components can be accounted for and controlled by the software DaVis (LaVision), which is used for image acquisition and processing.

3.4 Exhaust gas analyzer

The exhaust gas composition at the exit of the combustion chamber is measured using a system comprising of two analyzers that detect NO_x and $\text{CO}/\text{CO}_2/\text{O}_2$, respectively. The NO_x ($\text{NO} + \text{NO}_2$) concentrations are measured using a chemiluminescence-based analyzer (California Analyser Instruments 600 series CLD). The CLD analyzer is calibrated with a known composition of NO in nitrogen (N_2) prior to the measurements. The detector can operate in two ranges of 0 – 100-ppm and 0 – 2500-ppm. For the present investigation, the 0 - 100 ppm has been used. The response time of the analyzer is typically < 2 seconds to 90% full scale. The nominal repeatability and linearity have been reported by the manufacturer to be better than 0.5% of full scale.

The measurements of CO and CO_2 concentrations are performed using Non-Dispersive Infrared (NDIR) sensor while O_2 is measured using a paramagnetic detector (Fuji Electric ZRE series). The paramagnetic property of oxygen (O_2) is used for its fast and accurate measurements in the analyzer. The range of the sensor for the different species is as follows - CO : 0 – 200 ppm and 0 – 2000 ppm in dual range; CO_2 : 0 – 5% and 0 – 20% in dual range; O_2 : 0 – 10% and 0 – 25% in dual range. The response time is typically less than 60 seconds to 90% of full scale. The nominal repeatability is better than 0.5% of full scale while the linearity is better than 1% of full scale.

The analyzers are mounted in a single cabinet that also contains allied systems for sampling and conditioning (Analyser Instruments Company, Kota, India). The sampling

Experimental facilities

system consists of a diaphragm pump with a moisture trap. The sampling line is heated to avoid moisture condensation. The flow circuit consists of pressure regulators and rotameters that ensure proper flow rates and pressure for each analyzer. The system is calibrated using pressurized cylinders of zero gas (N₂) and span gas (O₂/CO diluted with N₂) of specified concentration. The system is warmed-up and calibrated before conducting the experimental measurements.

3.5 Microphone

The combustion noise was captured using a 1/4 inch microphone (PCB: 130E20). The sensor was tested using an acoustic calibrator (PCB CAL200) with a sound pressure level (SPL) of 94 dB and 114 dB (± 0.2 dB) at 1 kHz ($\pm 1\%$). The output was conditioned by a signal conditioner (PCB: 480E09) before the acquisition. The acquisition was performed using the NI-Labview software, while the data was processed separately using Labview and Matlab that produced similar results.

3.6 Summary

In this chapter, the details of the experimental facilities used for studying syngas combustion were described. The combustion test rig along with several other components of the experimental setup has been described in detail. The measuring instruments used in the current thesis and their working principle were also discussed. These instruments include laser-based optical diagnostic systems, microphone, and exhaust gas analyzer. The particular setup for performing these measurements will be discussed in the relevant portion in the subsequent chapters. The results of the investigations of syngas combustion using these instruments are also presented in the subsequent chapters.

Chapter 4

Transient combustion characteristics

In this chapter, the global characteristics of syngas combustion in the reverse flow configuration are presented. The focus is on the dynamics of combustion to better understand the static stability of various combustion modes which will be described in the following sections. This investigation forms the foundation before more involved laser diagnostic studies are presented and discussed in the subsequent chapters. To fulfill this objective, the combustion of a representative composition of syngas in the optically-accessible reverse flow (RF) combustion chamber at $P = 1$ atm is investigated using OH* chemiluminescence (5 kHz), noise (50 kHz) and emissions (NO_x and CO) measurements. The O₂ content in the oxidizer (7.6 - 21%), the global equivalence ratio ($\Phi_{\text{global}} = 0.32 - 0.89$), and the oxidizer preheat temperature ($\sim 400 - 800$ K) are the major parameters that have been varied to obtain a wide range of operating conditions such as conventional, ultra-lean, transition, and MILD. The purpose is to determine the limits of stable operation in terms of the operating parameters which has both practical and fundamental significance. The next few sections report the experimental setup and the operating conditions, followed by discussions of the results and a brief summary of the key findings.

4.1 Experimental details

4.1.1 Operating conditions

The fuel entering the chamber at ambient temperature represents syngas obtained from biomass gasification (20% H₂, 20% CO, 60% N₂ by vol.) with low calorific value (~ 4.6 MJ/kg). The fuel flow rate is maintained constant at 42 SLPM (**Table 4.1**) which results in a thermal input of 3.26 kW. An additional input of up to 1.23-kW enters due to preheating of the oxidizer (ultra-lean A125). The average velocity of the fuel jet is 99 m/s ($Re_f \sim 15600$), while that of the co-flowing oxidizer varies from 47 – 177 m/s ($Re_{ox} \sim 1880 - 4590$). The jet momentum ratio of the fuel and the oxidizer streams vary from 0.14 - 1.18 which is higher than the lower limit of $G_{fuel} / G_{air} = 0.006$ for stable operation reported by Szegö et al. [41] in their reverse flow chamber operating on methane and LPG. It must, however, be noted that the value of the jet momentum ratio is not universal and is a function of geometry, fuel, and inlet conditions. For the present case, the combustion was stable for the range of G_{fuel} / G_{air} reported.

Table 4.1: Experimental conditions.

Cases	Conventional		Ultra-lean	Transition	MILD
	A50		A125	A85N40	A45N80
Fuel (slpm)	42		42	42	42
Coflow (slpm)	Air	50	125	85	45
	N₂	0	0	40	80
O₂% in coflow	21		21	14.3	7.6
Φ_{global}	0.8		0.32	0.47	0.89
$T_{in,f}$ (K)	295		295	295	295
$T_{in,ox}$ (K)	605		789	784	749
Re_f	15670		15670	15670	15670
Re_{ox}	2018		4215	4233	4364
Mom. F (N)	0.0634		0.0634	0.0634	0.0634
Mom. Ox (N)	0.0535		0.4361	0.4333	0.414
Mom. flux ratio	5.27		0.65	0.65	0.68

Transient combustion characteristics

The global equivalence ratio (Φ_{global}), O_2 percentage, and the oxidizer preheat temperature (T_{ox}) are the major parameters that have been varied to obtain a wide and unique range of operating conditions. The Φ_{global} within the chamber varies from 0.32 - 0.89, while the volume percentage of O_2 in the oxidizer varies from 21% (conventional, ultra-lean) to 7.6% for the MILD case. The flow rates are maintained constant for the ultra-lean, transition, and the MILD cases while reducing the O_2 percentage (**Table 4.1**). With similar velocity and temperature fields for these cases, the effect of N_2 dilution and the Φ_{global} on the combustion stability can be clearly identified. The effect of preheat temperature on the combustion stability is investigated by turning-off the air-preheater once steady operating conditions are reached under MILD conditions. The oxidizer temperature gradually drops from around 800 K to 400 K, while the combustion noise and the emissions are measured at regular intervals. The objective is to identify the lowest preheat temperature at which the combustion is stable.

The Damköhler (Da) numbers (**Table 4.2**) are estimated for the conventional, ultra-lean, and MILD conditions using detailed 2-D RANS and 3-D DES simulations (EDC with Li et al. H_2/CO chemistry [97] with the modified H_2/O_2 chemistry by Burke et al. [98]), which will be reported in detail in subsequent chapters. Following Mardani et al. [99] the Kolmogorov (Da_η) and Integral (Da_I) Damköhler numbers are defined as follows:

$$Da_\eta = \left(\frac{v/\varepsilon}{\rho^2/C_r^2} \right)^{1/2} \quad (4.1)$$

$$Da_I = \frac{k/\varepsilon}{\rho/C_r} \quad (4.2)$$

Here, C_r is the local maximum of the reaction rate constant that provides an estimate of the upper limit of the Da . The Da values suggest that all the combustion modes are dominated by finite rate kinetic effects. The Da_I values are of the same order as reported by Ihme et al. [67]

Transient combustion characteristics

for the JHC burner and capture the trend reported in cases where the lowest Da is observed for the MILD case, followed by the ultra-lean and the conventional case.

Table 4.2: Estimated Damköhler number for the conventional, ultra-lean, and the MILD cases

Cases	Da_η	Da_l
conventional A50 (RANS)	0.0085	0.2688
ultra-lean A125 (RANS)	0.00097	0.0597
ultra-lean A125 (DES)	0.0021	0.0222
MILD A45N80 (RANS)	0.00065	0.0416
MILD A45N80 (DES)	0.0014	0.0143

The intensity of recirculation in the reverse flow configuration is characterized by the recirculation ratio (R).

$$R = \frac{\dot{m}_{total} - \dot{m}_{in}}{\dot{m}_{in}} \quad (4.3)$$

Here, \dot{m}_{in} represents the net mass of the incoming fresh reactants while \dot{m}_{total} is the total flow rate (reactants + entrained diluents) in the forward axial direction. The total mass flow rate (\dot{m}_{total}) in **Eqn. 4.3** for calculating the recirculation ratio has been estimated using data obtained from numerical simulations while the mass flow rate at the inlet (\dot{m}_{in}) is obtained from experimental measurements using digital mass flow controllers and given as boundary conditions into the numerical simulations. The estimated maximum recirculation ratio along the chamber centerline is R around 2.5 for the ultra-lean and the MILD cases, which is higher than that reported in the SPRF combustion chamber [19], but lower than the range ($R \geq 3$) specified by Plessing [38] to achieve flameless combustion of methane in their reverse flow furnace.

4.1.2 Measurement techniques and data processing

The experimental layout and instrumentation are shown in **Figure 4.1**. The natural flame luminosity images have been acquired using a DSLR camera (Make: Canon, Model: EOS 60D) with an exposure time of 0.5 seconds. The OH* chemiluminescence images were recorded at 5 kHz with a CMOS camera (Make: Photron, Model: Fastcam SA-5, 1024 x 1024 pixels upto 7000 fps) that was connected to an intensifier (Make: LaVision) with an exposure time of 76- μ s. A bandpass filter centered at 308-nm (FWHM = 10 nm) was used to collect the chemiluminescence with a resolution of around 80 μ m/pixel. The OH* images provided line-of-sight integrated images that were used to visualize the reaction zone. The high-speed images also provided statistics such as mean, standard deviation, and the power spectral density.

The combustion noise was captured at 50 kHz using a 1/4 inch microphone (Make: PCB, Model: 130E20). The sensor was tested using an acoustic calibrator (Make: PCB, Model: CAL200) with a SPL of 94 dB and 114 dB (\pm 0.2 dB) at 1 kHz (\pm 1%). The microphone was positioned 200-mm away from the exhaust nozzle at an angle of 45° with the horizontal. The output was conditioned by a signal conditioner (Make: PCB, Model: 480E09) and passed through a Butterworth type lowpass filter set at 25 kHz. The acquisition was performed using the NI-Labview software, while the data was processed separately using Labview and Matlab that produced similar results. For each case, the data were acquired for 10 seconds and processed to obtain the SPL and the power spectral density. The error in the SPL was estimated to be \pm 0.2 dB.

The emission of NO_x (NO + NO₂) from the combustion chamber is measured using a chemiluminescence-based analyzer (Make: California Analyser Instruments, Model: 600 series CLD) with a dual range of 0-100 ppm and 0-2500 ppm. For the current set of

Transient combustion characteristics

experiments, 0-100 ppm range of the instrument was used. The species CO (0-2000 ppm) and O₂ (0-25% by vol.) are measured using the ZRE gas analyzer (Make: Fuji Electric, Model: ZRE series, NDIR for CO/CO₂ and paramagnetic analyzer for O₂). The sensors were purged with N₂ and calibrated using calibration gas cylinders prior to every measurement. The measurements have been normalized at 15% O₂ and reported here.

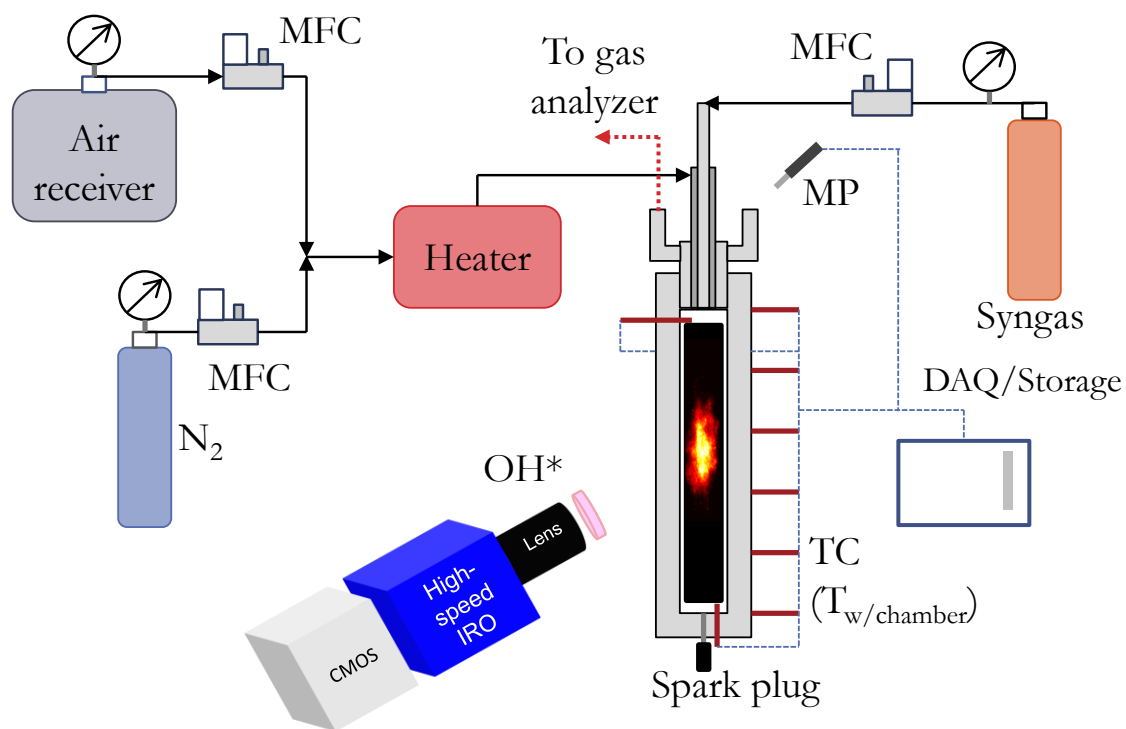


Figure 4.1: Schematic diagram of the experimental setup. (Acronyms: TC – thermocouple, DAQ – data acquisition system, MP - microphone).

4.2 Results and discussions

4.2.1 Flame visualization

The reactants are ignited in the non-premixed configuration and the initial flame is observed to be attached to the nozzle. With increasing flow rate, the reaction zone moves downstream and starts detaching from the nozzle-attached diffusion flame. The flame finally lifts-off and the nozzle-attached flame is quenched as can be observed for the conventional case (A50) in **Figure 4.2**. The luminous spindle-shaped flame appears highly localized with the lifted edge extending towards the inlet. Next, the flow rate of N_2 is increased to 80 slpm while the air flow rate is reduced to 45 slpm to reach the MILD condition. This mode of combustion is characterized by high percentage of the diluent N_2 (92.4%) and low percentage of O_2 (7.6%) in the oxidizer. The global adiabatic flame temperature is around 1450 K. It must be noted here that the O_2 content is still sufficient for complete combustion with 0.7% excess O_2 in the exhaust by volume. The flame is stabilized further downstream as compared to the conventional case. The flame appears volumetric and distributed with very low luminosity, although it is not completely invisible, or flameless, or colorless. Earlier studies on flameless or MILD combustion have also reported a weakly luminous flame, such as in [45], [47], [100], [34] where the flame is not altogether invisible but shows a high degree of transparency, low luminosity, and appears distributed. However, other studies have reported a yellowish-red glow from the chamber walls in the background with no visible emission from the flame, such as in [49] and [41]. Zhou et al. [49] used spectroscopic measurements to attribute this low luminosity in the flameless combustion of methane to a suppression of CH^* and C_2^* emissions along with a significant increase in the background emissions from CO_2^* emissions. It must be noted here that heat release signature from the reaction zone is often investigated by probing the OH radical that emits radiation in the UV region invisible to the

Transient combustion characteristics

eyes and as such, visible proof of “flamelessness” is insufficient to deem the reaction zone as volumetric and distributed [49]. The N_2 flow rate is subsequently decreased while increasing the air flow rate to reach the transition state (A85N40) with 14.3 % O_2 in the oxidizer. The flame here is stabilized closer to the nozzle and less distributed as compared to the MILD case. As the flow rate of air is further increased and N_2 dilution is stopped, the ultra-lean case (A125) is attained which appears similar to the transition case but is stabilized closer to the nozzle. Overall, the luminosity images show visible differences in the flame emissions and stabilization locations which are indicative of distinct combustion conditions. It is also noteworthy that the current combustor design can operate over a wide range of conditions in terms of N_2 dilution and global equivalence ratio.

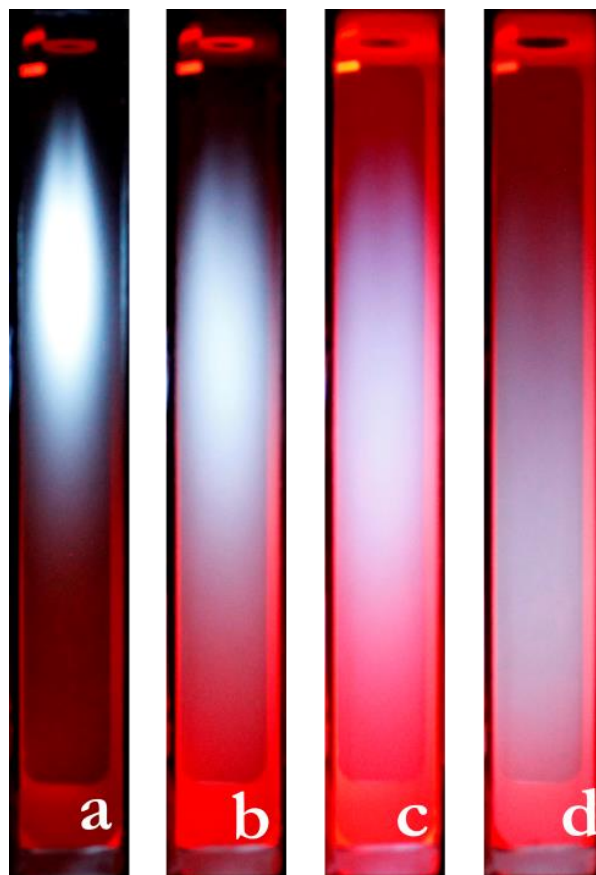


Figure 4.2: Natural flame luminosity images for the cases (a) conventional, (b) ultra-lean, (c) transition, and (d) MILD have been shown. The camera exposure time was 0.5 seconds.

4.2.2 Mean and standard deviation of the OH* chemiluminescence

The spontaneous OH emission (OH*) is investigated next to obtain greater insights into the location of the reaction zone. The line-of-sight integrated mean and standard deviation of the OH* chemiluminescence signal is shown in **Figure 4.3**. From counterflow diffusion flame simulations, the peak of the OH* is observed to correlate with the heat release rate, although the peak is shifted to the rich side of the stoichiometric plane with increasing N₂ dilution. The reaction zone is symmetric about the vertical axis and appears ellipsoidal in shape as observed in **Figure 4.3**. The figure shows that except at the leading edge, the signal is highest at the center and decreases with increasing radius, unlike diffusion flames in which high OH* is observed in the shear layer. This indicates good mixing between the fuel, the oxidizer, and the exhaust before ignition. For the conventional case, the strong OH* signal can be observed with the maximum at around 90-mm from the injector. However, the flame appears to be attached to the nozzle as the average signal is continuous near the leading edge. It will be seen in the next section that this region is dominated by the formation, growth, and merging of ignition kernels that appears as a continuous flame in the mean. As the air flow rate is increased to reach the ultra-lean conditions (A125), the peak OH* intensity decreases by a factor of 4, although the high-intensity region appears localized at the center of the chamber. The intensity further decreases and becomes wider in the lateral direction with an increase in the dilution of N₂ (transition and MILD). The lowest signal intensity is observed for the MILD case with a nearly uniform distribution, although the length of the OH* region in the axial direction appears similar to the other cases. The flame also stabilizes further downstream with dilution, probably due to longer times required to mix with sufficient O₂. The decrease in OH* intensity is different from the observation of Sidey et al. [57], who

Transient combustion characteristics

found that the intensity is not very sensitive to the O₂ concentration during the combustion of methane with heated and diluted cross flow. The difference in the OH* signal despite the presence of similar temperature and flow conditions for the ultra-lean–MILD cases highlights the role of kinetics in the position and distribution of the reaction zone.

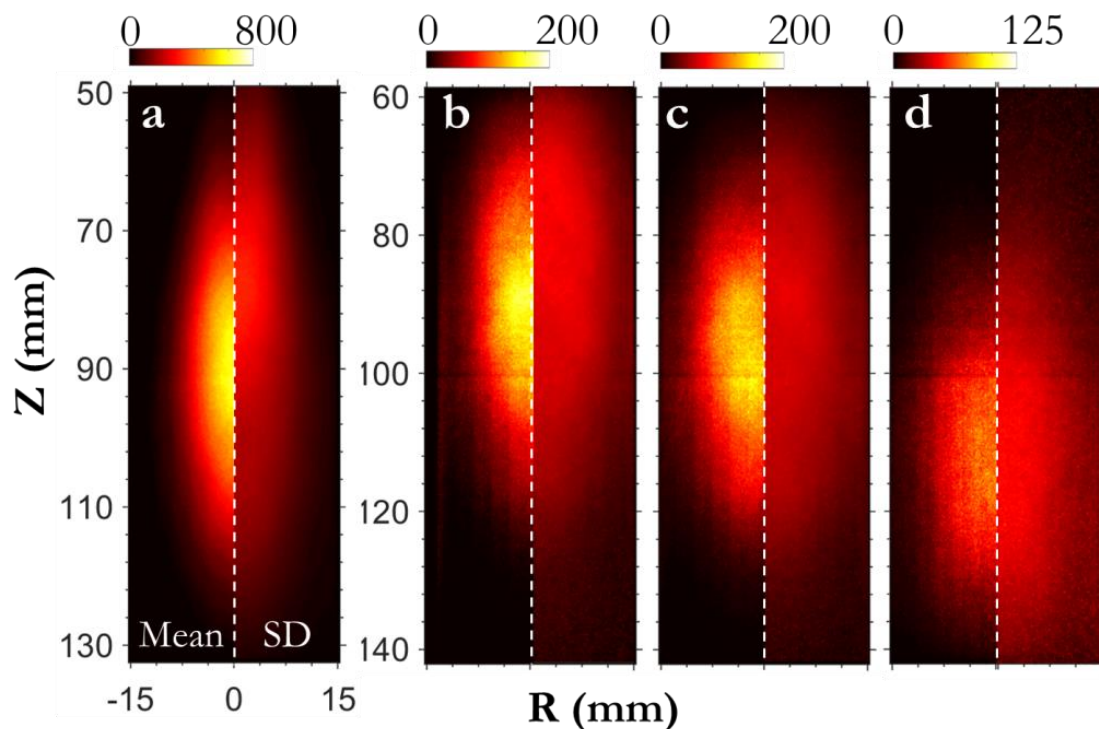


Figure 4.3: Mean and standard deviation images of OH* chemiluminescence signal. From left, the images are for the cases (a) conventional (A50), (b) ultra-lean (A125), (c) transition (A85N40), and (d) MILD (A45N80), respectively. Z refers to the distance from the exit plane of the reactants while R is the radial distance.

(Acronym: SD - standard deviation).

The standard deviation (SD) of the chemiluminescence signal is next analyzed to obtain insights into the flame unsteadiness and stability (**Figure 4.3**). The highest SD is observed for the conventional case (~ 260 counts) near the center of the flame (~ 90-mm),

Transient combustion characteristics

signifying marked unsteadiness in the intensity and location of the reaction zone. This is contrary to the luminosity image in which an intensely burning and well-defined flame can be observed in **Figure 4.2a**, thus highlighting the necessity of the high-speed imaging conducted here. The SD is comparable or even higher than the mean signal near the upstream location (~ 50-mm) and represents intermittency in the flame at this location. Similar observations can also be made at the upstream locations of the other three cases (**Figure 4.3b, c, d**). In the lateral direction, the flame movement is not significant, as can be observed in the conventional case. The magnitude and distribution of the SD are similar for the ultra-lean and the transition cases, suggesting that the combustion modes are similar despite dilution. The SD is the lowest for the MILD case (A45N80), suggesting steadiness and stability in the flame location.

The histogram of the average global intensity obtained from the high-speed images is shown in **Figure 4.4**. The histogram shows the mean and the spread in the distribution of the global OH* counts. The histogram corroborates with observations from the mean images regarding the decrease in intensity as transition occurs towards the MILD case. The spread in the global OH* counts is also highest for the conventional case as was observed in the contour images shown in **Figure 4.3**. Although the O₂ percentage in the oxidizer for the transition case (14.3% O₂) is midway between the ultra-lean (21% O₂) and the MILD (7.6% O₂) cases, the decrease in the mean counts is not proportional. The global mean counts for the ultra-lean case are 30, while that for the transition and MILD cases are 26 and 13, respectively. This variation can be attributed to the excess O₂ in the recirculating exhaust gases within the chamber. While the MILD case has around 0.7% excess O₂ in the exhaust, this value increases to 5.6% for the transition case and 10.7% for the ultra-lean case. This also shows that sufficient mixing takes place between the recirculating exhaust and fresh reactants before the onset of combustion. The variation in the global intensity follows a

Transient combustion characteristics

normal distribution for all the cases.

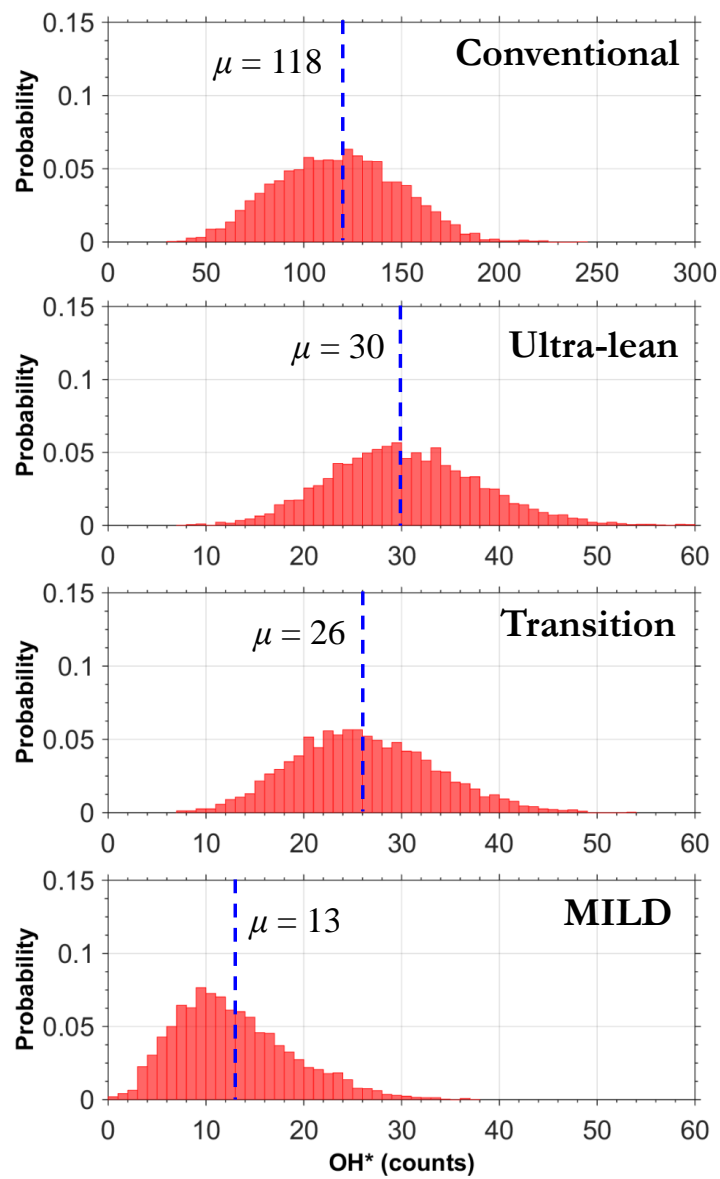


Figure 4.4: Histogram of the global OH* counts for the conventional, ultra-lean, transition, and the MILD cases.

4.2.3 Ignition kernel and stabilization

The instantaneous OH* chemiluminescence images are used to investigate the leading edge structure of the flame as observed in **Figure 4.5** to understand the mode of flame stabilization. The images show that the flame conforms to the large-scale turbulent structures within the chamber and appears completely lifted, as was also observed in the luminosity images (**Figure 4.2**). Several transient ignition kernels can be observed in all the cases which show that autoignition is the mode of flame stabilization (**Figure 4.5**). These kernels appear, grow, and subsequently merge with the flame downstream. However, Bobba [19] suggests that high levels of turbulence along with low average velocity is responsible for flame stabilization during methane combustion in the SPRF combustor both in the premixed and non-premixed modes. This indicates that the temperature of the coflow and the fuel composition is critical in determining the mode of stabilization (autoignition or flame propagation). Autoignition of ethylene, natural gas mixtures, and methane have also been observed in other canonical configurations (jet in heated coflow/ jet in heated crossflow) such as by Oldenhof et al. [55], Mendez et al. [56] and Sidey et al. [57], respectively, where the temperature of the coflow was > 1100 K, thus highlighting the sensitivity to temperature. In the present study, the coflow is preheated upto around 800 K, which is further augmented by the recirculation of the exhaust gases induced by high injection velocities (~100 - 200 m/s). The presence of H₂ also reduces the ignition delay as observed in **Table 1.1** such that the mixture autoignites before it obtains a location with low enough velocity to stabilize and propagate. This also indicates that H₂ containing fuels such as syngas may exhibit a propensity to stabilize by autoignition, although further investigation with different compositions (H₂/CO) are necessary to draw a definitive conclusion.

Transient combustion characteristics

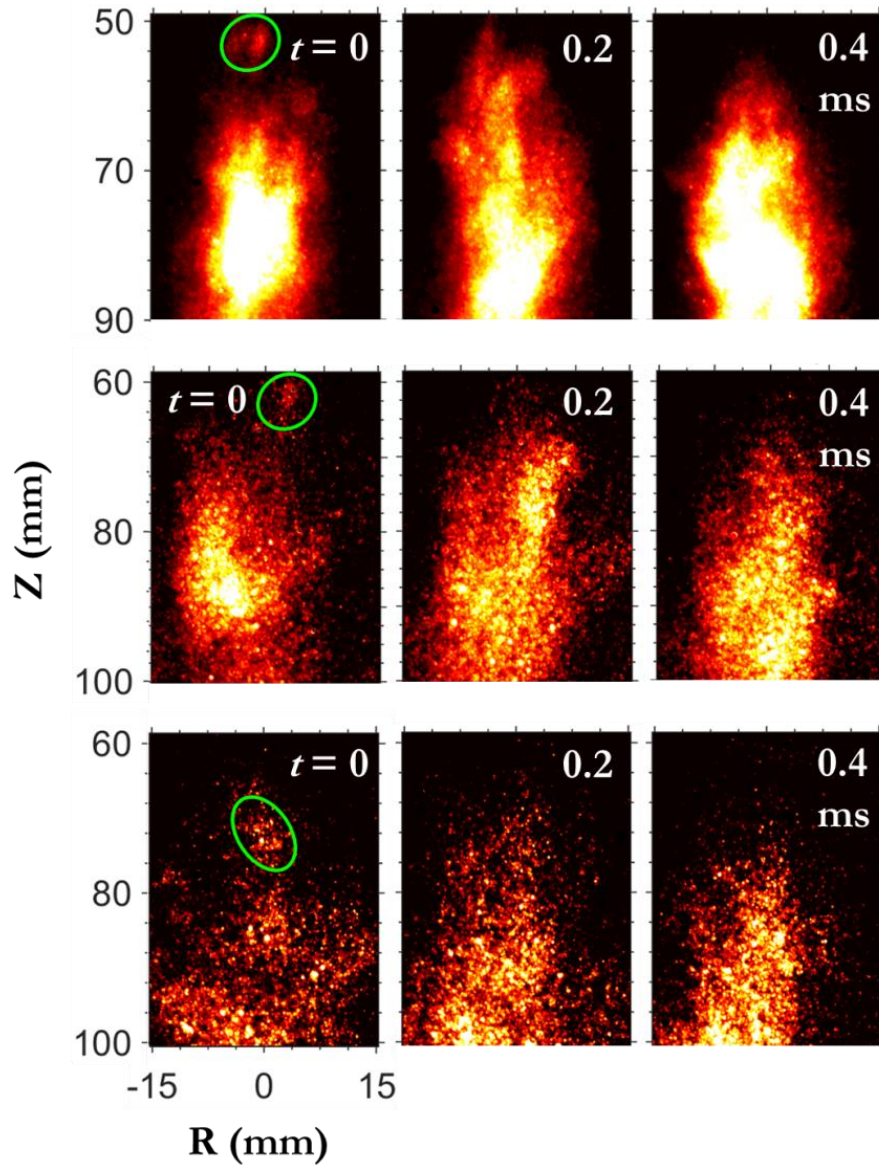


Figure 4.5: Instantaneous OH* chemiluminescence images showing the formation and merging of autoignition kernels for the conventional (top), ultra-lean (middle) and the MILD (bottom) cases. Z refers to the distance from the exit plane of the reactants while R is the radial distance.

4.2.4 Sound pressure level (SPL) measurements

To augment the understanding of the combustion modes, the noise emanating from the combustion chamber to determine the sound pressure level (SPL) is measured and possible interactions between the flame and the chamber acoustics are studied. The average background noise recorded without combustion was determined to be 69.2 dB. The highest SPL was recorded for the conventional case (84.5 dB). This value decreased slightly to 83.4 dB for the ultra-lean (A125) case. As the combustion progressed towards transition (A85N40) and MILD combustion modes (A45N80), the SPL also decreased. The decrease was moderate for transition (82 dB), while the lowest SPL of 78.6 dB was recorded for the MILD case. A decrease in the SPL has also been observed by other researchers during MILD combustion, although a higher noise level was recorded during transition [100]. The noise level is thus sensitive to how the transition is achieved. This also motivates us to investigate the transient characteristics of the chemiluminescence and the noise signal.

4.2.5 Power spectral density of the chemiluminescence and noise signal

To identify possible interactions between the flame and the acoustics of the chamber, the power spectral density (PSD) of the global OH* signal and the noise emanating from the combustion chamber are determined and shown in **Figure 4.6** and **Figure 4.7**, respectively. The PSD of the global OH* signal shows that the energy is higher at lower frequencies and decreases at higher frequencies; however, distinct resonant frequencies are not evident. The energy content is the highest for the conventional case, followed by the ultra-lean, transition, and MILD cases. The spectrum for the ultra-lean and the transition cases nearly overlap, thus following a trend similar to that of the SPL and the mean OH* intensity as observed in

Transient combustion characteristics

Figure 4.3. For the last three cases, the spectrum is similar in the low-frequency regime (< 200 Hz). However, the spectrum for the MILD case shows a sharp decrease in energy after 1000 Hz, suggesting a suppression of higher frequencies.

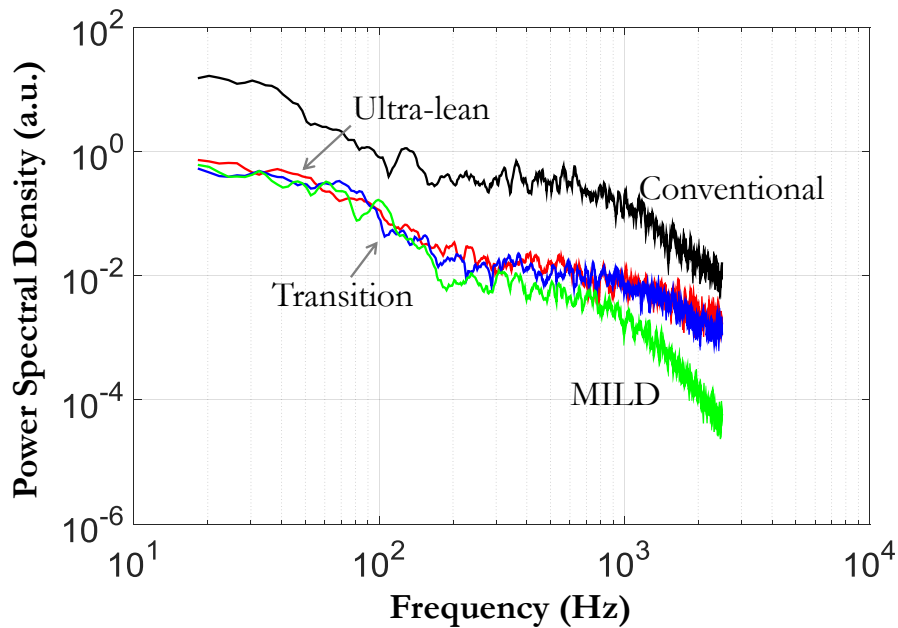


Figure 4.6: Power spectral density of the OH* chemiluminescence signal for the conventional (A50), ultra-lean (A125), transition (A85N40), and MILD (A45N80) cases.

The power spectrum of the combustion noise, however, shows several resonance modes that span the entire frequency range upto 5 kHz. The spectrum can be divided into two zones - < 200 Hz and > 800 Hz in which the noise is concentrated. The low-frequency noise is similar for all the cases with slight variations in the amplitude. On closer inspection, several peaks can be observed similar to the PSD of the OH* signal, although a distinct peak at 100 Hz can be observed in the noise spectrum that is not evident in the OH* signal. These low frequencies can be attributed to resonance modes corresponding to the total length of the

Transient combustion characteristics

system [101] consisting of the chamber, flow passages, and fuel and exhaust manifolds. The difference in temperature and length of these flow passages results in several frequencies of oscillation as observed in the OH* and noise signal.

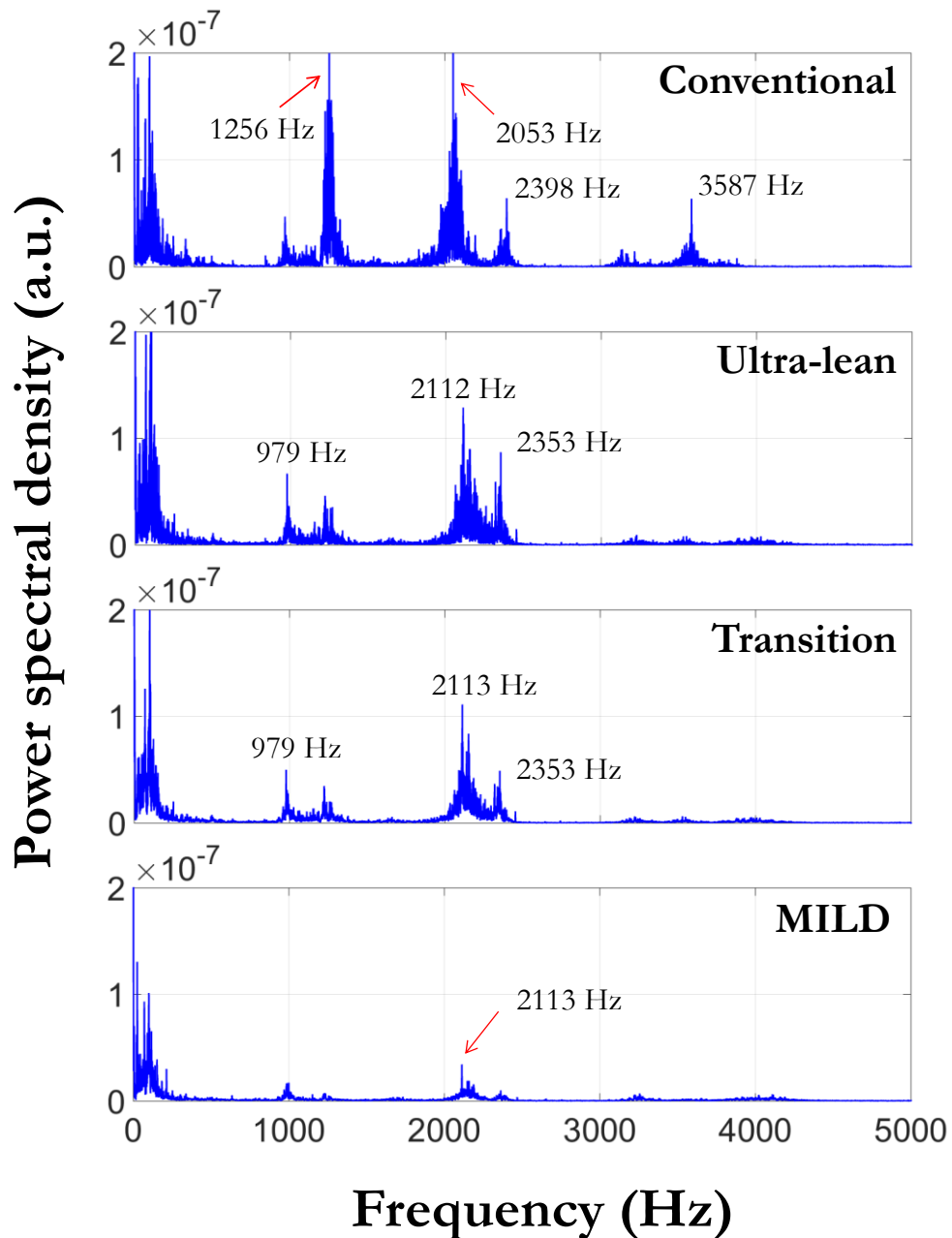


Figure 4.7: Power spectral density of the acoustic signal for the conventional (A50), ultra-lean (A125), transition (A85N40), and MILD (A45N80) cases.

Transient combustion characteristics

Significant suppression of the high-frequency modes (> 800 Hz) could be observed in **Figure 4.7** as a result of the transition to MILD combustion. Several clusters of peaks near 1000 Hz, 1250 Hz, 2050 Hz, 2400 Hz, and 3600 Hz are evident in the PSD. The amplitude of the signal follows the same trend as that of the OH* signal, with the conventional and the MILD cases being the highest and lowest, respectively. The amplitude is similar for the ultra-lean and transition cases as observed in the OH* data. The peaks in the PSD suggest that several acoustic modes of the chamber cavity are excited by the broadband spectrum generated due to turbulent combustion. The combustion chamber is nearly closed on both the ends and can be modeled as a half-wave resonator. Considering a mean chamber temperature of 1000 K, the fundamental and first two harmonics of the axial mode of this half-wave resonator occur at approximately 1200 Hz, 2400 Hz, and 3600 Hz, respectively. The interaction is complicated by the presence of heat loss to the walls, thermal inhomogeneity due to non-premixed combustion, and other three dimensional effects that may give rise to the remaining frequencies as observed in **Figure 4.7**. As the velocities and adiabatic flame temperature are similar for the cases ultra-lean, transition, and MILD cases, the suppression of the oscillations for the MILD case possibly indicates some fundamental change in the turbulence-chemistry interactions that reduce the fluctuations in the scalar variables such as temperature and pressure. The decrease in the temperature fluctuations for the MILD case is verified using Rayleigh thermometry measurements (to be presented in later chapter) that may possibly explain the reduction in the SPL and the amplitude of the resonance modes. The decrease in the acoustic amplitudes has been correlated with the flame speed or with the fuel reactivity [102] which controls the rate of expansion of the gases due to combustion and the consequent rise in pressure. Thus, the decreased reactivity under MILD conditions is responsible for this observed reduction in SPL and PSD amplitude. This suppression at higher frequencies is also consistent with the global OH* PSD, where the energy drops rapidly after

Transient combustion characteristics

1000 Hz as observed in **Figure 4.6**. This shows that MILD combustion generates lower SPL and is less susceptible to combustion oscillations than lean combustion under similar flow conditions.

4.2.6 Effect of oxidizer preheat temperature

Finally, the effect of preheat temperature of the oxidizer on the emissions and stability of the combustion in the MILD mode are investigated. The purpose is to obtain stable combustion with low emissions just with the aid of the recirculation of the high-temperature exhaust gases without preheating the oxidizer. This can provide tremendous operational advantages in terms of simplicity and requirement of auxiliary equipment. After steady operating conditions are achieved in the MILD combustion mode, the preheater is switched-off such that the oxidizer temperature gradually decreases as observed in **Figure 4.8**. The oxidizer temperature decreases from 783 K to 483 K over 2000 seconds of operation at an average rate of 9 K/min. The temperature drops at even slower rates after 2000 s with a decrease of 60 K in 900 s (4 K/min). The chamber temperatures at the top and the bottom, as well as a representative wall temperature ($Z = 215$ -mm from the inlet), are also shown in **Figure 4.8**. The wall temperature is nearly constant with a maximum variation of 26 K, while the maximum variation in the chamber temperature is 22 K over the same period. However, there is a three-fold rise in CO emissions from 470-ppm to 1333-ppm. The reasons for the observed changes in CO and NO_x emissions have been discussed in detail in **Chapter 6**. This shows that although the global furnace temperature is maintained due to the thermal inertia of the heated walls, the local combustion characteristics are significantly influenced by the temperature of the oxidizer leading to a rise in CO emissions. The NO_x emission was below the detection limit of the sensor (< 1-ppm) for all the cases. It must also be noted that the velocity of the oxidizer jet will decrease with a fall in the temperature leading to reduced

Transient combustion characteristics

entrainment and recirculation within the chamber. This is also observed to impact the stability and the local combustion characteristics as discussed in the next section. Thus, the system is unable to operate at low preheat temperatures both due to reduced recirculation and modification of the local combustion characteristics.

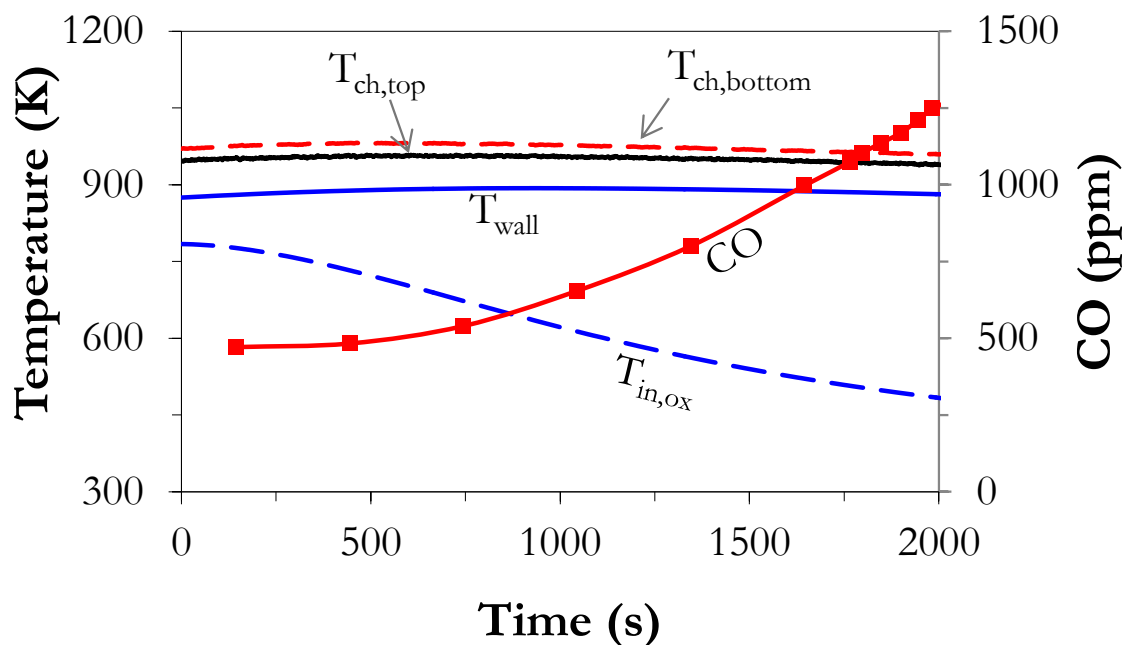


Figure 4.8: Variation of temperature and CO emissions with a decrease in the oxidizer preheat temperature.

The natural flame luminosity images with variation in the oxidizer temperature are shown in **Figure 4.9**. A transparent but clearly luminous region can be observed within the chamber when the jet temperature is high (> 700 K) which progressively becomes less luminous with a decrease in the temperature. As the jet temperature decreases below 600 K, no visible flame can be observed although the combustion is taking place as is evident by the CO emissions and the chamber temperature. The reaction zone appears very weak and nearly “flameless” although this regime is different from the flameless combustion reported in other

Transient combustion characteristics

studies, such as in [41] and [49] where the combustion is reported to be stable with very low emissions. The flame observed here may be very close to extinction with very high emissions and thus not a suitable regime for operation. Also, an increase in the audible noise from the combustion chamber is observed which is investigated further.

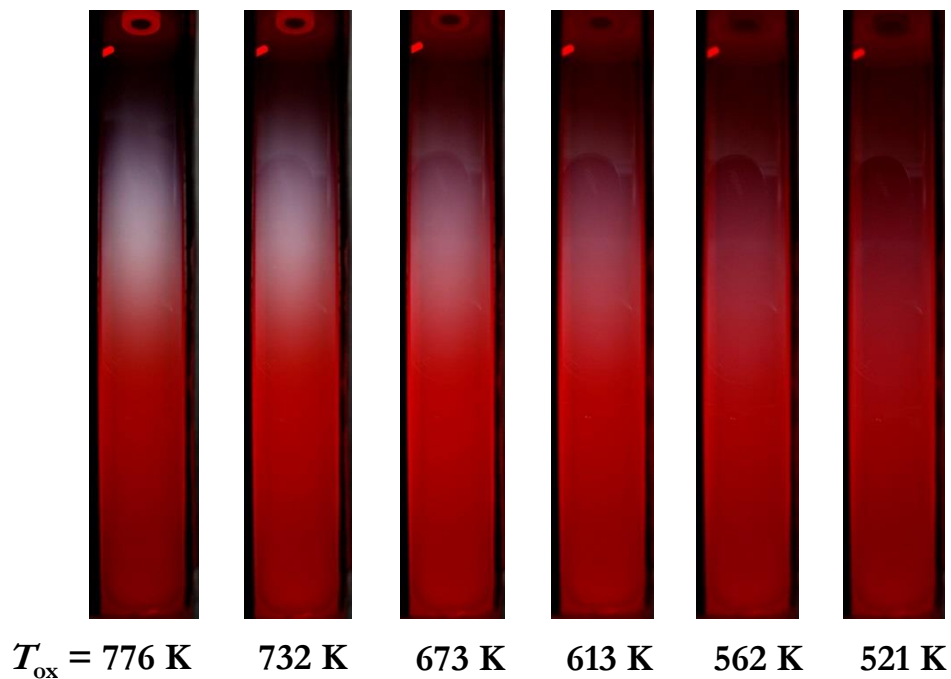


Figure 4.9: Flame visualization at different preheat temperatures of the oxidizer.

The variation in the sound pressure level (SPL) and the oxidizer temperature with time has been shown in **Figure 4.10**. As the temperature of the oxidizer stream decreased to 603 K in around 1200 s, the SPL was nearly constant in the range of 79 - 80 dB as was observed for the MILD case. With a further decrease in temperature to 547 K, the SPL suddenly increased by 6 dB to the range of 85 - 86 dB with a step jump. This sudden increase in the SPL occurs somewhere in between 603 K and 547 K. Here, the SPL is even higher than the conventional case (84.5 dB) and indicates a definite change in the combustion mode

Transient combustion characteristics

within the chamber. Plessing et al. [38] indicate an unstable mode of combustion between the conventional flame mode and the flameless mode due to lower chamber temperature and recirculation ratio and the present observation possibly indicates such a combustion regime.

Figure 4.10 also shows the lowest preheat temperature (~ 603 K) upto which the combustor can operate stably under the present conditions, although the CO emissions increase monotonically with a decrease in the temperature as observed in **Figure 4.8**.

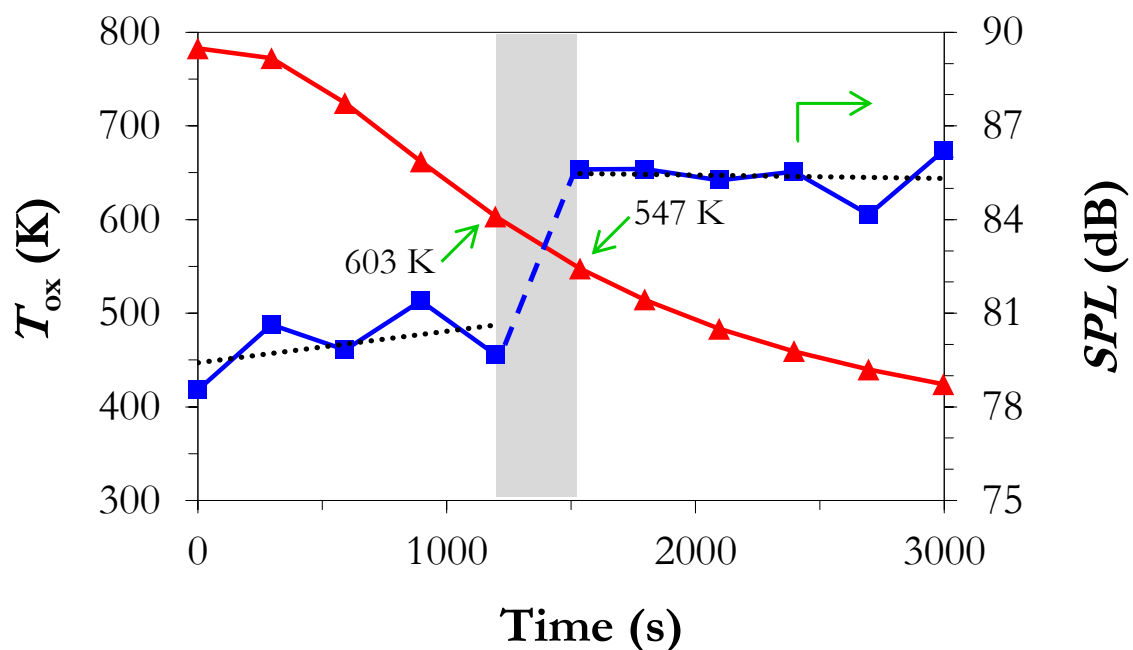


Figure 4.10: Variation of oxidizer temperature and sound pressure level (dB) with time. The dotted lines represent linear fits to the SPL data.

To further investigate the frequencies at which the sound pressure level (SPL) is intensified, the power spectral density (PSD) of the noise signal is calculated and compared with that of the MILD case in **Figure 4.11**. As observed in **Figure 4.7**, the noise for the MILD case is restricted predominantly below 5 kHz. With reduction in the oxidizer inlet

Transient combustion characteristics

temperature, the emergence of distinct high-frequency modes is observed that was not observed earlier. This noise is not broadband and comprises a distinct high-frequency peak in the range of 9 - 15 kHz with a few closely spaced peaks of lower amplitude. Such high-frequency oscillations have been observed earlier in swirl-stabilized combustion chambers that have been attributed to the first and second tangential modes (1T and 2T), while the low-frequency oscillations correspond to the longitudinal modes [103]. This also indicates that the high-frequency oscillations observed in the current configuration may correspond to the radius (R) of the chamber which is around 6 times smaller than the length (L) of the chamber. At $T_{in} = 724$ K, the PSD shows a peak at 14.38 kHz, although the amplitude is similar to that of the low-frequency noise ($A \sim 10^{-7}$) and does not increase the SPL significantly as observed in **Figure 4.10**. This peak shifts to lower frequencies as the inlet temperature decreases due to an overall decrease in the chamber temperature and corresponding decrease in the acoustic velocity. The frequency reduces to $f = 12.62$ kHz and 11.02 kHz as T_{in} decreases to 662 K and 603 K, respectively. However, the amplitude of the high-frequency peak increases with a decrease in the oxidizer inlet temperature. Thus, we observe a nearly tenfold increase in the amplitude from 603 K ($A \sim 10^{-6}$) to 547 K ($A \sim 10^{-5}$) which leads to a 6 dB increase in the SPL as observed in **Figure 4.10**. The amplitude subsequently remains nearly constant ($A \sim 10^{-5}$), while the frequency further shifts to lower values. At the lowest inlet temperature of $T_{in} = 424$ K, the high-frequency peak is observed at 9197 Hz, a drop of 5183 Hz from $T_{in} = 724$ K. These results thus show that the combustion shifts to an unstable regime below a temperature value of the oxidizer (603 - 547 K), which represents the threshold for stable operation.

Transient combustion characteristics

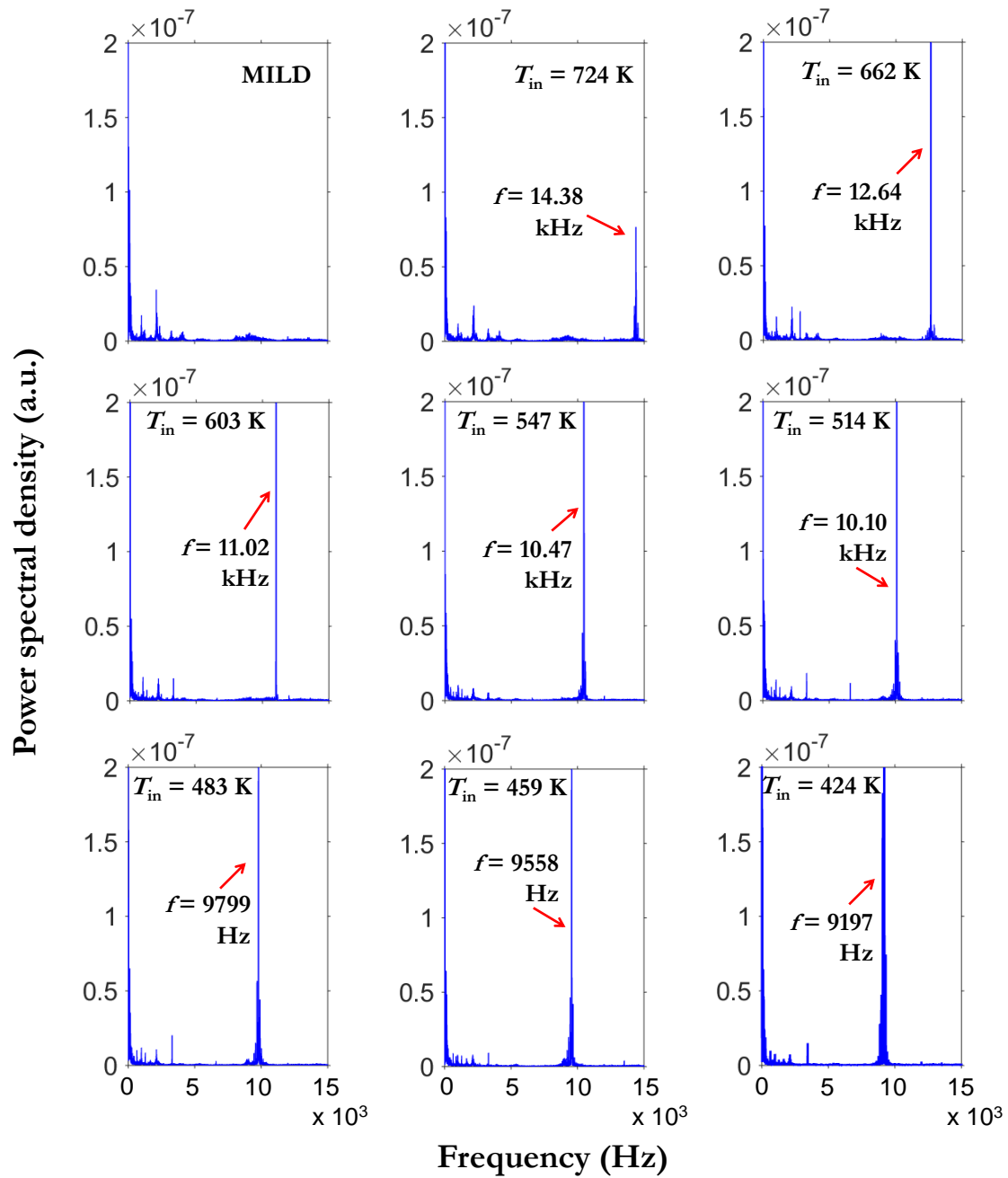


Figure 4.11: Power spectral density (*PSD*) of the noise signal at various inlet temperatures of the oxidizer stream.

4.3 Summary

In this chapter, the global and transient combustion characteristics of low calorific value syngas in the reverse flow configuration at $P = 1$ atm are investigated using OH* chemiluminescence (5 kHz), noise (50 kHz) and emissions measurements. The major parameters varied are the global equivalence ratio (0.32 - 0.89), O₂% in the coflow (7.6 - 21%), and the oxidizer preheat temperature (~ 400 - 800 K) to obtain a wide and diverse range of operating conditions such as the conventional, ultra-lean, and MILD combustion modes. For all cases, autoignition was observed to be the mode of flame stabilization that indicated the role of H₂ in reducing the ignition delay. The combustion chamber has been demonstrated to operate stably over the range of equivalence ratio and O₂% investigated, although the conventional mode displayed the highest SPL and fluctuations in the OH* intensity. The most stable operation was obtained for the MILD case for which the SPL decreased by 6 dB and the PSD of the OH* and noise signal showed a suppression of the high-frequency (> 800 Hz) longitudinal modes. The operational limits of the MILD mode were further investigated by gradually reducing the temperature of the oxidizer. The decrease in the preheat temperature increased the CO emissions from 470-ppm to 1333-ppm. It was observed that between $T_{ox} = 603$ K and 547 K, the operation of the chamber became unstable with 6 dB increase in the SPL caused due to very high-frequency oscillations (~ 9 - 15 kHz) that were not observed earlier which indicate the emergence of resonance modes other than the longitudinal mode. Overall, the study shows that the combustion chamber can operate stably over the range of Φ_{global} (0.32 - 0.89) and O₂% (7.6 - 21%) investigated although the system becomes unstable as the T_{ox} decreases below a threshold value. The various combustion modes outlined in this chapter are investigated using detailed laser diagnostic techniques, and the results of these investigations are presented in subsequent chapters.

Chapter 5

Laser diagnostics of combustion

In this chapter, a detailed investigation of the in-situ reaction zone and thermal field for various modes of syngas combustion is performed using OH-PLIF and Rayleigh thermometry [38]. This is particularly important as combustion with exhaust gas recirculation, and particularly MILD combustion is believed to occur in the low Damköhler regime ($Da \sim 1$) where both flow and chemical time scales are important. The next few sections present the details of the measurement techniques and data obtained. The experimental observations have been complemented by kinetic simulations in idealized reactors to obtain a better understanding of the physics of the various combustion modes.

5.1 Measurement techniques and data processing

5.1.1 Rayleigh thermometry

The setup for Rayleigh thermometry shown in **Figure 5.1** consisted of a pulsed Quanta-Ray Nd:YAG laser that pumps a 355-nm beam (third harmonic) at 10 Hz with energy of 250 mJ/ pulse. A similar procedure for temperature measurement has been used in an earlier study [104]. The pulse-to-pulse laser energy variation was recorded using an energy monitor. The laser beam was then passed through a polarization rotator which consists of a motorized plate to obtain the S and P polarization of the laser beam. The maximum Rayleigh scattering signal was obtained for the S polarization while the P polarization images contained noise signals other than the Rayleigh scattering signal (O_2 fluorescence,

Laser diagnostics of combustion

background scattering from walls). These images were subsequently subtracted to improve the signal-to-noise ratio. A polarization scan at 5° intervals was performed using air as the reference medium prior to capturing the experimental images to determine the S and P polarization angles. Subsequently, at every location, the images were captured both for the S and P polarizations of the laser beam. The laser beam of 10-mm diameter was subsequently passed through an $f = 300$ -mm plano-convex cylindrical lens to produce a laser sheet of height of 10-mm and thickness of 0.5-mm at the center of the chamber. The chamber was traversed in the vertical direction to acquire images at various axial locations as shown in **Figure 5.1**. Although the sheet height is 10-mm, the full width at half maximum for the sheet obtained from the average Rayleigh scattering images acquired in air is approximately 5-mm. The sheet profile is shown in **Figure 5.2**. The traverse of the chamber was adjusted to align the peak of the Gaussian sheet with the axial location (15-mm, 25-mm, etc.) at which the data is acquired.

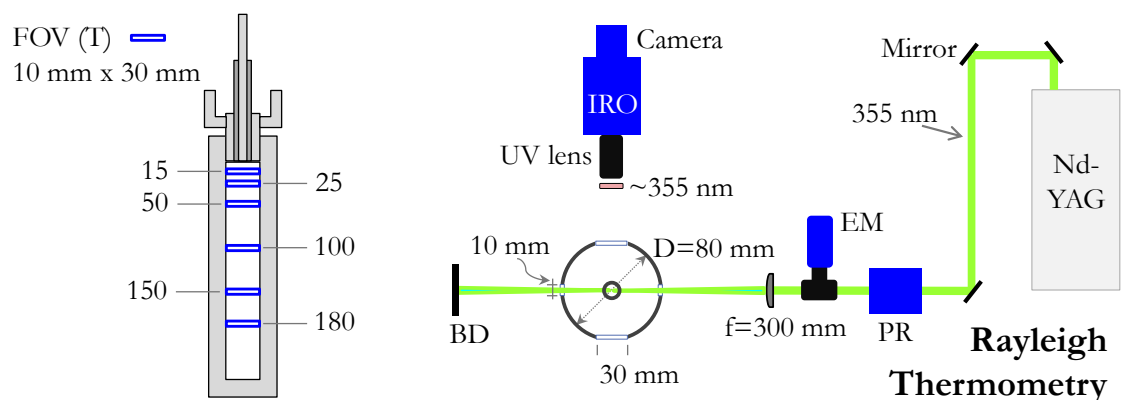


Figure 5.1: Schematic diagram of the laser diagnostics setup for Rayleigh thermometry measurements.

(Acronyms: IRO – intensified relay optics, EM - energy monitor, BD - beam dump, PR - polarization rotator,

FOV - field of view). All dimensions are in-mm.

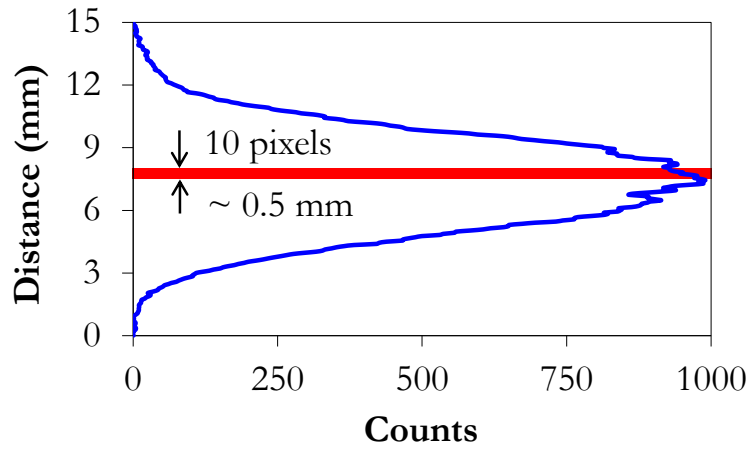


Figure 5.2: Sample sheet profile (blue line) obtained from Rayleigh scattering images in air (295 K) at an axial location of 100-mm from the injection plane. The region marked in red represents the area over which the signal was averaged to obtain the Rayleigh scattering signal.

An intensified CCD camera (Make: LaVision, Model: ImagerPro-X) equipped with a Nikon-Rayfact UV lens was positioned at 90° to capture the Rayleigh scattering signal. A bandpass filter centered at 355-nm (FWHM = 10 nm) was used to filter any external source of illumination. The 14-bit CCD sensor had 1200 x 1600 pixels that provided a resolution of around 0.05-mm/pixel. The intensifier exposure was set at 100-ns at a gain of 70%. For each case, 250 images were acquired that was corrected for the camera dark noise and pulse-to-pulse laser energy variations. The instantaneous images were also smoothed by a non-linear sliding average filter over an area of 5 pixel x 5 pixel to reduce the noise. In this filter, the average (S^{avg}) is computed by going over the image four times from left to right, right to left, top to bottom, and bottom to top. The average signal at the i^{th} pixel is calculated by the following formula:

Laser diagnostics of combustion

$$S^{avg}(i) = \left(\frac{n-1}{n}\right)S^{avg}(i-1) + \left(\frac{1}{n}\right)I(i) \quad (5.1)$$

where, I is the intensity at the i^{th} pixel and n is the length scale over which the averaging is performed. Subsequently, a band of 10 pixels in the vertical direction centred at the desired axial location is averaged to obtain the Rayleigh scattering signal. The same processing was performed for the reference image in air and the Rayleigh image under reacting conditions. The typical signal in the P polarization images is 50 counts while the standard deviation is 4 counts in the region of interest. Hence, the P signal can be considered nearly constant and the average P signal was subtracted from the instantaneous S images to obtain the instantaneous Rayleigh scattering signal. The peak signal in the reference (air) images was 1000 counts after S-P subtraction, while the minimum signal in the instantaneous images (S-P) in the flame varied in the range of 180 - 250 counts. The signal-to-noise-ratio (SNR) was calculated from the mean and standard deviation of the Rayleigh scattering signal obtained in the reacting environment [105]. The SNR was better than 7 for all the cases.

The Rayleigh scattering images were converted to temperature using the following relation:

$$T = \left(\frac{\bar{\sigma}}{\bar{\sigma}_c}\right)\left(\frac{I_c}{I}\right)T_c \quad (5.2)$$

Here, I_c represents the Rayleigh scattering signal at the calibration temperature T_c . $\bar{\sigma}$ and $\bar{\sigma}_c$ are the averaged Rayleigh scattering cross sections for the flame and the calibration gas mixtures, respectively. The Rayleigh scattering from air at 295 K was used as the calibration image. If the local gas composition is known, then the scattering cross section is given by:

$$\bar{\sigma} = \sum \sigma_i X_i \quad (5.3)$$

Laser diagnostics of combustion

Here, σ_i and X_i are the scattering cross sections and mole fractions of the species. The values for the Rayleigh scattering cross sections at 355-nm have been taken from Sutton et al. [106]. The variation in the Rayleigh scattering cross sections was estimated using detailed counterflow diffusion flame simulations at various strain rates as observed in **Figure 5.3**. These values were also verified using 2D RANS and 3D DES simulations using EDC and Li et al. H₂/CO chemistry [97] which are reported in detail in a subsequent chapter. Since the scattering cross sections did not vary significantly ($< 12\%$), a constant Rayleigh cross section was subsequently used to calculate the temperature. The maximum uncertainties in the predicted temperatures have been estimated to be $\pm 11.5\%$ for the conventional case (A50), $\pm 7\%$ for the ultra-lean case (A125), $\pm 7.5\%$ for the transition case (A8N405), and $\pm 8\%$ for the MILD case (A125). The variations arise from the difference in the composition of the oxidizer and product streams between various cases. Medwell et al. [107] reported a maximum variation of 20% in the Rayleigh scattering cross section in turbulent non-premixed jet flames in hot and diluted coflow. The temperature imaging has been performed at 6 axial locations (15, 25, 50, 100, 150, and 180-mm) covering 180-mm of the chamber from the inlet.

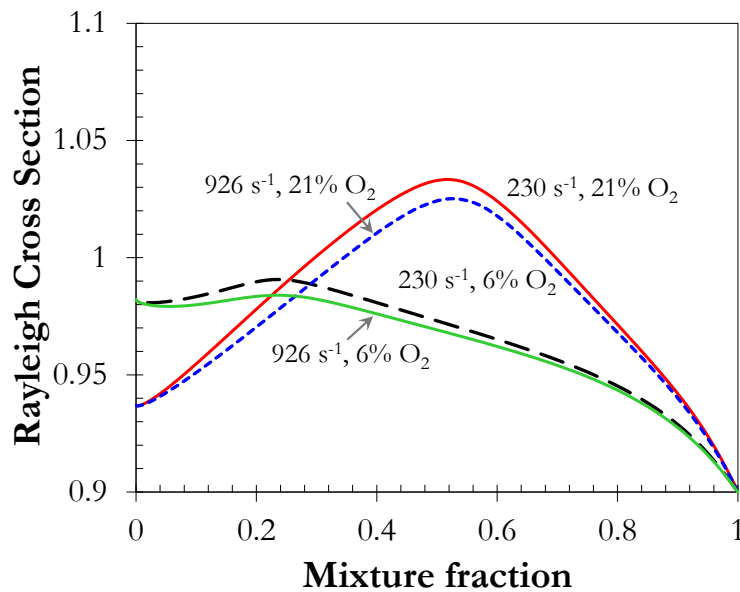


Figure 5.3: Variation of Rayleigh scattering cross section simulated in a counterflow diffusion flame of syngas with air and N₂ diluted air at two different strain rates. The oxidizer is at 1000 K.

5.1.2 OH planar laser-induced fluorescence

The setup for OH-PLIF shown in **Figure 5.4** consisted of a pulsed Quanta-Ray Nd:YAG laser that pumps a 532-nm beam to a dye laser (Make: Sirah Lasertechnik, Model: CSTR-G-3000). The pump beam had energy of 350 mJ/ pulse and was operated at 10 Hz. The output from the dye laser was 25 mJ/ pulse at a wavelength of 283.553-nm that excited the Q₁(8) line belonging to the $A^2\Sigma^+ \leftarrow X^2\Pi(1,0)$ band. The Boltzmann fraction is relatively insensitive to temperature (< 10%) for this transition. The linewidth of the beam is 0.001-nm while the laser fluence is approximately 0.25 J/cm². The beam was expanded into a collimated sheet of height 50-mm and thickness 0.5-mm using a collimator and sheet optics. The fluorescence signal was verified to be in the linear regime. The intensifier gate time was 50-ns and a total of 250 images were captured for each case with a resolution of around 100-

Laser diagnostics of combustion

μm per pixel using an ICCD camera. The acquired images were corrected for sheet non-uniformities and laser energy variation.

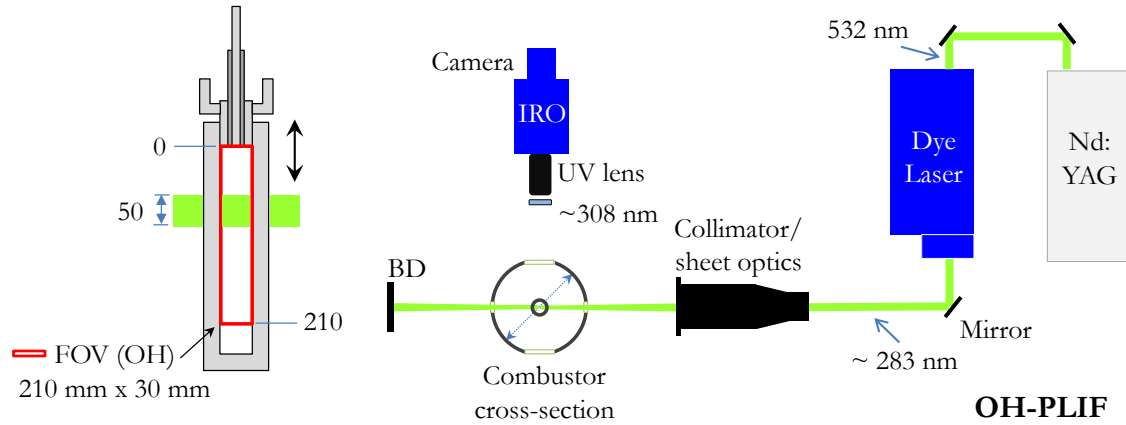


Figure 5.4: Schematic diagram of the laser diagnostics setup for OH-PLIF. (Acronyms: IRO – intensified relay optics, BD - beam dump, FOV - field of view). All dimensions are in-mm.

The calibration images for the quantification of OH were acquired in a stoichiometric and premixed CH_4/air flame at atmospheric pressure in a standard McKenna flat flame burner reported by Cattolica et al. [108]. The images of the burner and a representative OH-PLIF image are shown in **Figure 5.5**. The absolute concentration of OH in ppm is then calculated by the following expression:

$$N_{ppm,abs} = \left(\frac{T}{T_c}\right) \left(\frac{f_B(T_c)}{f_B(T)}\right) \left(\frac{\Gamma_c}{\Gamma}\right) \left\{\frac{(\alpha_1/\alpha_3)_c}{(\alpha_1/\alpha_3)}\right\} \left(\frac{I_{o,c}}{I_o}\right) \left(\frac{S_F}{S_{F,c}}\right) N_{ppm,c} \quad (5.4)$$

Here, T is the flame temperature, f_B is the Boltzmann fraction, Γ is the spectral overlap fraction, α_1/α_3 is the correction factor for quenching and vibrational energy transfer effects, I_o is the spectral irradiance, and S_F is the digital fluorescence signal. The subscript ‘C’ refers to the parameters in the calibration flame.

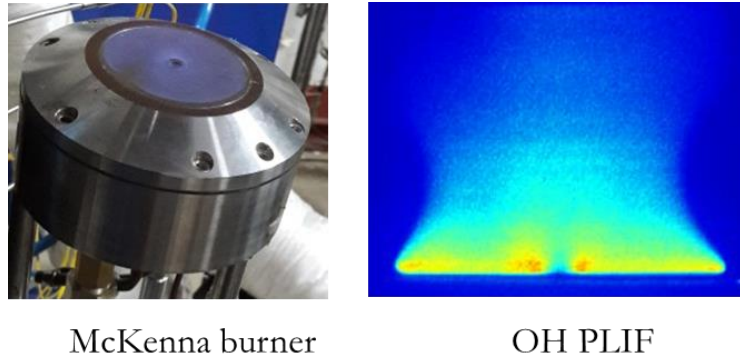


Figure 5.5: Image of the McKenna flat flame burner (left) and a sample OH PLIF image (right).

To correct for the quenching and the vibrational energy transfer (VET) effects, we use the 4-level integrated-quasi-steady-state (IQSS) model proposed by Dunn and Masri [109]. This model is applicable for linear and non-linear laser-induced fluorescence of OH under $A^2\Sigma^+ \leftarrow X^2\Pi(1,0)$ excitation. The quenching and VET cross sections for OH, σ_0 ($v' = 0$), σ_1 ($v' = 1$), and σ_{10} (VET from $v' = 1$ to $v' = 0$) have been taken from Paul [110]. For the species, H_2 and, H_2O , σ_0 ($v' = 0$) have been taken from Tamura et al. [111] while σ_1 and σ_{10} have been determined from guidelines provided by Paul [112] for $v' > 0$. The quenching and VET rates are expressed as

$$Q_{24}, Q_{31}, V_{41}, V_{23} = \sum_{i=1}^j C_i a_i \sigma_Q T^{0.5} \quad (5.5)$$

where C_i is the i^{th} species number density, a_i are species dependent constants, and σ_Q is the species quenching cross section. The σ_Q at a particular temperature can be related to the experimentally measured quenching cross sections at high temperatures using the following relation [111]:

$$\sigma_Q = \sigma_{Q,\infty} \exp(\varepsilon/kT) \quad (5.6)$$

where ε/k are experimentally fitted parameters for various species. The local species concentrations required for quantifying the quenching and VET rates have been estimated using detailed counterflow diffusion flame simulations, 2D-RANS, and 3D-DES simulations. Although the quenching and VET rates varied significantly near the inlet, it was observed that beyond 100-mm of the chamber, the variation in the rates was less than $\pm 9\%$ for all the four cases considering the major species. This also corroborates with the fact that the combustion is mostly complete beyond this region and the local composition is close to the composition of the exhaust gases. The actual variation in the quenching and VET rate terms beyond 100-mm of the chamber thus estimated are as follows: conventional (A50) = $\pm 6\%$, ultra-lean (A125) = $\pm 7.2\%$, transition (A85N40) = $\pm 8.6\%$, and MILD (A45N80) = $\pm 7.9\%$. As the variation is less than 9%, a constant value is used to correct for the quenching and VET rate terms. The final uncertainties in the [OH] considering the uncertainties in the temperature and the quenching/VET rate terms are $\pm 18.6\%$ for the conventional case (A50), $\pm 15.5\%$ for the ultra-lean case (A125), $\pm 17.6\%$ for the transition case (A85N40), and $\pm 17.3\%$ for the MILD case (A45N80).

5.2 Results and discussion

5.2.1 Mean centreline temperature

The variation of the centreline temperature with axial distance from the nozzle inlet plane for all the 4 cases is shown in **Figure 5.6**. The temperature gradually rises monotonically near the inlet due to mixing with the preheated oxidizer and entrainment of the exhaust gases. Except for the conventional case, the axial temperature for the other three cases follows a similar profile. This is also due to the similar inlet conditions of velocity and

Laser diagnostics of combustion

temperature for the ultra-lean, conventional, and the MILD cases. The inlet temperature at 15-mm is close to 600 K for all the cases. This can be attributed to the entrainment of the oxidizer and recirculating exhaust gases after injection. The initial temperature rise upto 50-mm is observed to be almost linear for all the cases. This temperature rise with axial distance is contrary to conventional flames and is characteristic of flameless oxidation furnaces in which the flame is stabilized further downstream [38].

For the conventional case (A50), the highest temperature of 1645 K is recorded at 100-mm from the injection plane as observed in **Figure 5.6**. This is also the location at which the maximum intensity of OH radicals can be observed in the PLIF images (discussed in subsequent sections). Downstream of 100-mm, the temperature is nearly constant upto 180-mm and appears to be the post-combustion region filled with high-temperature products. This also corroborates with the rapid decrease in the OH intensity after 100-mm. As the heat release for syngas combustion is closely associated with presence of OH radicals, this also shows that significant heat release does not take place in this downstream region. Without any additional sources of heat generation and losses, the average temperature is thus expected to remain constant after 180-mm except very near to the forward stagnation wall at 265-mm. The overall low temperature can be attributed to the low calorific value of the syngas (~ 4.6 MJ/kg) obtained from sources such as biomass.

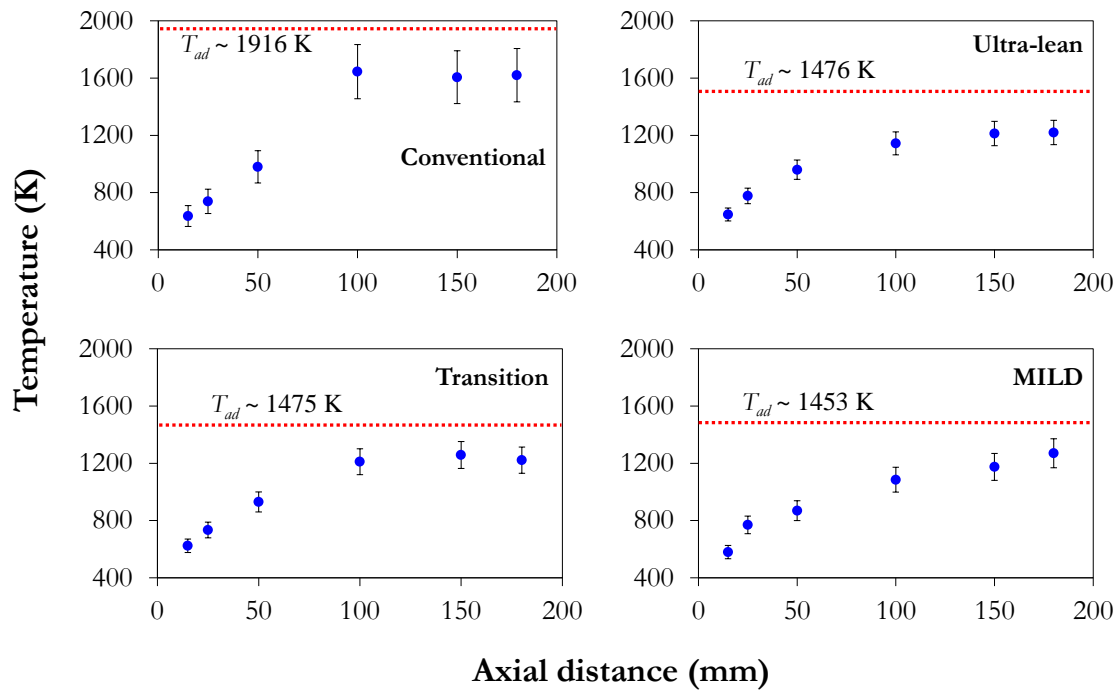


Figure 5.6: Axial variation of the centreline temperature for the 4 cases. The dashed red lines indicate the adiabatic flame temperatures calculated for the inlet conditions mentioned in **Table 4.1**.

The temperature profiles for the ultra-lean, transition, and MILD cases are observed to be nearly similar. The maximum average temperature does not exceed 1300 K. Near the inlet, the temperature increase is almost linear, as was also observed for the conventional case, although the rate of increase is lower. The temperature then gradually increases upto 1200 - 1300 K and remains nearly constant further downstream. It can also be observed that the rate of temperature rise is lowest for the MILD case. This also corroborates with the location of the maximum OH intensity which is further downstream compared to that for the ultra-lean and the transition cases. Overall, the centreline profiles indicate a nearly uniform temperature after 100-mm of the chamber. The combustion also occurs in a low-temperature environment which is beneficial from wall heat transfer considerations.

Laser diagnostics of combustion

The maximum temperature measured is lower than the adiabatic flame temperature for all the cases. This reduction in temperature can be attributed to the entrainment of recirculating products that reduces the adiabatic flame temperature. The measured wall temperatures show a maximum value of around 900 K suggesting some degree of heat loss from the recirculating exhaust gases. These gases when entrained into the incoming fresh reactants reduce the overall temperature to values lower than the adiabatic flame temperature. Such observations of a reduction in flame temperature from the adiabatic flame temperature due to entrainment have been observed by Bobba et al. [19]. A similar principle is used in MILD combustion furnaces to reduce the overall temperature of the exhaust gases using cooling coils or heat exchanger [40] such that maximum temperature in the furnace can be reduced. This also aids in the reduction of thermal NO_x emissions.

5.2.2 Temperature variation in the radial direction

The variation of temperature in the radial direction at different axial locations for the conventional case is shown in **Figure 5.7**. The profiles extend upto 15-mm in the radial direction which covers both the inner and the outer shear layers. As the centerline temperature increases with axial distance, the gradient of the temperature in the radial direction decreases and becomes nearly uniform. For the conventional case, the effect of the central jet can be observed upto 100-mm, while the profiles are nearly constant at 150-mm and 180-mm in the radial directions. The maximum variation in temperature in the radial direction at 150-mm and 180-mm are 156 K and 176 K, respectively. The maximum temperature observed for the conventional case is around 1730 K, which is still below 1800 K.

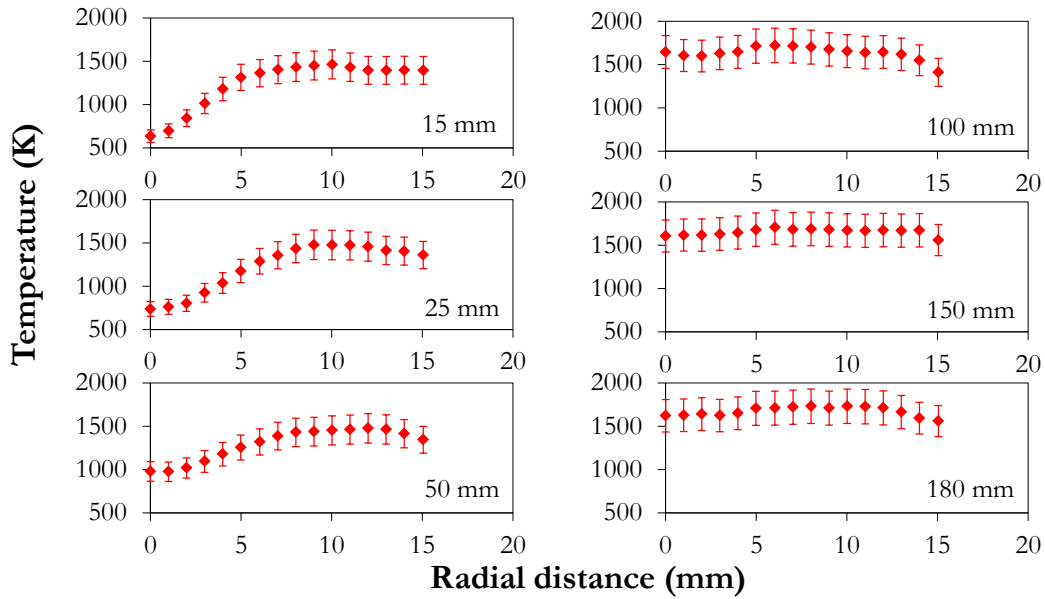


Figure 5.7: Radial distribution of temperature at various axial locations for the conventional (A50) case.

For the MILD case (**Figure 5.8**), the maximum temperature is significantly lower (1330 K) than that for the conventional case as was also observed in the centreline profiles in **Figure 5.6**. Nearly constant temperatures in the radial direction are observed at 150-mm and 180-mm similar to the trends observed for the conventional case. The maximum variation in the temperature at 150-mm and 180-mm are 140 K and 137 K, respectively. This uniformity in the temperature distribution is also corroborated by the OH distribution which is nearly uniform at 150-mm and 200-mm as discussed later. The effect of the central jet can be observed from the centreline upto around 7-mm in the radial direction. The temperature is expected to remain uniform upto very close to the radial walls at 40-mm due to the absence of any other sources of heat loss. This is characteristic of reverse flow chambers in which the temperature distribution is nearly uniform in most parts of the chamber due to the intense internal recirculation which favors superior heat transfer characteristics in furnaces.

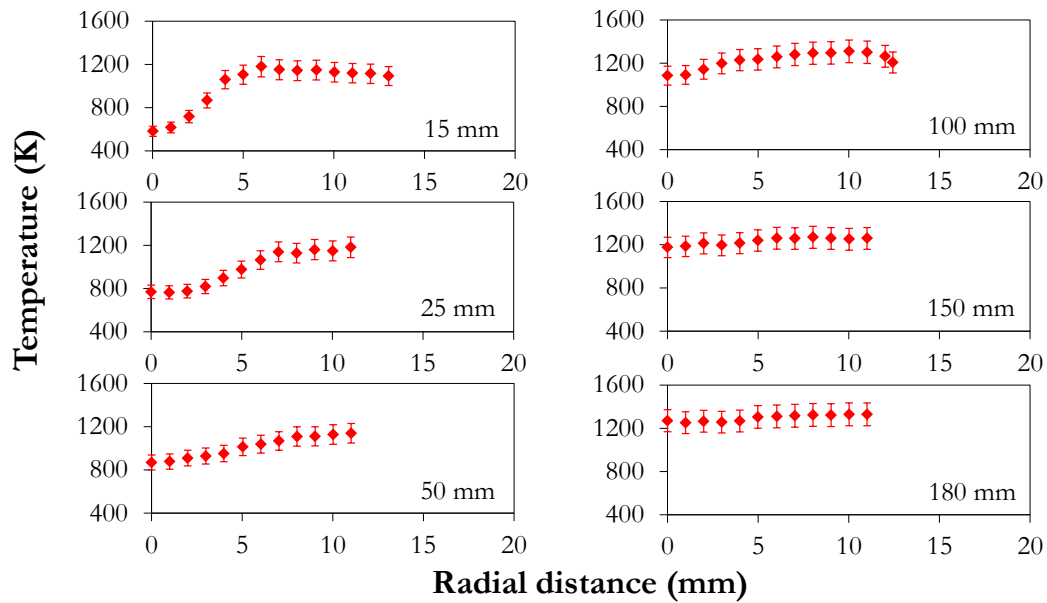


Figure 5.8: Radial distribution of temperature at various axial locations for the MILD (A45N80) case.

For the transition (**Figure 5.9**) and the ultra-lean (**Figure 5.10**) cases, the temperature is similar to that for the MILD case both in magnitude and in distribution. Here, the unreacted jet penetrates lesser as compared to that observed for the MILD case leading to a steeper rise in temperature. The temperature is thus nearly uniform from 100-mm of the chamber for these two cases. The maximum temperature is observed to be 1367 K which is slightly higher than that for the MILD case, but significantly lower than that for the conventional case. The effect of dilution is not very prominent in the temperature distribution due to similar adiabatic flame temperatures as observed in **Figure 5.6**. While counterflow diffusion flame simulations suggest that a non-premixed flame with diluted oxidizer should have lower peak temperatures, the presence of similar temperatures for these cases suggest that the combustion is not in the non-premixed mode but occurs after intense mixing between the fuel, the oxidizer, and the diluents. Finally, the radial profiles of temperature presented will

Laser diagnostics of combustion

be useful in the validation of combustion models for reverse flow configurations with finite-rate kinetic effects.

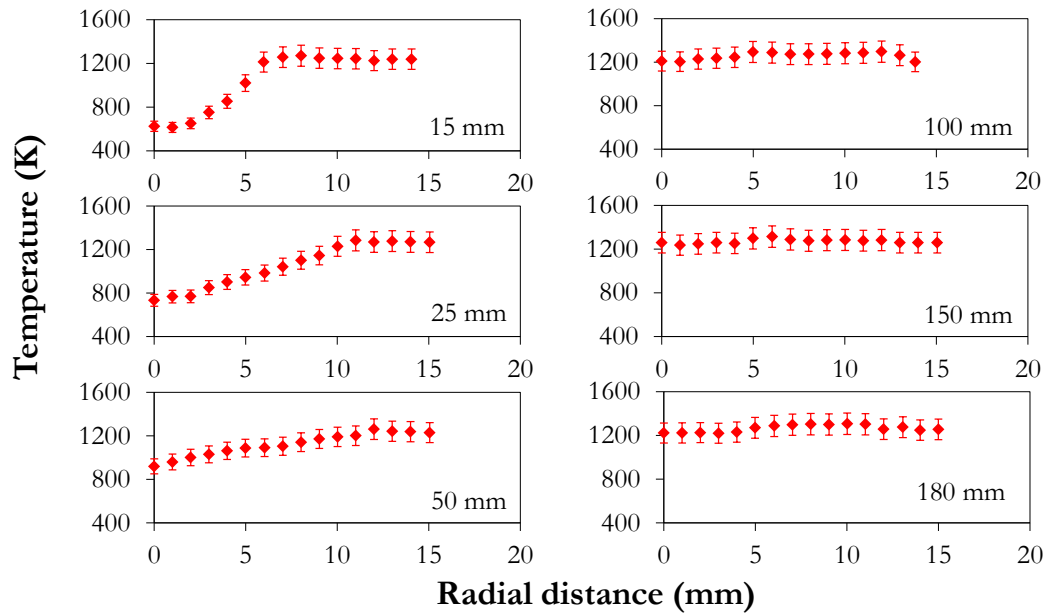


Figure 5.9: Radial distribution of temperature at various axial locations for the transition (A85N40) case.

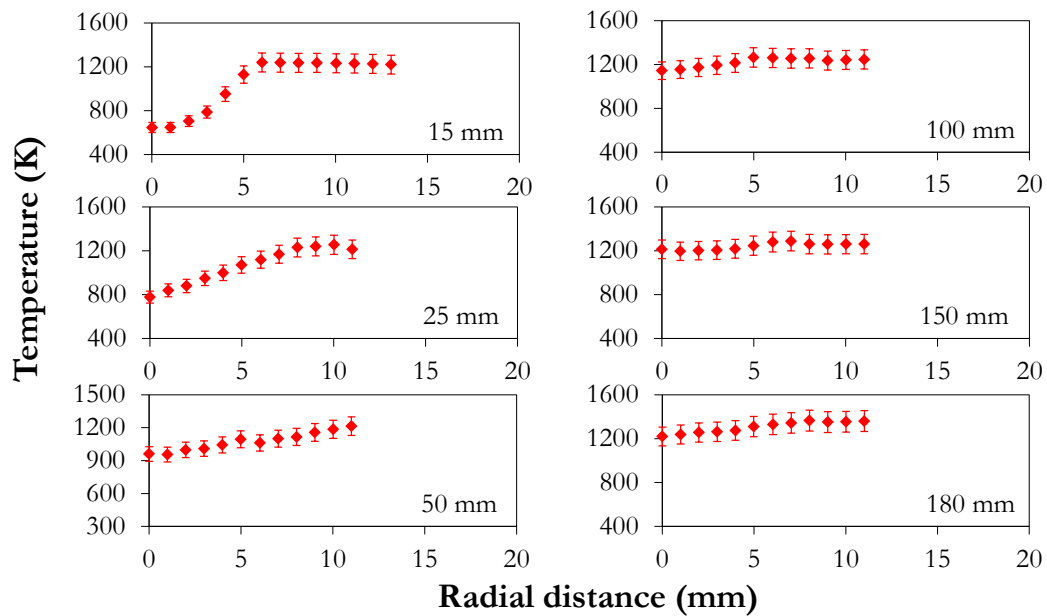


Figure 5.10: Radial distribution of temperature at various axial locations for the ultra-lean (A125) case.

5.2.3 Standard deviation of temperature along the centreline

The standard deviation (SD) of the temperature measured along the centreline at various axial locations is shown in **Figure 5.11**. The SD of the temperature shows a clear trend between the conventional, ultra-lean, transition, and the MILD cases. The maximum SD is observed for the conventional case (A50) followed by the ultra-lean and the transition cases. The lowest fluctuation in the temperature is recorded for the MILD case. This also corroborates with the SD of the OH-PLIF signal as observed in **Figure 5.15**, which will be discussed in the subsequent section. This shows that the reaction zone in the MILD combustion regime shows a quasi-steady behavior with very low fluctuations in the scalar quantities as compared to the other modes of operation. This observation also corroborates with the fact that the overall sound pressure level generated during MILD operation is lower than the other modes of combustion [52][100]. The increase in the SD along the axial distance can be attributed to the higher turbulent fluctuations downstream (u'_{rms}/U) as observed by Bobba et al. [19] in the stagnation point reverse flow combustor.

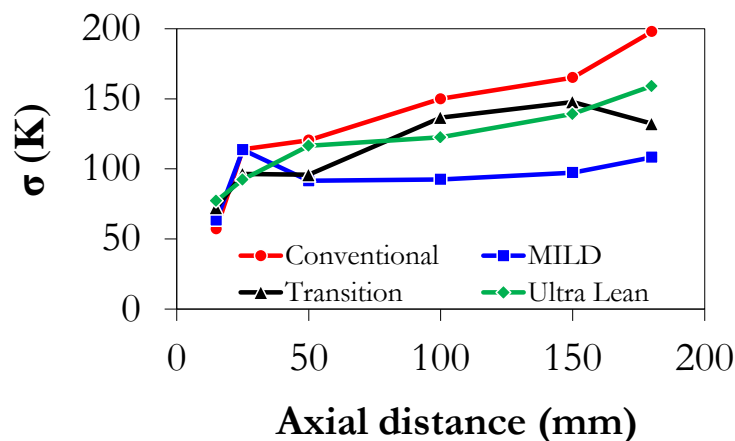


Figure 5.11: Standard deviation of temperature along the centreline at various axial locations for the conventional (A50), MILD (A45N80), transition (A85N40) and the ultra-lean (A125) cases

5.2.4 Mean OH distribution

The OH-PLIF images have been acquired at 5 axial locations in the chamber, covering nearly 210-mm out of the total axial length of 265-mm of the chamber. The primary observation from the OH-PLIF images is that the peak OH intensity decreases from the conventional (A50) case to the ultra-lean (A125), transition (A85N40), and the MILD cases (A45N80). The peak intensity is similar for the ultra-lean and transition cases but thereafter reduces significantly for the MILD case.

For the conventional case (A50), a highly localized and intensely burning reaction zone can be observed in **Figure 5.12** to be spanning from 75 - 135-mm of the chamber. The reaction zone appears compact and spindle-shaped. The intensity is the highest along the centreline and decreases with radius. In the upstream region near the injection plane, a small diffusion flame can be observed to be attached to the nozzle. Based on the location of this diffusion flame with respect to the fuel and oxidizer inlets, it can be inferred that the flame is stabilized on the lip of the injector between the fuel and the oxidizer inlets and extends into the inner shear layer. A low intensity OH bridge connects this diffusion flame to the downstream high-intensity reaction zone in the mean as observed in **Figure 5.12**. However, it will be shown later using the instantaneous images that these two regions are not physically connected with a continuous reaction zone, but actually dominated by autoignition kernels that appear as a continuous reaction zone in the mean images.

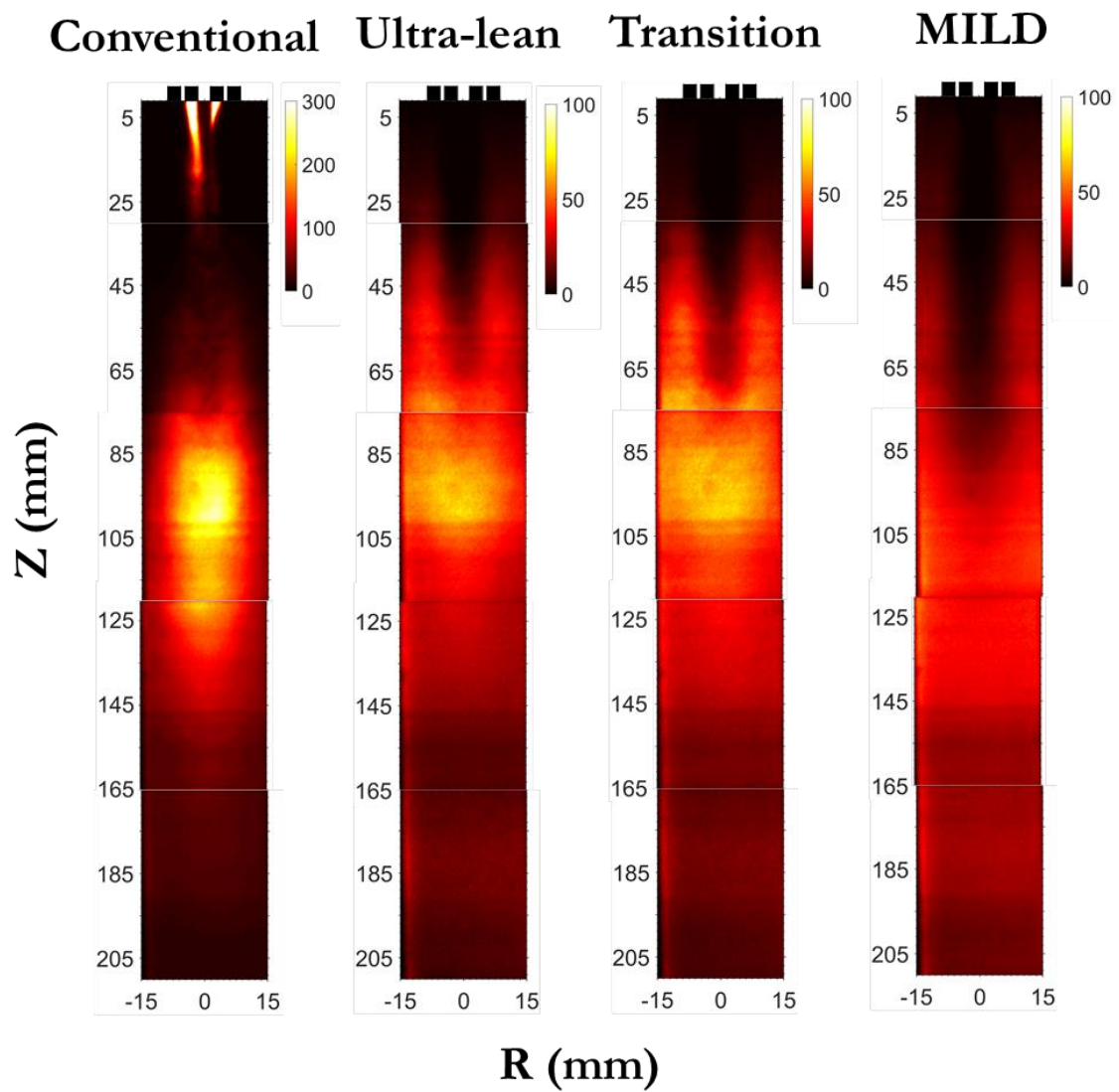


Figure 5.12: Mean OH contours for the conventional, ultra-lean, transition, and MILD cases. The color bar represents OH counts in arbitrary units.

Laser diagnostics of combustion

For the ultra-lean case (A125), the maximum OH intensity reduces approximately 4 times to around 60 counts. The diffusion flame attached to the nozzle extinguishes due to the higher jet velocities and the resulting strain. The location of the maximum intensity is unchanged at around 100-mm while the unreacted jet core penetrates up to 65-mm from the injection plane. The flame appears to be situated in the outer shear layer as OH signal cannot be observed in the region between the central fuel and the surrounding annular oxidizer inlets. After the maximum OH intensity location, the OH signal drops rapidly along the axial direction as observed in **Figure 5.13**. The reaction zone is wider both in the axial and lateral directions as compared to that for the conventional case (A50) indicating that the heat release is distributed over a larger region of the chamber.

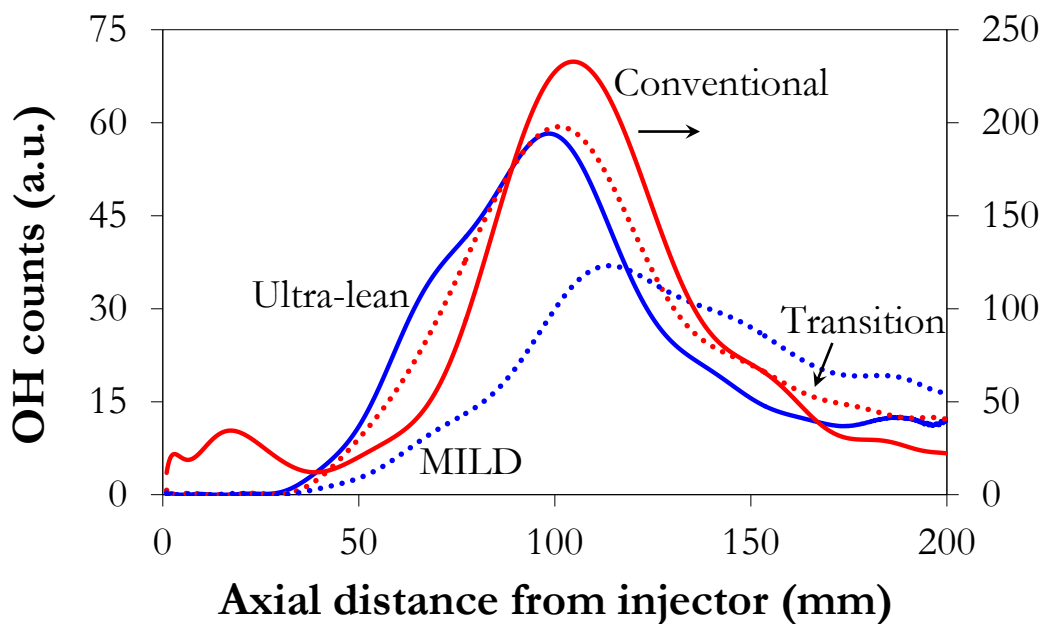


Figure 5.13: Mean OH distribution along the chamber centerline for the conventional, ultra-lean, transition, and MILD cases.

Laser diagnostics of combustion

For the transition case (A85N40), the location and intensity of the maximum OH signal are similar to those of the ultra-lean case, although the unreacted jet core penetrates slightly further into the chamber. This similarity to the ultra-lean case may be due to the fact that although the oxidizer contains 14.3% O₂, the global equivalence ratio is $\Phi_{\text{global}} = 0.47$ with sufficient excess O₂ in the chamber that gets entrained into the incoming fresh reactants due to internal recirculation. In the downstream region, however, the OH counts are slightly higher as compared to the ultra-lean case as observed in **Figure 5.13**.

For the MILD case (A45N80), the unreacted jet core penetrates the farthest as compared to the other cases. The peak OH intensity is observed at 115-mm while the maximum intensity is lowest among all the cases. Similar to the ultra-lean and the transition cases, the flame is observed to be located in the outer shear layer. The distribution of OH is widest in the MILD case as observed in **Figure 5.13**. The drop in the OH signal intensity after the peak is gradual as compared to the ultra-lean and the transition cases resulting in the highest OH signal intensity downstream. This also implies that the heat release is more distributed in the MILD case as compared to the other cases. This corroborates well with the description of MILD combustion in which the reaction zone is distributed with volumetric heat release.

5.2.5 Average profiles of OH in the radial direction

The average radial profiles of OH are shown in **Figure 5.14** at 6 different axial locations covering a span of 200-mm of the chamber. Each subplot contains data for the conventional (C), ultra-lean (UL), transition (T), and the MILD (M) cases. The OH count for the conventional case is shown on the right side of the figures due to higher counts.

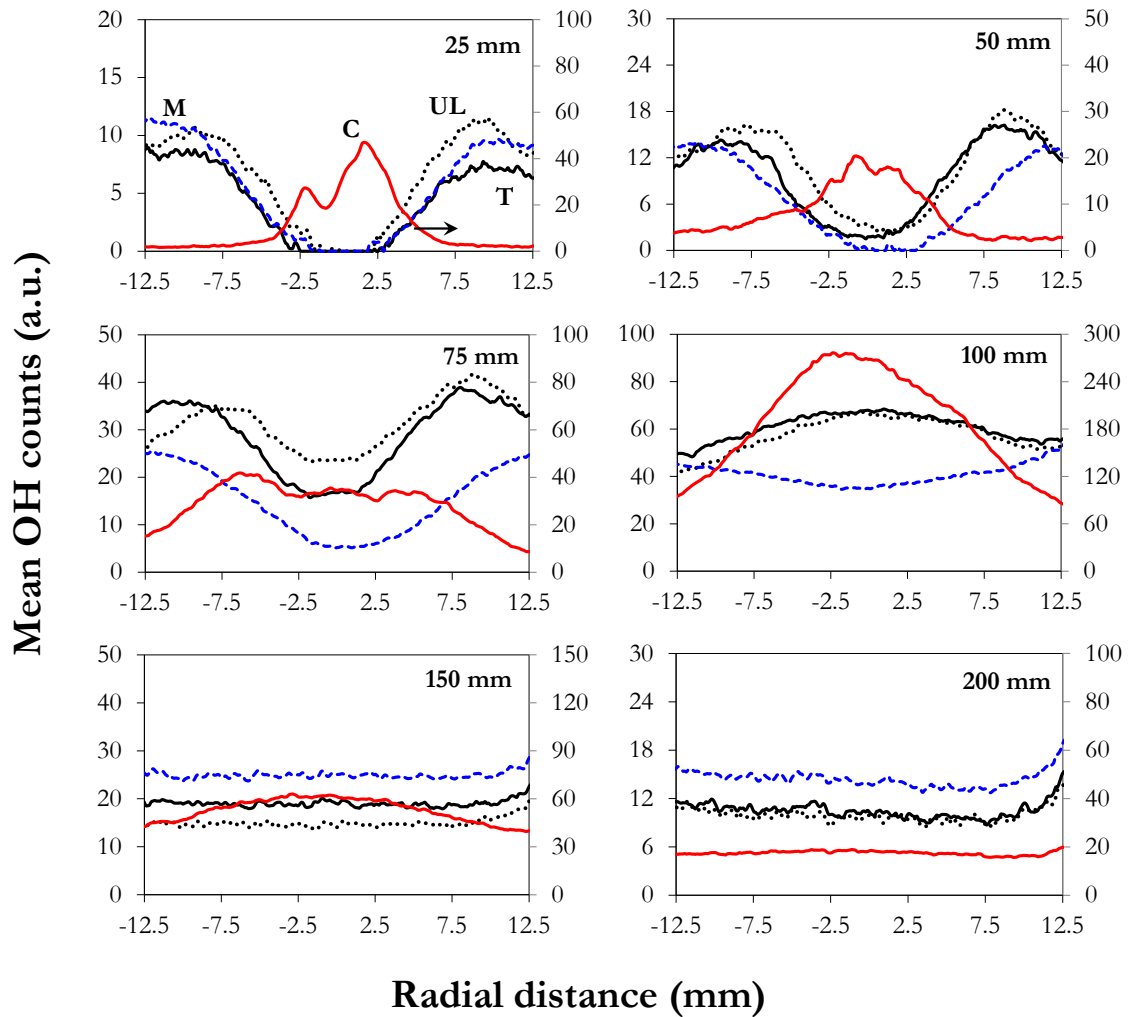


Figure 5.14: Mean OH distribution along the chamber radius for the conventional (C), ultra-lean (UL), transition (T), and MILD (M) cases at axial locations of 25-mm, 50-mm, 75-mm, 100-mm, 150-mm, and 200-mm. The axis for the OH counts for the conventional case is on the right side of the plots.

For the conventional case, the diffusion flame attached to the nozzle can be observed in the OH profile at $Z = 25$ -mm. The counts are higher along the axis but become nearly zero away from the centreline. As the exhaust port starts from $R = 8.5$ -mm, the absence of OH signal upto $r = 12.5$ -mm suggest that significant OH does not exist near the exhaust ports due

Laser diagnostics of combustion

to recirculation. This is different from the other three cases, where OH signal is observed near the exhaust port. The OH counts then subsequently decrease at 50-mm but increase again from 75-mm onwards. The decrease in the signal at 50-mm is mostly due to the fact that this region is dominated by intermittent ignition kernels at this location. The maximum signal is recorded at $Z = 100$ -mm (~ 270 counts) that decreases sharply in the radial direction. The signal subsequently decreases at $Z = 150$ -mm (~ 60 counts) and becomes nearly constant along the radial direction at 200-mm (~ 20 counts).

For the ultra-lean, transition, and the MILD cases, the profiles follow a similar trend. The signal is zero along the centreline upto $Z = 50$ -mm of the chamber. The distribution for the ultra-lean and transition cases is nearly identical. The signal increases along the radial direction, reaching a maximum at R around 9-mm for $Z = 25, 50,$ and 75-mm, but decreases thereafter for the ultra-lean and the transition cases. For the MILD case, the distribution is much more gradual and the maximum is reached at greater radial distances as can be observed for $Z = 50$ and 75-mm. The signal is also lower for the MILD case at these two locations. The maximum signal can be observed at $Z = 100$ -mm for all the three cases. But the peak is reached further downstream for the MILD case as observed from the concave radial profile as compared to the convex profiles for the ultra-lean and the transition cases. While the signal is lower for the MILD case upto 100-mm, a reversal of the trend at 150 and 200-mm is observed wherein the signal is greater for the MILD case as compared to that for the ultra-lean and the transition cases. This is in line with the distribution of the reaction zone and heat release for the MILD case as compared to the other two cases. Thus, the O_2 content in the chamber has a significant influence on the distribution of the OH radical and the reaction zone. The OH profiles at these downstream locations are nearly constant along the radial direction as was also observed in the temperature profiles in **Figure 5.6** and **Figure 5.7**.

5.2.6 Standard deviation of OH in the radial direction

The standard deviation (SD) of the OH signal along the radial direction at various axial distances from the injection plane is shown in **Figure 5.15**. Similar to the mean profiles of OH, the SD is also symmetric about the central axis of the chamber. The highest standard deviation is observed for the conventional case except at 200-mm where it is similar to that of the other cases. This observation is also consistent with the SD of temperature shown in **Figure 5.11** where the highest was observed for the conventional case. In this case, the SD follows a trend similar to the mean profiles in **Figure 5.14**. At $Z = 25, 50,$ and 75 -mm, the SD is higher than the mean OH value, suggesting unsteadiness in the flame at this location. However, at $Z = 100, 150,$ and 200 -mm, the SD is lower than the mean value, showing that the flame is predominantly stabilized in this region. For the ultra-lean, transition, and MILD cases, the SD is consistently equal or lower for the MILD case as compared to that for the other two cases, while the transition and the ultra-lean cases are nearly similar in this aspect. This correlates with the observation regarding the SD of temperature (**Figure 5.11**) in which the lowest SD was observed for the MILD case. This also suggests that the reaction zone for the MILD case is steadier as compared to the other cases.

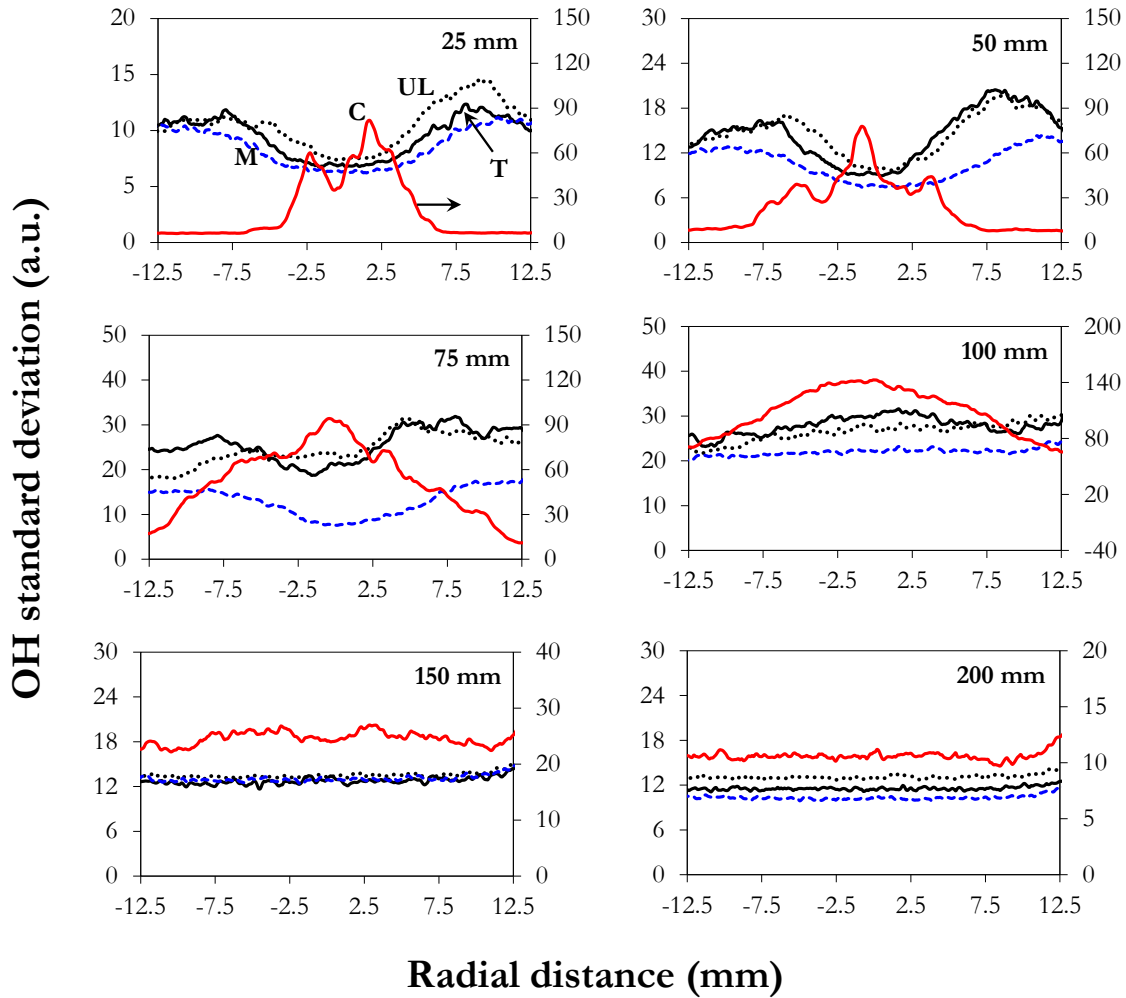


Figure 5.15: Distribution of OH standard deviation along the chamber radius for the conventional (C), ultra-lean (UL), transition (T), and MILD (M) cases at axial locations of 25-mm, 50-mm, 75-mm, 100-mm, 150-mm, and 200-mm. The axis for the OH counts for the conventional case is on the right side of the plots.

5.2.7 Instantaneous OH distribution

The instantaneous OH-PLIF images have been acquired at 5 locations, covering nearly 210-mm length of the chamber as observed in **Figure 5.16**. For the conventional case (A50), the OH contour is characterized by sharp gradients characterizing distinct flame fronts. The high intensity OH regions are localized in the instantaneous images which are characteristic of conventional flames. A clear diffusion flame can be observed in the inner

Laser diagnostics of combustion

shear layer attached to the wall between the fuel and air nozzles. The flame appears lifted thereafter and conforms to the large-scale turbulent flow structures. The lifted flame appears to be partially premixed as it gets sufficient time to mix the fuel, the oxidizer, and the recirculating exhaust. The region between this lifted flame and the nozzle attached flame is dominated by autoignition kernels and is not continuous as was observed in the mean images in **Figure 5.12**. This observation is also consistent with high-speed OH* chemiluminescence images at 5 kHz shown in **Section 4.2.3** where the formation and merging of ignition kernels could be clearly identified. This also suggests that autoignition is a possible mode of flame stabilization in these reverse flow chambers.

For the ultra-lean case (A125) the diffusion flame at the tip of the nozzle is extinguished which is also confirmed by the absence of OH radicals in this region. The flame appears completely lifted although thin reaction zones appear within 15-mm from the injector near the outer shear layer between the oxidizer and the exhaust. The peak intensity of the OH signal also decreases in comparison to the conventional case. The central region near the injector without OH signal represents the incoming fresh reactants. Similar to the conventional case, the flame is characterized by sharp gradients signifying localized reaction zones. A weak OH signal can be detected near the exhaust manifold in the returning flow. Another interesting observation is the presence of weak OH signal near the bottom of the chamber. For the conventional case, the signal at this region is still localized and seems to conform to the turbulent structures. For the ultra-lean case, however, the OH signal appears more diffuse and fills the width of the window (> 30-mm) as observed in **Figure 5.14**. This seems to indicate a distributed presence of OH in the chamber away from the primary reaction zones in the region spanning 30 - 120-mm of the chamber. For the transition case, the flame structure is similar to that of the ultra-lean case. Thin reaction zones can also be observed in this case in the vicinity of the fresh reactants with occasional intensely burning

Laser diagnostics of combustion

regions. The peak OH count is similar to that of the ultra-lean case, although the penetration of the central reactant jet is slightly higher. Also, the distributed layer of OH further downstream shows higher counts as compared to the ultra-lean case as observed in **Figure 5.13**. This indicates that the heat release is more distributed for the transition case as compared to the ultra-lean case. For the MILD case, the fresh reactants penetrate further into the chamber. The flame also appears completely lifted from the injector. The peak counts of OH have further decreased, signifying a weaker reaction zone. However, even with such high levels of dilution, thin reaction zones and distinct flame fronts are observed instead of a distributed reaction zone throughout the chamber. It must be noted that this observation is contrary to the idea that MILD combustion occurs in a distributed and volumetric reaction zone and requires further investigation. The presence of H₂ in syngas characterized by its fast chemistry can be a possible reason for this observation. The current observations are however consistent with the instantaneous OH-PLIF images reported by Plessing et al. [38] for the reverse flow furnace burning methane in which a distinct OH boundary could be identified. Similar observation of thin reaction zones was made by Sidey et al. [5] in the jet in heated and diluted (3% O₂) cross flow experiments. Some DNS studies [60] have also reported the presence of these thin reaction zones in MILD flames of methane. These observations with methane also highlight the importance and necessity of further investigations with syngas in the reverse flow configuration. The distribution of OH radical is however evident in the downstream section of the chamber where the intensity of the OH signal is higher as compared to that for the ultra-lean and the transition cases as observed in **Figure 5.13**.

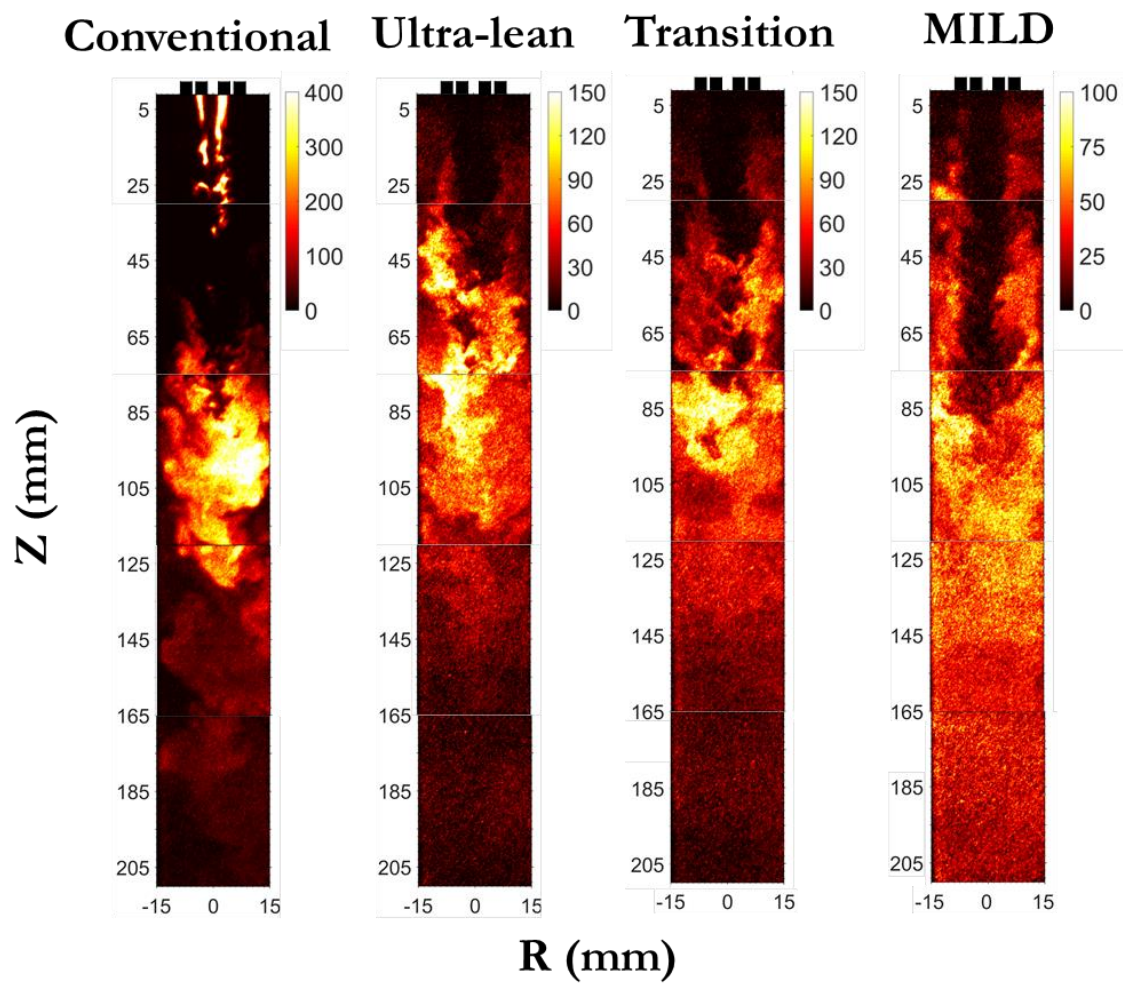


Figure 5.16: Instantaneous OH-PLIF images for the conventional, ultra-lean, transition, and MILD cases. Selected images captured at 5 axial locations (consecutively) in the chamber were stitched to generate these images. The colour bar represents OH counts in arbitrary units.

5.2.8 Near-nozzle flame structure

Finally, the reaction zone structure is investigated using OH-PLIF (**Figure 5.17**) as the OH radical was observed to directly correlate with the heat release rate in counterflow diffusion flame simulations with a varying O₂ percentage. The field of view extends axially in a region spanning 30 - 75-mm of the chamber from the injection plane and covers the shear layer. The primary observation from the mean images (**Figure 5.17, bottom**) is that the peak intensity decreases as we transition from the conventional to the MILD case suggesting that the reaction zone becomes weaker and less intense. The intensity is similar for the ultra-lean and transition cases, although the unreacted jet core penetrates further in the latter case due to a reduction in chemical kinetic rates.

The instantaneous images of OH reveal highly turbulent flame structures with different curvatures and length scales (**Figure 5.17 top**). The reaction front is clearly discernible in all these cases showing that the flame consists of thin reaction zones. The norm of the two-dimensional gradient shown for these instantaneous images (**Figure 5.17 middle**) also captures these fine structures. The present observations with syngas are also supported by experimental [57] and DNS studies [60] on MILD combustion of methane and reinforce the evidence for thin reaction zones in MILD flames. Thus, MILD combustion is not truly volumetric in the strict sense of the term. However, on further analysis, it is observed that the gradient is weaker for the MILD combustion as compared to the other modes. There appears to be a progressive thickening or distribution of the reaction zone with weaker gradients due to lower counts and overall uniformity of the reaction zone that merits further investigation.

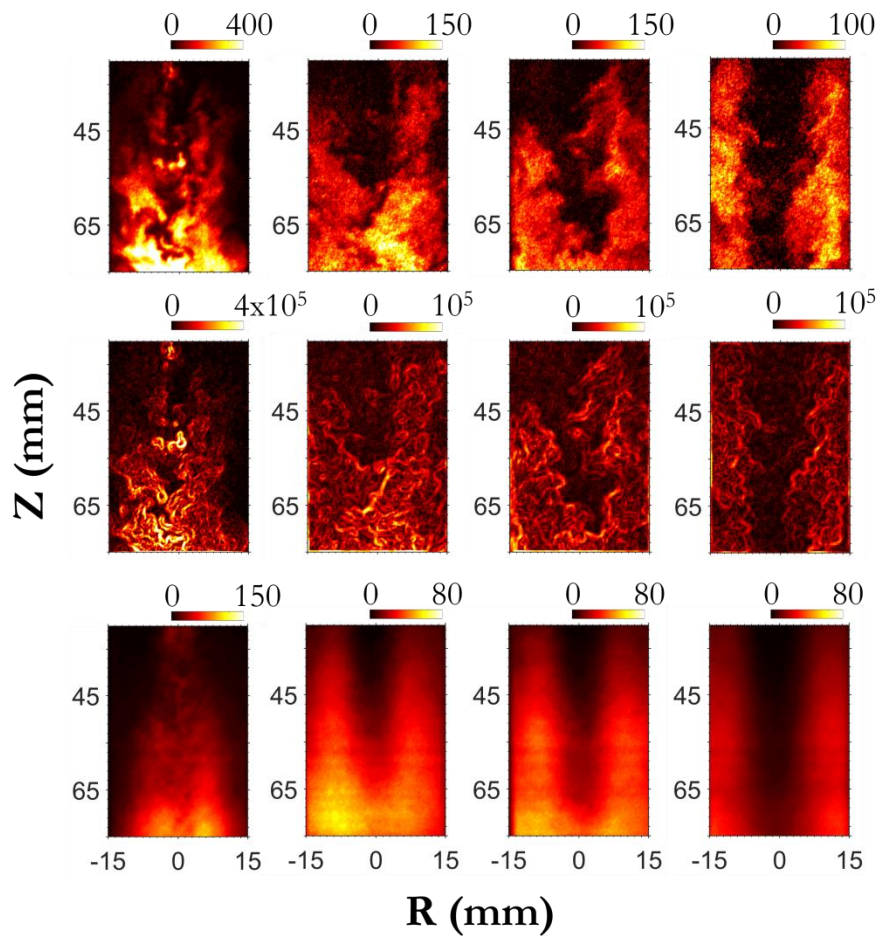


Figure 5.17: Instantaneous OH (top), the norm of the 2D OH gradient (middle), and the mean OH (bottom) for the (from left) conventional, ultra-lean, transition, and MILD cases. Z refers to the distance from the exit plane of the reactants while R is the radial distance.

To compare the weakening of the OH gradients, the PDF of the maximum gradient is evaluated from 250 images for each of the four cases as observed in **Figure 5.18**. The primary observation is that the gradients follow a nearly Gaussian distribution. The mean value of the distribution is highest for the conventional case, followed by the ultra-lean, transition, and MILD cases showing that the reaction zone gradients are weaker for the MILD

Laser diagnostics of combustion

case. The PDFs for the ultra-lean and transition cases are nearly identical, conforming to the earlier trends of OH* and noise measurements. The spread in the gradients is also the highest for the conventional and the lowest for the MILD case. As the 250 images were acquired for 25 seconds at 10 Hz, this represents a quasi-steady behavior of the reaction zone under MILD conditions. The PDFs along with OH intensity thus follow a pattern similar to the noise and OH* signal in which a clear trend can be identified from the conventional, ultra-lean, transition, and MILD cases.

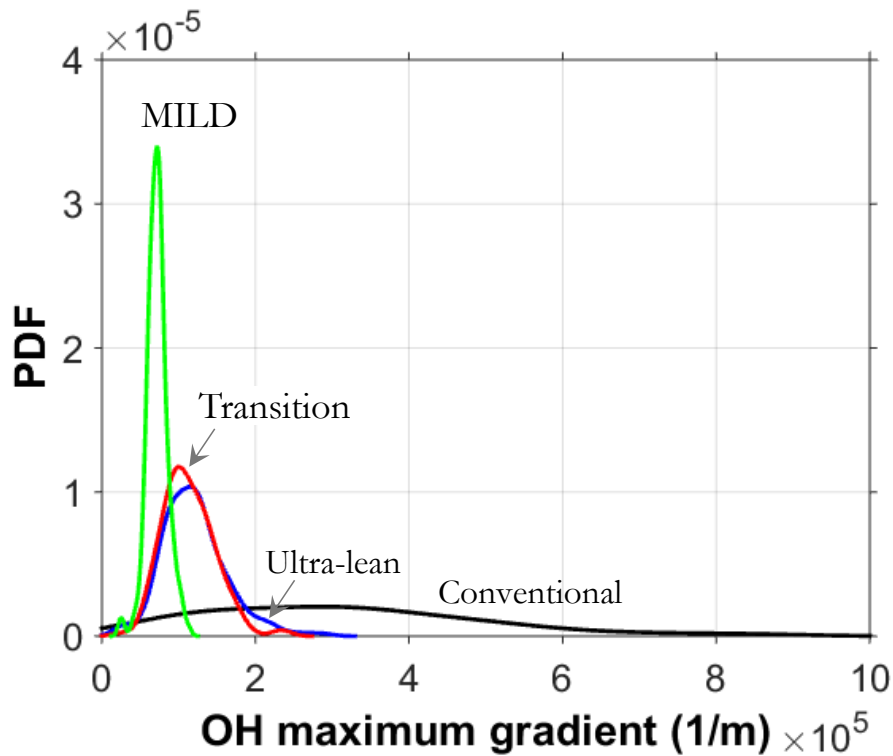


Figure 5.18: PDF of the maximum values of the norm of the 2D OH gradient obtained from 250 instantaneous images for each of the conventional, ultra-lean, transition, and MILD cases.

5.2.9 OH quantification at the downstream locations

Till now, we have presented the OH counts to describe and compare the characteristics of the reaction zone. In this section, the OH signal is quantified along the centreline of the chamber in the region spanning 100 to 180-mm. The calibration procedure is outlined in **Section 5.1.2**. To quantified data is used to further investigate the distribution of the OH radical in the downstream locations of the chamber (100- 180-mm) as observed in the instantaneous and mean images. The mole fraction of OH radical in ppm at $Z = 100$, 150, and 180-mm for the conventional, ultra-lean, transition, and MILD cases is shown in **Table 5.1**.

Table 5.1: OH radical mole fraction at various axial locations in the chamber.

Axial dist. (mm)	Conventional (ppm)	Ultra-lean (ppm)	Transition (ppm)	MILD (ppm)
100	4542	827	851	302
150	1371	235	312	295
180	582	178	199	226

The maximum OH volume fraction is obtained for the conventional case (~ 4542-ppm) suggesting an intense reaction zone in this mode of combustion. The OH volume fraction then sharply drops to 1371-ppm at $Z = 150$ -mm and to 582-ppm at $Z = 180$ -mm, a decrease of around 7.8 times over a distance of 80-mm. In comparison, the lowest OH ppm is measured for the MILD case (301-ppm) at $Z = 100$ -mm which is an order of magnitude lower compared to that for the conventional case. The OH mole fraction remains nearly constant (294-ppm) at $Z = 150$ -mm and decreases to 226-ppm at 180-mm. Trends in temperature and OH signal further suggest that OH ppm is nearly uniform downstream at least upto 210-mm for the MILD case. This quantitatively shows that the two combustion modes are significantly different in their reaction zone intensity. The maximum intensity for the ultra-lean and the transition cases are 3 times greater than that for the MILD case at $Z = 100$ -mm

Laser diagnostics of combustion

showing that the MILD case has the lowest intensity of the reaction zone and heat release. The decrease in the OH counts for the transition and ultra-lean cases are around 4.3 and 4.7 times, respectively, which follows the earlier trend that these two combustion modes are similar, with the transition case having slightly more uniform OH distribution due to dilution as observed by the lower decrease in the OH counts.

At 150-mm, the OH mole fraction is similar for the MILD and the transition cases and lower for the ultra-lean case. However, at $Z = 180$ -mm, the maximum counts is observed for the MILD case (~ 226 -ppm) followed by the transition (~ 199 -ppm) and ultra-lean case (~ 177 -ppm). A clear trend is observed at the downstream locations suggesting that the MILD case is more distributed as compared to the ultra-lean and the transition cases. Such an extension of the reaction zone has also been observed by earlier studies [57]. The uniformity of the OH profile for the MILD case also shows that the heat release is more uniform for the MILD case as compared to the other cases. Equilibrium calculations at $Z = 100, 150,$ and 180 -mm at constant temperature show that the local OH mole fraction is much higher than the equilibrium values predicted at these locations. This suggests that the reactions are still in progress at these locations. Further investigation with more precise measurements of the local composition is necessary to quantify the OH concentration in the downstream locations and identify the differences in the reaction zone and heat release distributions.

5.2.10 Modeling

Isothermal (1370 K) plug-flow reactor simulations are conducted to further investigate the distribution of OH radicals in the downstream locations with dilution. The temperature is close to the maximum temperature observed for the ultra-lean and the MILD cases. The O₂ percentage is set at 3% and 21% in the oxidizer. The simulations are conducted in CHEMKIN using the H₂/CO chemistry described by Li et al. [97] with the modified H₂/O₂

Laser diagnostics of combustion

chemistry proposed by Burke et al. [98]. The schematic diagram of the plug flow reactor model is shown in **Figure 5.19**.

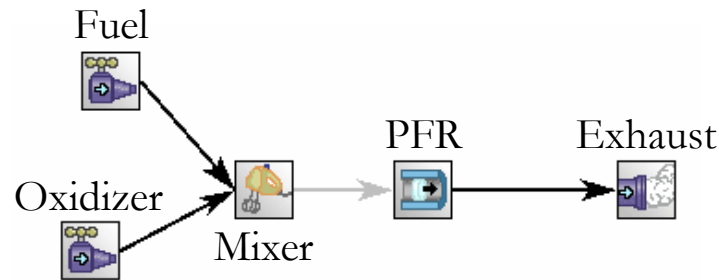


Figure 5.19: Schematic diagram of the plug flow reactor model.

The primary observation in **Figure 5.20** is that the OH lifetime increases with a decrease in the O₂ percentage. The OH concentration is higher over a longer distance of the reactor in the 3%-O₂ case as compared to the 21%-O₂ case, similar to the higher OH concentration in the downstream locations observed for the MILD case as compared to the ultra-lean case. This also matches well the standard description of MILD combustion in literature with a volumetric and extended reaction zone. From the net production curves, we observe that the region with positive OH production is localized, although it widens for the 3% O₂ case. However, the consumption of OH is gradual and spreads over a longer distance as observed in **Figure 5.20c**. The slow consumption leads to passive convection of OH along the channel length that is also responsible for the distributed OH and heat release. This also suggests that the production of OH is localized while the consumption is distributed under the effects of dilution. The ratio of the peak rates of consumption and production also reduces with increase in dilution, strengthening the explanation. This can also be observed in the

Laser diagnostics of combustion

instantaneous OH-PLIF images in **Figure 5.16**, where a distinction can be made between the thin reaction zones near the inlet (net production) and the diffuse region further downstream (net consumption). The near-nozzle regions become weaker and wider with dilution but still maintain their distinct structure, unlike the downstream locations. Hence, convection appears to be a possible mechanism for the distribution of the reaction zone. This also highlights the importance of finite-rate chemistry under MILD conditions.

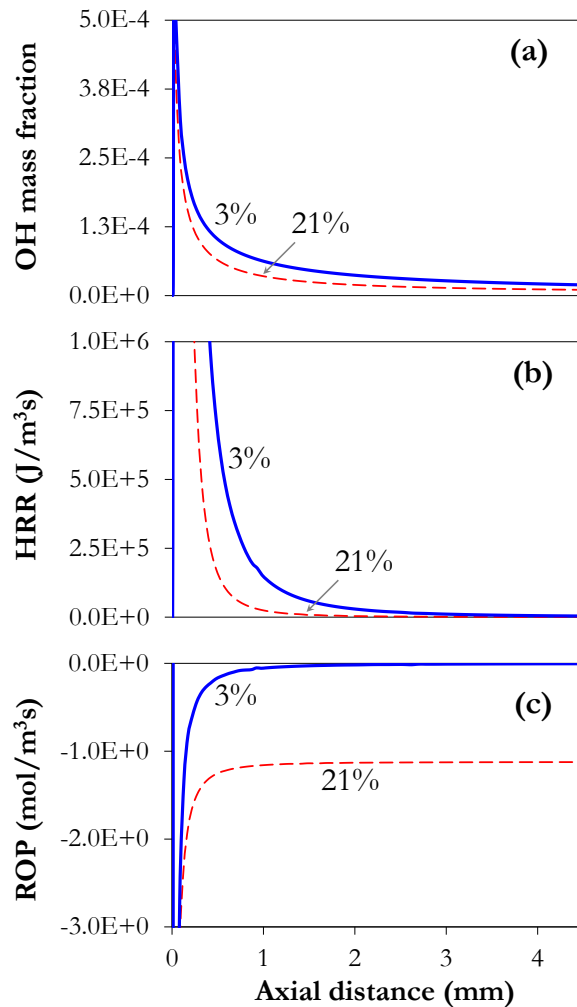


Figure 5.20: (a) OH mass fraction, (b) heat release rate, and (c) rate of production of OH with axial distance for the isothermal plug flow reactor with 3% and 21% O₂.

5.3 Summary

The present chapter experimentally investigates the reaction zone structure of combustion of a representative composition of syngas (20% CO, 20% H₂, 60% N₂) with low calorific value (4.6 MJ/kg) in an optically-accessible reverse flow combustion chamber at a fuel thermal input of 3.3 kW. Several modes of operation such as the conventional ($\Phi_{\text{global}} = 0.8$), ultra-lean ($\Phi_{\text{global}} = 0.32$), transition ($\Phi_{\text{global}} = 0.47$, O₂ = 14.3% in oxidizer), and MILD ($\Phi_{\text{global}} = 0.89$, O₂ = 7.6% in oxidizer) have been investigated at $P = 1$ atm to identify the best strategy for stable operation with low emissions. The OH-PLIF and Rayleigh thermometry techniques are utilized to investigate the reaction zone structure and the temperature distribution. The reaction zone structure shows that the OH intensity is highest for the conventional case, whereas it is the lowest for the MILD case. The intensity and distribution of OH for the ultra-lean and the transition cases are similar. The standard deviation of the OH signal shows the highest fluctuation for the conventional case while the MILD mode exhibits a quasi-steady behavior with the lowest fluctuations. The instantaneous images show thin reaction zones near the inlet for all the cases, which is contrary to the idea of a distributed and volumetric reaction zone under MILD conditions. However, the OH signal near the bottom of the chamber is higher for the MILD case as compared to the ultra-lean and the transition cases, indicating a distributed reaction zone downstream. The quantification of OH at these locations shows a clear trend of higher OH concentration for the MILD case, although more accurate measurements of temperature and species compositions are necessary to draw a definitive conclusion. This observed structure with thin reaction zones near the inlet and uniform OH downstream was explained by the passive advection of OH radicals under diluted conditions using plug flow reactor simulations. These simulations showed that the production of OH is localized while the consumption is delayed with dilution leading to a

Laser diagnostics of combustion

more uniform and extended reaction zone along the reactor length. The Rayleigh thermometry measurements showed that the temperature is nearly uniform throughout the chamber except very close to the centreline. The maximum temperature is measured for the conventional case (~ 1700 K) while the temperature is similar for the ultra-lean, transition, and the MILD cases (~ 1300 K). The standard deviation of temperature shows that the fluctuation is lowest for the MILD case, highest for the conventional case, and similar for the ultra-lean and the transition cases.

Chapter 6

Combustor Emissions

In this chapter, the performance of the reverse flow combustor utilizing syngas is reported in terms of NO_x and CO emissions. This is also one of the primary objectives of the current thesis. The experimental setup for the measurement of emissions is described in **Section 3.4** and **Section 4.1.2**. The optimal chamber temperature at which both the emissions of NO_x and CO are the lowest is also studied using a perfectly stirred reactor network model validated using the experimental emissions data.

6.1 Results and discussions

6.1.1 Emissions of CO and NO_x

The emissions of NO_x and CO (**Table 6.1**) from the system are measured over the entire range of flow conditions. It is observed that the NO_x emission is less than 1-ppm for all the cases. Even the cases A45 and A50 for which the adiabatic flame temperature is 1937 K and 1874 K, respectively, the NO_x emissions are < 1-ppm. Similar observations of low NO_x emissions have been made for methane combustion in the stagnation point reverse flow combustion chamber [19]. The reason was attributed to the good mixing between the fuel, the oxidizer and the exhaust such that the combustion is nearly lean-premixed even in the non-premixed configuration. The temperature measurements (**Figure 5.6**) in the present combustion chamber also show that the maximum temperature is less than 1800 K. For the other cases A125-A45N80, the adiabatic flame temperature as well as the measured

Combustor Emissions

temperature are below 1800 K and hence produce near-zero thermal NO_x . Due to the absence of hydrocarbons, the other pathways such as prompt NO_x are not significant. The NNH pathway was also observed to be not significant under the given conditions. The minimum CO emissions have been obtained for the conventional case (A50), followed by the case A45 (**Table 6.1**). The CO emissions from the system, however, increase with an increase in the N_2 percentage in the oxidizer. Among the cases from ultra-lean to MILD, the lowest emission was observed for the ultra-lean case. The results, however, show near complete conversion of fuel in the combustor with very low emissions of NO_x .

Table 6.1: Emissions of CO and NO_x from the combustion chamber normalized to 15% O_2 .

Cases*	O_2 (%) in the outlet	NO_x (ppmv @ 15% O_2)	CO (ppmv @ 15% O_2)
A45	1.6	< 1	51
A50	2.7	< 1	32
A125	11.7	< 1	353
A105N20	10.3	< 1	375
A85N40	7.4	< 1	392
A65N60	4.0	< 1	429
A45N80	1.5	< 1	461

*Here A represents the air flow rate (slpm) and N represents the N_2 flow rate (slpm) in the oxidizer. The fuel flow rate is constant at 42 slpm; Case A50 (conventional), A125 (ultra-lean), A85N40 (transition), and A45N80 (MILD).

6.1.2 Comparison of emissions with PSR

To understand the interaction between the kinetics and the recirculation within the chamber, perfectly stirred reactor (PSR) simulations are performed using CHEMKIN with the GRI 3.0 kinetic mechanism [113]. The schematic of the reactor network model is shown in **Figure 6.1**. To model the recirculation, the exhaust from another PSR at 1050 K with a residence time of 10 s is used. The temperature and concentration of the reactants in this PSR is same as that of the fresh reactants in the main PSR. The temperature 1050 K was selected as representative of the average temperature of the recirculating gases. The recirculation ratio was varied from $R = 0 - 2$, while the residence time was varied between 0.05 – 0.15 seconds.

Combustor Emissions

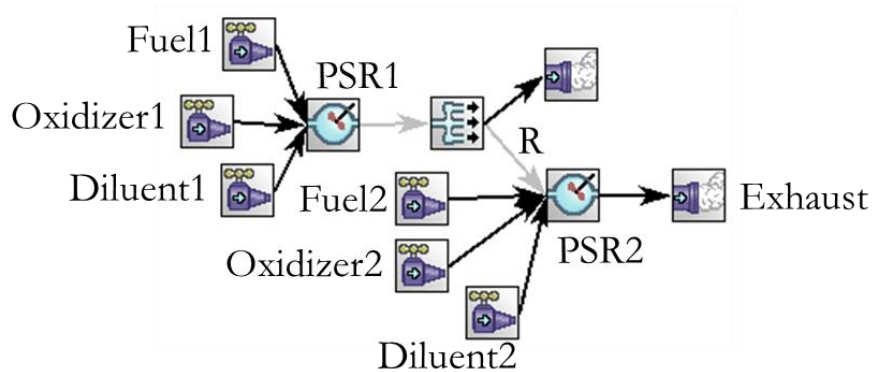


Figure 6.1: Reactor network diagram for comparison of emissions. Here, R is the recirculation ratio. The value of R varies from 0 - 2.

The results from the PSR and experimental measurements have been compared in **Figure 6.2**. Without recirculation ($R = 0$), the emissions show a completely different trend from that of the measured data. A similar trend was obtained if recirculation was included at the adiabatic flame temperature. This also shows that recirculation at realistic chamber temperatures (with heat loss) is required to correctly model the emissions. As the recirculation ratio is increased, the CO emissions get closer to the experimentally measured values. A close match between the measurements and the simulations is obtained for $R = 2$, which is a realistic value for these type of reverse flow combustors [19]. Similar results were obtained for NO_x emissions with and without recirculation, although the difference between the cases is not very prominent due to the low temperatures involved. The model, however, over-predicts the CO emissions for the cases A50 and A45. This is because these conventional cases have a strongly localized reaction zone as observed in the OH-PLIF images (**Figure 5.16**) with temperature in the range of 1600 - 1700 K (**Figure 5.6**). However, the PSR predicts a uniform temperature in the range of 1300 - 1400 K under the given

Combustor Emissions

conditions. The recirculation rate R is also expected to be lower as the velocity of the oxidizer stream is reduced due to low flow rate and temperature, and thus there is a deviation from idealized PSR behavior. Nevertheless, the trend in the CO and NO_x emissions is clearly captured with this simple PSR network model. The results also indicate good mixing between the reactants and the exhaust within the chamber.

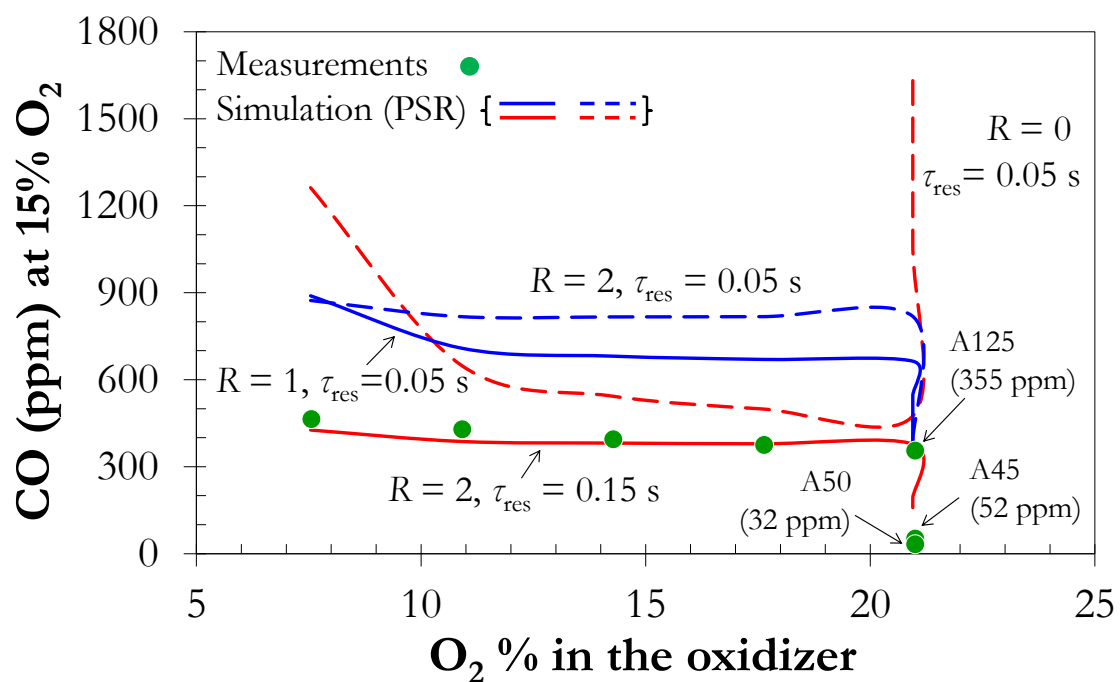


Figure 6.2: Comparison of CO emissions from the chamber and that from the perfectly stirred reactor model.

Acronyms: τ_{res} = residence time, R = recirculation ratio. The R varies from 0 - 2 while τ_{res} varies from 0.05 - 0.15s.

The conversion of CO to CO₂ in the combustion of syngas is primarily channelized by the exothermic reaction $\text{CO} + \text{OH} \rightarrow \text{CO}_2 + \text{H}$. Since the flow rates are constant, the temperature is nearly identical for the cases A125 – A45N80. The conversion of CO to CO₂ thus depends on the OH concentration as the CO mole fraction is identical in the fuel.

Combustor Emissions

Considering the rate of production of OH, the reactions $\text{H} + \text{O}_2 \rightarrow \text{OH} + \text{O}$ and $\text{O} + \text{H}_2\text{O} \rightarrow 2\text{OH}$ are the most important. In fact, the former reaction is most important for the formation of the O radical, while the latter reaction is responsible for the consumption of O. In both the cases, the decrease in the concentration of O_2 in the oxidizer is responsible for the reduced production of O and OH and increased CO emission. The decrease in the CO emissions for A45 and A50 cases are due to higher chamber temperature as compared to the ultra-lean and the MILD cases. However, the data for $R = 0$ and $\tau_{\text{res}} = 0.05$ s shows increase in CO emissions for the A50 and A45 cases. The increase in CO emissions can be attributed to the balance between O_2 concentration and CO_2 dissociation at high temperatures (~ 1900 K). With the increase in temperature, the reverse rate in the reaction $\text{CO} + \text{OH} \rightarrow \text{CO}_2 + \text{H}$ increases, leading to a reduced consumption of CO. This also suggests that the combustor behaves as a PSR, where kinetics and temperature plays a key role in determining the emissions.

6.1.3 Effect of chamber temperature

Next, the effect of the chamber temperature on the CO and NO_x emissions is investigated (**Figure 6.3** and **Figure 6.4**) to determine the optimum operating temperature. Such an optimum temperature can be reached by altering the preheating of the reactant streams or changing the calorific value of the fuel. Both the PSRs are maintained at the same isothermal temperature while the exhaust from the first PSR is injected into the second PSR to simulate the effect of recirculation. The recirculation ratio is fixed at $R = 2$ and the residence time in the second PSR is maintained at $\tau_{\text{res}} = 0.15$ s. The predicted emissions corresponding to the experimental conditions as observed in **Figure 6.2** are shown with large markers and thus help to identify the subsequent variation in emissions with chamber temperature.

Combustor Emissions

For the conventional case (A50), the CO emission is nearly insensitive to a temperature at the operating condition, although it increases sharply at lower chamber temperatures. From **Figure 6.3** is observed that CO emission reduces from 161-ppm at 1360-K to 147-ppm at a chamber temperature of 1450-K. However, it increases subsequently with a rise in the temperature. Thus, the chamber is operated very close to the optimum condition although some decrease in CO emissions (~ 14 -ppm) is expected as the chamber temperature increases. For the transition and the ultra-lean cases, the emissions are nearly identical and decrease with an increase in the chamber temperature. For the transition case (A85N40), the minimum of 114-ppm is reached at $T_{\text{chamber}} = 1550$ K, which then increases gradually with an increase in the temperature. For the ultra-lean case (A125), the CO emissions decrease monotonically to 84-ppm upto $T_{\text{chamber}} = 1750$ K but slightly increases to 96-ppm at 1850 K. The rate of change of CO emissions is also low, suggesting that the minimum is very close to $T_{\text{chamber}} = 1750$ K for the ultra-lean case. For the MILD case (A45N80), the minimum of 322-ppm is reached at a much lower temperature $T_{\text{chamber}} = 1350$ K. However, the CO emissions strongly rise both below and above this chamber temperature. Thus, under MILD conditions, a narrow window from 1250 - 1450 K exists at which the CO emission is nearly insensitive to temperature. This is the optimum operating range under MILD conditions in the present configuration. This also explains why the CO emission increased almost three times from 470-ppm to 1333-ppm as the oxidizer preheating temperature was decreased from 783 K to 483 K, as observed in **Figure 4.8**.

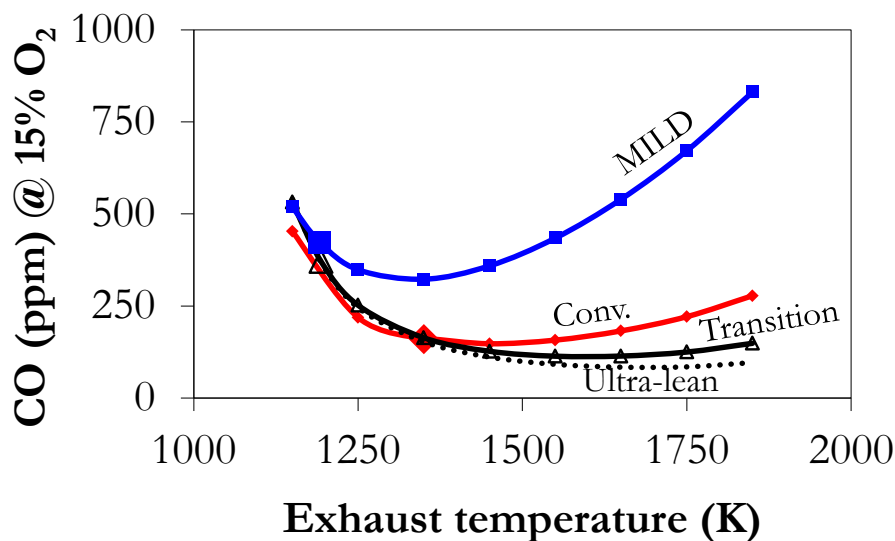


Figure 6.3: Variation of CO emissions (normalized to 15% O₂) with exhaust temperature using the PSR model. The fuel is 20% CO, 20% H₂, and 60% N₂. The temperature has been varied by changing the temperature of the exhaust that is recirculated. The recirculation ratio $R = 2$ and $\tau_{res} = 0.15$ s. The emission corresponding to the experimental conditions is shown with larger markers.

The emission of NO from the chamber with temperature is shown in **Figure 6.4**. For the A50 case, the NO emission is < 10-ppm upto 1650 K, but increases to 107-ppm at 1850 K. Hence, the operating temperature near 1450 K is ideal considering both NO and CO emissions. For the ultra-lean and the transition cases, the NO emissions exceed 10-ppm beyond 1650 K. However, the minimum CO emission is reached at a much higher temperature for the ultra-lean case, although the variation is gradual with < 15-ppm change in the range of 1550 - 1750 K. Considering both NO and CO emissions, the temperature range 1550 - 1600 K seems to be optimum for the ultra-lean and the transition cases. For the MILD case, the NO emission is < 10-ppm below 1550 K. This temperature range also corresponds

Combustor Emissions

to the minimum in CO emissions (1250 - 1450 K) and hence, the current operating condition is close to the optimum operating point.

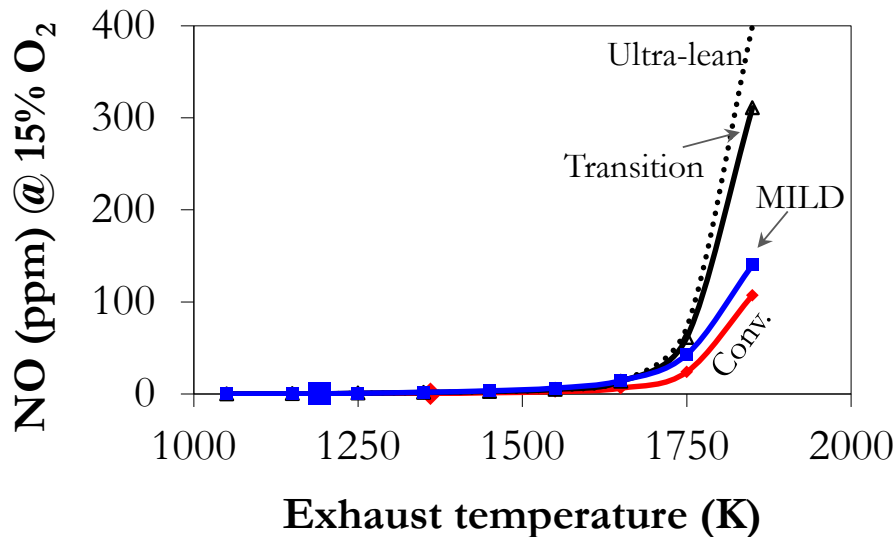


Figure 6.4: Variation of NO emissions (normalized to 15% O₂) with exhaust temperature using the PSR model. The fuel is 20% CO, 20% H₂, and 60% N₂. The temperature has been varied by changing the temperature of the exhaust that is recirculated. The recirculation ratio $R = 2$ and $\tau_{\text{res}} = 0.15$ s. The emission corresponding to the experimental conditions is shown with larger markers.

The relative differences in the NO emission led to investigation of the major pathways for NO formation in this combustion chamber. The analysis of the quantitative reaction path diagram (QRPD) and the absolute rate of production (ROP) delineated several pathways for the formation of NO as observed in **Figure 6.5**. For the conventional case A50, the thermal NO was the most important at $T_{\text{chamber}} = 1850$ K, closely followed by the N₂O intermediate pathway. The NNH pathway was also significant but the rate of production was one order of magnitude lower. At lower temperatures ($T_{\text{chamber}} = 1650$ K), the N₂O intermediate pathway is observed to overtake the thermal route. A similar trend is observed for the ultra-lean and

Combustor Emissions

MILD cases. The NNH pathway is weakest for the ultra-lean case. The relative magnitude of the thermal routes at 1850 K follow the trend of NO emissions as observed in **Figure 6.4**. However, the lower NO production for the conventional and MILD cases at similar temperatures can be attributed to the decrease in the O₂ content in the chamber. Thus, both the reduced temperature fluctuation as observed in **Figure 5.11** and the low excess O₂ can help in the reduction of NO_x emissions in the MILD mode of operation. Under actual experimental conditions, the peak temperature measured using Rayleigh thermometry is ~ 1700 K for the conventional case, which is just below the value where the NO emission starts to increase exponentially, as shown in **Figure 6.4**. As a result, the NO emission is measured to be less than 1 ppm for all the cases. Any further increase in the operating temperature would significantly increase the NO emission as predicted by the idealized reactor simulations shown in **Figure 6.4**.

Combustor Emissions

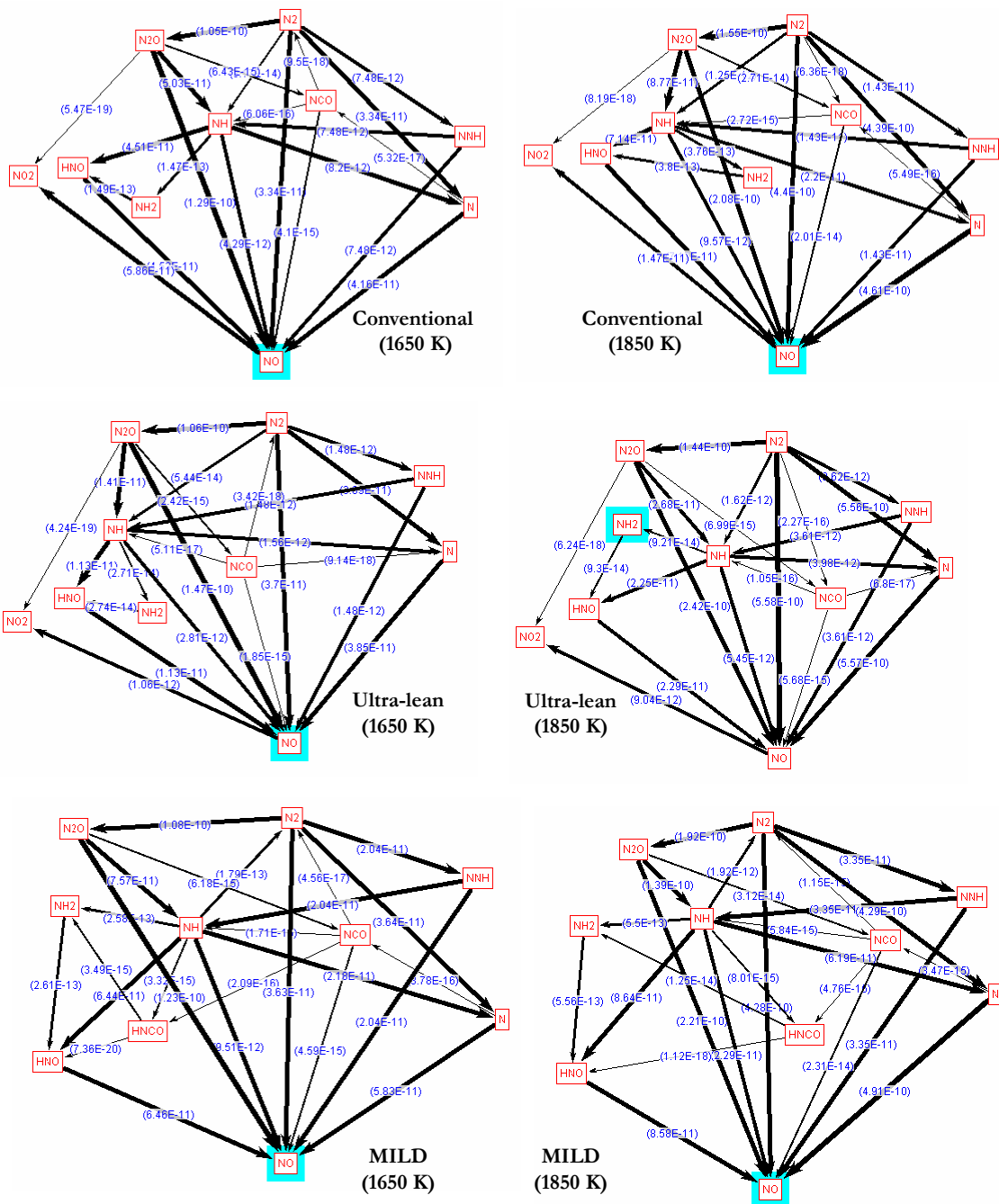


Figure 6.5: Quantitative reaction path diagram (QRPD) with the absolute rate of production (ROP) from various reactions showing the pathways for NO formation for the cases conventional (A50), ultra-lean (A125), and MILD (A45N80) cases at 1650 K and 1850 K.

6.1.4 Effect of H₂ content in the fuel

The PSR model is used next to determine the performance of the combustion chamber with variation in the H₂ percentage of the fuel. The total flow rates and temperature has been kept constant as shown in **Table 4.1**, thereby ensuring mixing equivalent to the base case of 20% CO, 20% O₂, and 60% N₂. The H₂ percentage in the fuel has been changed to 10% and 30%, respectively, from 20% for the base fuel keeping all other parameters as constant. The recirculation ratio $R = 2$ and the residence time τ_{res} has been maintained at 0.15 s as these parameters predicted the measured CO emissions with good accuracy. It must be mentioned here that the NO_x emission was < 1-ppm for all the cases with 10% and 30% H₂, similar to the base case with 20% H₂. It is also to be noted that the temperature difference in the reactor due to a change in the H₂ content from 10% to 30% is within 15 K and does not contribute significantly to the variation in emissions.

The predicted CO emission normalized to 15% O₂ is shown in **Figure 6.6**. A clear decrease in CO emissions can be observed with an increase in the H₂ content of the fuel. The lowest emission of 74-ppm is obtained for the conventional case (A50) with 30% H₂. The actual emission may be lower as the model over-predicted the CO emissions for the base case (20% H₂) for A45 and A50 as shown in **Figure 6.2**. The CO emission for the case A45 ($\Phi_{global} = 0.89$) is slightly higher than that of the case A50. This can be attributed to the lower O₂ content in the chamber for the A45 case as compared to A50. The emissions from the ultra-lean and the transition cases are nearly same (~ 188-ppm at 30% H₂ and 629-ppm at 10% H₂) and are both higher than those for the cases A45 and A50. This similarity in emissions is in agreement with the earlier observations of temperature and OH radical distribution. The highest CO emission is observed for the MILD case for all H₂ content in the fuel. The difference between the MILD and the ultra-lean cases is only 10-ppm at 30% H₂,

Combustor Emissions

but this difference increases to 49-ppm and 125-ppm for 20% and 10% H₂ content in the fuel, respectively. Thus, an increase in the H₂ content of the syngas can reduce the CO emissions from the combustion chamber under similar operating conditions.

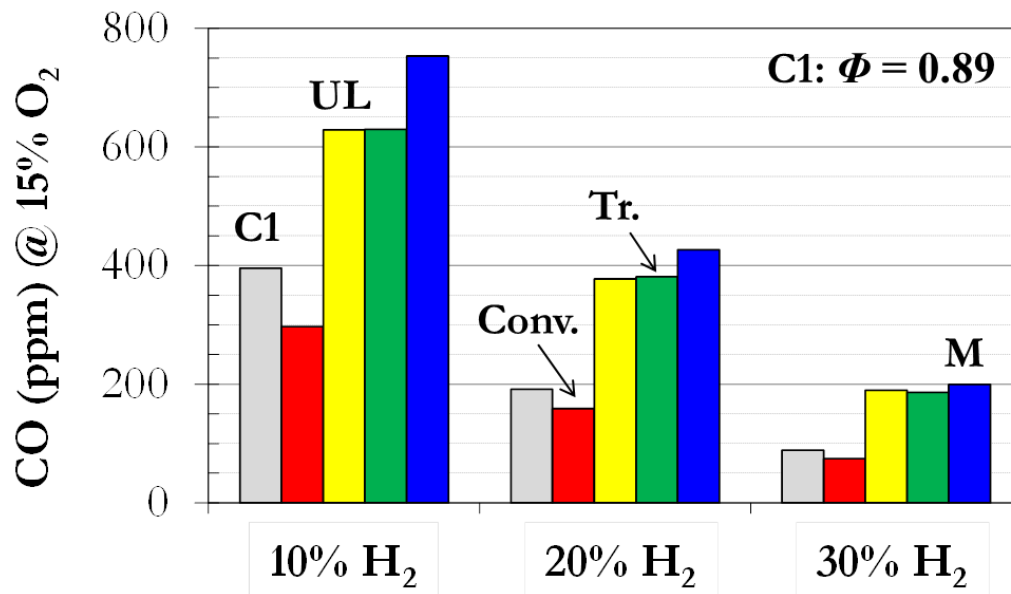


Figure 6.6: Comparison of CO emissions (normalized to 15% O₂) for 10%, 20% (base case), and 30% H₂ (by vol.) in the fuel (30%, 20%, and 10% CO, respectively) with 60% N₂ in all the cases using the PSR model. The recirculation ratio $R = 2$ and $\tau_{\text{res}} = 0.15$ s. Acronyms: τ_{res} = residence time, UL - ultra-lean, Conv. - conventional, Tr. - transition, M - MILD, C1 - conventional case with $\Phi = 0.89$, R = recirculation ratio.

6.2 Summary

The present chapter evaluates the low emission capability of the reverse flow combustor for various modes of syngas combustion using measured NO_x and CO emissions. The NO_x emission is less than 1-ppm for all the cases, while the CO emission is highest for the MILD case (461-ppm) and lowest for the conventional case (32-ppm). A network of perfectly stirred reactors was developed and used to explain the observed trend in emissions. The effect of H_2 content in the fuel and the chamber temperature on the emissions was also investigated with this model to identify the optimum operating conditions with lowest CO and NO_x emissions. Based on the emission measurements, it can be concluded that for low calorific value syngas in the reverse flow configuration, the conventional mode offers stable operation with lowest emissions. However, the advantages of the MILD mode in reducing NO_x emissions can be expected to be observed at elevated chamber temperatures with a higher calorific value of syngas and possibly operation at higher pressures. These studies could be the basis for future investigations.

Chapter 7

Numerical modelling studies

The present chapter numerically investigates the combustion of low calorific value syngas in the reverse flow (RF) chamber operating under ultra-lean and MILD conditions. Experiments have earlier been conducted in the optically-accessible chamber as described in the previous chapters. This experimental data is used to validate and compare the performance of several flow and turbulence-chemistry interaction models. The turbulent flow models used are SST- $k\omega$ (RANS) and Detached Eddy Simulation (DES). For combustion, the Flamelet generated manifold (FGM) model and the Eddy dissipation concept (EDC) model are compared. Thus, four combinations (2 turbulence models x 2 combustion models) of these models are investigated and compared as shown in **Table 7.1**. Special focus has been directed in understanding the ability of these models to predict both the qualitative and quantitative distribution of the intermediate radical OH. The next few sections describe the numerical modelling, results, and discussions followed by a summary of the key findings.

Table 7.1: Turbulence and combustion models

Turbulence	Combustion
RANS (SST- $k\omega$)	Flamelet generated manifold (FGM)
Detached Eddy Simulation (DES)	Eddy dissipation concept (EDC)

7.1 Experimental conditions modelled

The ultra-lean and the MILD cases described in **Table 4.1** are modelled as these combustion modes vary distinctly in their characteristics. The experimental setup has been described in **Section 4.1**. The combustion chamber and the flame luminosity images for the ultra-lean and the MILD cases are shown again in **Figure 7.1a,b**. Detailed measurements of OH* (chemiluminescence at 5 kHz), noise (50 kHz), exhaust emissions (CO and NO_x), OH (planar laser-induced fluorescence) and temperature (Rayleigh thermometry) reported in earlier chapters are used to validate and compare the numerical models analyzed in the present study. The temperature measured as observed in **Figure 7.1c** is used as boundary conditions for the inner walls of the chamber. The remaining walls are considered adiabatic. The other boundary conditions are described in **Table 7.2**.

Table 7.2: Boundary conditions for the MILD and the ultra-lean cases.

Case	MILD	ultra-lean
Fuel (slpm)	42	42
Coflow	Air (slpm)	45
	N ₂ (slpm)	80
O ₂ % in coflow	7.6	21
Φ_{global}	0.89	0.32
$T_{\text{in, fuel}}$ (K)	544	536
$T_{\text{in, ox}}$ (K)	768	785
Re_f	10624	10213
Re_{ox}	4318	4242

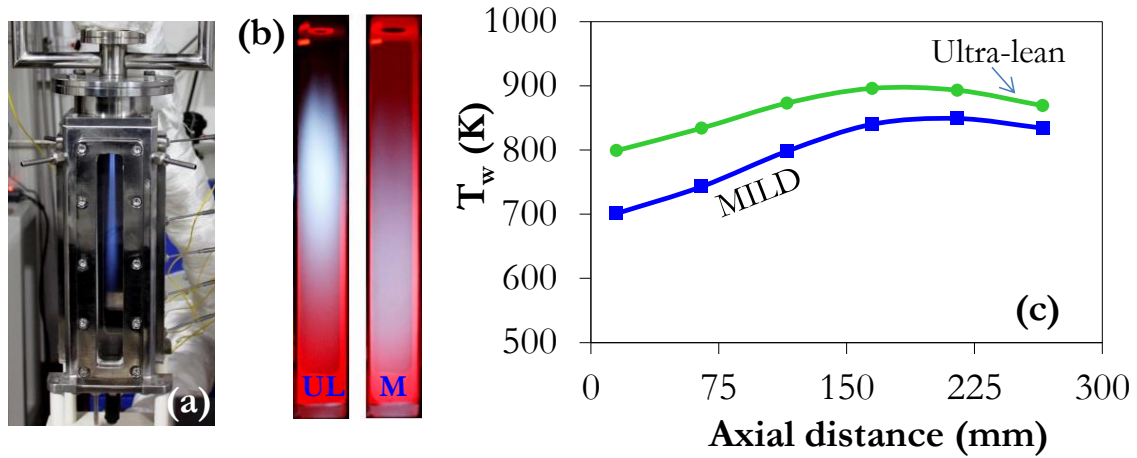


Figure 7.1: (a) Image of the experimental test rig in operation where the flame is visible through the optical access, (b) flame luminosity images for the ultra-lean (UL) and the MILD (M) cases, (c) wall temperature profile for the ultra-lean and the MILD cases.

7.2 Numerical formulation

7.2.1 Computational domain and boundary conditions

The three dimensional computational geometry was discretized into 1.45 million (130 x 250 x 44) hexahedral cells with smaller cells near the inlet, walls, and the shear layer as observed in **Figure 7.2c**. Near the inlet, the cells are almost isotropic with $\Delta x = 0.125$ -mm, which are gradually stretched further downstream by a bias factor of 3. The power spectrum of the axial turbulent kinetic energy in the shear layer as observed in **Figure 7.2b** follows Kolmogorov's $-5/3$ profile for at least one decade which is considered reasonable for LES [65]. The results were verified to be grid independent by comparison with another mesh consisting of nearly 1.1 million cells (110 x 220 x 44). The mass flow rate is specified at the inlets with uniform species mole fractions and temperature. The injector length has been

Numerical modelling studies

restricted to 100-mm which was sufficient to obtain fully-developed turbulent velocity profiles similar to the experimental setup. As the full injector was not modelled, the heat transfer between the fuel, the oxidizer, and the exhaust streams was accounted for by performing apriori RANS simulations with the full injector and using inlet temperatures measured at the upstream. These walls between the reactant streams were subsequently removed in the DES simulations and the temperature obtained from the RANS simulations 100-mm upstream of the injection plane were provided as boundary conditions. A turbulence intensity of 5% was imposed onto the mean velocity at the inlet using the spectral synthesizer method. A pressure outlet boundary condition is set at the exit of the chamber as it was open to the atmosphere. No slip and non-catalytic conditions were prescribed on all the solid walls.

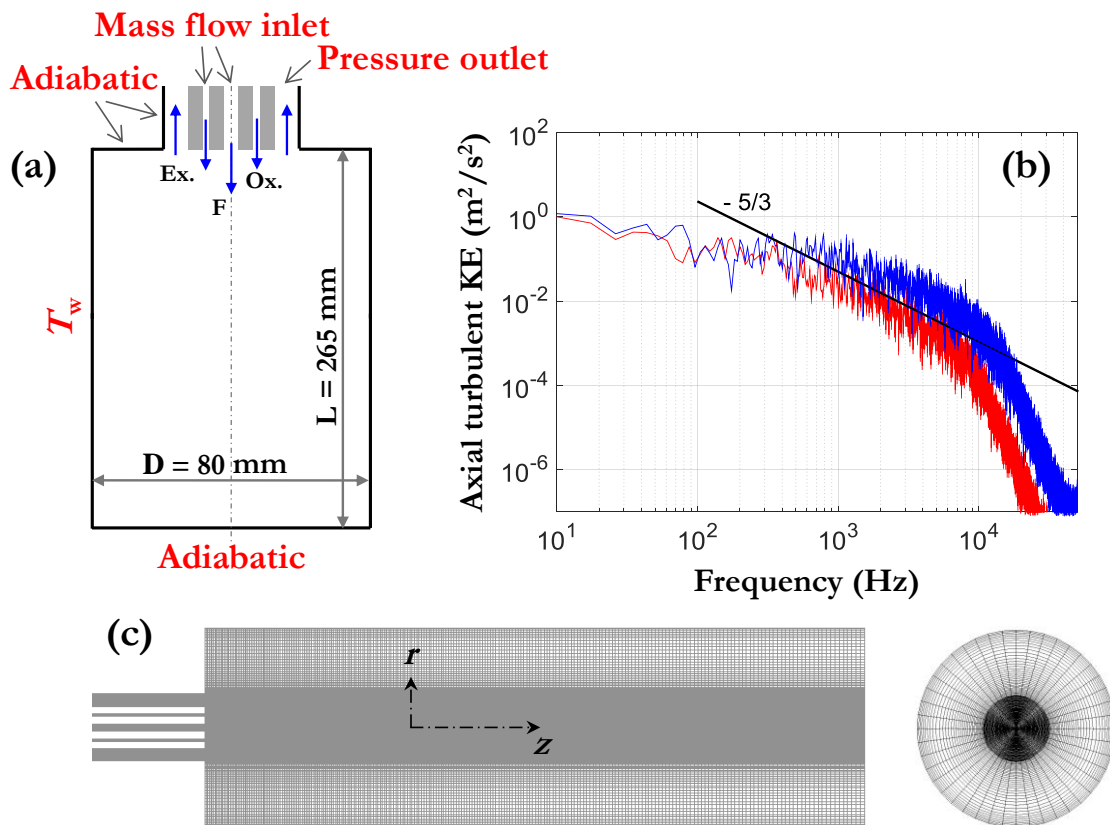


Figure 7.2: (a) Schematic of the combustion chamber with boundary conditions, (b) Power spectrum of the axial turbulent kinetic energy at two different locations in the outer shear layer, $(r, z) = (7, 64)$ -mm and $(7, 144)$ -mm from the injection plane, (c) image of the grid used for simulations.

7.2.2 Numerical details

The CFD code Ansys-Fluent based on the finite-volume method is used to conduct the simulations. The pressure based solver is used for all the simulations. For the RANS simulations, the PISO scheme was used for the pressure-velocity coupling, while the second-order scheme was chosen for pressure interpolation. The second-order UPWIND scheme has been used to discretize the momentum, turbulent kinetic energy, specific dissipation rate, and energy equations. Initially, the convergence criteria had been set with residuals of 10^{-6} for energy and 10^{-5} for all other equations, although the simulations were subsequently run unless no further change in the residuals could be observed. For the DES model, the momentum equation was discretized using the central difference scheme while the species equations were discretized using the bounded central difference scheme. Other equations such as density, energy, turbulent kinetic energy, and specific dissipation rate were discretized using the second-order upwind scheme. The PISO scheme with skewness and neighbour correction was used for the pressure-velocity coupling. The second-order implicit scheme was used for time discretization. A time step size of $\Delta t = 10^{-6}$ seconds was chosen such that $CFL < 1$ throughout the domain. This led to a run-time of around 1 month on an AMD FX-8350 octa-core processor with a clock speed of 4 GHz for the DES-EDC case. The initial condition for the DES simulations was a nearly converged RANS simulation. For the DES-FGM cases, the time required was > 10 days on the same system. The convergence criteria were set at 10^{-5} for energy and 10^{-3} for the remaining equations. Markers for velocity, temperature, pressure, and major species mole fractions were placed at several locations in the computational domain to check for a statistical stationary solution. The simulations were then time-averaged to obtain smooth profiles for the mean and the RMS quantities. The averaging time is around 200-ms which is close to twice the residence time in the chamber [40].

7.2.3 Governing equations

The steady-state three dimensional RANS simulations were conducted using the SST k - ω model developed by Menter [114] that blends the robustness of the k - ω model in the near-wall region with the freestream independence of the k - ε model in the far-field. The Favre-averaged continuity and momentum equations are as follows:

$$\frac{\partial \bar{\rho}}{\partial t} + \frac{\partial}{\partial x_i} (\bar{\rho} \tilde{u}_i) = 0 \quad (7.1)$$

$$\frac{\partial (\bar{\rho} \tilde{u}_i)}{\partial t} + \frac{\partial}{\partial x_j} (\bar{\rho} \tilde{u}_i \tilde{u}_j) = \frac{\partial}{\partial x_j} (\sigma_{ij}) - \frac{\partial \bar{P}}{\partial x_i} + \frac{\partial}{\partial x_j} (-\overline{\rho u'_i u'_j}) \quad (7.2)$$

Here, σ_{ij} is the stress tensor due to molecular viscosity and is defined as:

$$\sigma_{ij} = \left[\mu \left(\frac{\partial \tilde{u}_i}{\partial x_j} + \frac{\partial \tilde{u}_j}{\partial x_i} \right) \right] - \frac{2}{3} \frac{\partial \tilde{u}_k}{\partial x_i} \delta_{ij} \quad (7.3)$$

The Reynolds' stress tensor is modelled using the Boussinesq hypothesis as follows:

$$-\overline{\rho u'_i u'_j} = \left[\mu_t \left(\frac{\partial \tilde{u}_i}{\partial x_j} + \frac{\partial \tilde{u}_j}{\partial x_i} \right) \right] - \frac{2}{3} \frac{\partial \tilde{u}_k}{\partial x_i} \delta_{ij} - \frac{2}{3} \bar{\rho} k \delta_{ij} \quad (7.4)$$

The equations for the turbulent kinetic energy (k) and the specific dissipation rate ($\omega = \varepsilon/k$) are the following:

$$\frac{\partial (\bar{\rho} k)}{\partial t} + \frac{\partial}{\partial x_i} (\bar{\rho} k \tilde{u}_i) = \frac{\partial}{\partial x_j} \left[\left(\mu + \frac{\mu_t}{\sigma_k} \right) \frac{\partial k}{\partial x_j} \right] + G_k - Y_k \quad (7.5)$$

$$\frac{\partial (\bar{\rho} \omega)}{\partial t} + \frac{\partial}{\partial x_i} (\bar{\rho} \omega \tilde{u}_i) = \frac{\partial}{\partial x_j} \left[\left(\mu + \frac{\mu_t}{\sigma_\omega} \right) \frac{\partial \omega}{\partial x_j} \right] + G_\omega - Y_\omega \quad (7.6)$$

The term G_k represents the generation of turbulent kinetic energy due to mean velocity gradients, while G_ω represents the generation of ω . The terms σ_k and σ_ω are the turbulent Prandtl numbers for k and ω , respectively. The terms Y_k and Y_ω represent the dissipation of k

Numerical modelling studies

and ω due to turbulence, respectively. The turbulent viscosity for the $k - \omega$ model is calculated using the following expression:

$$\mu_t = \frac{\bar{\rho}k}{\omega} \frac{1}{\max\left[\frac{1}{\alpha^*}, \frac{F_2 S}{\omega \alpha_1}\right]} \quad (7.7)$$

Here, S is the strain rate magnitude, F_2 is a blending function, and $\alpha^* = 1$ in the high Re form of the $k-\omega$ model, $\alpha_1 = 0.31$. Further details of the blending function can be found elsewhere [114].

In the current investigation, for the SST $k-\omega$ Detached Eddy Simulation (DES) model, the RANS model is used in the boundary layer, whereas the DES treatment is performed in the separated regions. The computational cost of DES models, also known as hybrid RANS/LES models, is lower than that of full LES models, but significantly higher than that of the RANS models. The DES form of the SST $k-\omega$ model is similar to the RANS model except in the dissipation term of the turbulent kinetic energy [115].

$$Y_k = \bar{\rho}\beta^*k\omega F_{DES} \quad (7.8)$$

$$F_{DES} = \max\left[\frac{L_t}{C_{DES}\Delta_{max}}, 1\right] \quad (7.9)$$

$$L_t = \frac{\sqrt{k}}{\beta^*\omega} \quad (7.10)$$

Here, L_t is the turbulence length scale that defines the shift between the RANS and DES modes. The term Δ_{max} is the maximum local grid spacing (Δx , Δy , Δz) and C_{des} is a calibration constant = 0.61. β^* is a function of the turbulent Reynolds' number ($Re_t = \rho k/\mu\omega$).

For combustion modelling, two different approaches are used in the simulations. First, the species transport formulation is used in which the closure of the reaction source terms is obtained using the Eddy Dissipation Concept (EDC) model. Although this model is

Numerical modelling studies

suitable over a wide range reacting conditions and chemical timescales, it is more expensive as it solves transport equations for the individual species. The mixture fraction/progress variable formulation [Flamelet Generated Manifold (FGM) model] is also used which is less computationally expensive due to only two additional equations and tabulated chemistry, but may not be suitable to capture the finite-rate chemistry effects ($Da \sim 1$) that is typically encountered in reverse flow MILD combustion systems. The FGM model is, however, an improvement over the steady flamelet model as it is parameterized in terms of mixture fraction and the progress variable [67][116].

The Eddy Dissipation Concept model incorporates detailed chemistry to account for finite-rate kinetic effects in turbulent flows. In this model, it is assumed that the reactions occur in the small-scale turbulent structures called fine scales at constant pressure with initial conditions as the current species and temperature in the cell. The length fraction of the fine scales is calculated as:

$$\zeta^* = C_\zeta \left(\frac{\nu \varepsilon}{k^2} \right)^{1/4} \quad (7.11)$$

Here, ‘*’ denotes the fine scale quantities, ν is the kinematic viscosity, and C_ζ is a volume fraction constant = 2.1377. The volume fraction of the fine-scale quantities is denoted by ζ^{*3} .

The species reacts over a time scale denoted by:

$$\tau^* = C_\tau \left(\frac{\nu}{\varepsilon} \right)^{1/2} \quad (7.12)$$

The reactions proceed over the time scale τ^* governed by the Arrhenius rates and is integrated numerically using the ISAT algorithm [117] with a residual of 10^{-4} . The source term in the conservation equation for the i^{th} mean species is denoted by:

Numerical modelling studies

$$R_i = \frac{\rho(\zeta^*)^2}{\tau^*[1 - (\zeta^*)^3]}(Y_i^* - Y_i) \quad (7.13)$$

The mixture averaged diffusivities is used for species, while the Fick's Law is used to describe the diffusion process. The ideal gas law is used as the state equation for all the cases.

The FGM model uses a low-dimensional manifold created by solving the flamelet equations and is parameterized by the mixture fraction (f) and reaction progress (c). The FGM model has earlier been used for the simulation of non-premixed laminar co-flow flames [118]. The flamelet table is generated by solving the flamelet equations for a counterflow diffusion flame due to the non-premixed configuration of the current setup. Only steady flamelets have been considered in the current formulation. The accuracy of the FGM table was validated by comparison with the tables generated from standard chemical kinetic software such as CHEMKIN. The reaction progress is determined by solving an equation for the non-normalized progress variable, Y_c as follows:

$$\bar{\rho} \frac{\partial \tilde{Y}_c}{\partial t} + \frac{\partial}{\partial x_i} (\bar{\rho} \tilde{u}_i \tilde{Y}_c) = \frac{\partial}{\partial x_i} \left(\bar{\rho} D_{eff} \frac{\partial \tilde{Y}_c}{\partial x_i} \right) + \bar{S}_c \quad (7.14)$$

The mean source term \bar{S}_c is modelled as

$$\bar{S}_c = \bar{\rho} \iint S_{FR}(c, f) P(c, f) dc df = \bar{S}_{FR} \quad (7.15)$$

Here, S_{FR} is the finite-rate source term from the flamelet library, $c = Y_c/Y_c^{eq}$ is the normalized reaction progress variable, f is the mixture fraction, and P is the joint PDF of mixture fraction (f) and the reaction progress variable (c). The mixture fraction (f) and reaction progress (c) are assumed to be independent beta (β) functions and the joint PDF is expressed as the product of these two β -PDFs. The source term \bar{S}_c is also modelled using a turbulent flame speed model as follows:

Numerical modelling studies

$$\bar{S}_c = \rho_u S_t |\nabla \tilde{c}| = \bar{S}_{TFS} \quad (7.16)$$

Here, ρ_u is the unburnt density and S_t is the turbulent flame speed which is modelled by the correlation by Zimont [119]. Separate laminar flame speed simulations were conducted for syngas using Li et al. mechanism [97] at various mixture fractions and provided as input for calculation of the turbulent flame speed. The minimum of the source terms \bar{S}_{FR} and \bar{S}_{TFS} is used as the mean source term \bar{S}_c . The variance of the non-normalized progress variable Y_c is required for the β -PDF and is calculated using an algebraic equation:

$$\widetilde{Y_c^2} = C_{var} \frac{l_{turb}^2}{Sc_t} (\nabla \tilde{Y}_c^2) \quad (7.17)$$

Here, l_{turb} is the turbulent length scale, Sc_t is the turbulent Schmidt number = 0.7, and C_{var} is a constant with a value of 0.1. The variance of the mixture fraction is calculated by solving a transport equation as follows:

$$\frac{\partial \bar{\rho} \widetilde{f''^2}}{\partial t} + \frac{\partial}{\partial x_i} (\bar{\rho} \tilde{u}_i \widetilde{f''^2}) = \frac{\partial}{\partial x_i} \left(\frac{\mu_l + \mu_t}{\sigma_t} \frac{\partial \widetilde{f''^2}}{\partial x_i} \right) + C_g \mu_t \left(\frac{\partial \tilde{f}}{\partial x_i} \right)^2 - C_d \bar{\rho} \frac{\varepsilon}{k} \widetilde{f''^2} \quad (7.18)$$

where $f'' = f - \tilde{f}$, The default values for the constants σ_t , C_g , and C_d are 0.85, 2.86, and 2.0, respectively. The mean thermochemical properties are determined from the PDF table using the following equation:

$$\bar{\varphi} = \iint \varphi(c, f) P(c, f) dc df \quad (7.19)$$

The Discrete Ordinate radiation model is used with the domain-based weighted-sum-of-gray-gas model (WSGGM) to calculate the absorption coefficient of the participating gases, notably CO₂ and H₂O. The emissivity of steel was set at 0.8. However, the radiation model did not have a significant impact on the thermal field as the temperature is nearly uniform throughout the combustion chamber due to the reverse flow configuration.

7.2.4 Chemical kinetics

The kinetic mechanism selected was the H₂/CO chemistry proposed by Li et al. [97] with the modified H₂/O₂ chemistry given by Burke et al. [98] containing 12 species and 35 reactions. The mechanism developed by Li et al. provides detailed chemistry for fuels containing H₂ and CO with the minimum number of reactions suitable for DES simulations with EDC. Smaller schemes, such as the 4-step mechanism of Jones and Lindstedt [120] do not contain the intermediate radical OH which is a key focus of the present study. To assess the importance of NO_x chemistry, detailed zero dimensional perfectly stirred reactor (PSR) simulations are conducted with the GRI 3.0 reaction mechanism [113]. It is observed that the NO_x chemistry was not significant for the given range of temperature and composition. The measured NO_x emissions under MILD and ultra-lean conditions were also less than 1-ppm. Hence, all the simulations have been conducted without the NO_x chemistry.

7.3 Results and discussions

This section presents a comparison of the predictions of the RANS/DES and EDC/FGM models with the experimentally measured temperature, OH distribution, and emissions. Subsequently, analyses of other scalar and vector quantities are presented to provide insights to the understanding of the combustion phenomena.

7.3.1 Comparison with temperature measurements

The numerical predictions of temperature are compared against the experimentally measured values in this section. **Figure 7.3** compares the centreline temperatures for the MILD and the ultra-lean cases with the numerical predictions. The maximum temperature is close to 1200 K for both the cases as predicted by all the models. Unlike conventional flames, the temperature increases with axial distance as the flame are stabilized further downstream

Numerical modelling studies

due to high injection velocities and shear near the inlet [38]. For the MILD case, the temperature rise is more gradual as compared to the ultra-lean case. This trend is captured by all models except the RANS-EDC which predicts a delayed rise in temperature. The RANS-EDC model consistently under-predicts the temperature for both the cases, particularly upto 150-mm. The RANS-FGM model again predicts a slightly sharper rise in temperature (~ 30 to 100-mm) as compared to the experimental values, suggesting earlier ignition typical of flamelet-based models. This was also noted by Parisi et al. [121] while simulating the SPRF combustor. However, the FGM model prediction is closer to that of the EDC model as compared to the SF model suggesting that it can incorporate finite-rate chemistry effects. Both the DES-EDC and DES-FGM models predict the centreline temperature profiles with reasonable accuracy, although the DES-EDC model is slightly better than the DES-FGM model. This also suggests that the temperature prediction is more sensitive to the turbulence model (DES or RANS) and mixing near the inlet as compared to the combustion model (EDC or FGM). This is particularly crucial for predictions in the reverse flow (RF) configuration, where the recirculating flow is entrained into the fresh reactants.

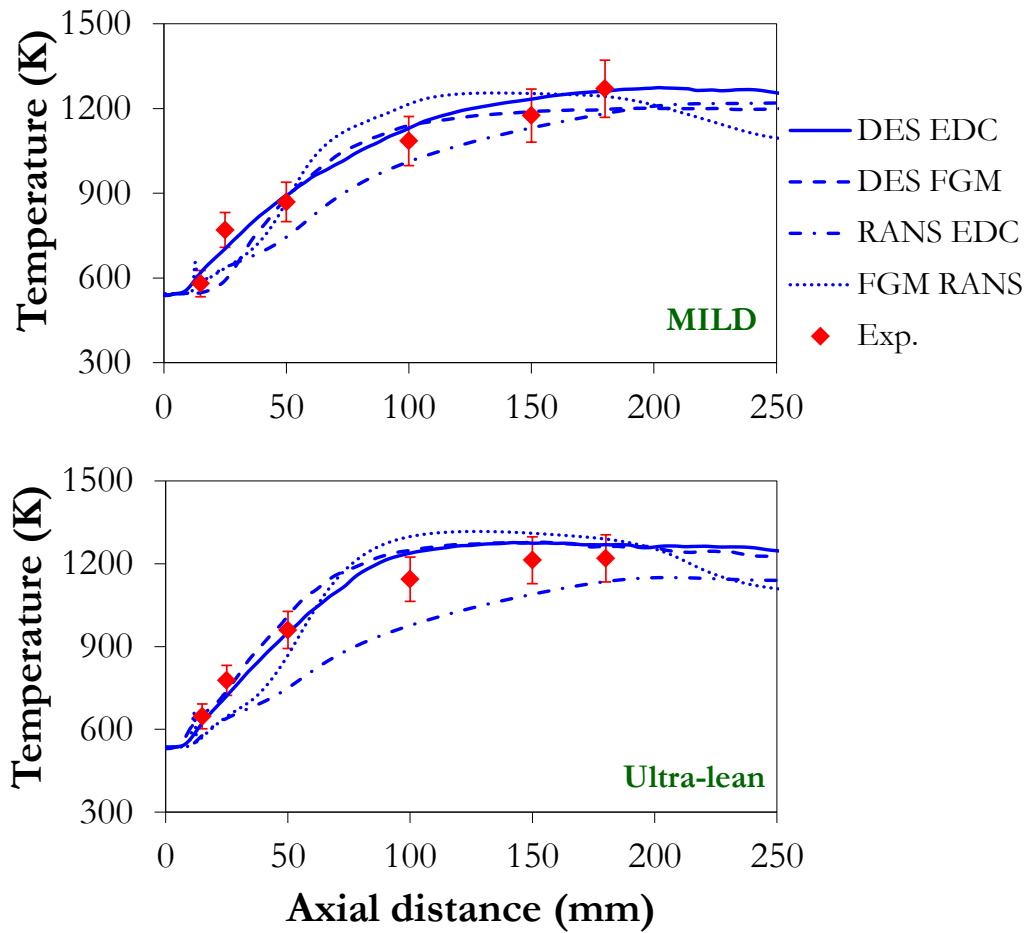


Figure 7.3: Comparison of the experimentally measured mean centerline temperature with the predictions of the numerical simulations for the MILD (top) and ultra-lean (bottom) cases.

Figure 7.4 and **Figure 7.5** compare the temperature predictions in the radial direction with the experimental data at different axial locations for the MILD and the ultra-lean cases, respectively. The temperature increases in the radial direction due to combustion and the entrainment of exhaust gases. As the centerline temperature increases, the radial temperature profiles become more and more uniform. The radial temperature profiles become nearly constant after 150-mm ($z/D_f = 50$) suggesting that the reactions are nearly complete by this

Numerical modelling studies

location in the chamber. For the MILD case, almost all the models are able to capture the radial temperature profiles with minor variations. At 15-mm, the RANS-EDC model over-predicts the temperature while the DES-FGM model under-predicts the temperature. A similar trend is observed at $z = 25$ -mm, although the predictions are within the measurement uncertainties. The RANS-EDC model under-predicts the temperature near the centerline at $z = 50$ and 100-mm as observed in **Figure 7.3**. At $z = 150$ and 180-mm, the temperatures are nearly uniform and all the models predict values close to the experimental measurements. Another point to note is that at $z = 100$ -mm, the temperature gradually increases in the radial direction while the models predict a nearly uniform value except for the RANS-EDC model. This shows a slight discrepancy in the prediction of the unreacted jet penetration by the models. The RANS-EDC model, however, over-predicts the penetration of the unreacted jet core.

For the ultra-lean case, all the models predict the temperatures near the inlet ($z = 15$, 25-mm) with good accuracy, although both the RANS-EDC and RANS-FGM model under-predicts the temperature close to the centerline as observed in **Figure 7.5**. However, similar to the MILD case, the RANS-EDC models consistently under-predicts the temperature at $z = 50$ -mm and further downstream. The predictions of the RANS-FGM, DES-EDC/FGM models are consistent and predict the temperatures with good accuracy throughout the chamber. The differences between the RANS-EDC and RANS-FGM models suggest the presence of two opposite effects which allows the RANS-FGM model to make reasonably accurate predictions. While the RANS model predicts a delay in ignition due to mixing, the FGM model predicts early ignition as observed in the sharper rise in centerline temperature (**Figure 7.3**). These two effects possibly compensate and will be discussed in detail in the subsequent sections.

Numerical modelling studies

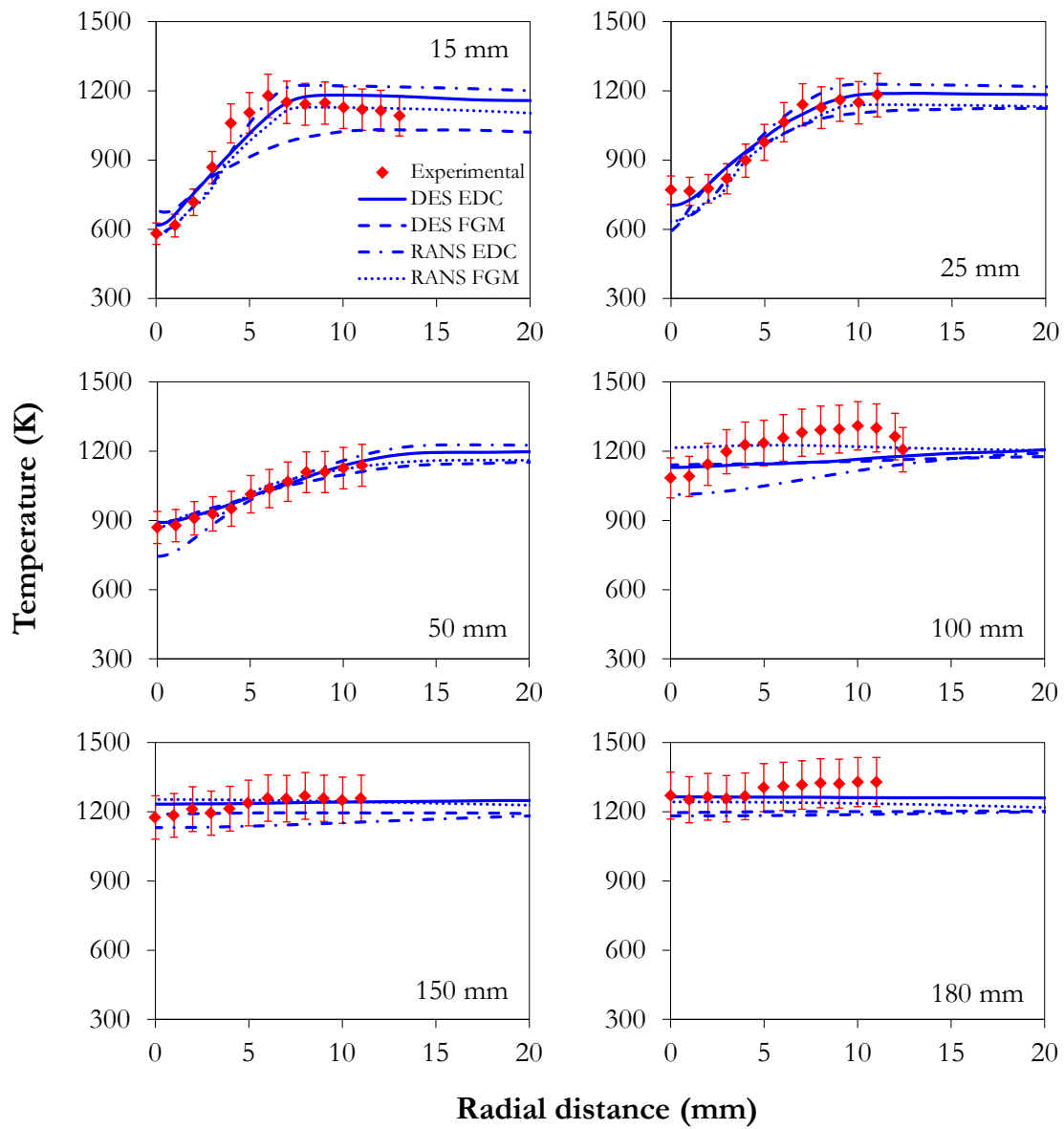


Figure 7.4: Comparison of the experimentally measured mean radial temperature with the predictions of the numerical simulations for the MILD case.

Numerical modelling studies

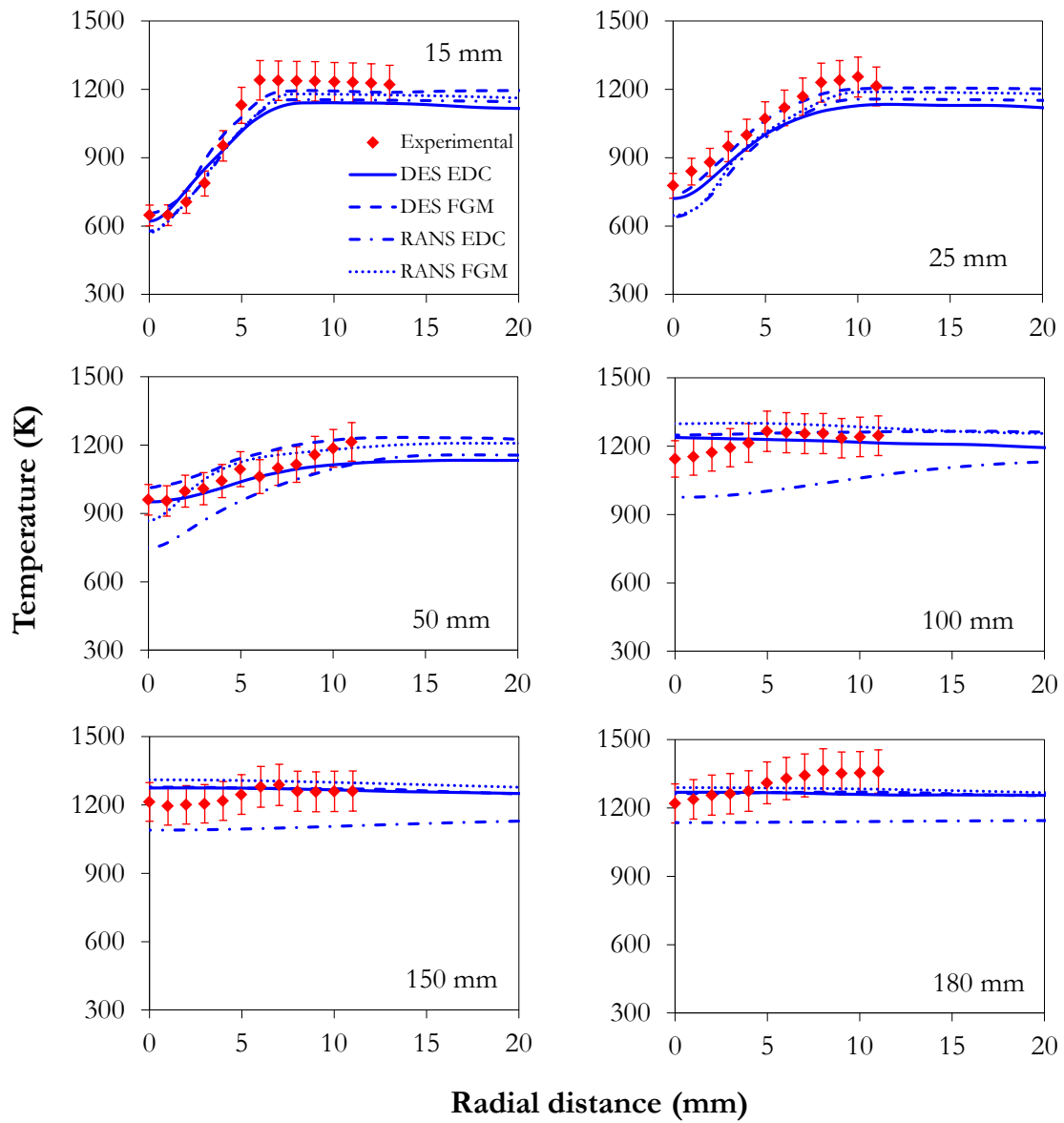


Figure 7.5: Comparison of the experimentally measured mean radial temperature with the predictions of the numerical simulations for the ultra-lean case.

7.3.2 Comparison with OH-PLIF

The instantaneous OH-PLIF images are qualitatively compared with the predictions from the simulations in **Figure 7.6**. The OH-PLIF images have been acquired at 5 axial locations within the chamber. As observed, there is a significant difference between the OH signal for the MILD and the ultra-lean cases. The penetration of the unreacted jet core is shorter for the ultra-lean case as compared to the MILD case and is attributed to the overall decrease in the O₂ percentage. An intense OH signal with thin reaction zones can be observed for the ultra-lean case from 40 - 120-mm, after which the signal sharply decreases. On the contrary, the OH signal for the MILD case is rather distributed with high intensity from 80 - 160-mm that gradually decreases further downstream. However, sharp gradients in OH are observed near the inlet for both the MILD and the ultra-lean cases. When compared with the numerical simulations, the DES-EDC model predicts the qualitative features of the reaction zone with good accuracy for both the cases. The turbulent structures similar to that observed in the instantaneous PLIF images are also observed to be resolved in the simulations. The RANS-EDC model over-predicts the unreacted jet penetration, leading to a delayed ignition and high OH concentration further downstream. This is in line with the centreline temperature predictions as observed in **Figure 7.3** wherein the RANS-EDC models predict a slower rise in the temperature. The FGM models predict the OH location better than the RANS-EDC model, although the flame ignites early. However, the trend of delayed ignition for the MILD case as compared to the ultra-lean case is captured by the FGM model. The structure of the reaction zone predicted by the FGM model is also different from that observed in the OH-PLIF images. The DES-FGM model predicts early ignition in the shear layer and an extended OH layer downstream. The reaction zone also appears highly wrinkled with finer structures resembling flamelets as compared to the PLIF images where the OH

Numerical modelling studies

regions are wider. The RANS-FGM model predicts delayed ignition along the centreline as compared to the DES-FGM model which suggests the compensatory effect between delayed mixing in RANS models and early ignition in flamelet models.

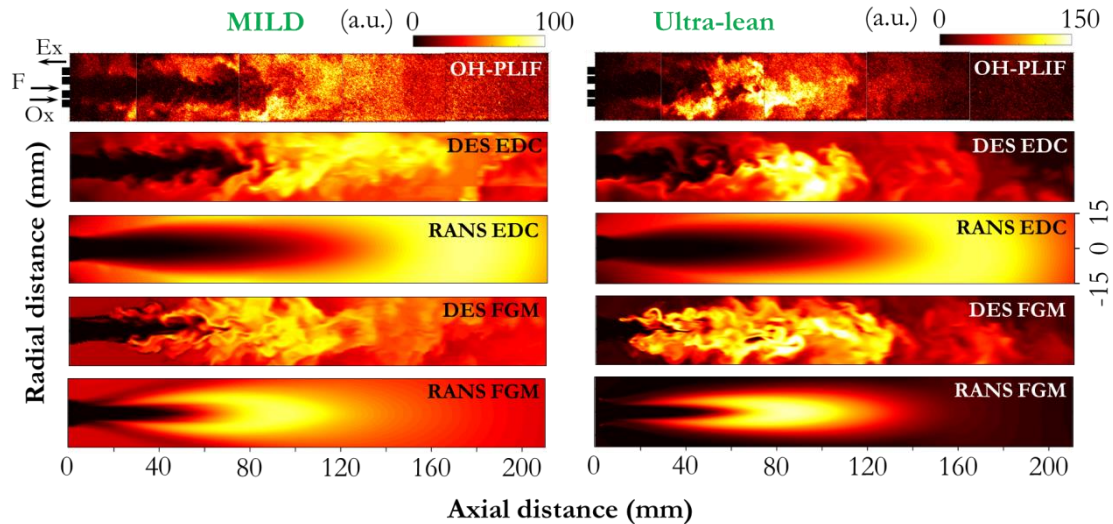


Figure 7.6: Qualitative comparison of the experimentally obtained instantaneous OH-PLIF images with the predictions of the numerical simulations for the MILD and the ultra-lean cases.

The comparison of the normalized OH signal along the centreline with the numerical predictions is shown in **Figure 7.7**. For the ultra-lean case, the OH signal peaks at 100-mm from the inlet, while the maximum is reached at 115-mm for the MILD case. The decay of the OH signal is also faster for the ultra-lean case, suggesting a smaller and more concentrated reaction zone. The normalized intensity reaches 0.2 at 150-mm for the ultra-lean case, while the intensity is 0.4 at 210-mm for the MILD case, showing more uniformity in the distribution. For both the MILD and the ultra-lean cases, the DES-EDC model predicts the flame location with good accuracy. All the other models either over-predict or under-predict the flame location. For the MILD case, the RANS-EDC model over-predicts the peak OH

Numerical modelling studies

location by around 60-mm. This was also observed in the centreline temperature profiles in **Figure 7.3** where delayed ignition was predicted by the RANS-EDC model. Even for the ultra-lean case, the RANS-EDC model over-predicts the peak flame location by around 60-mm. For the MILD case, both the DES-FGM and RANS-FGM model under-predicted the peak OH location by around 15-mm. However, for the ultra-lean case, the DES-FGM model under-predicted the peak OH location while the RANS-FGM model predicted similarly to the DES-EDC model.

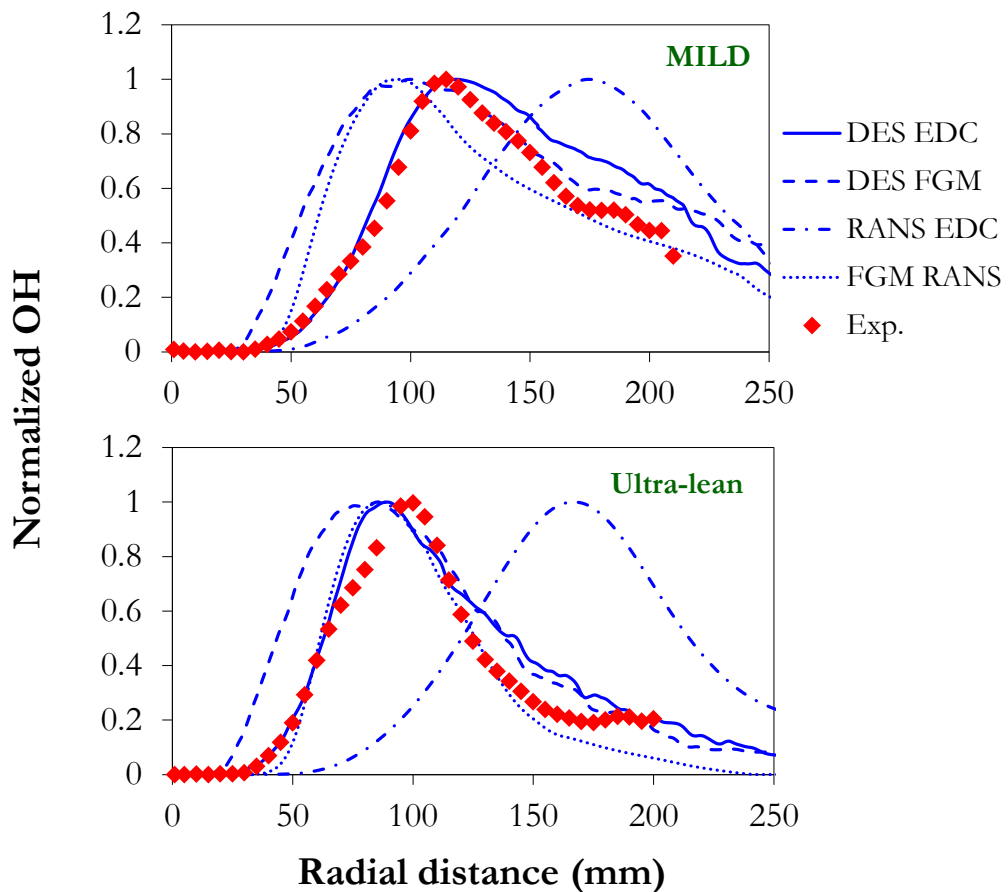


Figure 7.7: Comparison of the experimentally measured mean OH distribution with the predictions of the numerical simulations for the MILD (top) and ultra-lean (bottom) cases.

Numerical modelling studies

The radial variation of the OH intensity is compared with the numerical predictions for the MILD case in **Figure 7.8**. At $z = 25$ -mm, the DES-EDC model captures the OH distribution most accurately. While the RANS-EDC model prediction is also similar to the DES-EDC model, the FGM models predict an earlier peak in the OH intensity with radius. Similar trends are observed at $z = 50$ and 75 -mm. While the FGM models capture the shift in the OH peak in the radial direction with increasing axial distance, the locations are still under-predicted by around 7-mm. At $z = 75$ -mm, the FGM models predict the peak close to the centerline as was also observed in the centerline plots in **Figure 7.7**. Even at $z = 100$ -mm, the OH intensity increases radially, while the DES-EDC model predicts slightly early ignition as the signal is radially decreasing. Beyond $z = 100$ -mm, the signal is nearly uniform and is captured by all the models except RANS-EDC due to its delayed ignition. Overall, the DES-EDC model captures the radial variation of OH for the MILD case with maximum accuracy.

For the ultra-lean case, trends similar to those for the MILD case are observed in **Figure 7.9**. At $z = 25$ -mm, the DES-EDC model predicts the OH distribution most accurately, followed by the RANS-EDC, DES-FGM, and RANS-FGM. At $z = 50$ -mm, although it appears that RANS-EDC model provides improved predictions, it is mostly due to the delayed ignition. By $z = 100$ -mm, the mixture ignites at the centerline while the OH is mostly restricted to the shear layers at the upstream locations. The rapid decrease of the OH intensity with radius at $z = 100$ -mm shows that the reaction zone is more narrow and concentrated as compared to the MILD case. Similar to the MILD case, the profiles at $z = 150$ -mm and 180 -mm are nearly uniform and are predicted accurately by all models except RANS-FGM. Overall, the DES-EDC model predicts the OH profiles most accurately as compared to the other models. It must also be noted that the DES-EDC model is computationally the most expensive among all the models used.

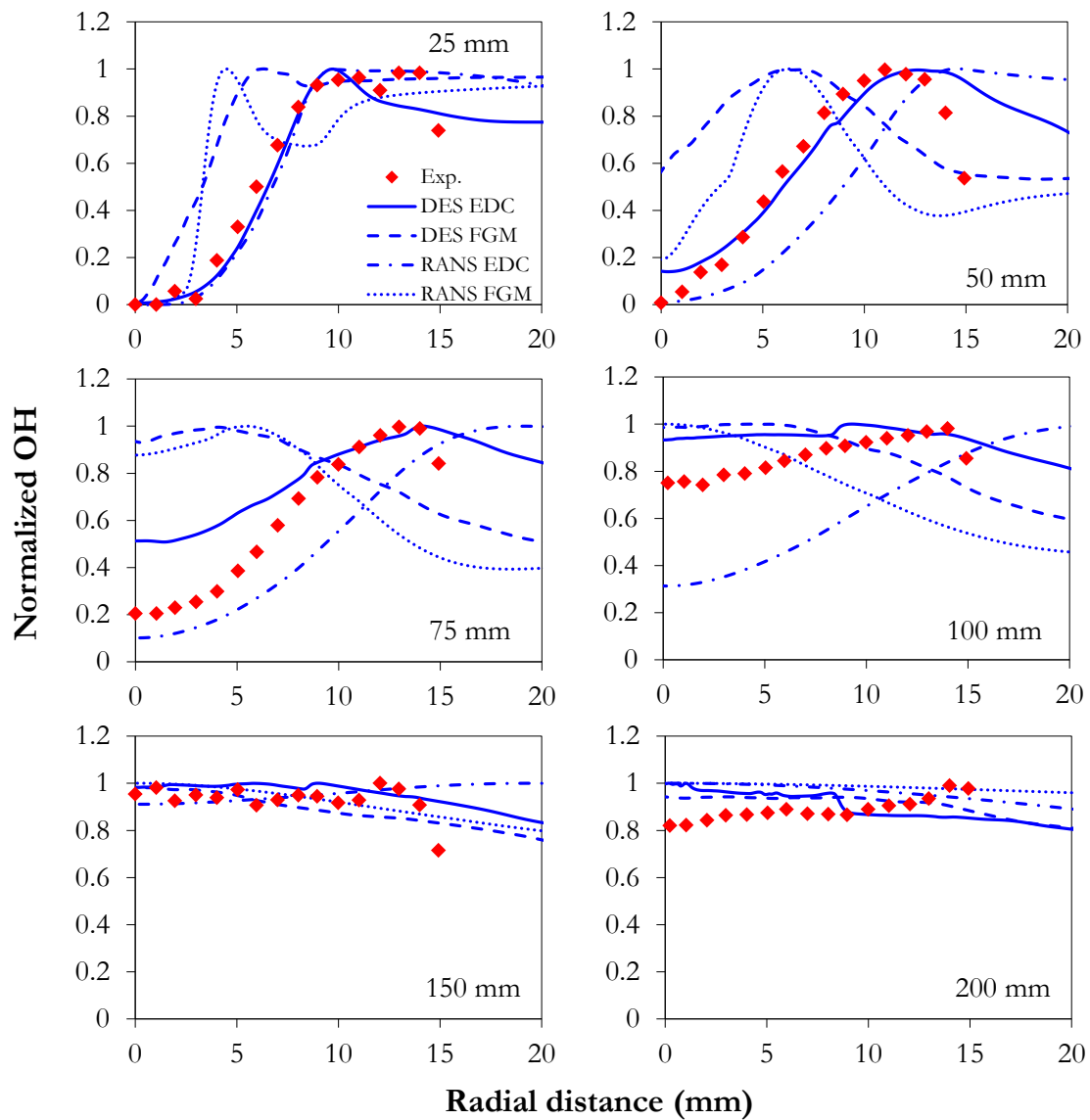


Figure 7.8: Comparison of the experimentally measured mean OH distribution with the predictions of the numerical simulations for the MILD case.

Numerical modelling studies

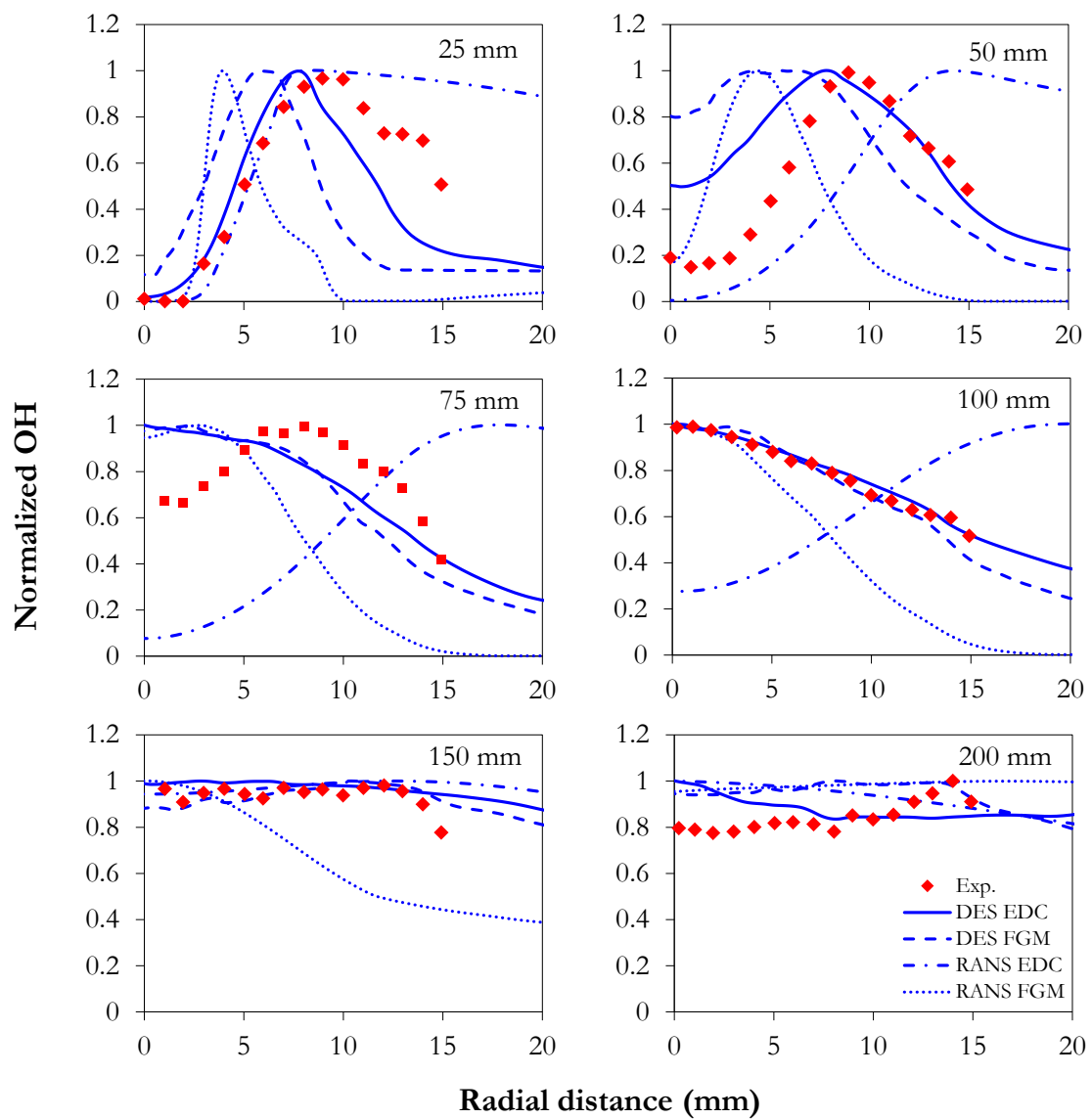


Figure 7.9: Comparison of the experimentally measured mean OH distribution with the predictions of the numerical simulations for the ultra-lean case.

Numerical modelling studies

Finally, the quantified OH volume fraction (ppm) is compared with the numerically predicted values in **Figure 7.10**. As mentioned earlier in **Chapter 5**, the OH-PLIF data is quantified using a standard McKenna flat flame as the calibration source [108]. As observed in **Figure 7.10**, there is significant variation in the peak OH concentration predicted by various models. All the models, however, predict a lower peak OH for the MILD case as compared to the ultra-lean case which is in agreement with experimental observations. The DES models also predict a lower peak OH concentration as compared to the FGM models both for the MILD and the ultra-lean cases and are closer to experimental observations. For the MILD case, the predictions by the DES-FGM and RANS-FGM models are similar with a peak OH ppm value of around 780. In contrast, the RANS-EDC model predicts a peak OH ppm value of 568-ppm. The DES-EDC model prediction is nearest to the experimentally obtained values with a peak OH ppm value of 496-ppm.

For the ultra-lean case, the RANS-FGM model predicts a peak OH ppm value of around 2000-ppm which is more than twice the experimentally obtained value. The decrease in OH concentration after the peak is sharper for RANS-FGM and matches with the experimental values at 150-mm and 180-mm. The DES-FGM model predicts a lower peak of 1581-ppm which is still significantly higher than the experimental value. The RANS-EDC model, however, predicts a lower peak as compared to the data. This can be attributed to the under-prediction of temperature by the model as OH concentration is highly sensitive to the temperature. As in the MILD case, the DES-EDC model predictions are nearest to the experimentally measured values.

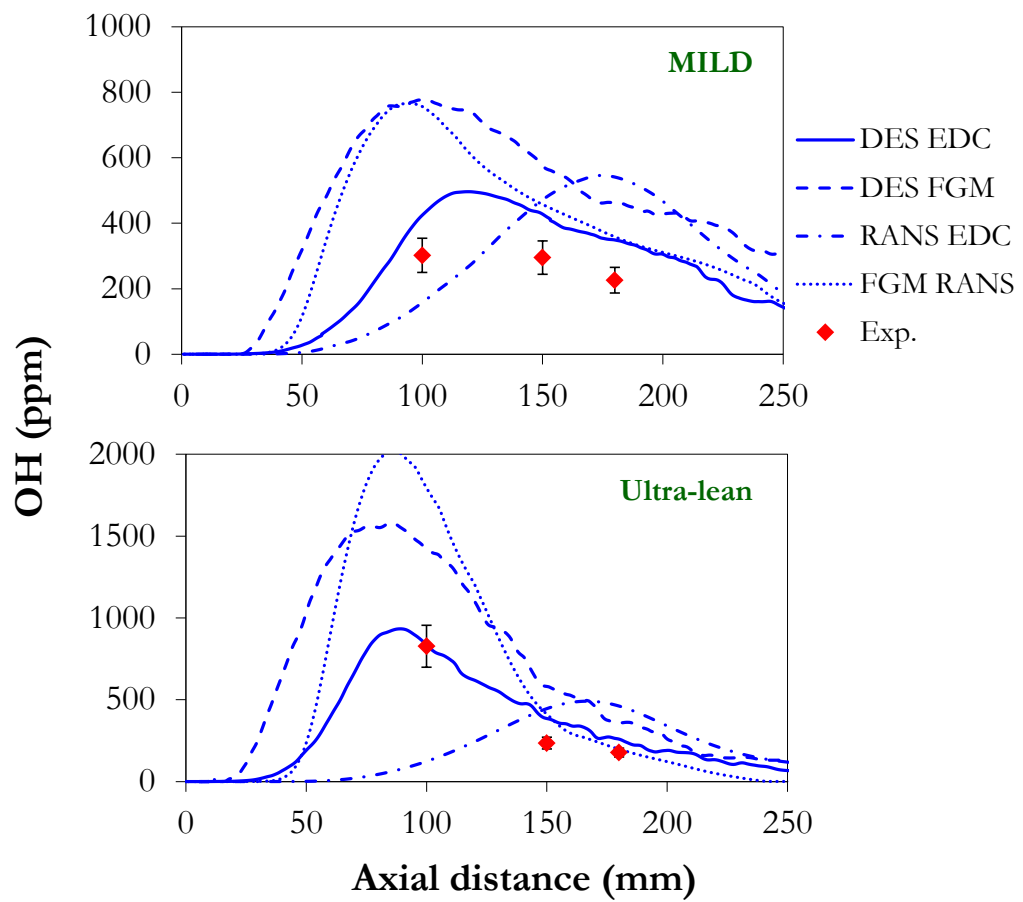


Figure 7.10: Comparison of the experimentally measured mean OH volume fraction (ppm) with the predictions of the numerical simulations for the MILD (top) and ultra-lean (bottom) cases.

7.3.3 Comparison with measured CO emissions

Finally, the predicted CO emissions are compared with the experimentally measured values in **Figure 7.11**. The CO ppm values are absolute and have not been normalized to a specified level of O₂ due to similar inlet conditions. For the MILD case, the DES-EDC model predicts 807-ppm as compared to the experimentally measured value of 706-ppm. All the other models over-predict the CO emissions by more than 450-ppm. The RANS-EDC model predicts 1189-ppm, while the DES-FGM and RANS-FGM models predict 1570 and 1388-ppm, respectively. For the ultra-lean case, the models mostly under-predict the CO emission except for the RANS-EDC model. The DES-EDC model predicts 238-ppm as compared to the experimentally measured value of 541-ppm. The DES-FGM and RANS-FGM models predict 287 and 125-ppm, respectively. However, the RANS-EDC model predicts 1622-ppm which is significantly higher than all the other predictions. It must be noted that the RANS-EDC model consistently under-predicts the measured temperature, which is a possible explanation for this discrepancy as CO emissions are highly sensitive to the chamber temperature. This was noted in **Chapter 6**, where the CO emissions were observed to be highly sensitive to the chamber temperature. Overall, the DES-EDC model predicts the CO emissions most accurately for the MILD case, while its prediction is similar to the DES-FGM model for the ultra-lean case. Thus, hybrid RANS/LES model with EDC is able to predict the experimental data with reasonable accuracy and at a lower computational cost as compared to LES models.

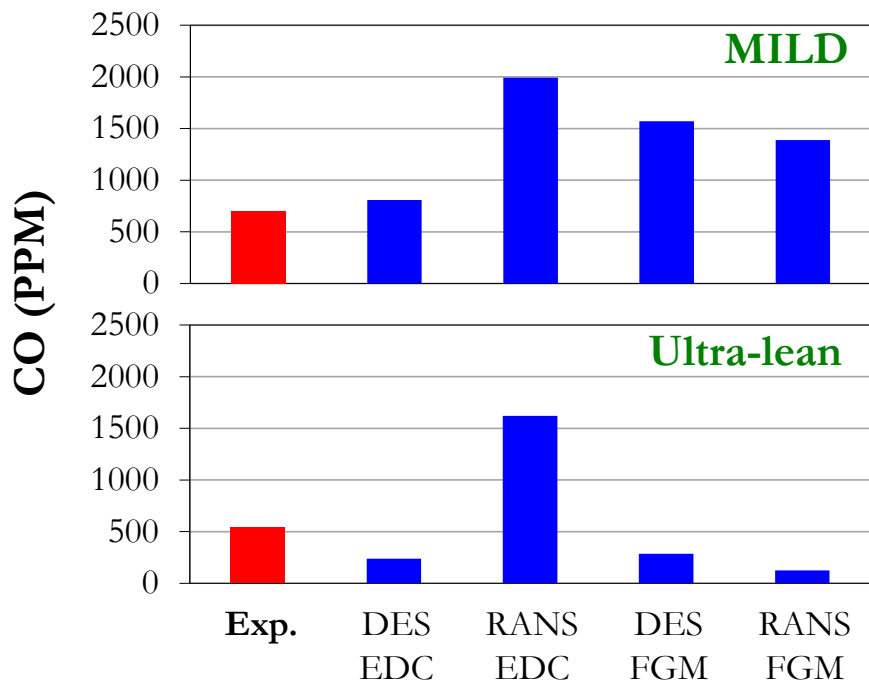


Figure 7.11: Comparison of the experimentally measured CO emissions with the numerically predicted values for the MILD (top) and the ultra-lean (bottom) cases.

7.3.4 Mean velocity

The mean flow streamlines superimposed over the mean axial velocity contours for the MILD case obtained from DES-EDC simulation are shown in **Figure 7.12**. This figure shows the general flow pattern in the reverse flow (RF) configuration. The inlet velocities at the centreline for the fuel jet are as high as 240 m/s. The oxidizer jet surrounding the fuel jet is forced radially inward towards the centreline by the returning exhaust. The axial velocities decrease monotonically with axial distance and become close to zero upstream of the stagnation plane. The flow then traverses radially outward and reverses in direction before reaching the stagnation plane. The velocity of the returning flow is as high as 20 m/s at the

Numerical modelling studies

point of maximum width of the central jet. The radial diffusion of the jet axial momentum increases with axial distance, confining the returning flow close to the cylindrical walls. However, the returning velocity of -40 m/s is highest in the exhaust manifold. Overall, the streamlines clearly show the formation of a toroidal recirculation zone inside the cylindrical chamber formed due to the presence of the forward stagnation plane. The streamlines also show the entrainment of the returning flow into the incoming fresh reactants. This increases the residence time while vitiating the fresh reactants that help in stabilizing the flame under MILD (ultra-diluted) and ultra-lean conditions. The residence time under the present conditions is estimated to be around 130-ms, which can be attributed mostly to the reverse flow. This is an order of magnitude higher than typical forward-flow combustion chambers of the same volume. From the velocity and the streamlines, it is clear that the shear and the corresponding entrainment can be increased by reducing the confinement diameter or by increasing the inlet velocities [39].

The variation in the axial velocity predicted by the different models is studied to investigate the difference in the location of the reaction zones as observed in **Figure 7.6** to **Figure 7.10**. The variation of the centerline axial velocity with axial distance is shown in **Figure 7.12(b-c)**. The velocities predicted by the models nearly overlap and decay monotonically with axial distance, although the RANS models predict higher velocity by up to 25 m/s. A higher axial velocity is expected to cause a downstream shift in the location of the reaction zone as was observed for the RANS-EDC case. The axial penetration of the jet is slightly higher for the MILD case as compared to that for the ultra-lean case. The DES models show that the trailing edge of the jet close to the stagnation plane undergoes higher lateral movement for the ultra-lean case as compared to the MILD case leading to a lower jet penetration. This possibly is a reason for the higher sound pressure level (SPL) and increase

Numerical modelling studies

in the amplitudes for the resonant modes of the chamber observed in experiments for the ultra-lean case.

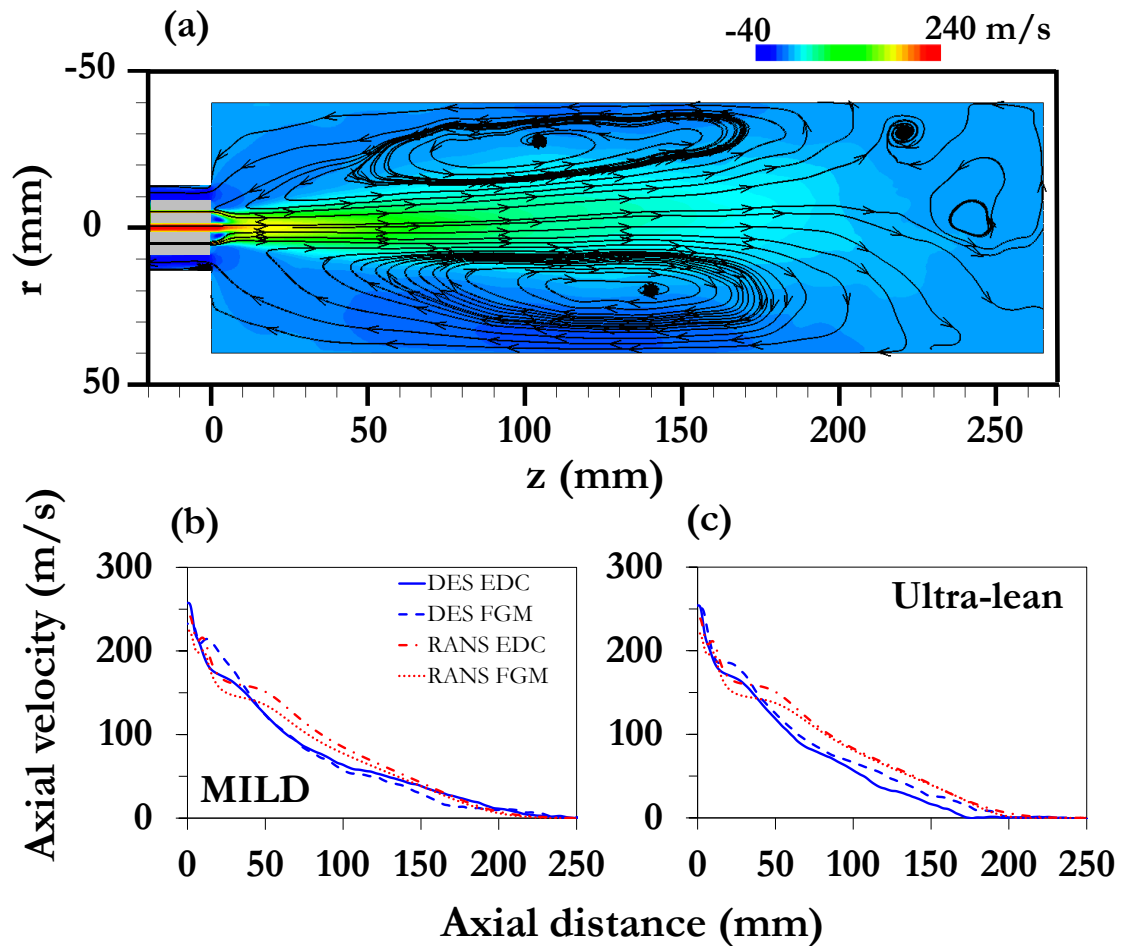


Figure 7.12: (a) Streamlines superimposed over the mean axial velocity for the MILD case obtained from DES-EDC simulation. Variation of axial velocity along the centerline with axial distance for the (b) MILD and the (c) ultra-lean cases.

7.3.5 Mixing between the oxidizer and the exhaust in the outer shear layer

The variation of the recirculation ratio (R) with axial distance for the MILD and the ultra-lean cases as predicted by the models is shown in **Figure 7.13**. The entrainment occurs in the outer shear layer between the oxidizer stream and the returning exhaust. A higher entrainment will lead to an early rise in temperature and can possibly explain the differences in the predictions of temperature and OH.

Figure 7.13 shows that the peak values of R are similar and lie in the range of 2 - 2.5. However, the axial profiles of R are significantly different between the DES-EDC and RANS-EDC cases. The R increases early for the DES-EDC case as compared to the RANS-EDC case both for the MILD and the ultra-lean cases. This implies earlier entrainment of hot exhaust gases and diluents into the oxidizer stream for the DES-EDC case, leading to the rise in temperature as observed in **Figure 7.3**. Although the peak value of R by the RANS-EDC model is higher, it is lower than that for the DES-EDC model upto around 75-mm for the MILD case. For the ultra-lean case also, the value of R for the DES-EDC case exceeds that for the RANS-EDC case upto 60-mm of the chamber. The entrainment of diluents can also delay the ignition, although the major diluents profiles along the centerline do not show significant variation. Although the RANS-EDC models predict a higher peak R , they also predict a delayed entrainment of the exhaust gases, leading to a delayed rise in the temperature and ignition. However, the FGM models do not show this trend as they predict consistent early ignition when compared with experimental data.

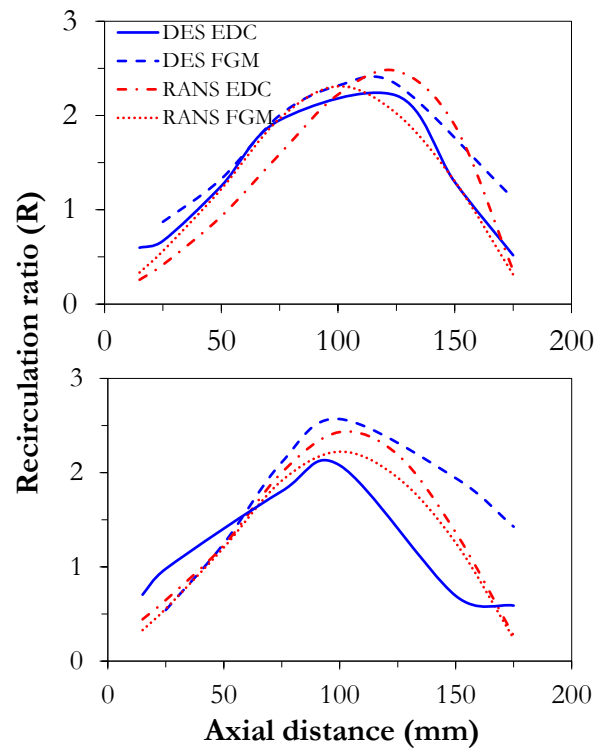


Figure 7.13: Variation of the recirculation ratio (R) with axial distance for the MILD and the ultra-lean cases.

7.3.6 Mixing between the fuel and oxidizer in the inner shear layer

Next, the mixing between the fuel and oxidizer streams in the inner shear layer is studied using the mixture fraction (f) as shown in **Figure 7.14**. The mixture fraction (f) denotes the mass fraction of the total mixture that has originated in the fuel stream and varies from 0 to 1 between the oxidizer and the fuel streams. The delay in the mixing between the fuel and the oxidizer streams can also lead to the differences observed. For the MILD case, the stoichiometric mixture fraction (f_{st}) is close to the actual mixture fraction at $z = 75$ -mm suggesting that the overall mixture is close to stoichiometric ($\Phi_{global} = 0.89$). However, for the

Numerical modelling studies

ultra-lean case, the overall mixture is lean as the f_{st} is greater than the actual mixture fraction at $z = 75$ -mm. From the figures, it is observed that the DES-EDC model causes more uniform and early mixing between the fuel and the oxidizer streams leading to a lower f along the centreline. Even in the oxidizer side, the value of f is higher suggesting greater mixing between the fuel and the oxidizer. This trend is observed both for the MILD and the ultra-lean cases upto 75-mm after which the profiles of f are nearly uniform. The RANS-EDC model, however, predicts reduced mixing between the fuel and the oxidizer streams as compared to the DES-EDC model. The value of f is higher along the centreline for the RANS-EDC model, while it is lower in the oxidizer side. It must be noted here that the turbulent viscosity ratio (μ_t/μ) defined as the ratio of the turbulent to molecular viscosity is one order of magnitude lower for the DES case as compared to the RANS case. Such low effective viscosity leads to the formation of finer turbulent structures that lead to more effective mixing. Thus, the delayed mixing between the fuel and the oxidizer streams between the RANS-EDC and DES-EDC models, coupled with the high velocity predicted by the RANS model can explain the differences in the predictions along the centreline. The lower rate of mixing will also lead to a more gradual rise in temperature and delayed ignition. However, mixing in the inner shear layer alone does not explain the observed differences between the FGM and the EDC models. The DES-FGM model shows a higher value of f (around 1) for the MILD case at $z = 15$ -mm as compared to the DES-EDC model although the ignition is earlier. Similar observations can be made for the RANS-FGM model where the OH peaks earlier although the value of f is higher along the centreline. Thus it appears that there are significant differences between the combustion models that lead to earlier ignition for the FGM model as compared to the EDC model. These differences in the predictions cannot be explained based on fluid dynamic considerations (DES/RANS) alone and will be discussed in more detail in the next section.

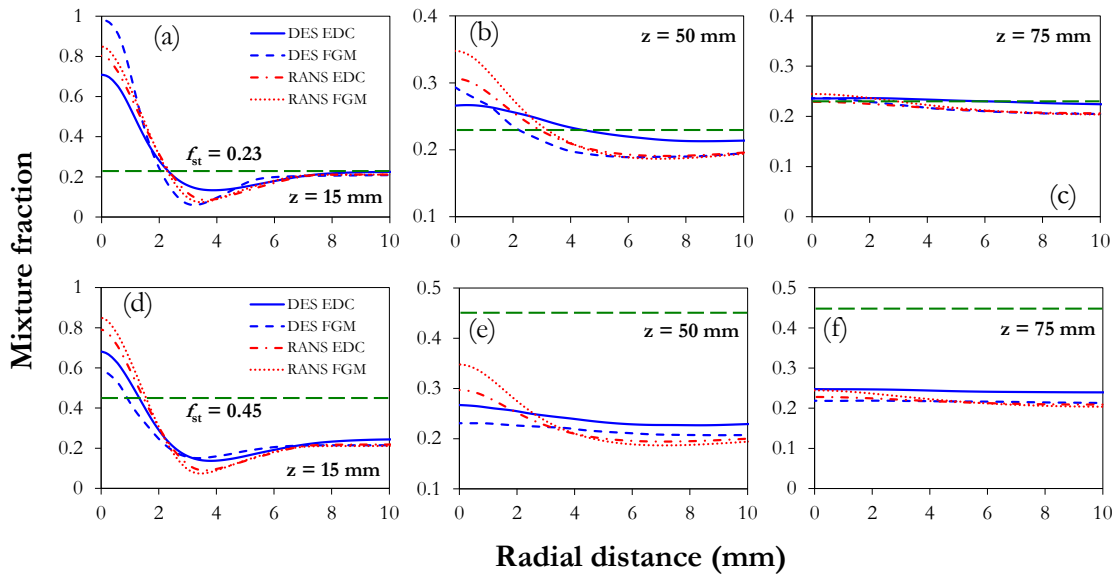


Figure 7.14: Variation of the mean mixture fraction with radial distance for the MILD (top) and the ultra-lean (bottom) cases. The green dashed line shows the stoichiometric mixture fraction for the two cases.

7.3.7 Early ignition in FGM models

To understand the differences in the OH predictions between the EDC and the FGM models, the isoline for the stoichiometric mixture fraction (f_{st}) are superimposed onto the contours of instantaneous OH mole fraction (X_{OH}) and temperature (T) for the MILD and the ultra-lean cases as observed in **Figure 7.15**. The value of f_{st} for the MILD and the ultra-lean cases are 0.23 and 0.45, respectively. At the inlet, the f_{st} isoline lies between the fuel and the oxidizer streams and there is no ignition as is evident from the absence of OH radical. At downstream locations, it is observed that the regions of OH gradient conform to the f_{st} line fully for the FGM but only partially for the EDC model. This is more evident in the ultra-lean case where clear distinctions can be made between the predictions of the EDC and the FGM models. It thus appears that the FGM model ignites very close to the f_{st} line, while the EDC

Numerical modelling studies

model does not strictly conform to this line. This also leads to early ignition in the DES-FGM model as compared to the DES-EDC model.

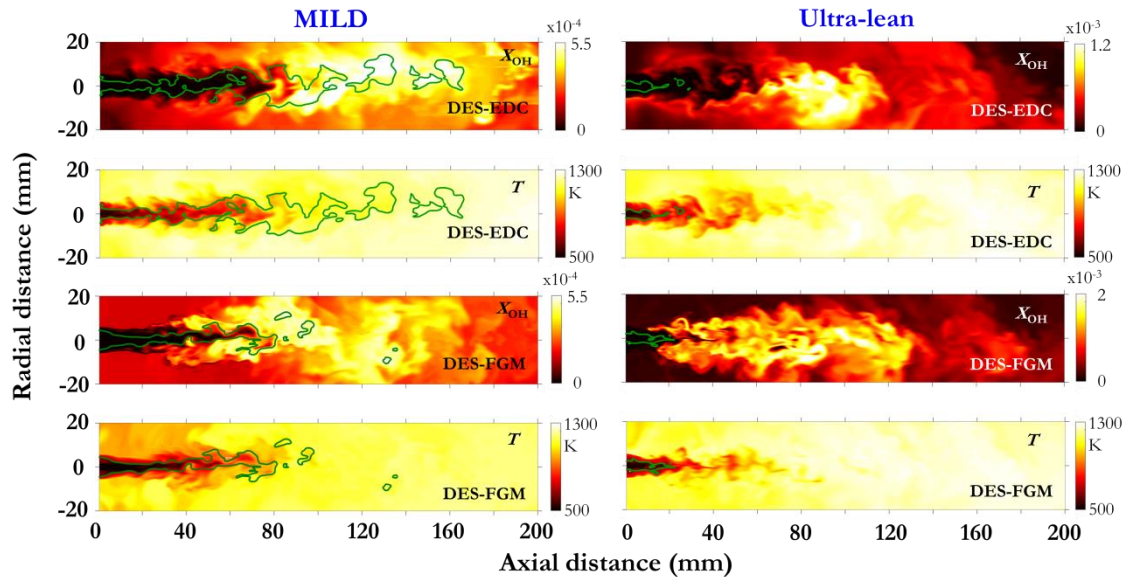


Figure 7.15: Contours of predicted OH mole fraction (X_{OH}) and temperatures (T) for the MILD and ultra-lean cases. The green line represents instantaneous isoline for the stoichiometric mixture fraction (f_{st}). The f_{st} for the MILD and the ultra-lean cases are 0.23 and 0.45, respectively.

The reason for the early ignition predicted by the FGM model is analyzed next. The number of chemical degrees of freedom (number of independent progress variables) required to model the thermochemical states is an important parameter. For simple fuels such as CO/H₂ mixtures, a single progress variable is reported to be sufficient [122]. Other studies on methane using the FGM model [123][124] have also used a single progress variable to define the thermochemistry. Hence, in the present study, we have also used a single progress variable that is deemed sufficient.

Numerical modelling studies

In the current configuration, the flamelet table is generated for a diffusion flame to represent the thermochemistry as the inlet to the chamber is non-premixed. Diffusion flamelets perform better in cases where the combustion is predominantly non-premixed. Vreman et al. [125] have shown that non-premixed flamelets predict CO and H₂ concentrations better as compared to premixed flamelets for the simulation of piloted partially premixed flames of CH₄ and air (Sandia flames D and F). While the inlet is non-premixed, the combustion in the reverse flow (RF) system is different from purely non-premixed systems due to the strong mixing between the fuel, the oxidizer, and the exhaust streams. This was also observed by Bobba et al. [19] who reported similarities in the performance of the SPRF combustor with both premixed and non-premixed injections. This could be a source of discrepancy between the measured and predicted results.

Only steady flamelets are considered in the current simulation which is another simplification in the present model. The states between the unburnt reactants and the progress variable at extinction are obtained from the final extinguishing flamelet using interpolation. The flame stabilization in the current RF system is, however, dominated by autoignition both for the MILD and the ultra-lean cases as stated in **Chapter 4**. Autoignition is an unsteady phenomenon and has been noted to be the predominant mode of stabilization in jet in hot coflow studies representing MILD conditions [55]. It must also be noted that autoignition occurs along surfaces of the most reactive mixture fraction (f_{MR}) defined as the location with the shortest autoignition time and is different from the f_{st} surface [126]. Steady diffusion flamelets, however, react close to the stoichiometric surface where the maximum reaction rates, temperatures and concentration of intermediate radicals such as OH can be observed.

Finally, the definition of the progress variable is not unique for these systems and the choice relies on a fair degree of experience. No suitable definition of the progress variable is

Numerical modelling studies

currently available in the literature that can capture these autoigniting systems due to the presence of a large number of stages of combustion such as pre-ignition, autoignition, and oxidation. Several definitions of progress variable have been used in earlier studies [118][127] to capture the reaction variables with varying degree of success and is a continuing field of research. Other approaches such as the flamelet/progress variable (FPV) by Ihme et al. [66][67] include the introduction of another conserved scalar to account for the dilution between the fuel and the oxidizer streams and is beyond the scope of the current work. Also, the present formulation defines the progress variable based on H₂O mass fraction. To quantitatively distinguish the difference, we extract the progress variable from the EDC simulation by post-processing the species distribution as shown in **Figure 7.16**. The results show that the progress variable predictions are significantly different for the FGM and the EDC cases. These results are observed to corroborate with the observed differences in the OH predictions. The FGM model ignites earlier than the EDC model as can be observed from the progress variable profiles. However, the axial expanse of the reaction zone is longer for the FGM model as compared to the EDC model which reaches $c = 1$ much earlier. This also shows that a better progress variable prediction that may include a more comprehensive definition for the same is necessary for improved predictions.

The EDC model addresses these issues by solving transport equations for all the species, although at a higher computational cost. The RANS models predict delayed mixing and are unable to capture the unsteady phenomenon of autoignition. The reasonable prediction by the RANS-FGM model is also fortuitous due to the compensatory effects of the delayed mixing by the RANS model and early ignition by the FGM model.

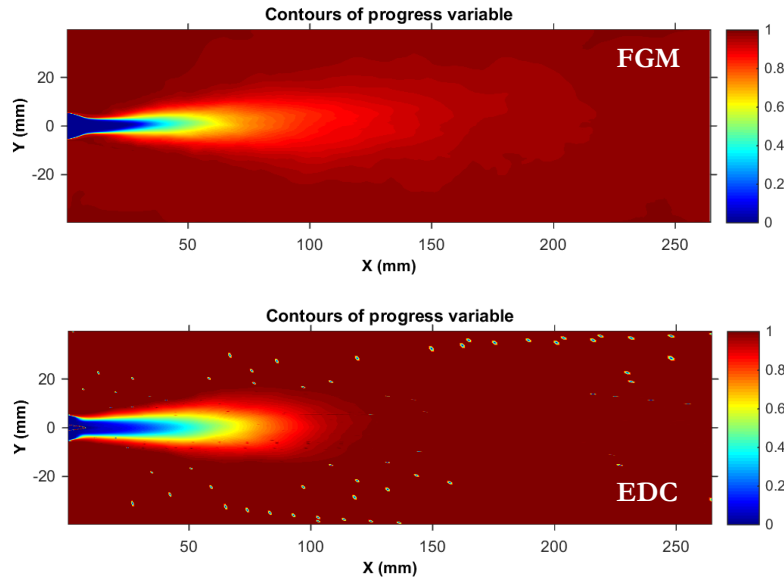


Figure 7.16: Contours of predicted time-averaged progress variable for the FGM and the EDC cases under MILD conditions.

7.4 Summary

The present chapter numerically investigates combustion of low calorific value syngas (20% H₂, 20% CO, 60% N₂, 4.6 MJ/m³) in a 3.3 kW reverse flow chamber under MILD ($\Phi_{\text{global}} = 0.89$) and ultra-lean ($\Phi_{\text{global}} = 0.32$) conditions. The flow streamlines show the establishment of a toroidal vortical structure within the chamber that causes the recirculating exhaust to entrain into the fresh reactants. The RANS/DES and FGM/EDC model predictions are compared with the temperature, OH, and emissions measurements performed in the chamber. Special focus has been directed to the prediction of the OH radical concentration and its spatial distribution which is critical in predicting the reaction zone under MILD conditions. The differences in the predictions have been explained based on the capability of the models to predict mixing, ignition, and heat release. Overall, the DES-EDC model performs the best, particularly in capturing the temperature and the OH distribution. The

Numerical modelling studies

RANS-EDC model predicts the location of the reaction zone downstream due to higher centreline velocity and slower mixing near the inlet. While the peak recirculation ratio (R) varied between 2 - 2.5 for all the models, the profile of R was found to be more important in determining the near-nozzle mixing and the location of the reaction zone. The FGM models ignite early as is evident from the OH distributions, while the temperature rises faster near the inlet. The DES-FGM model predicts ignition very close to the stoichiometric isosurfaces and highlights the necessity of defining a more comprehensive progress variable. The RANS-FGM model, however, predicts the location of the reaction zone more accurately as compared to the DES-FGM model rather fortuitously due to the compensatory effects of delayed mixing by the RANS models and early ignition by the FGM model.

Chapter 8

Scaling of the combustor

In the present chapter, a validated CFD model is used to scale the experimental 3.3-kW reverse flow combustion chamber upto 25-kW operating on syngas under MILD conditions. Although 25-kW is lower than typical industrial requirements which can range from 100-kW to 1-MW, the results are applicable to scaling of combustion chambers in general and reverse flow chambers in particular. This chapter presents results of studies evaluating the performance of four different scaling criteria in capturing the fluid dynamic, thermal, and kinetic similarities between the lab-scale and scaled-up combustors. The scaling criteria investigated are: constant velocity (CV), constant residence time (CRT), and two other novel scaling approaches proposed in this work, namely, constant volume to jet momentum ratio (CM), and constant volume to jet kinetic energy ratio (CK). The next few sections present the mathematical formulation of the scaling approaches, followed by numerical formulation, results and discussions, and a summary of the key findings.

8.1 Scaling criteria

This section briefly describes the mathematical formulation for the various scaling approaches used in the present study and closely follows a similar development reported elsewhere [85][90]. The total thermal input into a given burner is denoted by:

$$Q = \dot{m}_F H = K \rho U_o D_o^2 \quad (8.1)$$

Scaling of the combustor

where Q is the thermal input, \dot{m}_F is the fuel mass flow rate, H is the heating value, ρ is the density, U_o is the velocity, D_o is the injector diameter, and K is a constant. From here on, the subscripts 1 and 2 denote the baseline case and the scaled-up versions, respectively.

8.1.1 Constant velocity

In the constant velocity approach, the inlet velocities are maintained constant which results in the following scaling laws for the burner dimensions and velocities:

$$\frac{D_2}{D_1} = \left(\frac{Q_2}{Q_1}\right)^{1/2} \quad (8.2)$$

$$\frac{U_2}{U_1} = \text{constant} \quad (8.3)$$

Here, U and D are characteristic velocity and dimension, respectively, of the burner.

8.1.2 Constant residence time

In the constant residence time approach, the large macro-mixing timescale which is proportional to the ratio of the characteristic dimension and velocity is held constant.

$$\tau_{mixing} \propto \frac{D_o}{U_o} = \text{constant} \quad (8.4)$$

This gives rise to the following scaling exponents for dimensions and velocities:

$$\frac{D_2}{D_1} = \left(\frac{Q_2}{Q_1}\right)^{1/3} \quad (8.5)$$

$$\frac{U_2}{U_1} = \left(\frac{Q_2}{Q_1}\right)^{1/3} \quad (8.6)$$

However, Kumar et al. [90] noted several limitations of the CV and CRT approaches in terms of mixing and pressure drop, although they need to be verified for a reverse flow chamber. In an effort to develop newer scaling criteria, several physical insights from MILD

Scaling of the combustor

combustion can be incorporated. First, the inlet velocities in MILD combustion chambers are maintained high (~ 100 m/s) to improve mixing and the entrainment of the exhaust gases. Scaling a laboratory-scale MILD combustion chamber using the CRT criterion leads to prohibitively high inlet velocities ($U \sim Q^{1/3}$) and pressure drop. This had also led Kumar et al. [90] to limit their inlet velocities at 100 m/s while the injector arrangement was reconfigured to enhance mixing. A lower scaling exponent for velocity is thus desirable in any new scaling criterion. Second, MILD combustion is characterized by intense recirculation of the exhaust gases, which increases with distance from the injection plane. From Han and Mungal [17], the recirculation ratio in the momentum driven region of a non-reacting turbulent jet can be described as:

$$R = \frac{\dot{m}_{rec}}{\dot{m}_o} = C_e \left[\frac{x}{d^*} \right] \propto \frac{L_o}{D_o} \quad (8.7)$$

where, L_o and D_o are characteristic dimensions of the chamber and the burner. Here, x is the axial distance and d^* is the equivalent source diameter. To maintain a constant recirculation ratio (R), the injector dimension and the chamber dimension must be proportional. This condition is implicitly satisfied in the CV and CRT scaling criteria [90]. Finally, MILD combustion is a volumetric mode of combustion with distributed heat release and intense recirculation of exhaust gases, as noted in several earlier studies [30]-[34]. The chamber geometry and volume play a key role in directing the exhaust into the fresh reactants while controlling the residence time and thermal intensity. This is particularly relevant in the reverse flow configuration [38][40], where the flow turns 180° and is entrained into the incoming fresh reactants before exiting the chamber. Improper sizing of the reverse flow chamber can also form unused dead volume near the forward stagnation plane that increases material costs and decreases thermal intensity. From these physical insights, two additional

Scaling of the combustor

scaling methods are proposed that relate the injection parameters with the characteristic dimension (L_o) which governs the chamber volume and the recirculation ratio.

8.1.3 Constant volume to jet momentum ratio (CM)

In this scaling method, the ratio of the chamber volume to the incoming jet momentum is kept constant such that:

$$\frac{L_o^3}{U_o^2 D_o^2} = constant \quad (8.8)$$

In addition, if we maintain the criterion for constant recirculation ratio ($L_o \propto D_o$) as discussed earlier, this gives rise to the following scaling rules:

$$\frac{D_2}{D_1} = \left(\frac{Q_2}{Q_1}\right)^{2/5} \quad (8.9)$$

$$\frac{U_2}{U_1} = \left(\frac{Q_2}{Q_1}\right)^{1/5} \quad (8.10)$$

8.1.4 Constant volume to jet kinetic energy ratio (CK)

In this scaling method, the ratio of the chamber volume to the incoming jet kinetic energy is kept constant such that:

$$\frac{L_o^3}{U_o^3 D_o^2} = constant \quad (8.11)$$

This, when coupled with the criterion for constant recirculation ratio ($L_o \propto D_o$) gives rise to the following scaling rules:

$$\frac{D_2}{D_1} = \left(\frac{Q_2}{Q_1}\right)^{3/7} \quad (8.12)$$

Scaling of the combustor

$$\frac{U_2}{U_1} = \left(\frac{Q_2}{Q_1}\right)^{1/7} \quad (8.13)$$

Although the CM and CK scaling methods are derived from phenomenological arguments, it can be clearly seen that the velocity scaling exponent is lower than that of the CRT criterion. The penalty can be observed in the higher exponent for the dimension scaling (2/5 for CM and 3/7 for CK) as compared to (1/3) for the CRT criterion, although it is lower than the CV method. The mixing time τ_{mixing} also increases at a lower rate as compared to the CV approach. A summary of all the scaling approaches investigated is given in **Table 8.1**. The suitability of these proposed criteria along with the CV and CRT approaches in scaling MILD combustion chambers will be discussed in the subsequent sections.

Table 8.1: Summary of the scaling approaches

Scaling approach	Geometric scaling (D)	Velocity scaling (U)	τ_{mixing}	Re	\dot{Q}'''
CV	$\sim Q^{1/2}$	Constant	$\sim Q^{1/2}$	$\sim Q^{1/2}$	$\sim Q^{-1/2}$
CRT	$\sim Q^{1/3}$	$\sim Q^{1/3}$	Constant	$\sim Q^{2/3}$	Constant
CM	$\sim Q^{2/5}$	$\sim Q^{1/5}$	$\sim Q^{1/5}$	$\sim Q^{3/5}$	$\sim Q^{-1/5}$
CK	$\sim Q^{3/7}$	$\sim Q^{1/7}$	$\sim Q^{2/7}$	$\sim Q^{4/7}$	$\sim Q^{-2/7}$

8.2 Problem formulation

The baseline experimental rig has already been described in **Chapter 3**. The inlet boundary conditions for the baseline case are shown in **Table 7.2**. The high velocity of the reactants for the baseline case limited the maximum thermal input of the scaled-up versions to 25-kW. For scaling to higher thermal inputs, a suitable optimization of the injection system with lower inlet velocities for the baseline is required. The major dimensions of the baseline and the scaled combustors are shown in **Table 8.2**, and a suitable comparison of the dimensions of the combustors can be seen in **Figure 8.1**. The scaled-up domains for the CV, CRT, CM, and CK criteria are meshed with approximately 10, 5.6, 7.3, and 8.3 million

Scaling of the combustor

hexahedral cells, respectively. The meshes were verified for grid independence and the simulations reproduced the Kolmogorov's (-5/3) decay of the turbulent kinetic energy at several points within the shear layer.

Table 8.2: Summary of the dimensions and inlet conditions for the baseline and the scaled-up models.

	Baseline	CV	CRT	CM	CK
Q (kW)	3.3	25	25	25	25
Q_{fuel} (slpm)	42	317.9	317.9	317.9	317.9
U_{fuel} (m/s)	179.5	179.5	352.5	269.1	239.7
D_{fuel} (mm)	3	8.25	5.89	6.74	7.14
Q_{ox} (slpm)	125	946.3	946.3	946.3	946.3
U_{ox} (m/s)	169.7	169.7	333.3	254.5	226.6
$D_{\text{ox,inner}}$ (mm)	9	24.76	17.67	20.22	21.43
$D_{\text{ox,outer}}$ (mm)	11	30.27	21.6	24.72	26.19
$D_{\text{ex,inner}}$ (mm)	17	46.77	33.38	38.20	40.48
$D_{\text{ex,outer}}$ (mm)	27	74.29	50.01	60.67	64.29
D_{chamber} (mm)	80	220.11	157.08	179.78	190.48
L_{chamber} (mm)	265	729.11	520.33	595.5	630.96
\dot{Q}''' (MW/m ³)	2.48	0.9	2.48	1.65	1.39

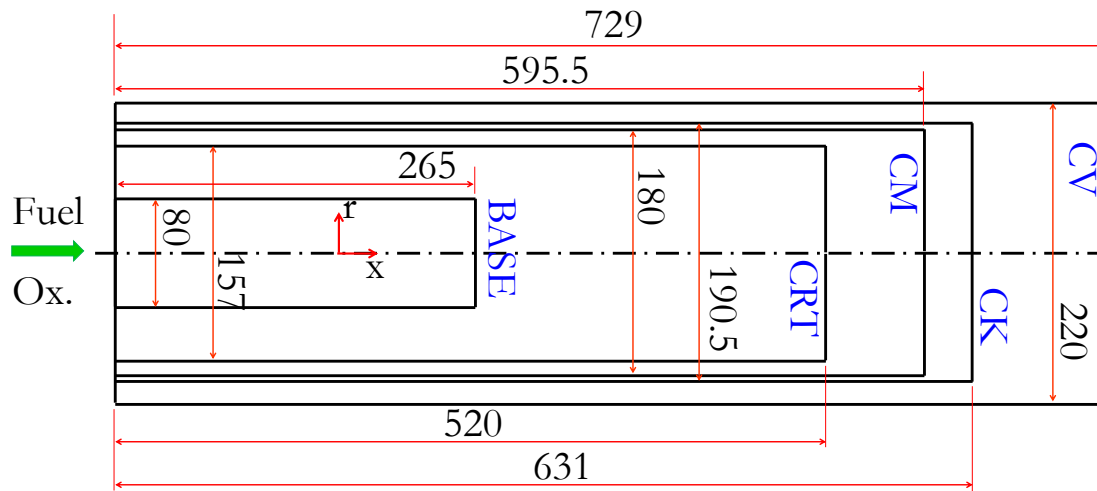


Figure 8.1: Comparison of the sizes of the baseline and the scaled-up combustion chambers.

8.3 Results and discussions

The computational results for the baseline MILD case have already been compared with the experimental data (temperature and OH) in **Chapter 7**. The next few sections will discuss and compare the computational results of the baseline case with the scaled-up combustion chambers for assessment of the influence of the scaling criterion.

8.3.1 Pressure drop

The pressure drop in a combustion chamber needs to be minimized as it decreases the work output in the turbine. Bobba et al. [19] estimated the pressure drop inherent to the reverse flow of the SPRF combustor neglecting the combustion and viscous losses using isentropic relations. The authors estimated that the pressure drop can be limited to $< 1\%$ if the injection velocity for air is less than 50 m/s. Kumar et al. [90] had also limited the air injection velocity in their MILD combustion chamber to 100 m/s such that the static pressure drop was 5.9-kPa. This section compares the mean static and total pressure drop in the baseline and the scaled-up chambers including viscous losses in the flow lines, combustion losses, and losses inherent to the reverse flow configuration. The injector length has been restricted to 100-mm for the baseline case to reduce computational cost, although the injector along with the flow lines is longer for the actual experimental setup. However, the length of 100-mm is sufficient to achieve a fully developed turbulent flow for the baseline case, similar to that achieved in the experiments. The injector lengths for the scaled-up cases have also been modified according to the respective geometric scaling factors (**Table 8.1**) to ensure fully developed turbulent flow at the inlet of the chambers.

The maximum pressure drop is incurred in the oxidizer flow line due to the size of the channel ($t = 1\text{-mm}$ for the baseline). The mean static pressure drop for the baseline case is

Scaling of the combustor

around 15 kPa from the injection point 100-mm upstream of the inlet to the exit of the chamber, whereas the total pressure drop (static + dynamic) is 22.3 kPa. The lowest static pressure drop is obtained for the CV case (12.3 kPa) due to the larger dimensions ($D \sim Q^{1/2}$), while the velocity is maintained constant. The total pressure drop for the CV case is 20.2 kPa which is close to the baseline value. The static pressure drop is the highest for the CRT criterion (53.8 kPa) and is approximately 3.6 times higher as compared to the baseline value, while the total pressure drop is 73 kPa. The large pressure drop associated with the CRT scaling criterion was also noted by Kumar et al. [87]. The static pressure drop is moderate at 30.7 kPa and 24.1 kPa for the CM and CK cases. These values are higher than the baseline value, but much lower than the value associated with the CRT criterion. The total pressure drop for the CM and CK cases is 46.4 kPa and 39 kPa, respectively. Hence, the CV approach offers the lowest pressure drop for a reverse flow MILD combustion chamber, although performance in terms of other parameters such as mixing and emissions needs to be considered. The CK and CM criteria proposed in the present investigation offer moderately higher pressure drop as compared to the baseline, but at a lower material cost and higher thermal intensity as compared to the CV criterion. The high-pressure drop associated with the CRT criterion may make it unattractive for aero-propulsion applications, although a modification of the injection configuration for the baseline case can restrict the pressure drop to within allowable levels for the scaled-up version.

8.3.2 Axial velocity along the centreline

The velocity field within the combustion chamber determines the mixing and utilization of the chamber volume for the reverse flow configuration. The non-dimensional mean axial velocities ($U/U_{o,fuel}$) along the centreline of the chamber for the various scaling criteria are shown in **Figure 8.2**. The centreline velocities at the inlet vary in the range of

Scaling of the combustor

around 250 m/s for the baseline and upto 425 m/s for the CRT case. In comparison to the SPRF combustor [19] that uses methane, the high centreline velocity in the present study is occurring due to the use of low calorific value syngas with a diluent percentage of 60%. The high velocity associated with the CRT criterion is due to the $Q^{1/3}$ scaling, which is the highest among all the criteria. The velocities associated with the CM and CK criteria are 344 m/s and 311 m/s, respectively, due to their moderate scaling exponents (1/5 and 1/7, respectively). The velocities along the centreline decrease monotonically due to the presence of the stagnation plane downstream. The velocities become nearly zero by $x/D_f = 80$ which corresponds to more than 90% of the length of the chamber. This implies that the jet penetration is greater than 90% of the chamber length leading to proper utilization of the chamber volume by the reactants.

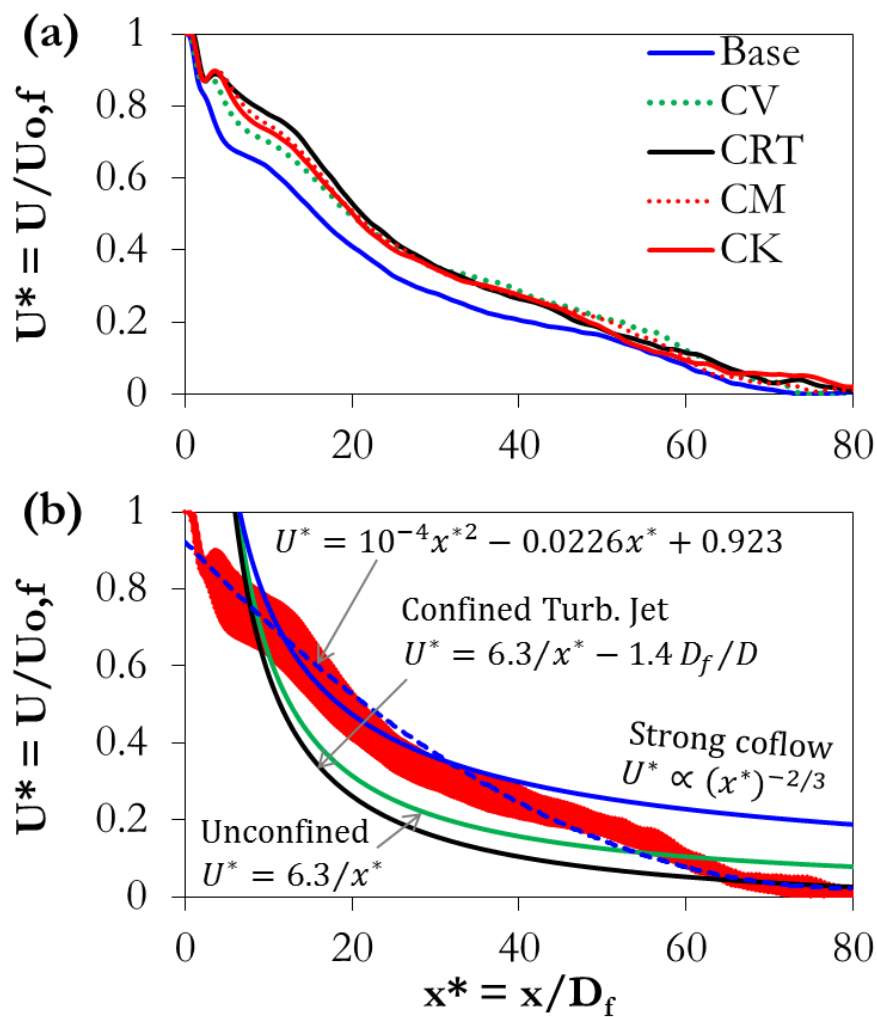


Figure 8.2: (a) Variation of the non-dimensional axial velocity ($U^* = U/U_{0,f}$) along the centreline with non-dimensional axial distance (x/D_f) for the baseline, constant velocity (CV), constant residence time (CRT), constant volume to jet momentum (CM), and constant volume to jet kinetic energy (CK) cases. (b) Plot showing a quadratic fit to the non-dimensional velocity profiles, overlapped with velocity correlations for unconfined circular turbulent jet [128], confined circular turbulent jet [129], and circular turbulent jets with strong coflow [27].

Scaling of the combustor

The non-dimensional velocities (U^*) are nearly similar for all the cases and collapse onto a single curve. The profiles are weakly quadratic as observed from the least squares quadratic fit shown in **Figure 8.2b**. In comparison, the axial velocity of an unconfined circular turbulent jet exhibits a hyperbolic dependence on the axial distance ($U^* \propto 1/x^*$) and hence deviates from the observed velocity profiles [128]. For a confined turbulent jet, the decay of the axial velocity is faster and is a function of both the non-dimensional axial distance and the ratio of the jet diameter to the confinement diameter (D_f/D) [129]. In the present investigation, the central fuel jet is surrounded by an annular coaxial jet of oxidizer, forming a compound jet. For an isothermal compound jet in which the velocity of the coflow is much smaller than the central flow ($U_f \gg U_{ox}$), the velocity decay is similar to a free turbulent jet ($U^* \propto 1/x^*$). However, for an isothermal circular compound jet with strong coflow ($U_f \ll U_{ox}$), the decay is proportional to $x^{-2/3}$ as shown in **Figure 8.2b** [27]. It is observed that the velocity profile in the current investigations varies as $x^{-2/3}$ to some extent in the range of $10 < x^* < 30$ as the momentum flux ratio is less than 1. However, the velocities decay faster beyond this point possibly due to the combined effects of the reverse flow and the forward stagnation plane. It must also be noted that the jets are not isothermal in the present configuration due to different inlet temperatures and heat release due to combustion which is possibly another cause for the deviation.

The similarity of the velocity profiles for the baseline and the scaled-up versions suggest the presence of a parameter that is constant for all the cases. Indeed, the velocity ratio (U_{ox}/U_f) has been noted to be the most important parameter in determining the flow field and mixing in isothermal coaxial jets [26]. For coaxial jets with different densities, the momentum ratio replaces the velocity ratio in determining the flow characteristics. In the present investigations, the densities are identical and the velocities have been scaled up by a constant factor both for the fuel and the oxidizer jets. This maintains a constant momentum

Scaling of the combustor

ratio for the baseline and the scaled-up chambers, thus explaining the similarity of the non-dimensional velocity profiles. The mixing between the central fuel and the coaxial oxidizer is also governed by the jet momentum ratio and is expected to be similar for all the cases. This was also noted by Bobba et al. [19] who suggested that identical mixing between the fuel and the oxidizer can be obtained at lower velocities if the momentum ratios are maintained constant. From this observation, the CV approach is expected to provide mixing similar to the baseline case at lower inlet velocities and pressure drop. Also, the effect of the momentum ratio on recirculation and entrainment needs to be investigated further.

8.3.3 Mean axial velocity along the radius

The non-dimensional axial velocity ($U^* = U/U_{o,f}$) along the non-dimensional radius ($r^* = r/D_f$) at various axial distances (x/D_f) is shown in **Figure 8.3**. Just as in the case of the centreline velocity (**Figure 8.2a**), the velocities in the radial direction for all the cases also exhibit similar profiles and nearly overlap. This is also true for the velocity of the reverse flow which also collapses onto the non-dimensional velocity curves. At $x/D_f = 5$, the oxidizer and fuel jets can be distinctly identified for the CRT, CM, and CK cases, whereas the jets appear to have merged for the baseline and the CV cases. The maximum velocities decrease with axial distance as observed in **Figure 8.2a**, while the radial penetration of the jet increases. As a result, the reverse flow velocity is the lowest at $x/D_f = 5$ due to the larger area obtained at this location. The magnitude of the reverse flow velocity is less than 8 m/s for $10 < r^* < 13$ at $x/D_f = 5$ for all the cases. As the jet expands in the radial direction further downstream, the reverse flow is confined closer to the wall leading to higher velocities as observed at $x/D_f = 17, 33, \text{ and } 50$. At $x/D_f = 33$, the maximum reverse flow velocity is around 20 m/s for the baseline case and around 40 m/s for the CRT case. The maximum reverse flow velocity associated with the CV criterion is lower than that corresponding to the baseline

Scaling of the combustor

case, while the velocity corresponding to the CM and CK criteria are similar to the corresponding baseline value.

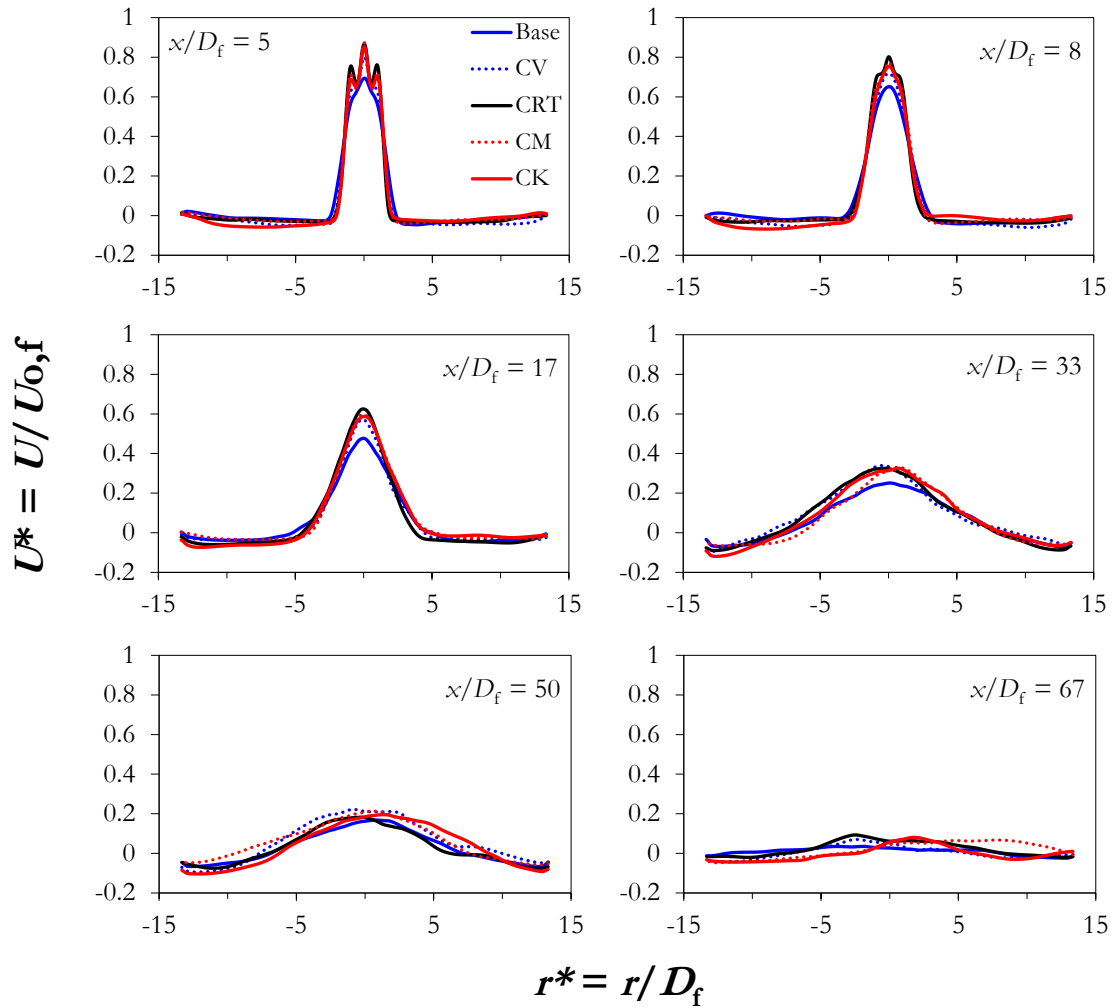


Figure 8.3: Variation of the non-dimensional axial velocity ($U^* = U/U_{o,f}$) with non-dimensional radial distance ($r^* = r/D_f$) at various axial distances (x/D_f) for the baseline, constant velocity (CV), constant residence time (CRT), constant volume to jet momentum (CM), and constant volume to jet kinetic energy (CK) cases.

For an isothermal compound jet with a weak coflow ($U_f \gg U_{ox}$), the jet diverges as $b \sim x$ whereas for a strong coflow ($U_f \ll U_{ox}$), $b \sim x^{1/3}$ [27]. Here, b is the radial distance at

Scaling of the combustor

which the mean centreline velocity decreases to half the value. In the present case, the jet is expected to diverge at a faster rate as compared to the strong coflow case due to the effect of the reverse flow also. At $x/D_f = 5$, $b = 1.52$ as determined from the velocity plot for the baseline case. We subsequently use the relation $b_2 = b_1(x_2^*/x_1^*)^{1/3}$ to predict the b values at various axial distances. It must again be noted that the jets are not isothermal and the effect of temperature and heat release have not been accounted for in the present relation. At $x/D_f = 8$, the predicted b is 1.78 as compared to 1.63 obtained from the velocity profiles. The predicted and actual b values at $x/D_f = 17$ are 2.28 and 2.23, respectively, which are nearly equal. However, the jet diverges at a faster rate than the predicted values farther downstream. At $x/D_f = 33$, the actual $b = 4.44$ as compared to the predicted value of 2.85. A similar observation is also made at $x/D_f = 50$ and $x/D_f = 67$ although the actual rate of change of b has become lower. Thus, it appears that the jet divergence rate is non-uniform with axial distance. It initially increases faster than $\sim x^{1/3}$ upto $x/D_f = 33$ but subsequently decreases. This is primarily due to the effect of the confinement that causes a varying reverse flow velocity and shear which initially increases with axial distance but decreases subsequently.

8.3.4 Standard deviation of the velocity along the radius

The variation of the normalized velocity fluctuations with radius at various axial distances is shown in **Figure 8.4**. This represents the intensity of turbulent fluctuations at the various locations for all the cases. As observed, the turbulent fluctuations are also similar and the curves overlap in a narrow band. This is expected as the mean velocity profiles in the axial and radial directions are similar causing similar velocity gradients or strain in the flow field as observed in **Figure 8.2** and **Figure 8.3**. However, the absolute standard deviation is the highest for the CRT case, followed by the CM, CK, and CV cases. The values are similar for the baseline and the CV case. The maximum variation in the peak turbulent intensities

Scaling of the combustor

among the various cases is around 2% as shown in **Figure 8.4**. At $x/D_f = 5$, the maximum turbulent fluctuation ($\sim 11\%$) is observed in the inner shear layer between the central fuel and the annular oxidizer. The fluctuations in the outer shear layer upto the chamber wall in the radial direction are nearly constant. The maximum standard deviation is 47 m/s in the inner shear layer for the CRT case, whereas it is around 32 m/s for the CM and CK cases. At $x/D_f = 8$ and 17, the peak fluctuations increase to 13%, respectively. Away from the centreline ($|r^*| > 5$), the fluctuations is less than 3%. The highest magnitude of the standard deviation is also observed at these axial locations, and is around 59 m/s for the CRT case and 40 m/s for the CM case. The peak fluctuations decrease with axial distance causing a flattening of the curves in the radial direction. The maximum fluctuations decrease to 8.6% at $x/D_f = 33$ and to 7% at $x/D_f = 50$. However, at these axial locations, the fluctuations at $r/D_f = 10$ have increased to around 5%. The shear at these axial locations is higher than that at the upstream locations ($x/D_f = 5, 8, \text{ and } 17$) due to the radial penetration of the reactant jets and the increase in velocity of the reverse flow (**Figure 8.3**). The fluctuations are lowest at $x/D_f = 67$ and are nearly uniform due to lower and smoother velocity profiles. Thus, it is observed that all the scaling criteria produce similar mean and standard deviation profiles in the reverse flow chamber.

Scaling of the combustor

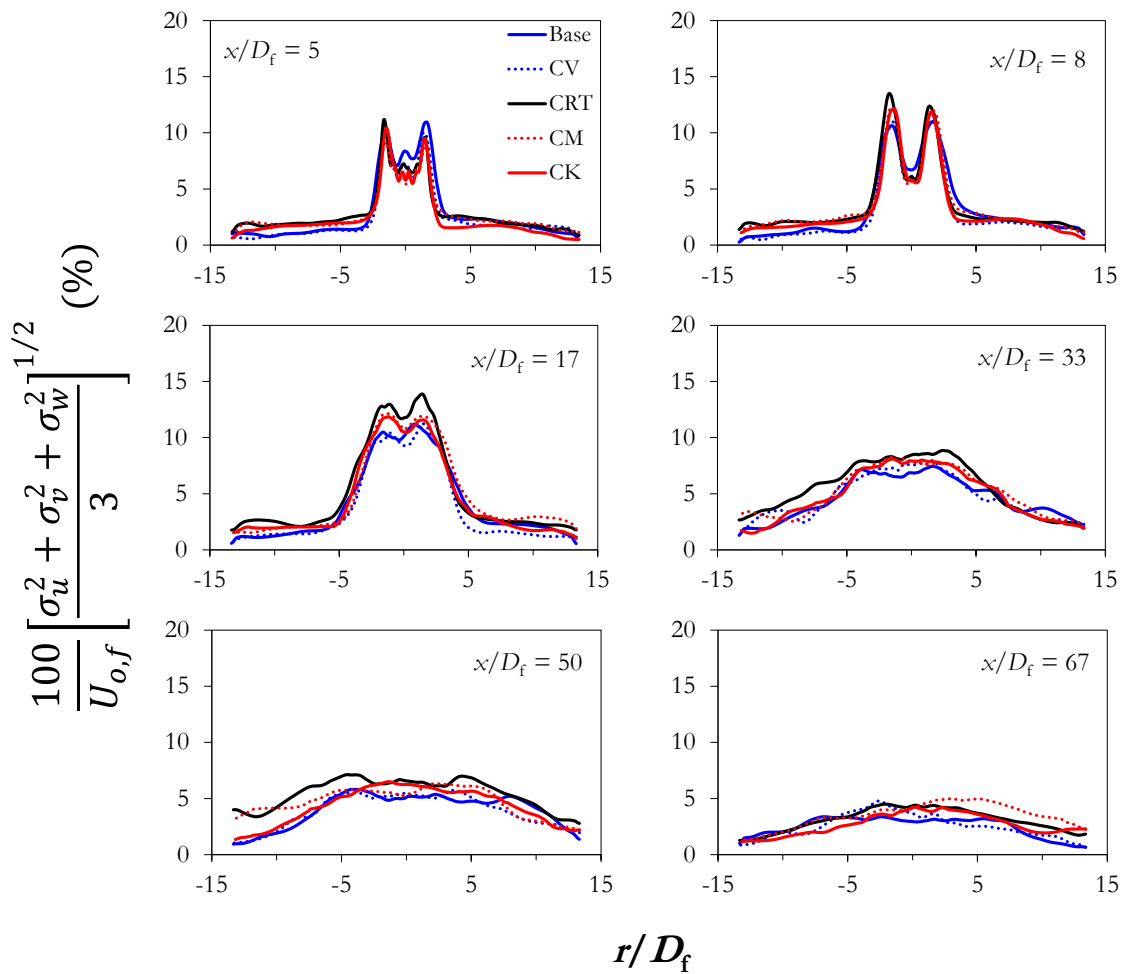


Figure 8.4: Radial variation of the standard deviation of the velocity normalized by mean inlet velocity along the centreline at various axial distances for the baseline, constant velocity (CV), constant residence time (CRT), constant volume to jet momentum (CM), and constant volume to jet kinetic energy (CK) cases.

8.3.5 Recirculation ratio

As mentioned earlier, the recirculation ratio (R) quantifies the entrainment of hot diluted combustion products into the fresh reactants stream that helps in achieving MILD combustion. The R is calculated by determining the total mass flow rate over an area in the cross-section of the chamber where the velocity is in the forward direction. The variation of R

Scaling of the combustor

with axial distance for all the cases is shown in **Figure 8.5a**. **Figure 8.5b** represents a snapshot of the instantaneous velocity vectors for the CK case showing the vortices causing entrainment of the recirculating exhaust gases. The value of R initially increases with axial distance as more exhaust is entrained into the reactants stream and reaches a maximum value. The maximum value of R varies in the range of 2 - 2.35 for all the cases investigated. This value is higher than that for the SPRF combustion chamber reported by Bobba et al. [19] but lower than the values specified by Plessing ($R \geq 3$) [38] to achieve flameless combustion of methane in their reverse flow furnace. It must be noted here that the value of R necessary to achieve MILD combustion is not universal and is dependent on the fuel and diluent percentage in the oxidizer. A higher value of recirculation ratio helps in stabilizing the combustion by entrainment of hot exhaust gases. The maximum in R is reached at $30 < x/D_f < 50$, after which it gradually decreases. This happens as the flow starts to reverse thereby reducing the total mass carried in the forward direction.

The similarity in the recirculation ratio (R) is a consequence of the similar velocity profiles obtained for all the cases as observed in **Figure 8.2**. However, Kumar et al. [90] report that the CRT criterion causes higher values of R as compared to the CV criterion. The authors use RANS simulations to predict values of R in their MILD combustion chamber. Also, the injection arrangement is not coaxial jets but consists of alternate fuel and air injection ports arranged on the circumference of a circle around the central axis. Hence, the similarity of the velocity field due to constant momentum ratio as obtained in the present study may not hold true for the CRT and CV cases reported by Kumar et al. [90] leading to differences in R . Thus, no significant difference in the R values obtained with the various scaling criteria is observed in the reverse flow MILD combustion chamber. Thus, the CV criterion provides a recirculation ratio similar to that observed with the CRT, CM, and CK criteria at a lower inlet velocity and pressure drop.

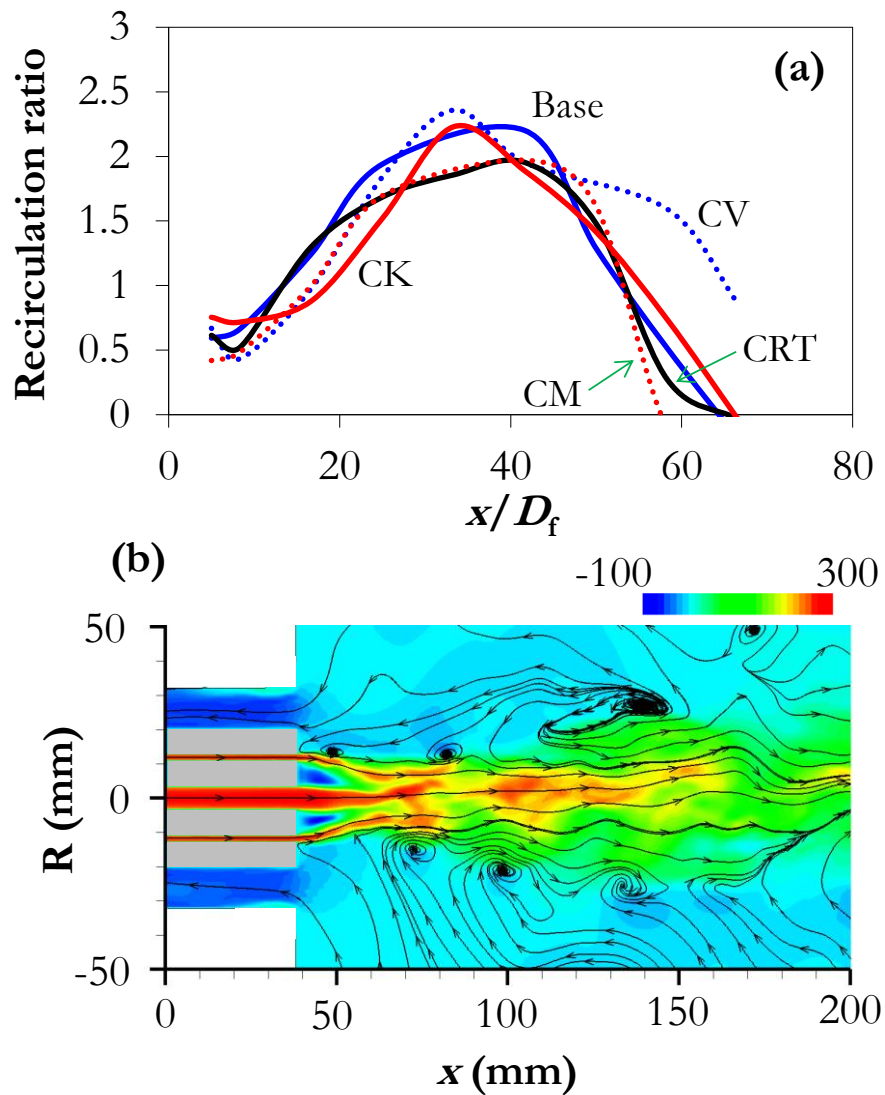


Figure 8.5: (a) Variation of the recirculation ratio (R) with non-dimensional axial distance for the baseline, constant velocity (CV), constant residence time (CRT), constant volume to jet momentum (CM), and constant volume to jet kinetic energy (CK) cases. (b) Instantaneous velocity vectors with streamlines for the CK case showing the entrainment of returning exhaust gases.

8.3.6 Residence time

The residence time in the combustion chamber significantly influences the performance of the system in terms of combustion efficiency and emissions. The residence time is higher in the reverse flow chamber as the flow traverses twice the path length as compared to that in a forward flow combustion chamber. To estimate the residence time, the paths along the centreline and at $r/D_f = 12$ are chosen for the forward and the reverse flow in all the cases. The predicted axial velocities along these paths are used to calculate the residence time. The global residence time (τ_G) definition proposed by Turns and Myhr [130] and adapted by Szegö et al. [40] is used in this study. The definition is based on the volume of the chamber and the flow rate of the reactants and is given by:

$$\tau_G = \frac{4V_F f \rho_{rct}}{\pi d^2 u \rho_{fuel}} \quad (8.15)$$

where, V_F is the chamber volume, f is the fuel mixture fraction, ρ_{rct} is the density of the reactant mixture at the chamber temperature, d is the fuel nozzle diameter, u is the fuel inlet velocity, and ρ_{fuel} is the density of the fuel at inlet conditions. The reference temperature at which the ρ_{rct} is calculated is set at 1200 K. This definition of a global residence time is suitable for a reverse flow chamber where there is an optimal utilization of the chamber volume due to intense mixing and recirculation.

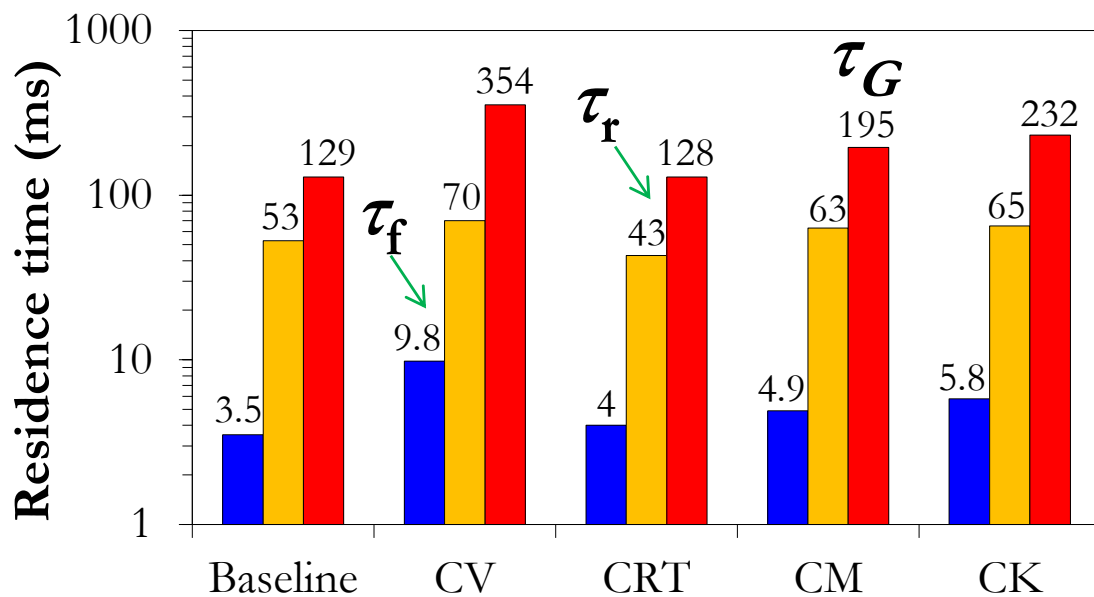


Figure 8.6: Estimated forward (τ_f), reverse flow (τ_r), and global (τ_G) residence times for the baseline, constant velocity (CV), constant residence time (CRT), constant volume to jet momentum (CM), and constant volume to jet kinetic energy (CK) cases.

The estimated residence times for all the cases is shown in **Figure 8.6**. For the baseline, the τ_f is estimated to be around 3.5 ms which is reasonable considering the high inlet velocities. However, the reverse flow residence time (τ_r) is estimated to be around 53 ms over the same path length at $r/D_f = 12$, which is 15 times greater than the forward-flow residence time. The τ_r estimated at $r/D_f = 10$ is around 30.5 ms, which is 8.7 times greater than τ_f . This happens as the maximum velocities at $r/D_f = 10$ and 12 are 12.5 m/s and 17.2 m/s, which are around 19 and 14 times lesser than the peak forward flow velocity. This shows that the residence time of the reverse flow dominates the overall residence time in the chamber,

Scaling of the combustor

unlike the forward-flow configuration. The global residence time (τ_G) estimated with **Eq. (8.15)** is around 129 ms.

The highest residence time is obtained for the CV criterion as can be observed in **Figure 8.6**. The value of τ_f is around 9.8 ms, whereas τ_r at $r/D_f = 12$ is around 70 ms, both of which are higher than the baseline values. This is because of the longer path lengths in a CV chamber although the velocity is similar to that of the baseline as observed in **Figure 8.2** and **Figure 8.3**. Here also, the τ_r dominates the overall residence time in the chamber. The τ_G obtained is 354 ms which is the highest among all the cases. The residence time for the CRT criterion is similar to the baseline case. The values of residence time obtained for the CM and CK criteria lie in between that of the CV and the CRT criteria.

8.3.7 Instantaneous and mean temperature distribution

After discussing the velocity field, its influence on recirculation rate (R) and the residence time (τ), the thermal field within the combustion chamber is analyzed for the baseline and the scaled-up versions. The instantaneous temperature contours for all the cases are shown in **Figure 8.7**. As observed, the simulations resolve the turbulent flow structures and unsteadiness. The temperature is nearly uniform throughout the combustion chamber except close to the inlet due to the low temperature of the reactants. Near the inlet, three distinct layers can be identified corresponding to the fuel, the oxidizer, and the exhaust. The fuel stream is at the lowest temperature of 544 K, followed by the oxidizer at 768 K. The exhaust is at the highest temperature close to 1200 K. The low-temperature fuel stream mixes with the oxidizer due to which its temperature increases with axial distance. The boundary between the oxidizer and the returning exhaust can also be clearly identified from the temperature contours. The vortices in the oxidizer side are observed due to the shear from the exhaust. Intermittent packets of high-temperature exhaust can also be identified to entrain

Scaling of the combustor

into the fuel-oxidizer stream causing mixing between them. Large temperature gradients and fluctuations are also observed between the exhaust and the wall. The wall thermal inertia and lower temperature cause this sharp gradients and fluctuations. The uniform high-temperature region extends from $x/D_f \sim 30$ axially and from $|r/D_f| \sim 4$ upto the walls in the radial direction. Such uniform instantaneous temperature in most parts of the chamber can provide efficient heat transfer characteristics in furnaces. This is a consequence of the reverse flow configuration that provides efficient mixing and recirculation. Thus, it is observed that the temperature distribution is not very sensitive to the scaling criterion investigated in the present study. This can be attributed to the similar velocity distribution and inlet thermal and species boundary conditions.

The mean temperature variation along the chamber centreline and radius for all the cases is shown in **Figure 8.8**. The temperature curves nearly overlap indicating similar thermal distribution. Along the centreline, the temperature increases monotonically with axial distance from 544 K to 1300 K at the bottom of the chamber. The temperature is nearly uniform after $x/D_f = 60$ with a maximum variation of less than 30 K. This can also be observed in the instantaneous images shown in **Figure 8.7**. In the radial direction, the temperature increases sharply in the mixing layer from the centreline and becomes nearly constant thereafter. The temperature then decreases near the wall due to heat loss. The temperature gradient in the radial direction decreases with an increase in axial distance as the mean centreline temperature increases. At $x/D_f = 33$, the maximum variation in temperature is less than 160 K, which decreases to less than 40 K at $x/D_f = 50$. This shows that reactions are incomplete at this location as the temperature has not reached the maximum value. Further downstream, at $x/D_f = 67$, the maximum temperature is observed at the centreline suggesting that the reactions are nearly complete and the region consists mostly of burnt gases. It must be noted here that the major species such as CO_2 , O_2 , and H_2O exhibit similar and nearly

Scaling of the combustor

uniform profiles. However, there is an observable difference in the distribution of minor species such as OH as discussed in the next section. The uniform species and temperature fields suggest that the reverse flow MILD chamber operates close to a perfectly stirred reactor (PSR) as was also observed in **Chapter 6**. Plessing et al. [38] had also concluded that flameless oxidation in their reverse flow furnace occurred in the perfectly-stirred region devoid of ignition and quenching events and matches well with the present observations both for the baseline and the scaled-up versions.

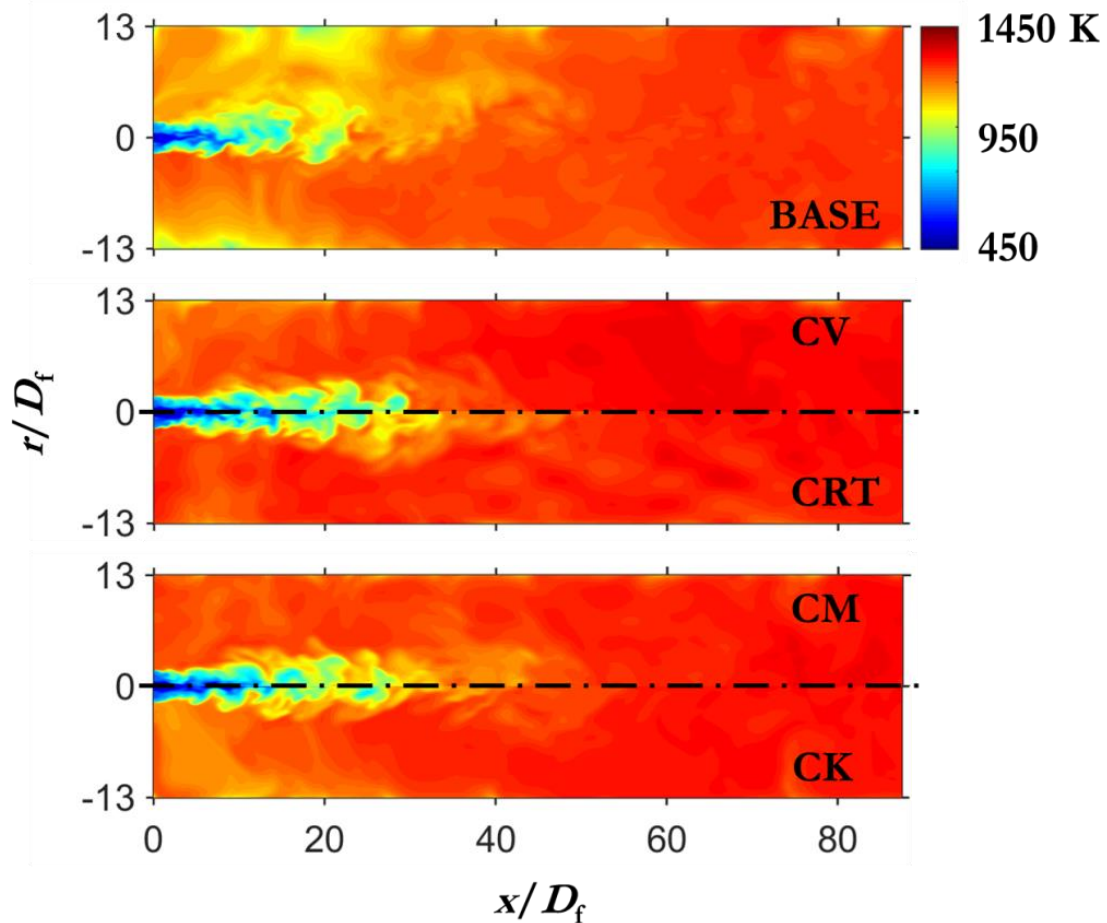


Figure 8.7: Instantaneous temperature contours for the baseline, constant velocity (CV), constant residence time (CRT), constant volume to jet momentum (CM), and constant volume to jet kinetic energy (CK) cases

Scaling of the combustor

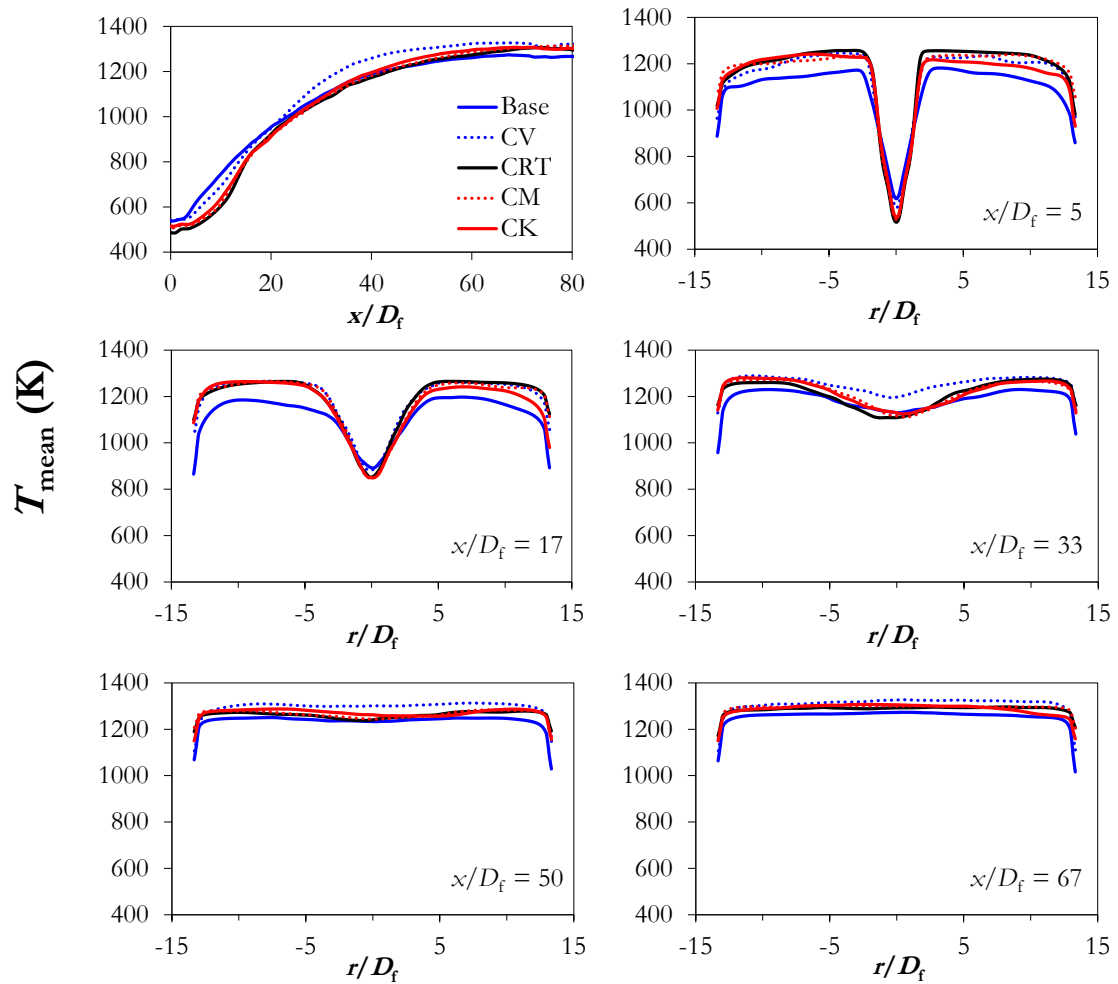


Figure 8.8: Variation of the mean temperature with non-dimensional axial and radial distances for the baseline, constant velocity (CV), constant residence time (CRT), constant volume to jet momentum (CM), and constant volume to jet kinetic energy (CK) cases.

8.3.8 Instantaneous and mean OH mass fraction

For syngas combustion, the OH radical is closely associated with the heat release rate as observed in counterflow diffusion flame simulations at different strain rates and oxidizer compositions. This is because the primary reactions for the conversion of H₂ and CO in syngas to H₂O and CO₂ involve the OH radical. The OH radical is thus a suitable flame marker for syngas combustion and has been used here to investigate the distribution of the reaction zone. The instantaneous OH mass fraction contours for all the cases is shown in **Figure 8.9**.

The jets of fresh reactants can be clearly identified near the inlet devoid of the OH radical. This unreacted jet core penetrates upto around $x/D_f = 30$ before the onset of combustion along the centreline. The mean temperature at this location along the centreline is around 1100 K as shown in **Figure 8.8**. For all the cases, distinct OH gradients are observed in the shear layer near the inlet and upto $x/D_f = 30$. However, these regions with strong OH gradients are not associated with high temperature (> 1800 K) as observed in **Figure 8.7** and do not lead to the formation of thermal NO_x. For the baseline, the high OH mass fraction ($Y_{OH} > 3 \times 10^{-4}$) is limited to a very small region near the centreline. A rather wide distribution of $Y_{OH} = 1 \times 10^{-4}$ is observed throughout the chamber signifying the distributed nature of the reaction zone. For the CV case, the region of $Y_{OH} > 3 \times 10^{-4}$ is wider than that for the baseline case. However, the reaction zone is more compact as can be observed from the isocontour lines which are closely spaced. The $Y_{OH} = 1 \times 10^{-4}$ isocontour does not cover the entire chamber as was observed for the baseline case. This observation can be explained based on the finite lifetime of the OH radical and the residence time. As noted in **Figure 8.6**, both the forward (τ_f) and the reverse flow (τ_r) residence times are higher for the CV case as compared to the baseline case. The global residence time (τ_G) is almost twice that of the baseline case.

Scaling of the combustor

The inlet conditions, velocity distribution, and temperature distribution within the chamber is similar for the baseline and the CV criterion. This results in a fixed lifetime of the OH radical. The distribution of the OH radical is then governed by the balance between the radical lifetime and the residence time as the radical is convected with the flow after formation. The fact that convection of the OH radical plays a crucial role in the distribution of the reaction zone as was demonstrated in **Chapter 5** using idealized plug flow reactor simulations with different O₂ percentages at the inlet. Due to the similar OH radical lifetimes and longer residence times due to bigger chamber volume for the CV case, the reaction zone appears narrower and more compact. The widest distribution of the OH radical is observed for the CRT case. However, the presence of OH near the exit suggests that the reactions are still in progress and may lead to higher CO emissions as discussed in the next section. The CM and CK cases also show highly distributed reaction zones similar to the baseline case but with lower OH concentration near the outlet as compared to the CRT case.

Scaling of the combustor

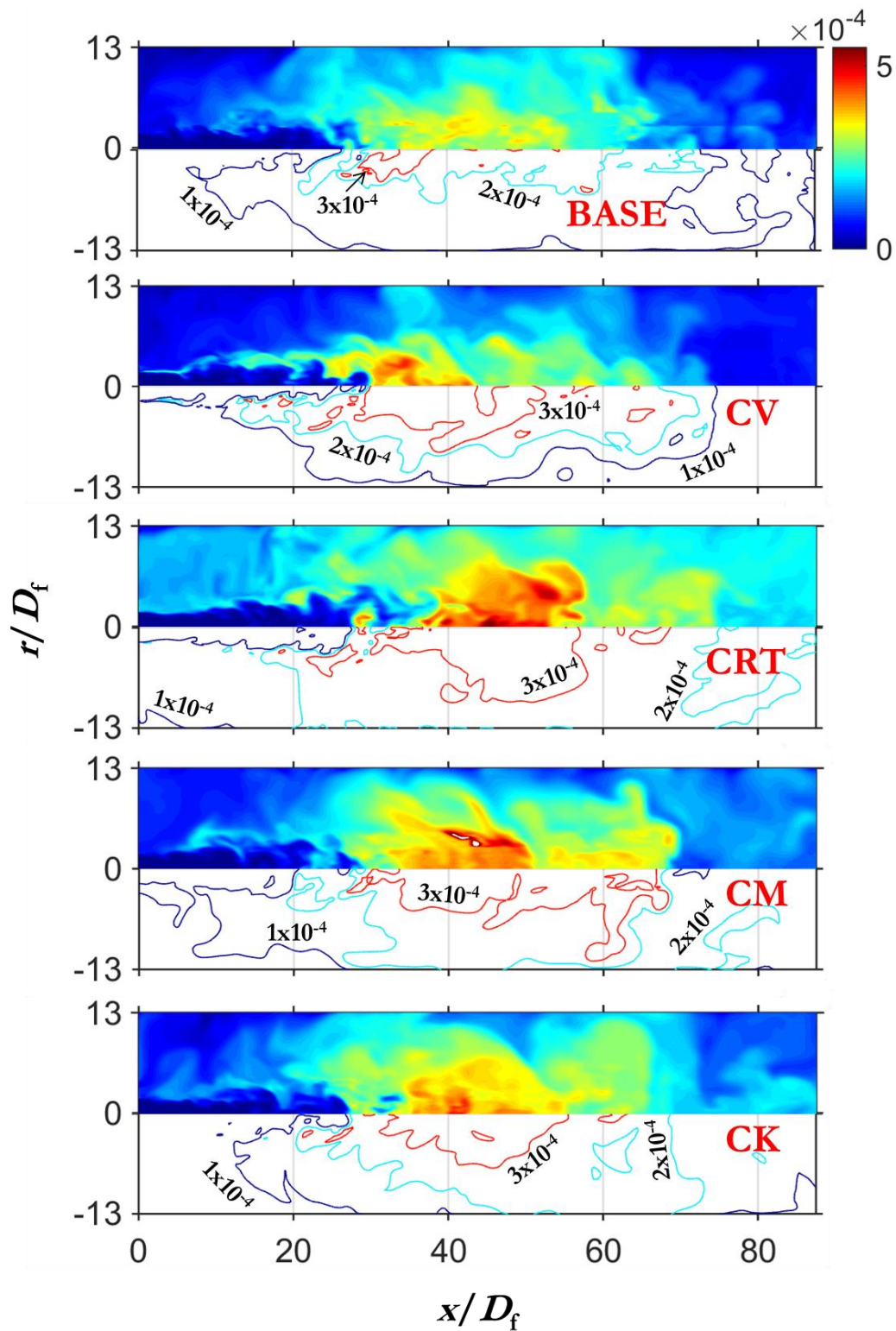


Figure 8.9: Instantaneous OH mass fraction contours and contourlines at OH mass fractions of 1×10^{-4} , 2×10^{-4} , and 3×10^{-4} for the baseline, constant velocity (CV), constant residence time (CRT), constant volume to jet momentum (CM), and constant volume to jet kinetic energy (CK) cases.

Scaling of the combustor

The variation of the mean OH mass fraction along the centreline and radial variation at various axial distances is shown in **Figure 8.10**. The OH mass fraction (Y_{OH}) increases along the centreline and reaches a maximum in the region $30 < x/D_f < 50$, after which it starts to decrease. The peak Y_{OH} is the lowest for the baseline case and highest for the CRT criterion. The decrease in Y_{OH} is gradual for the baseline case, while the sharpest drop is observed for the CV case. This corresponds to the trends observed in the instantaneous images shown in **Figure 8.9**. In the radial direction, the Y_{OH} is zero near the centreline, then increases to a finite value and subsequently decreases near the wall. The radial profiles are nearly uniform upto $r/D_f = 10$ after the initial rise. The maximum gradient is observed for the CV case, while it is similar for the baseline, CRT, CM, and CK cases. At $x/D_f = 17$, the presence of high Y_{OH} in the shear layer for the CV case suggests the presence of a reaction zone due to low shear. The radial OH profiles become nearly uniform and decrease radially after $x/D_f = 50$, where no presence of the unreacted jet can be observed. Thus, the mean OH profiles also exhibit the highest concentration for the CRT case and the lowest for the CV case away from the centreline similar to the trend observed in the instantaneous OH contours. This indicates that the reaction zone and heat release are more uniform for the CRT case as compared to the CV case. Here, it must be noted that due to the low operating temperature of the chamber, the thin reaction zones near the inlet do not play a significant role in thermal NO_x formation. However, at higher operating temperatures and with high-calorific value fuels, the CV criterion is expected to produce higher thermal NO_x both due to the presence of the thin reaction zones and longer residence times.

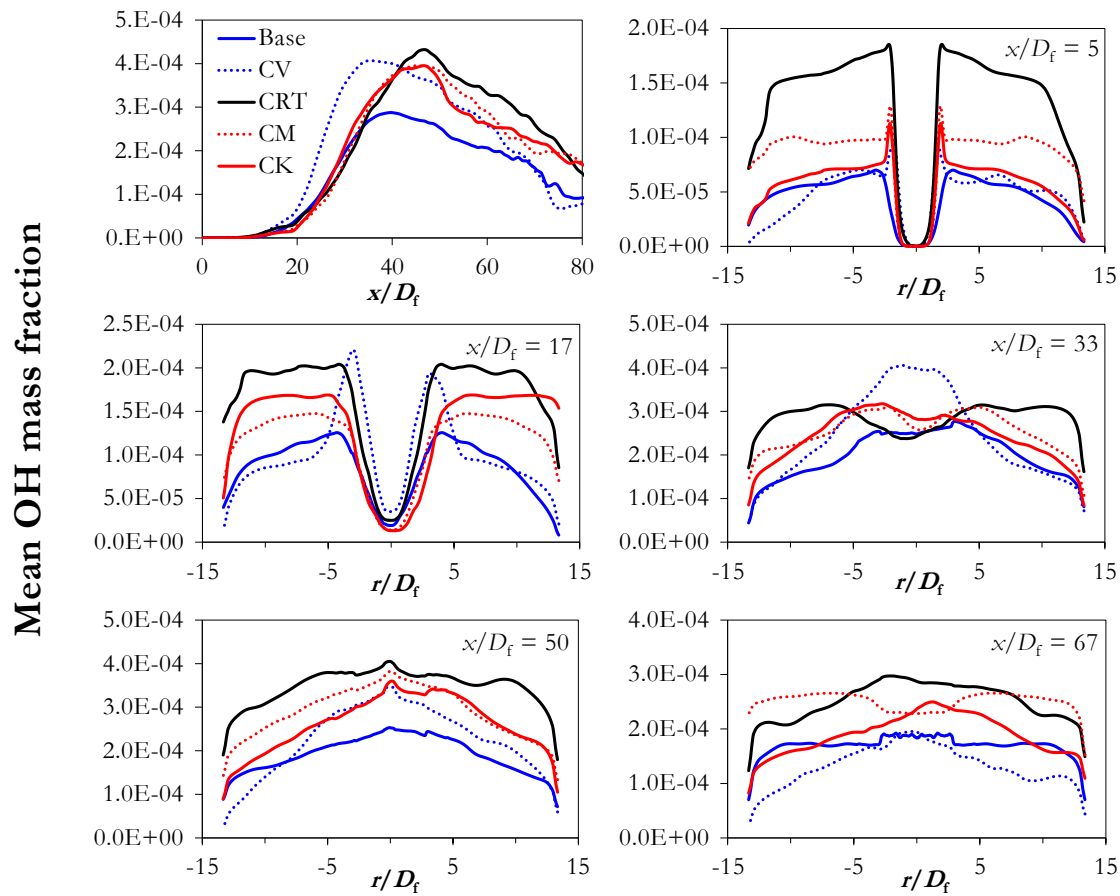


Figure 8.10: Variation of the mean OH mass fraction with non-dimensional axial and radial distances for the baseline, constant velocity (CV), constant residence time (CRT), constant volume to jet momentum (CM), and constant volume to jet kinetic energy (CK) cases.

8.3.9 CO emissions

Finally, the variation of the CO emissions is investigated for all cases as shown in **Figure 8.11**. The CO emission values are absolute and have not been normalized as the O₂ percentage at the outlet was similar for all the cases. The CO emission predicted for the baseline case is 807-ppm. When normalized with the predicted O₂ mole fraction at the outlet, the CO emission is 236-ppm which is close to the experimentally obtained value of 206-ppm.

Scaling of the combustor

The lowest absolute CO emission of 339-ppm is obtained for the CV case. This can be attributed to the higher global residence time for the CV case as compared to that for the baseline case as observed in **Figure 8.6**. Under similar flow and thermal conditions, the increase in residence time decreases the CO emissions as was observed in perfectly stirred reactor simulations in **Chapter 6**. This is also evident in the OH contours shown in **Figure 8.9** where a significant presence of OH near the outlet implies the incompleteness of the recombination reactions. The CO emission for the CRT case is 762-ppm that is lower than that for the baseline case. Although the residence time for the CRT case is around 47 ms which is lesser than that obtained for the baseline case, the temperature is higher than the baseline by around 50 K as can be observed in the radial temperature profiles in **Figure 8.8**. These two coupled effects lower the CO emissions for the CRT case as compared to the baseline case. The predicted CO emissions of 584-ppm (CM case) and 483-ppm (CRT case) show consistent trends with the calculated residence times of 67.9 ms and 70.8 ms, respectively.

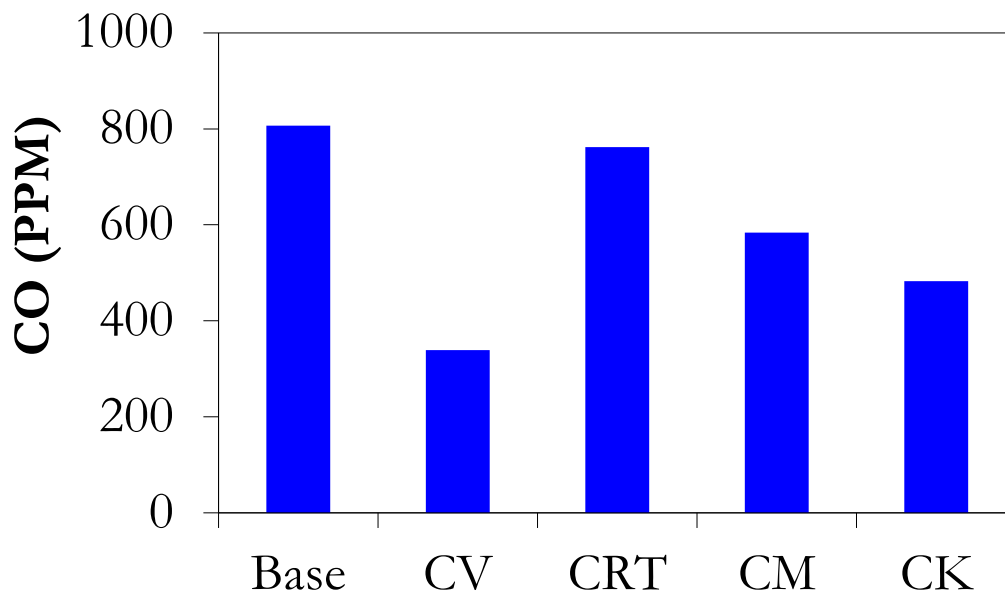


Figure 8.11: Mean CO emissions for the baseline, constant velocity (CV), constant residence time (CRT), constant volume to jet momentum (CM), and constant volume to jet kinetic energy (CK) cases.

8.4 Summary

In the present chapter, the influence of four different scaling criteria on the performance of a reverse flow chamber under MILD conditions is investigated using hybrid RANS/LES simulations. The chamber is scaled-up from 3.3-kW to 25-kW using constant velocity (CV), constant residence time (CRT), constant volume to jet momentum ratio (CM), and constant volume to jet kinetic energy ratio (CK) scaling approaches, of which the CM and CK criteria have been proposed in this work based on phenomenological observations pertaining to MILD combustion. The pressure drop is the lowest for the CV criterion, followed by the CK, CM, and CRT criteria. However, the non-dimensional mean and standard deviation of the velocity fields collapsed onto a single curve showing that the ratio

Scaling of the combustor

of the jet momentum is the key parameter in determining the mixing and velocity fields which is constant across all the cases. The highest residence time is obtained for the CV case, followed by the CK, CM, and CRT cases. This also leads to the lowest CO emissions for the CV case (339-ppm) and the highest for the CRT case (762-ppm), similar to the baseline. Both the instantaneous and mean temperature fields are nearly uniform throughout the chamber in the range of 1200 - 1300 K thereby leading to near zero NO_x emissions. However, the OH fields show that the reaction zone is most distributed for the CRT case, and most compact for the CV case. Overall, the CV criterion performs the best in terms of pressure drop and CO emissions although at a higher chamber volume and lower thermal intensity. The CM and CK criteria are potential alternatives to the CV and the CRT criteria in terms of their performance.

Chapter 9

Conclusions

9.1 Summary of present work

The present thesis experimentally and numerically investigates the combustion of low calorific value syngas (20% CO, 20% H₂, 60% N₂) in an optically accessible reverse flow combustion chamber at a fuel thermal input of 3.3-kW. Several modes of operation such as the conventional ($\Phi_{\text{global}} = 0.8$), ultra-lean ($\Phi_{\text{global}} = 0.32$), transition ($\Phi_{\text{global}} = 0.47$, O₂ = 14.3% in oxidizer), and MILD ($\Phi_{\text{global}} = 0.89$, O₂ = 7.6% in oxidizer) are investigated at atmospheric pressure to identify the best strategy for stable operation with low emissions. The first part of the thesis deals with investigating the global and transient combustion characteristics of these various modes using OH* chemiluminescence, noise and emission measurements. In all cases, autoignition was observed to be the mode of flame stabilization that indicated the role of H₂ in reducing the ignition delay. The most stable operation was obtained for the MILD case, where the SPL decreased by 6 dB due to a suppression of the high-frequency (> 800 Hz) longitudinal modes as compared to the conventional case.

A detailed investigation of these various combustion modes was performed using in-situ laser diagnostic techniques. The planar laser-induced fluorescence (PLIF) and Rayleigh thermometry techniques are used to investigate the reaction zone structure and the temperature distribution, respectively. The reaction zone structure shows that the OH intensity is highest for the conventional case, while it is the lowest for the MILD case. The intensity and distribution of OH for the ultra-lean and the transition cases are observed to be

Conclusions

similar. The standard deviation of the OH signal shows the highest fluctuation for the conventional case while the MILD mode exhibits a quasi-steady behavior with the lowest fluctuations. The instantaneous OH-PLIF images show thin reaction zones near the inlet for all the cases, which is contrary to the idea of a distributed and volumetric reaction zone under MILD conditions. However, the OH signal near the bottom of the chamber is higher for the MILD case as compared to the ultra-lean and the transition cases, indicating a distributed reaction zone downstream. The quantification of OH at these locations shows a clear trend of higher OH ppm for the MILD case. This is believed to be caused by the passive advection of OH radicals under diluted conditions. The Rayleigh thermometry measurements showed that the temperature is nearly uniform throughout the chamber except very close to the centreline. A maximum temperature of around 1700 K is measured for the conventional case, while the maximum temperature is around 1300 K for the ultra-lean, transition, and the MILD cases. The standard deviation of temperature shows that the fluctuation is lowest for the MILD case and highest for the conventional case, while it is similar for the ultra-lean and the transition cases.

The low emission capability of the reverse flow combustor is then assessed by measuring NO_x and CO emissions. It is observed that the NO_x emission is less than 1-ppm for all cases, while the CO emission is highest for the MILD case (461-ppm) and lowest for the conventional case (32-ppm). A network of perfectly stirred reactor models is developed to explain the observed trend in emissions. The effect of H_2 content in the fuel and the chamber temperature on the emissions is investigated with this model to identify the optimum operating conditions with lowest CO and NO_x emissions.

The in-situ experimental data on OH concentration and temperature is then used to validate and select numerical models for simulating the combustion phenomenon. For

Conclusions

turbulence, the SST- $k\omega$ RANS and the detached eddy simulation (DES) models are used, whereas for turbulence-chemistry interaction, the Flamelet generated manifold (FGM) and the Eddy dissipation concept (EDC) models are selected. The flow streamlines show the establishment of a toroidal vortical structure within the chamber that causes the recirculating exhaust to entrain into the fresh reactants. The differences in the predictions have been explained based on the capability of the models to predict mixing, ignition, and heat release. Overall, the DES-EDC model performs the best, particularly in capturing the temperature and the OH distribution. The RANS-EDC model predicts the location of the reaction zone downstream due to higher centreline velocity and slower mixing near the inlet. The FGM models ignite early close to the stoichiometric isosurfaces and highlight the necessity of defining a more comprehensive progress variable. The RANS-FGM model, however, predicts the location of the reaction zone more accurately as compared to the DES-FGM model rather fortuitously due to the compensating effects of delayed mixing by the RANS model and early ignition by the FGM model.

Finally, the validated numerical model (DES-EDC) is used to investigate the efficacy of four different scaling criteria on the performance of the combustion chamber under MILD conditions. The 3.3-kW chamber is scaled-up to 25-kW using constant velocity (CV), constant residence time (CRT), constant volume to jet momentum ratio (CM), and constant volume to jet kinetic energy ratio (CK) scaling criteria, of which the CM and CK criteria are novel criteria proposed in this work based on phenomenological observations pertaining to MILD combustion. The ratio of the oxidizer to fuel jet momentum is the key parameter in determining the mixing and velocity fields which is constant across all the cases. The pressure drop is the lowest for the CV case, followed by the CK, CM, and CRT cases due to lower velocities and higher channel dimensions. The temperature and velocity fields are nearly uniform across all the cases. The highest residence time is obtained for the CV case,

Conclusions

followed by the CK, CM, and CRT cases and leads to the lowest CO emissions for the CV case (339-ppm) and the highest for the CRT case (762-ppm), similar to the baseline. Both the instantaneous and mean temperature fields are nearly uniform throughout the chamber in the range of 1200 - 1300 K thereby leading to near zero NO_x emissions. However, the OH fields show that the reaction zone is most distributed for the CRT case and most compact for the CV case. Overall, the CV criterion performs the best in terms of pressure drop and CO emissions. The CRT criterion shows exactly the opposite trend in these parameters. The CM and CK criteria are potential alternatives to the CV and the CRT criteria in terms of their performance.

9.2 Contributions of the present work

The following are the major contributions of the present work:

- Syngas combustion in the reverse flow chamber under various combustion modes such as conventional, ultra-lean, transition, and MILD is analyzed for the first time.
- The noise measurements revealed the presence of longitudinal modes of oscillation that are strongest under conventional conditions. The MILD mode was observed to be least susceptible to the acoustics of the chamber due to a suppression of high frequency oscillations.
- Quantitative in-situ measurements of temperature and OH have been performed in the reverse flow chamber that provides insight into the reaction zone structure under the various combustion modes. The reaction zone is observed to be a complicated structure of thin regions near the inlet that progressively become distributed further downstream aided by passive advection of the OH radical.

Conclusions

- The chamber has achieved < 1 -ppm NO_x emissions for all the combustion modes showing the low emission capability of the combustor. The CO emissions are also low and vary between 32-ppm to 461-ppm across the four modes.
- Scaling of the combustion chamber (3.3-kW) to higher power ratings (25-kW) has been studied numerically. Two new scaling criteria are proposed, namely constant volume to jet momentum ratio (CM) and constant volume to jet kinetic energy ratio (CK) that perform reasonably well while overcoming challenges associated with other conventional scaling criteria such as constant velocity and constant residence time.

9.3 Recommendations for future work

The current thesis opens up several avenues for future research that can further enhance our understanding of reverse flow combustion of syngas. More precise quantification of temperature and OH can be performed using measurements of major species by Raman scattering. A detailed understanding of the flow field using PIV in this challenging environment can give us insights into the turbulence-chemistry interaction while providing quantitative data. Finally, investigation at higher pressures can provide more understanding of the physics at practically relevant conditions.

Bibliography

- [1] R.Y. T. Liewen, V. Yang, Synthesis gas combustion: fundamentals and applications, CRC Press, 2009.
- [2] IPCC, Carbon Dioxide Capture and Storage, Cambridge, UK Cambridge Univ. Press. (2005).
- [3] C. Descamps, C. Bouallou, M. Kanniche, Efficiency of an Integrated Gasification Combined Cycle (IGCC) power plant including CO₂ removal, *Energy*. 33 (2008) 874–881. doi:10.1016/j.energy.2007.07.013.
- [4] P.Sayad, A. Schönborn, J. Klingmann, Experimental investigation of the stability limits of premixed syngas-air flames at two moderate swirl numbers, *Combust. Flame*. 164 (2016) 270–282. doi:10.1016/j.combustflame.2015.11.026.
- [5] Y. Huang, V. Yang, Dynamics and stability of lean-premixed swirl-stabilized combustion, *Prog. Energy Combust. Sci.* 35 (2009) 293–364. doi:10.1016/j.pecs.2009.01.002.
- [6] M.C. Lee, J. Yoon, S. Joo, J. Kim, J. Hwang, Y. Yoon, Investigation into the cause of high multi-mode combustion instability of H₂/CO/CH₄ syngas in a partially premixed gas turbine model combustor, *Proc. Combust. Inst.* 35 (2015) 3263–3271. doi:10.1016/j.proci.2014.07.013.
- [7] D. Zhao, E. Gutmark, P. de Goey, A review of cavity-based trapped vortex, ultra-compact, high-g, inter-turbine combustors, *Prog. Energy Combust. Sci.* 66 (2018) 42–82. doi:10.1016/j.pecs.2017.12.001.
- [8] S. Krishna, R. V. Ravikrishna, Optical diagnostics of fuel-air mixing and vortex formation in a cavity combustor, *Exp. Therm. Fluid Sci.* 61 (2015) 163–176. doi:10.1016/j.expthermflusci.2014.10.012.
- [9] S. Krishna, R. V. Ravikrishna, Quantitative OH Planar Laser Induced Fluorescence Diagnostics of Syngas and Methane Combustion in a Cavity Combustor, *Combust. Sci. Technol.* 187 (2015) 1661–1682. doi:10.1080/00102202.2015.1047015.
- [10] S. Krishna, Laser-based Diagnostics and Numerical Simulations of Syngas Combustion in a Trapped Vortex Combustor, Indian Institute of Science, 2015.

Bibliography

- <http://etd.ncsi.iisc.ernet.in/handle/2005/2768>.
- [11] A.T. Evulet, A.M. ELKady, A.R. Branda, D. Chinn, On the Performance and Operability of GE's Dry Low NO_x Combustors utilizing Exhaust Gas Recirculation for PostCombustion Carbon Capture, *Energy Procedia*. 1 (2009) 3809–3816. doi:10.1016/j.egypro.2009.02.182.
- [12] G.M. Choi, M. Katsuki, Advanced low NO_x combustion using highly preheated air, *Energy Convers. Manag.* 42 (2001) 639–652. doi:10.1016/S0196-8904(00)00074-1.
- [13] M. Katsuki, T. Hasegawa, The science and technology of combustion in highly preheated air, in: *Symp. Combust.*, 1998: pp. 3135–3146. doi:10.1016/S0082-0784(98)80176-8.
- [14] M. Nishimura, T. Suzuki, R. Nakanishi, R. Kitamura, Low-NO_x combustion under high preheated air temperature condition in an industrial furnace, *Energy Convers. Manag.* (1997). doi:10.1016/S0196-8904(96)00165-3.
- [15] C. Ellul, M. Pourkashanian, A. Williams, K.A.M. Rabea, Effects of fuel composition in high temperature air combustion, *J. Energy Inst.* 81 (2008) 143–148. doi:10.1179/174602208X331643.
- [16] J. Wüning, Flameless oxidation to reduce thermal no-formation, *Prog. Energy Combust. Sci.* 23 (1997) 81–94. doi:10.1016/S0360-1285(97)00006-3.
- [17] D. Han, M.G. Mungal, Direct measurement of entrainment in reacting/nonreacting turbulent jets, *Combust. Flame*. 124 (2001) 370–386. doi:10.1016/S0010-2180(00)00211-X.
- [18] P. Gopalakrishnan, M.K. Bobba, J.M. Seitzman, Controlling mechanisms for low NO_x emissions in a non-premixed stagnation point reverse flow combustor, *Proc. Combust. Inst.* 31 II (2007) 3401–3408. doi:10.1016/j.proci.2006.07.256.
- [19] M.K. Bobba, Flame stabilization and mixing characteristics in a stagnation point reverse flow combustor, Georgia Institute of Technology, 2007. https://smartech.gatech.edu/bitstream/handle/1853/26502/bobba_mohan_k_200712_phd.pdf.
- [20] P. Gopalakrishnan, Effects of the Reacting Flowfield on Combustion Processes in a Stagnation Point Reverse Flow Combustor, Georgia Institute of Technology, 2008. http://seitzman.gatech.edu/priya_thesis_final.pdf.
- [21] A. Radhakrishnan, Self-sustained combustion of low grade solid fuels in a stagnation-point reverse-flow combustor, Georgia Institute of Technology, 2013.
- [22] A.R. Smith, J. Klosek, A review of air separation technologies and their integration

Bibliography

- with energy conversion processes, *Fuel Process. Technol.* (2001). doi:10.1016/S0378-3820(01)00131-X.
- [23] S. Beltaos, N. Rajaratnam, Circular Turbulent Jet in an Opposing Infinite Stream, in: *Proc. 1st Can. Hydr. Conf.*, 1973.
- [24] K.M. Lam, C.H.C. Chan, Time-Averaged Mixing Behavior of Circular Jet in Counterflow: Velocity and Concentration Measurements, *J. Hydraul. Eng.* (2002). doi:10.1061/(ASCE)0733-9429(2002)128:9(861).
- [25] M. Sivapragasam, M.D. Deshpande, S. Ramamurthy, P. White, Turbulent jet in confined counterflow, *Sadhana - Acad. Proc. Eng. Sci.* (2014). doi:10.1007/s12046-013-0225-2.
- [26] E. Villermaux, H. Rehab, Mixing in coaxial jets, *J. Fluid Mech.* 425 (2000) S002211200000210X. doi:10.1017/S002211200000210X.
- [27] N. Rajaratnam, Turbulent jets, *Dev. Water Sci.* 5 (1976) 303–304. doi:10.1016/S0167-5648(08)70915-8.
- [28] J. Wüning, Flammenlose Oxidation von Brennstoff mit hochvorgewärmter Luft, *Chemie Ing. Tech.* 63 (1991) 1243–1245. doi:10.1002/cite.330631219.
- [29] B.B. Dally, A.N. Karpetis, R.S. Barlow, Structure of turbulent non-premixed jet flames in a diluted hot coflow, *Proc. Combust. Inst.* 29 (2002) 1147–1154. doi:10.1016/S1540-7489(02)80145-6.
- [30] A. Cavaliere, M. De Joannon, Mild combustion, *Prog. Energy Combust. Sci.* 30 (2004) 329–366. doi:10.1016/j.pecs.2004.02.003.
- [31] H. Tsuji, A. Gupta, T. Hasegawa, M. Katsuki, K. Kishimoto, M. Morita, *High Temperature Air Combustion: From Energy Conservation to Pollution Reduction*, CRC Press, 2002.
- [32] V.K. Arghode, A.K. Gupta, Investigation of reverse flow distributed combustion for gas turbine application, *Appl. Energy.* 88 (2011) 1096–1104. doi:10.1016/j.apenergy.2010.10.039.
- [33] P. Li, B.B. Dally, J. Mi, F. Wang, MILD oxy-combustion of gaseous fuels in a laboratory-scale furnace, *Combust. Flame.* 160 (2013) 933–946. doi:10.1016/j.combustflame.2013.01.024.
- [34] A.E.E. Khalil, A.K. Gupta, Thermal field investigation under distributed combustion conditions, *Appl. Energy.* 160 (2015) 477–488. doi:10.1016/j.apenergy.2015.09.058.
- [35] A.A.V. Perpignan, A. Gangoli Rao, D.J.E.M. Roekaerts, Flameless combustion and its potential towards gas turbines, *Prog. Energy Combust. Sci.* 69 (2018) 28–62.

Bibliography

- doi:10.1016/j.pecs.2018.06.002.
- [36] A.G. Rao, Y. Levy, A new combustion methodology for low emission gas turbine engines, in: Proc. 8th Int. Symp. High Temp. Air Combust. Gasification., Pozan, Poland, 2010. https://www.researchgate.net/profile/Arvind_Gangoli_Rao/publication/303820917_A_New_Combustion_Methodology_for_Low_Emission_Gas_Turbine_Engines/links/5755e98e08ae10c72b66ebe3/A-New-Combustion-Methodology-for-Low-Emission-Gas-Turbine-Engines.pdf.
- [37] A. Cavigiolo, M.A. Galbiati, A. Effuggi, D. Gelosa, R. Rota, Mild combustion in a laboratory-scale apparatus, *Combust. Sci. Technol.* (2003). doi:10.1080/00102200302356.
- [38] T. Plessing, N. Peters, J.G. Wüning, Laseroptical investigation of highly preheated combustion with strong exhaust gas recirculation, in: Symp. Combust., 1998: pp. 3197–3204. doi:10.1016/S0082-0784(98)80183-5.
- [39] S. Kruse, B. Kerschgens, L. Berger, E. Varea, H. Pitsch, Experimental and numerical study of MILD combustion for gas turbine applications, *Appl. Energy.* 148 (2015) 456–465. doi:10.1016/j.apenergy.2015.03.054.
- [40] G.G. Szegö, B.B. Dally, G.J. Nathan, Scaling of NO_x emissions from a laboratory-scale mild combustion furnace, *Combust. Flame.* 154 (2008) 281–295. doi:10.1016/j.combustflame.2008.02.001.
- [41] G.G. Szegö, B.B. Dally, G.J. Nathan, Operational characteristics of a parallel jet MILD combustion burner system, *Combust. Flame.* 156 (2009) 429–438. doi:10.1016/j.combustflame.2008.08.009.
- [42] J. Ye, P.R. Medwell, E. Varea, S. Kruse, B.B. Dally, H.G. Pitsch, An experimental study on MILD combustion of prevaporised liquid fuels, *Appl. Energy.* 151 (2015) 93–101. doi:10.1016/j.apenergy.2015.04.019.
- [43] M. Castela, a. S. Veríssimo, A.M.A. Rocha, M. Costa, Experimental Study of the Combustion Regimes Occurring in a Laboratory Combustor, *Combust. Sci. Technol.* 184 (2012) 243–258. doi:10.1080/00102202.2011.630592.
- [44] A.S. Veríssimo, A.M.A. Rocha, M. Costa, Importance of the inlet air velocity on the establishment of flameless combustion in a laboratory combustor, *Exp. Therm. Fluid Sci.* 44 (2013) 75–81. doi:10.1016/j.expthermflusci.2012.05.015.
- [45] V.K. Arghode, A.K. Gupta, K.M. Bryden, High intensity colorless distributed combustion for ultra low emissions and enhanced performance, *Appl. Energy.* 92

Bibliography

- (2012) 822–830. doi:10.1016/j.apenergy.2011.08.039.
- [46] A.E.E. Khalil, V.K. Arghode, A.K. Gupta, Novel mixing for ultra-high thermal intensity distributed combustion, *Appl. Energy*. 105 (2013) 327–334. doi:10.1016/j.apenergy.2012.12.071.
- [47] M. Huang, Z. Zhang, W. Shao, Y. Xiong, Y. Liu, F. Lei, Y. Xiao, Effect of air preheat temperature on the MILD combustion of syngas, *Energy Convers. Manag.* 86 (2014) 356–364. doi:10.1016/j.enconman.2014.05.038.
- [48] T. Zornek, T. Monz, M. Aigner, Performance analysis of the micro gas turbine Turbec T100 with a new FLOX-combustion system for low calorific fuels, *Appl. Energy*. 159 (2015) 276–284. doi:10.1016/j.apenergy.2015.08.075.
- [49] B. Zhou, M. Costa, Z. Li, M. Aldén, X.S. Bai, Characterization of the reaction zone structures in a laboratory combustor using optical diagnostics: From flame to flameless combustion, *Proc. Combust. Inst.* 36 (2017) 4305–4312. doi:10.1016/j.proci.2016.06.182.
- [50] K. Kwiatkowski, E. Mastorakos, Regimes of Nonpremixed Combustion of Hot Low-Calorific-Value Gases Derived from Biomass Gasification, *Energy and Fuels*. 30 (2016) 4386–4397. doi:10.1021/acs.energyfuels.5b02580.
- [51] S. Pramanik, R. V. Ravikrishna, Reaction Zone Structure of Syngas Combustion under MILD and Conventional Conditions, in: 11th Asia-Pacific Conf. Combust., The University of Sydney, NSW Australia, 10th -14th December, 2017.
- [52] S. Pramanik, R. V. Ravikrishna, Non-premixed Combustion of Syngas Under MILD and Conventional Conditions, in: 25th Natl. Conf. IC Engines Combust., National Institute of Technology, Surathkal, Karnataka, India, 2017.
- [53] S. Pramanik, R. V. Ravikrishna, Large Eddy Simulation of MILD Combustion of Syngas, in: 11th Asia Pacific Conf. Combust., The University of Sydney, NSW Australia, 10th -14th December, 2017.
- [54] P.R. Medwell, P.A.M. Kalt, B.B. Dally, Imaging of diluted turbulent ethylene flames stabilized on a Jet in Hot Coflow (JHC) burner, *Combust. Flame*. 152 (2008) 100–113. doi:10.1016/j.combustflame.2007.09.003.
- [55] E. Oldenhof, M.J. Tummers, E.H. van Veen, D.J.E.M. Roekaerts, Ignition kernel formation and lift-off behaviour of jet-in-hot-coflow flames, *Combust. Flame*. 157 (2010) 1167–1178. doi:10.1016/j.combustflame.2010.01.002.
- [56] L.D. Arteaga Mendez, M.J. Tummers, E.H. Van Veen, D.J.E.M. Roekaerts, Effect of hydrogen addition on the structure of natural-gas jet-in-hot-coflow flames, *Proc.*

Bibliography

- Combust. Inst. 35 (2015) 3557–3564. doi:10.1016/j.proci.2014.06.146.
- [57] J. Sidey, E. Mastorakos, Visualization of MILD combustion from jets in cross-flow, Proc. Combust. Inst. 35 (2015) 3537–3545. doi:10.1016/j.proci.2014.07.028.
- [58] M.K. Bobba, P. Gopalakrishnan, A. Radhakrishnan, J. Seitzman, Y. Neumeier, B. Zinn, J. Jagoda, Flame Stabilization and Mixing Studies in a Novel Ultra-Low Emissions Combustor, 44th AIAA Aerosp. Sci. Meet. Exhib. (2006). doi:10.2514/6.2006-963.
- [59] Y. Minamoto, N. Swaminathan, S.R. Cant, T. Leung, Morphological and statistical features of reaction zones in MILD and premixed combustion, Combust. Flame. (2014). doi:10.1016/j.combustflame.2014.04.018.
- [60] Y. Minamoto, N. Swaminathan, Scalar gradient behaviour in MILD combustion, Combust. Flame. 161 (2014) 1063–1075. doi:10.1016/j.combustflame.2013.10.005.
- [61] N.A.K. Doan, N. Swaminathan, Y. Minamoto, DNS of MILD combustion with mixture fraction variations, Combust. Flame. (2018). doi:10.1016/j.combustflame.2017.10.030.
- [62] P.J. Coelho, N. Peters, Numerical simulation of a mild combustion burner, Combust. Flame. 124 (2001) 503–518. doi:10.1016/S0010-2180(00)00206-6.
- [63] M. Graça, A. Duarte, P.J. Coelho, M. Costa, Numerical simulation of a reversed flow small-scale combustor, Fuel Process. Technol. (2013). doi:10.1016/j.fuproc.2012.06.028.
- [64] C. Duwig, P. Iudiciani, Large Eddy Simulation of turbulent combustion in a stagnation point reverse flow combustor using detailed chemistry, Fuel. (2014). doi:10.1016/j.fuel.2014.01.072.
- [65] S. Undapalli, S. Srinivasan, S. Menon, LES of premixed and non-premixed combustion in a stagnation point reverse flow combustor, Proc. Combust. Inst. 32 I (2009) 1537–1544. doi:10.1016/j.proci.2008.06.167.
- [66] M. Ihme, Y.C. See, LES flamelet modeling of a three-stream MILD combustor: Analysis of flame sensitivity to scalar inflow conditions, Proc. Combust. Inst. (2011). doi:10.1016/j.proci.2010.05.019.
- [67] M. Ihme, J. Zhang, G. He, B. Dally, Large-eddy simulation of a jet-in-hot-coflow burner operating in the oxygen-diluted combustion regime, Flow, Turbul. Combust. 89 (2012) 449–464. doi:10.1007/s10494-012-9399-7.
- [68] J. Lamouroux, M. Ihme, B. Fiorina, O. Gicquel, Tabulated chemistry approach for diluted combustion regimes with internal recirculation and heat losses, Combust.

Bibliography

- Flame. (2014). doi:10.1016/j.combustflame.2014.01.015.
- [69] B. Danon, W. De Jong, D.J.E.M. Roekaerts, Experimental and numerical investigation of a FLOX combustor firing low calorific value gases, *Combust. Sci. Technol.* (2010). doi:10.1080/00102201003639284.
- [70] A. De, E. Oldenhof, P. Sathiah, D. Roekaerts, Numerical simulation of Delft-Jet-in-Hot-Coflow (DJHC) flames using the eddy dissipation concept model for turbulence-chemistry interaction, *Flow, Turbul. Combust.* 87 (2011) 537–567. doi:10.1007/s10494-011-9337-0.
- [71] M.J. Evans, P.R. Medwell, Z.F. Tian, Modeling Lifted Jet Flames in a Heated Coflow using an Optimized Eddy Dissipation Concept Model, *Combust. Sci. Technol.* (2015). doi:10.1080/00102202.2014.1002836.
- [72] J. Aminian, C. Galletti, S. Shahhosseini, L. Tognotti, Key modeling issues in prediction of minor species in diluted-preheated combustion conditions, *Appl. Therm. Eng.* (2011). doi:10.1016/j.applthermaleng.2011.06.007.
- [73] J. Aminian, C. Galletti, S. Shahhosseini, L. Tognotti, Numerical investigation of a MILD combustion burner: Analysis of mixing field, chemical kinetics and turbulence-chemistry interaction, *Flow, Turbul. Combust.* (2012). doi:10.1007/s10494-012-9386-z.
- [74] Y. Afarin, S. Tabejamaat, Effect of hydrogen on H₂/CH₄ flame structure of MILD combustion using the les method, *Int. J. Hydrogen Energy.* (2013). doi:10.1016/j.ijhydene.2012.12.065.
- [75] A. Parente, M.R. Malik, F. Contino, A. Cuoci, B.B. Dally, Extension of the Eddy Dissipation Concept for turbulence/chemistry interactions to MILD combustion, *Fuel.* (2016). doi:10.1016/j.fuel.2015.09.020.
- [76] L. Cifuentes, E. Fooladgar, C. Duwig, Chemical Explosive Mode Analysis for a Jet-in-Hot-Coflow burner operating in MILD combustion, *Fuel.* 232 (2018) 712–723. doi:10.1016/j.fuel.2018.05.171.
- [77] R.M. Kulkarni, W. Polifke, LES of Delft-Jet-In-Hot-Coflow (DJHC) with tabulated chemistry and stochastic fields combustion model, *Fuel Process. Technol.* (2013). doi:10.1016/j.fuproc.2012.06.015.
- [78] R. Bhaya, A. De, R. Yadav, Large eddy simulation of mild combustion using PDF-based turbulence-chemistry interaction models, *Combust. Sci. Technol.* (2014). doi:10.1080/00102202.2014.916702.
- [79] J. Van Oijen, Direct numerical simulation of autoigniting mixing layers in MILD

Bibliography

- combustion, *Proc. Combust. Inst.* (2013). doi:10.1016/j.proci.2012.05.070.
- [80] Y. Minamoto, T.D. Dunstan, N. Swaminathan, R.S. Cant, DNS of EGR-type turbulent flame in MILD condition, *Proc. Combust. Inst.* (2013). doi:10.1016/j.proci.2012.06.041.
- [81] S. Pramanik, R.V. Ravikrishna, Reaction zone structure of syngas combustion under MILD and conventional conditions, in: 11th Asia-Pacific Conf. Combust. ASPACC 2017, 2017.
- [82] D.B. Spalding, H.C. Hottel, S.L. Bragg, A.H. Lefebvre, D.G. Shepherd, A.C. Scurlock, The art of partial modeling, *Symp. Combust.* 9 (1963) 833–843. doi:10.1016/S0082-0784(63)80090-9.
- [83] R. Weber, Scaling characteristics of aerodynamics, heat transfer, and pollutant emissions in industrial flames, *Symp. Combust.* 26 (1996) 3343–3354. doi:10.1016/S0082-0784(96)80182-2.
- [84] R. Weber, F. Breussin, Scaling properties of swirling pulverized coal flames: From 180 kW to 50 MW thermal input, in: *Symp. Combust.*, 1998: pp. 2957–2964. doi:10.1016/S0082-0784(98)80155-0.
- [85] J.P. Smart, D.J. Morgan, P.A. Roberts, The effect of scale on the performance of swirl stabilised pulverised coal burners, *Symp. Combust.* 24 (1992) 1365–1372. doi:10.1016/S0082-0784(06)80159-1.
- [86] J.P. Smart, D.J. Morgan, Exploring the Effects of Employing Different Scaling Criteria on Swirl Stabilised Pulverised Coal Burner Performance, *Combust. Sci. Technol.* 100 (1994) 331–343. doi:10.1080/00102209408935459.
- [87] T.C.A. Hsieh, W.J.A. Dahm, J.F. Driscoll, Scaling laws for NO(x) emission performance of burners and furnaces from 30 kW to 12 MW, *Combust. Flame.* 114 (1998) 54–80. doi:10.1016/S0010-2180(97)00289-7.
- [88] J.A. Cole, T.P. Parr, N.C. Widmer, K.J. Wilson, K.C. Schadow, W.R. Seeker, Scaling criteria for the development of an acoustically stabilized dump combustor, *Proc. Combust. Inst.* 28 (2000) 1297–1304. doi:10.1016/S0082-0784(00)80343-4.
- [89] A.D. Al-Fawaz, L.M. Dearden, J.T. Hedley, M. Missaghi, M. Pourkashanian, A. Williams, L.T. Yap, NO_x formation in geometrically scaled gas-fired industrial burners, *Symp. Combust.* 25 (1994) 1027–1034. doi:10.1016/S0082-0784(06)80740-X.
- [90] S. Kumar, P.J. Paul, H.S. Mukunda, Investigations of the scaling criteria for a mild combustion burner, *Proc. Combust. Inst.* 30 II (2005) 2613–2621. doi:10.1016/j.proci.2004.07.045.

Bibliography

- [91] A.E.E. Khalil, A.K. Gupta, Swirling flowfield for colorless distributed combustion, *Appl. Energy*. 113 (2014) 208–218. doi:10.1016/j.apenergy.2013.07.029.
- [92] A.E.E. Khalil, A.K. Gupta, Fuel property effects on distributed combustion, *Fuel*. 171 (2016) 116–124. doi:10.1016/j.fuel.2015.12.068.
- [93] X. Silvani, F. Morandini, Fire spread experiments in the field: Temperature and heat fluxes measurements, *Fire Saf. J.* (2009). doi:10.1016/j.firesaf.2008.06.004.
- [94] R. Sadanandan, P. Kutne, A. Steinberg, W. Meier, Investigation of the syngas flame characteristics at elevated pressures using optical and laser diagnostic methods, in: *Flow, Turbul. Combust.*, 2012. doi:10.1007/s10494-011-9354-z.
- [95] Spectra-Physics, (n.d.). <https://www.spectra-physics.com/products/high-energy-pulsed-lasers/cobra-stretch#4> (accessed September 11, 2018).
- [96] L. GmbH, *LaVision Product Manual*, Göttingen, 2008.
- [97] J. Li, Z. Zhao, A. Kazakov, M. Chaos, F.L. Dryer, A Comprehensive Kinetic Mechanism for CO, CH₂O, and CH₃OH Combustion, *Int. J. Chem. Kinet.* 39 (2007) 109–136. doi:10.1002/kin.20218.
- [98] M.P. Burke, M. Chaos, Y. Ju, F.L. Dryer, S.J. Klippenstein, Comprehensive H₂/O₂ kinetic model for high-pressure combustion, *Int. J. Chem. Kinet.* 44 (2012) 444–474. doi:10.1002/kin.20603.
- [99] A. Mardani, A. Fazlollahi Ghomshi, Numerical study of oxy-fuel MILD (moderate or intense low-oxygen dilution combustion) combustion for CH₄-H₂fuel, *Energy*. 99 (2016) 136–151. doi:10.1016/j.energy.2016.01.016.
- [100] V. Mahendra Reddy, D. Sawant, D. Trivedi, S. Kumar, Studies on a liquid fuel based two stage flameless combustor, *Proc. Combust. Inst.* 34 (2013) 3319–3326. doi:10.1016/j.proci.2012.06.028.
- [101] M. Ditaranto, J. Hals, Combustion instabilities in sudden expansion oxy-fuel flames, *Combust. Flame*. 146 (2006) 493–512. doi:10.1016/j.combustflame.2006.04.015.
- [102] A.H. Lefebvre, D.R. Ballal, *Gas turbine combustion: alternative fuels and emissions*, 2010. doi:10.1002/1521-3773(20010316)40:6<9823::AID-ANIE9823>3.3.CO;2-C.
- [103] Y. Huang, V. Yang, Effect of swirl on combustion dynamics in a lean-premixed swirl-stabilized combustor, *Proc. Combust. Inst.* 30 II (2005) 1775–1782. doi:10.1016/j.proci.2004.08.237.
- [104] A.B. Sahu, S. Krishna, R. V. Ravikrishna, Quantitative OH measurements and numerical investigation of H₂/CO kinetics in syngas-air counterflow diffusion flames, *Fuel*. (2017). doi:10.1016/j.fuel.2016.12.023.

Bibliography

- [105] F.T.C. Yuen, Ö.L. Gülder, Premixed turbulent flame front structure investigation by Rayleigh scattering in the thin reaction zone regime, *Proc. Combust. Inst.* (2009). doi:10.1016/j.proci.2008.08.005.
- [106] J. a Sutton, J.F. Driscoll, Rayleigh scattering cross sections of combustion species at 266, 355, and 532 nm for thermometry applications., *Opt. Lett.* 29 (2004) 2620–2622. doi:10.1364/OL.29.002620.
- [107] P.R. Medwell, P.A.M. Kalt, B.B. Dally, Simultaneous imaging of OH, formaldehyde, and temperature of turbulent nonpremixed jet flames in a heated and diluted coflow, *Combust. Flame.* 148 (2007) 48–61. doi:10.1016/j.combustflame.2006.10.002.
- [108] S. Yoon, E.L. Knuth, R.J. Cattolica, OH concentration in an atmospheric-pressure methane-air flame from molecular-beam mass spectrometry and laser-absorption spectroscopy, *Combust. Sci. Technol.* 28 (1982) 225–239. doi:10.1080/00102208208952557.
- [109] M.J. Dunn, A.R. Masri, A comprehensive model for the quantification of linear and nonlinear regime laser-induced fluorescence of OH under $A2\Sigma^+ \leftarrow X2\Pi(1,0)$ excitation, *Appl. Phys. B Lasers Opt.* 101 (2010) 445–463. doi:10.1007/s00340-010-4129-0.
- [110] P.H. Paul, Vibrational Energy Transfer and Quenching of OH $A2\Sigma^+(v'=1)$ Measured at High Temperatures in a Shock Tube, *J. Chem. Phys.* 99 (1995) 8472–8476. doi:10.1021/j100021a004.
- [111] M. Tamura, P.A. Berg, J.E. Harrington, J. Luque, J.B. Jeffries, G.P. Smith, D.R. Crosley, Collisional quenching of CH(A), OH(A), and NO(A) in low pressure hydrocarbon flames, *Combust. Flame.* 114 (1998) 502–514. doi:10.1016/S0010-2180(97)00324-6.
- [112] P.H. Paul, A model for temperature-dependent collisional quenching of OH $A2\Sigma^+$, *J. Quant. Spectrosc. Radiat. Transf.* 51 (1994) 511–524. doi:10.1016/0022-4073(94)90150-3.
- [113] G.P. Smith, D.M. Golden, M. Frenklach, N.W. Moriarty, B. Eiteneer, GRI-Mech 3.0, (2000). <http://combustion.berkeley.edu/gri-mech/version30/text30.html>.
- [114] F.R. Menter, Two-equation eddy-viscosity turbulence models for engineering applications, *AIAA J.* 32 (1994) 1598–1605. doi:10.2514/3.12149.
- [115] F.R. Menter, M. Kuntz, R. Langtry, Ten Years of Industrial Experience with the SST Turbulence Model, *Turbul. Heat Mass Transf.* 4. 4 (2003) 625–632. doi:10.4028/www.scientific.net/AMR.576.60.

Bibliography

- [116] E. Abtahizadeh, P. De Goey, J. Van Oijen, Development of a novel flamelet-based model to include preferential diffusion effects in autoignition of CH₄/H₂ flames, *Combust. Flame*. 162 (2015) 4358–4369. doi:10.1016/j.combustflame.2015.06.015.
- [117] S.B. Pope, Computationally efficient implementation of combustion chemistry using in situ adaptive tabulation, *Combust. Theory Model.* (1997). doi:10.1088/1364-7830/1/1/006.
- [118] L.M. Verhoeven, W.J.S. Ramaekers, J.A. van Oijen, L.P.H. De Goey, Modeling non-premixed laminar co-flow flames using flamelet-generated manifolds, *Combust. Flame*. 159 (2012) 230–241. doi:10.1016/j.combustflame.2011.07.011.
- [119] V. Zimont, W. Polifke, M. Bettelini, W. Weisenstein, An Efficient Computational Model for Premixed Turbulent Combustion at High Reynolds Numbers Based on a Turbulent Flame Speed Closure, *J. Eng. Gas Turbines Power*. 120 (1998) 526. doi:10.1115/1.2818178.
- [120] W.P. Jones, R.P. Lindstedt, Global reaction schemes for hydrocarbon combustion, *Combust. Flame*. 73 (1988) 233–249. doi:10.1016/0010-2180(88)90021-1.
- [121] V. Parisi, Large Eddy Simulation of a Non-Premixed Stagnation Point Reverse Flow Combustor, Georgia Institute of Technology, 2006. <http://hdl.handle.net/1853/13995>.
- [122] R.L.G.M. Eggels, L.P.H. de Goey, Mathematically reduced reaction mechanisms applied to adiabatic flat hydrogen/air flames, *Combust. Flame*. (1995). doi:10.1016/0010-2180(94)00108-5.
- [123] W.J.S. Ramaekers, J.A. Van Oijen, L.P.H. De Goey, A priori testing of flamelet generated manifolds for turbulent partially premixed methane/air flames, *Flow, Turbul. Combust.* (2010). doi:10.1007/s10494-009-9223-1.
- [124] E. Knudsen, H. Pitsch, Capabilities and limitations of multi-regime flamelet combustion models, *Combust. Flame*. (2012). doi:10.1016/j.combustflame.2011.05.025.
- [125] A.W. Vreman, B.A. Albrecht, J.A. van Oijen, L.P.H. de Goey, R.J.M. Bastiaans, Premixed and nonpremixed generated manifolds in large-eddy simulation of Sandia flame D and F, *Combust. Flame*. (2008). doi:10.1016/j.combustflame.2008.01.009.
- [126] T.C. Lieuwen, Unsteady combustor physics, 2009. doi:10.1017/CBO9781139059961.
- [127] M.U. Göktolga, J.A. Van Oijen, L.P.H. De Goey, Modeling MILD combustion using a novel multistage FGM method, *Proc. Combust. Inst.* (2017). doi:10.1016/j.proci.2016.06.004.
- [128] F.M. White, *Viscous Fluid Flow* Viscous, New York. Second (2000) 413.

Bibliography

- [129] H. Liu, S.H. Winoto, D. a Shah, Velocity measurements within confined turbulent jets: application to cardiovalvular regurgitation, *Ann. Biomed. Eng.* 25 (1997) 939–48. doi:10.1007/BF02648120.
- [130] S.R. Turns, F.H. Myhr, Oxides of nitrogen emissions from turbulent jet flames: Part I- Fuel effects and flame radiation, *Combust. Flame.* 87 (1991) 319–335. doi:10.1016/0010-2180(91)90116-S.